GLACIER VELOCITIES AND ICE DYNAMICS IN THE ST. ELIAS MOUNTAINS, YUKON-ALASKA

BRITTANY MAIN

A thesis submitted in partial fulfillment of the requirements for the

Doctorate in Philosophy degree in Geography

Department of Geography, Environment, and Geomatics

Faculty of Arts

University of Ottawa

Abstract

Despite their relatively small ice volume, mountain glaciers contributed nearly one third of global sea level rise since 2000, with one of the largest total mass loss rates (73 ± 17 Gt a^{-1}) occurring in the Yukon-Alaska region. However, there is uncertainty surrounding how ice dynamics are being affected by such losses and whether glacier flow instabilities, such as surges, are changing in a warming climate. The St. Elias Mountains contain a major cluster of surge-type glaciers, yet a detailed analysis of their characteristics, including surge frequency, morphology, magnitude, and propensity over time has not been undertaken on a regional basis. This thesis presents a review of surging behaviour and an updated surge event inventory in the St. Elias Mountains, and quantifies the processes influencing both surging and non-surging glacier velocity variability using a variety of remote sensing and field measurements.

An updated inventory of surge-type glaciers and observed surge events (1874-2023), compiled from existing inventories, recently published articles, and velocity analysis, is used to analyze the characteristics of surge-type glaciers and velocity patterns during surge events. The modern (1985-2023) trends in annual, winter and summer velocities of selected surge-type glaciers is then used to classify dynamic instability events into 4 categories. While 231 glaciers were classified as surge-type, only 42 were observed to have experienced rapid velocity events over the period 1985-2023, through either direct measurements or remote sensing observations. For glaciers with observed rapid velocity events, these predominantly fall into two categories: Alaskan-style surges with short active and quiescent phases, and glacier pulses, which are velocity accelerations that are limited in both magnitude and extent.

An unnamed former tributary to Kluane Glacier underwent a dramatic surge from 2013-18. Using a combination of air photos, remote sensing and field observations, the characteristics and changes of 'Little Kluane Glacier' were reconstructed from the 1940s until 2021. While only the single full surge of 2013-18 was identified, it is likely that a partial surge of just the upper north arm occurred between 1963 and 1972. Repeat Digital Elevation Models (DEMs) and velocity profiles show that the recent surge initiated from the upper north arm accumulation area in 2013, which developed into a full surge of the main trunk from 2017-18. Terminus positions show long-term retreat from 1949-2017, followed by rapid advance of >2 km from May to September 2018, with surface velocities reaching a peak of ~3600 m a^{-1} in summer 2018 over the lower ablation area. This was

likely enhanced by the drainage of supraglacial lakes and streams to the glacier bed through crevassing as the surge progressed. Changes in surface topography caused by initial mass movement, the resulting reorganization of the supraglacial hydrological system, and ponding of surface water, may drive a partial surge into a full surge, and therefore exert a direct control on glacier dynamics.

In May 2016, Kaskawulsh Glacier underwent a dramatic proglacial hydrologic reorganization instigated by the rapid drainage of proglacial Slims Lake: as a result, water which previously drained north into Ä'äy Chú, (Slims River) toward Lhú'áán Män (Kluane Lake), was redirected south into Kaskawulsh River, eventually flowing into the Gulf of Alaska. A long-term (up to ~120 year) record of terminus retreat, thinning and surface velocities from in-situ and remote sensing observations is used to determine the impact of this reorganization on glacier dynamics. After an initial deceleration during the late 1990s, terminus velocities increased at a rate of 3 m a^{-2} from 2000-12, while the area of proglacial Slims Lake increased simultaneously. The rapid drainage of the lake substantially altered the velocity profile of the adjacent glacier, decreasing annual velocities by 48% within 3 km of the terminus between 2015 and 2021, at an average rate of ~12.5 m a^{-2}. A key cause of the rapid drop in glacier motion was a reduction in flotation of the lower part of the terminus after lake drainage. This has important implications for glacier dynamics and provides one of the first assessments of the impacts of a rapid proglacial lake drainage event on local terminus velocities.

The results of this study provide an examination of factors controlling glacier dynamics, as well as the characteristics of rapid glacier velocity events, in the St. Elias Mountains. This provides insights into the behaviour of mountain glaciers, how they are changing in a warming climate, controls on glacier surging, and the hazards they may pose for downstream communities, which are particularly vulnerable to disturbances.

Preface

Thesis Format

This doctoral thesis is written in article format and consists of three manuscripts (Chapters 2, 3, and 4). Chapter 1 provides the Introduction, including an outline of the literature motivating the work in this thesis. Chapter 2 provides an updated inventory of surge-type glaciers and surge events in the St. Elias Mountains from 1874-2023, as well as a detailed assessment of observed rapid glacier velocity events from 1985 to 2023. Chapter 3 uses a dataset of glacier velocities and optical images to create a comprehensive analysis of the surging behaviour of "Little Kluane Glacier" (unofficial name) from the 1940's until 2021, and establishes the first observed partial surge of a glacier in the St. Elias Mountains. Chapter 4 delivers a detailed study of the dynamics at the terminus of Kaskawulsh Glacier, through the analysis of historical imagery, glacier velocities, terminus positions, ice surface elevations and proglacial lake areas from 1899-2021. Chapter 5 synthesizes the findings of these articles, presenting key findings and discussing areas for future research. References are listed at the end of each respective chapter.

Chapter 4 has been published in the Journal of Glaciology, and Chapter 3 has been submitted for review in the Journal of Glaciology, so those chapters reflect the stylistic requirements for that journal. Chapter 2 will be submitted to a peer-reviewed journal after completion of the thesis. The titles and authorship for the resulting papers are as follows:

Chapter 2: Main B, Copland L, Dow C, Van Wychen W, Sevestre H, and Samsonov S. (In preparation). Characteristics of observed glacier surges in the St. Elias Mountains, Yukon-Alaska.

Chapter 3: Main B, Copland L, Flowers G, Dow C, Van Wychen W, Samsonov S, Kochtitzky W. (In review – Journal of Glaciology). Little Kluane Glacier: varying dynamic instabilities in a medium-sized glacier, Yukon, Canada.

Chapter 4: Main B, Copland L, Smeda B, Kochtitzky W, Samsonov S, Dudley J, Skidmore M, Dow C, Van Wychen W, Medrzycka D, Higgs E and Mingo L. (2023) Terminus change of Kaskawulsh Glacier, Yukon, under a warming climate: retreat, thinning, slowdown and modified proglacial lake geometry. Journal of Glaciology, 69(276), 936-952. https://doi.org/10.1017/jog.2022.114.

Author Contributions

I am the primary author for each chapter and am responsible for the research methodology, satellite image processing, fieldwork and data collection, data analysis, and manuscript writing, with guidance and input from my supervisor, Luke Copland. Specific contributions of co-authors to the individual manuscripts are as follows:

Chapter 2: Heidi Sevestre provided the initial surge-type glacier inventory. Luke Copland contributed to the manuscript conceptualization. All co-authors contributed to the final manuscript.

Chapter 3: Luke Copland and Christine Dow contributed to data collection in the field, including photographic surveys of the glacier surface. Sergey Samsonov provided the GAMMA speckle-tracking algorithm to derive unfiltered surface velocities. Will Kochtitzky provided the DEM dataset. Gwenn Flowers contributed the ice thickness dataset. Christine Dow, Gwenn Flowers and Wesley Van Wychen provided guidance during the manuscript conceptualization. All co-authors contributed to reviewing and editing the final manuscript.

Chapter 4: Luke Copland, Christine Dow, and Dorota Medrzycka contributed to data collection in the field, including dGPS development, construction and deployment, and photogrammetric surveys of the glacier surface. Laurent Mingo built and operated the ice penetrating radar system. Sergey Samsonov and Jonathon Dudley provided the GAMMA speckle-tracking algorithm to derive unfiltered surface velocities. Braden Smeda provided the majority of the terminus position dataset. Will Kochtitzky provided the satellite-derived DEM dataset. Dorota Medrzycka processed the lakebed DEM using Structure from Motion. Eric Higgs provided the historical images via the Mountain Legacy Project. Christine Dow processed the ice thickness dataset. All co-authors contributed to the final manuscript. Changes to the manuscript were also made in response to reviews by Dr. Jenna Sutherland and Dr. Martin Truffer for the Journal of Glaciology, and input from editor Dr. Liss Andreassen.

Table of Contents

List of Tables

List of Figures

Acknowledgements

I would first like to thank my supervisor, Dr. Luke Copland, without whom this thesis would not have been possible. The opportunities that I have been provided to work on glaciers in the Yukon, Canadian high Arctic, and Svalbard have provided a wealth of hands-on experience which will guide my career moving forward. On a personal level, I thank Luke for his support and compassion during the particularly challenging moments of this degree, and the endless encouragement to keep going, even when progress felt impossible. You have shown me that being a mentor has so many more facets than simply producing excellent work, and I thank you for the guidance during this journey.

I would like to acknowledge that the field research for this thesis was conducted on the Traditional Territory of Kluane First Nation (KFN), White River First Nation, and the Champagne and Aishihik First Nation (CAFN). I thank these communities and Parks Canada for permission to work there, and hope we can continue to build these partnerships moving forward.

This work would not have been possible without the financial support of various organizations who provided grants and scholarships. Support for this project was provided by the Natural Sciences and Engineering Research Council of Canada, Ontario Graduate Scholarship, Canada Foundation for Innovation, New Frontiers in Research Fund, Canada Research Chairs Program, Polar Continental Shelf Program, Ontario Research Fund, University of Ottawa, Kluane Lake Research Station, Northern Scientific Training Program, Royal Canadian Geographical Society, Canada Centre for Mapping and Earth Observation (Natural Resources Canada), Canadian Space Agency (RADARSAT Constellation Mission Data Utilization and Application Plan), Library and Archives Canada, and Parks Canada. Support for travel to conferences and attendance of courses was generously provided by the ArcticNet Network of Centres of Excellence Canada Student Training Fund, GlacioEx, and RemoteEx. Travel to conferences and attendance of courses was also generously supported by the RemoteEx project of the Norwegian Centre for International Cooperation in Higher Education (SIU), ArcticNet Network of Centres of Excellence Canada, and the International Arctic Science Committee.

To all members, past and present of the Laboratory for Cryospheric Research at the University of Ottawa, thank you for the endless memories and support, and I look forward to collaborating with you moving forward. I also wish to thank my committee members, Dr. Christine Dow, Dr. David

Burgess, Dr. Anders Knudby and external examiner Dr. Tim Bartholomaus for their time, feedback, and contributions to this thesis. I would like to specifically thank Dr. Christine Dow for her personal mentorship throughout this process, and for her support both in academia and in larger life.

Finally, it would not have been possible to complete this thesis without the unwavering support of my family and friends. To my family, especially my parents Debbie and William Main, sister Callan Langdon, Aunt Carol and Uncle John, thank you for encouraging me to stay curious, and to keep moving forward on my own path. Your support has made all of the difference on this journey. Chris, thank you for the good years. To my dear friends Ian Gabriel, Conor Kelly, and Olivia Mussells, thank you for supporting me in immeasurable and countless ways.

Chapter 1: Introduction

Recent studies have highlighted the impact of anthropogenic climate change on the cryosphere, resulting in significant changes across the Arctic and sub-Arctic mountain regions. Since 1971, mean annual air temperatures in the Arctic have risen by ~3°C, at a rate of more than three times the global average (Cowtan and Way, 2014; AMAP, 2021; IPCC, 2021). Over the same time period, total Arctic precipitation also increased by 9%, dominated mainly by a 25% increase in rainfall, although there is higher uncertainty in these trends (Copernicus, 2020; IPCC, 2021). Some of the major impacts of Arctic warming include marked decreases in glacier extents, areas and mass balance, particularly since the start of the 21st century (Zemp and others, 2019; Hugonnet and others, 2021; Kochtitzky and Copland, 2022).

While it can be difficult to establish long-term glacier trends due to variability in response times and lack of historical data, across the Arctic there have been consistent, and accelerating, retreat of glacier termini from their Little Ice Age (LIA) maxima, as well as significant area losses (WGMS, 2015; Gutiérrez and others, 2021; AMAP, 2021). During the period 2000-19, all glaciated regions outside of the ice sheets lost land ice mass at an average rate of -267 ± 16 Gt a^{-1}, with loss accelerating at 48 ± 16 Gt a^{-1} per decade (Hugonnet and others, 2021). One result of increasingly negative mass balance in the Canadian Arctic Archipelago, Alaska and Greenland is down-wasting and/or thinning of glaciers, which can further accelerate mass losses by shifting the Equilibrium Line Altitude (ELA) further up-glacier, and exposing a larger area to higher temperatures (Arendt and others, 2002; Muskett and others, 2008; Ciracì and others, 2020). Some studies have demonstrated an extensive slow-down of glacier velocities in regions associated with negative mass balance, including Alaska, the Caucasus, and the Canadian High Arctic (Heid and Kääb, 2012; Schaffer and others, 2017; Thomson and Copland, 2018). A significant global effect of the loss of Arctic land ice is their contribution to global sea level rise (SLR), which has increased every successive decade since the 1970s (IPCC, 2021).

Glacier sensitivity, or response time, to changes in mass balance varies based on individual glacier size and local characteristics such as the equilibrium line altitude and accumulation area ratio (Furbish and Andrews, 1984). It has been suggested that the committed losses required to balance glacier geometries with the current climate will increase as the Arctic continues to warm (Fox-Kemper and others, 2021; Young and others, 2021). In addition, the relationships between

increasing surface melt and ice dynamics (such as increases in glacier motion via basal sliding due to increased meltwater routing to the bed) are particularly complex, and differ between land-terminating, calving and ice-shelf-terminating glaciers (Moon and others, 2012; Enderlin and others, 2014). A major uncertainty in projecting sea level rise is the impact of a warming climate on glacier velocities: some argue that increased surface melt will lead to glacier acceleration through increased basal lubrication and bed-ice decoupling (Zwally and others, 2002; Nanni and others, 2020), but others suggest that increased melt will result in a net slowdown caused by increased efficiency of the subglacial drainage system (Werder and others, 2013; Burgess and others, 2013a; Tedstone and others, 2015).

Glaciers and ice caps outside of Greenland and Antarctica are projected to contribute between 79-157 mm sea level equivalent by the end of the century, making these the largest contributors to SLR associated with 21st century warming (Huss and Hock, 2015; Fox-Kemper and others, 2021; AMAP, 2021). The latest global climate predictions suggest that by 2100, mean annual air temperatures in the Arctic will rise by a minimum of 3.3°C above the 1985-2014 average (AMAP, 2021). However, a key component that is currently not well constrained within these existing projections is the contribution of glacier dynamics, and therefore without a more comprehensive understanding of how ice dynamics will impact glacier velocities under a warming climate, it is not possible to properly quantify this impact on SLR projections.

1.1 Ice dynamics and fast glacier flow

Glaciers deform and flow due to stresses stemming from gravity and the overlying weight of the ice, known as internal deformation. The rate of internal deformation is based on the driving stress, which is a combination of gravitational acceleration, ice thickness, surface slope and a number of other factors (Benn and Evans, 2010; Dobhal, 2011). At long time scales, glacier velocities are governed through glacier mass balance, known as the balance velocity: to maintain a steady state, the glacier must transfer mass gained in the accumulation area to replace that lost in the ablation zone, and ice discharge through any vertical cross-section on the glacier must equal the rate of net mass gain up-glacier of it (Benn and Evans, 2010; Jiskoot, 2011a). However, glacier motion can vary spatially and temporally due to internal (e.g., ice thickness, ice temperature) and external (e.g., glacier bed properties, proglacial lake presence) factors. Glacier dynamics refers to the ice flow processes which occur as a result of the interaction between forces resisting ice motion (e.g.,

friction) and those factors which increase ice movement (e.g., gravity or basal lubrication) (Jiskoot, 2011b). Basal sliding, or slip at the ice-bed interface, is another mechanism by which glaciers flow by overcoming resistive forces (e.g., basal drag) at the glacier bed, and usually contributes more to glacial motion than internal deformation: as basal water pressure increases, the glacier can decouple from the bed, allowing the ice to accelerate rapidly, lubricating flow (Willis, 1995).

Fast glacier flow is found in three main forms: ice streams, surging, and tidewater glaciers, and is underpinned by fast basal sliding, rather than rapid creep (Clarke, 1987). Some glaciologists have theorized that surging glaciers can be studied to understand fast flow mechanisms as a whole: since these entities fluctuate between fast and slow flow cyclically, they must therefore traverse the threshold between the physical processes governing slow and fast flow numerous times (Clarke, 1987). Globally, knowledge of surge-type glacier behaviour has the potential to advance understanding of dynamic ice flow instabilities, to understand how these dynamics will respond to a warming climate, and how this will ultimately impact sea level rise (Yde and Paasche, 2010). Ice flow dynamics underpinning glacier surges have been regarded as analogous to ice stream behaviour: these regions of fast flow within ice sheets exert a substantial influence on ice sheet stability, and if climatic warming enhances ice flow, these features have the potential to contribute significantly to global sea level rise (Benn and Evans, 2010; Jiskoot, 2011a). Initial surge-like behaviour of ice caps or sheets may cause them to transition into ice streams, which have long term, consistently high ice flow. For example, as Vavilov Ice Cap, Severnaya Zemlya, evolved from surge-like behaviour beginning in 2013, to an ice stream regime, 11% of the basin mass was lost over a 6-year period (Zheng and others, 2019). As such, surging glaciers provide an opportunity to investigate ice dynamics in a less remote environment than the ice sheets, and to understand how increasing temperatures may instigate long term fast ice flow, resulting in ultimately higher mass loss.

While comprising only 1% of glaciers globally, surging glaciers exhibit significant clustering, often occurring in the St. Elias region of Yukon-Alaska, Svalbard, the Canadian high Arctic, East Greenland, the Karakoram Himalaya and Patagonia (Jiskoot, 2011a; Waechter and others, 2015; Sevestre and Benn, 2015; Guillet and others, 2022; Lovell and others, 2023; Kääb and others, 2023). Surging glaciers undergo cyclic oscillations between “active” or rapid ice flow for a short period (usually months to years), before returning to an inactive or “quiescent” phase which is

characterized by a longer period (usually years to decades) of "slow" flow. The periods of rapid flow can be 10-1000 times as fast as those during the quiescent phase (Jiskoot, 2011a). During the quiescent phase, ice mass is collected in the reservoir area (often located in the accumulation zone), which can result in localized thickening, and ice is lost in the receiving zone, causing localized thinning; together these create a steeper glacier surface slope, altering the driving stress (Kamb and others, 1985; Kamb, 1987; Raymond, 1987). During a surge, mass is rapidly redistributed to the receiving zone, usually situated in the ablation area, frequently resulting in an advance of the glacier front (Jiskoot, 2011a; Benn and Evans, 2010).

Previous studies have typically classified glacier surges into two main types, with differing driving mechanisms based on ice temperature: these are Alaskan-type surges on temperate glaciers (driven by changes in efficiency of the subglacial hydrological system), and Svalbard-type surges on polythermal glaciers (driven by changes in basal thermal conditions) (Murray and others, 2003; Jiskoot, 2011a). Alaskan-type surges typically last for ~1-2 years, with an intervening quiescent phase of a few decades, and tend to initiate in the upper regions of a glacier and propagate towards the terminus (Kamb and others, 1985; Jiskoot, 2011a). Strongly influenced by work on the 1982-83 surge of Variegated Glacier, Alaska, theories of the initiation of Alaskan-type surges have focused on hydrologic triggers driven by transformation of the subglacial water drainage system from a channelized to a distributed system, and vice versa at the end of a surge (Kamb and others, 1985; Kamb, 1987; Fowler, 1987). A distributed system is inefficient at moving water across the glacier bed, resulting in high basal water pressure and enhanced basal sliding, while a channelized system can evacuate subglacial water rapidly, resulting in lower basal water pressure and reduced glacier sliding capability (Benn and Evans, 2010). In Kamb's (1987) study on Variegated Glacier, borehole measurements revealed high basal water pressures during a surge, while dye-tracing indicated slow basal water movement and the storage of a significant amount of basal water at this time. Once the surge stopped, dye-tracing showed that subglacial water flow became much more efficient, together with a 0.1 m drop in the elevation of the glacier surface, indicative of the loss of a high-pressure layer of water at the bed. Recent research also supports this theory: Alaskan-type surges tend to initiate in the winter, when a drop in available meltwater permits ice creep closure of subglacial channels and a switch of the subglacial system to distributed. This results in repressurization of the glacier bed and the initiation of basal sliding (Abe and Furuya, 2014).

Svalbard-type (polythermal) glacier surges also experience cyclic variability between fast and slow flow, but instead of being driven primarily by switches in subglacial hydrology, fast flow is thought to initiate by a shift from frozen to unfrozen bed conditions (Murray and others, 2003). These glaciers typically have much longer active (~4-10 years) and quiescent (50-500 years) phases than occur on Alaskan surge-type glaciers, and are located in colder regions including the Canadian high Arctic and Svalbard (Dowdeswell and others, 1991, Murray and others, 2003). During quiescence, low velocities facilitate mass build up in the reservoir zone where the ice is cold-based (i.e., below the pressure-melting point), causing increased ice thickness. Over time this results in increased insulation of the glacier bed, as well as increased driving stress and higher ice flow rates as the pressure melting point is reached (Murray and others, 2003). Increased velocities generate heat through strain heating, further increasing acceleration, creating a localized temperate zone of ice and producing meltwater. As the surrounding ice remains cold-based it hinders subglacial water flow, which increases basal water pressure in the temperate zone, reducing basal drag there and ultimately leading to increased basal sliding and surge initiation. As the ice continues to flow, deformation of the underlying sediment further increases melting and water pressure through frictional heating, continuing until the subglacial water exits the system, ending the surge (Murray and others, 2003). Svalbard-type surges tend to initiate in the lower regions of a glacier, and propagate up-glacier, although this is not necessarily a defining feature (Murray and others, 2003; Frappé and Clarke, 2007).

The enthalpy model has recently emerged as a way to unify the driving mechanisms behind both temperate and polythermal glacier surges into a single theory. Enthalpy is defined as the internal energy of the glacier system, a function of ice temperature and water content (Sevestre and Benn, 2015; Benn and others, 2019; Terleth and others, 2019; Benn and others, 2023). Changes in enthalpy result from: i) energy exchanges at the glacier surface (radiative and turbulent fluxes, runoff) and the bed (geothermal heat flux, runoff), and ii) frictional heating associated with ice flow (Aschwanden and others, 2012). In this context, a steady state occurs only when the cumulative energy gains are dissipated by heat conduction and meltwater runoff, which is most easily fulfilled in either cold, dry environments or warm, humid environments (Sevestre and Benn, 2015). As such, intermediate climatic conditions, such as those found in Alaska (warm and humid) and Svalbard (cold and dry) correspond to the optimal surge zone, where the gains in enthalpy are not effectively released (Sevestre and Benn, 2015). As these enthalpy gains build, surging results

due to positive feedbacks between sliding velocity and frictional heating at the glacier bed, instigating fast ice flow (Sevestre and Benn, 2015; Benn and others, 2019, 2023). While this model provides a possible explanation for connections between climate and the global distribution of surge-type glaciers, it does not provide a detailed understanding of the triggers, mechanisms or subglacial drainage network configurations for individual surging glaciers, meaning that further investigation is warranted.

1.2 Changes to glaciers in Yukon-Alaska

Consistent with other high latitude regions, the Yukon has been experiencing climatic warming, with an increase of 2°C in mean annual surface air temperatures since the 1970s, with winters experiencing the most warming (ECCC, 2021; Perrin and Jolkowski, 2022). At high elevations warming is further amplified: for example, Williamson and others (2020) determined that the rate of increase of surface air temperatures was 1.5 times greater at elevations of 5500-6000 m than 2000-2500 m over the period 1979-2016, although warming occurred at all elevations between 2000-6000 m. Precipitation trends are less clear in this region, although some estimates suggest that annual total precipitation has increased by 3% from 1966-2015 (ECCC, 2015; Perrin and Jolkowski, 2022). Annual average temperature is predicted to increase by between 0.7 to 3.7°C over the next 50 years (Bush and Lemmen, 2019; IPCC, 2021; Perrin and Jolkowski, 2022).

In response to climatic change, glaciers in Yukon-Alaska are losing mass at one of the highest rates (66.7 Gt a^{-1}) globally, outside of the Greenland and Antarctic ice sheets, and are responsible for ~38% of the acceleration of global glacier thinning over the period 2000-2019 (Hugonnet and others, 2021). The St. Elias Mountains, which straddle the borders of Alaska, the Yukon and British Columbia, contain the largest non-polar icefield in the world, covering an area of ~33,000 km^2 (Young and others, 2021). Yukon glaciers specifically have experienced significant area loss, negative mass balance, and glacier thinning since investigations began around the mid-1900s (Foy and others, 2011; Young and others, 2021). For example, from 1957-58 to 2007-08, glaciers in the Yukon region lost 22% of their surface area, representing a total area loss of 2,541 ±189 km^2 and a total mass loss of 406 ± 177 Gt, equivalent to 1.12 ± 0.49 mm of global SLR (Barrand and Sharp, 2010; Derksen and others, 2012). Meanwhile, from 1994-2013, the regional mass balance of Alaskan glaciers was -75 ± 11 Gt a^{-1}, and losses were dominated by surface melt (Larsen and others, 2015). In particular, glaciers bordering the Gulf of Alaska supplied one third of the

estimated 0.6 mm a^{-1} SLR contribution from retreating glaciers and ice caps (Chen and others, 2017). This region is projected to continue contributing to future sea level rise, as land-ice there will persist longer than in regions such as Central Europe, where most glaciers are expected to be lost by 2050 (Zemp and others, 2019).

1.3 Fast glacier flow in the St. Elias Mountains

The St. Elias Mountains (Fig. 1-1) contain the highest number of surging glaciers in North America, with most characterized as Alaskan-type (Post, 1969; Clarke and Holdsworth, 2002; Sevestre and Benn, 2015). As there have been few comprehensive studies of the regional behaviour of surging glaciers in the St. Elias, it is difficult to point to long-term trends in surging frequency. A detailed study of the past 5 surges of Lowell Glacier by Bevington and Copland (2014) suggests that surge frequency is increasing towards present day, despite a decrease in surge magnitude, as demonstrated by decreasing maximum terminus extents. Similarly, the 1995 surge of Variegated Glacier was weaker than previously observed surges, with a shorter duration and a smaller impact on glacier advance (Eisen and others, 2005). However, Kochtitzky et al. (2019) reported no significant change in surge frequency over time for the past 8 surges of Donjek Glacier since the 1940s, despite reductions in terminus extent. Many surging glaciers in the St. Elias Mountains experience velocity speed-ups in winter, and often surges will initiate during this time, suggesting that englacial water storage may play a role in this behaviour (Abe and Furuya, 2014).

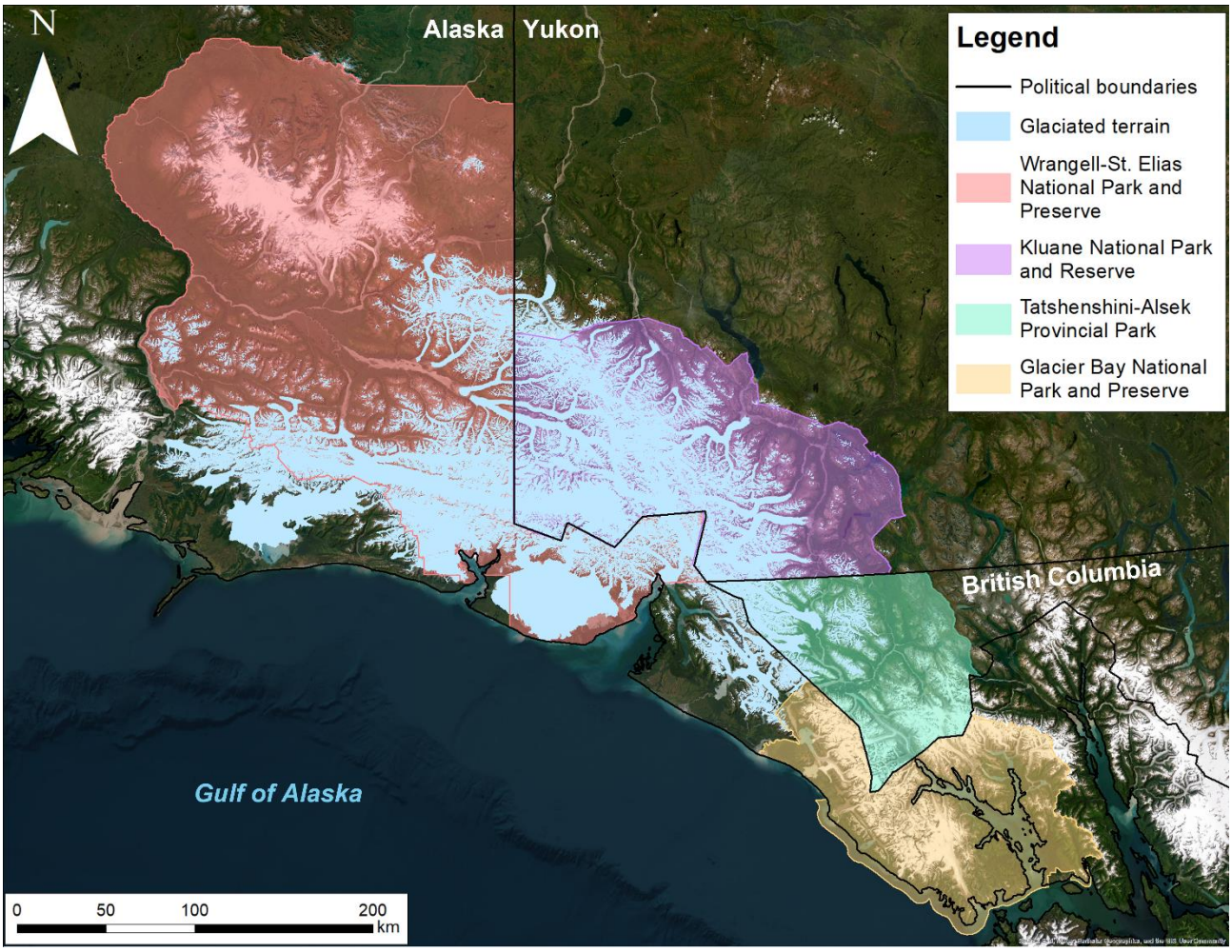

Figure 1-1: Regional map of the St. Elias Mountains, Yukon-Alaska, identifying key locations. Glacierized terrain is defined by RGI v6.0. Base image: ESRI World Imagery from 2018-2023, UTM Zone 7N.

1.4 Knowledge gaps in ice dynamics of mountain glaciers in the St. Elias Mountains

Recent studies in the St. Elias Mountains have focused on determining mass change (e.g., Ciracì and others, 2020; Hugonnet and others, 2021) and producing regional velocity products (Burgess and others, 2013a, 2013b; Abe and Furuya, 2014; Waechter and others, 2015; Altena and others, 2019; Millan and others, 2022). However, these studies mainly characterized surface velocities over 1-2 year periods, and none have analyzed velocity trends over multi-decadal periods, meaning that there is currently little understanding of what the impact of decreasing mass balance has been on glacier velocities. This lack of long-term glacier velocity observations and analysis in the St. Elias Mountains is thus a major knowledge gap. This is important because without long-term records, it is challenging to understand the regional controls on glacier velocities and glacier surging, to predict the potential impact of a changing climate on glacier velocities, or to accurately predict future sea level rise.

Surging glaciers are important features in the St. Elias Mountains, and while a number of studies have focused on individual glaciers (e.g., Kamb and others, 1985; Eisen and others, 2005; Frappé and Clarke, 2007; Harrison and others, 2008; Bevington and Copland, 2014; Kochtitzky and others, 2019; Nolan and others, 2021), few have studied the features in a regional context. There is therefore still a limited understanding of: i) the regional controls on glacier surging, ii) whether surge events share common characteristics (e.g., where on glaciers surges initiate, seasonal timing of surge initiation, subsequent propagation/cessation patterns), and c) whether the frequency of surging events has changed over time.

In addition to considering regional controls on velocities, studies on individual glaciers are still valuable due to the high variability in surging and non-surging behaviours across the St. Elias Mountains. The detailed evidence provided by individual glacier studies enables glacier dynamics to be more fully understood, and provides a baseline for future work. The St. Elias is a geographically large and complex region, with a high diversity of velocity regimes among individual glaciers, (e.g., slow and Alaskan-style surges), as identified in past research. By quantifying the impact of specific conditions (e.g., climatic, geometric, topographic) on individual glaciers' velocity regimes, a framework for understanding factors contributing to ice dynamics can be established. This framework facilitates understanding the processes found at single glaciers, but also serves as a template for examining similar phenomena across other glaciers and, eventually

the region as a whole. These kinds of studies are only now possible because the quality and quantity of data, particularly in relation to glacier velocities, has improved significantly with the increase in available satellite imagery within the last ~10 years.

1.5 Objectives

In light of the knowledge gaps identified above, this thesis focuses on the following central research objectives:

1. Complete a regional inventory and analysis of surge-type glaciers and glacier surging behaviour in the St. Elias Mountains. We analyze regional velocities derived from optical satellite data, and winter velocities derived from SAR data in detail to understand the commonalities behind fast glacier flow. This includes analysis of the distinct types of surges, geographic distribution of surge-type glaciers, surge recurrence intervals, surge initiation timing and location, and the roles of glacier tributaries in surging.
2. Reconstruct the detailed flow history of a previously undescribed surge-type glacier in the eastern St. Elias Mountains (Little Kluane Glacier), using a variety of remote sensing and field observations from 1940s until present. Changes in terminus position, ice surface elevations, glacier velocities, supraglacial hydrology and surface features are used to quantitatively understand the factors which may push a partial surge into a full surge.
3. The rapid drainage of proglacial Slims Lake located at the front of Kaskawulsh Glacier provides an interesting opportunity to examine the relationships between hydrology and glacier dynamics. Therefore, we examine how long-term changes in the spatial extent and velocity patterns across the terminus are controlled by factors outside of surging. Glacier velocities, ice surface elevations, ice thicknesses, terminus outlines and reconstructions of changes in the depth and extent of proglacial lakes are used to provide insights into the interrelationships between changes in ice dynamics and proglacial conditions at a single glacier.

In fulfilling the above objectives, this thesis explores the factors influencing glacier velocity variability in the St. Elias Mountains (Fig. 1-1). This research significantly improves our understanding of ice dynamics in this region for both surge-type and non surge-type glaciers, and can provide insight into factors which may affect dynamic instabilities and fast-flow processes on glaciers elsewhere.

References

Abe T and Furuya M (2014) Winter speed-up of quiescent surge-type glaciers in Yukon, Canada. *The Cryosphere*, **9**, 1183–1190. doi: 10.5194/tc-9-1183-2015.

AMAP (2021) Arctic Climate Change Update 2021: Key Trends and Impacts. Summary for Policy-makers. Arctic Monitoring and Assessment Programme (AMAP), Tromsø, Norway. 16 pp

Altena B, Scambos T, Fahnestock M and Kääb A (2019) Extracting recent short-term glacier velocity evolution over southern Alaska and the Yukon from a large collection of Landsat data. *The Cryosphere*, **13**(3), 795-814. doi: 10.5194/tc-13-795-2019.

Arendt A, Echelmeyer KA, Harrison WD, Kingle CS and Valentine VB (2002) Rapid wastage of Alaska glacier and their contribution to rising sea level. *Science*, **297**(5580), 382-386. doi: 10.1126/science.1072497.

Aschwanden A, Bueler E, Khroulev C and Blatter H (2012) An enthalpy formulation for glaciers and ice sheets. *Journal of Glaciology*, **58**(209), 441-457. doi: 10.3189/2012JoG11J088.

Barrand NE and Sharp MJ (2010) Sustained rapid shrinkage of Yukon glaciers since the 1957 – 1958 International Geophysical Year. *Geophysical Research Letters*, **37**, 1-5. doi:10.1029/2009GL042030.

Benn DI and Evans DJA (2010) Glaciers and Glaciation, 2nd Edition. Hodder Education. United Kingdom. pp 789.

Benn D, Jones R, Luckman A, Fürst J, Hewitt I, and Sommer C (2019) Mass and enthalpy budget evolution during the surge of a polythermal glacier: A test of theory. *Journal of Glaciology*, **65**(253), 717-731. doi:10.1017/jog.2019.63

Benn D, Hewitt I and Luckman A (2023) Enthalpy balance theory unifies diverse glacier surge behaviour. *Annals of Glaciology*, 1-7. doi:10.1017/aog.2023.23

Berthier E, Schiefer E, Clarke GKC, Menounos B and Rémy F (2010) Contribution of Alaskan glaciers to sea-level rise derived from satellite imagery. *Nature Geoscience*, **3**, 92-95. doi: 10.1038/ngeo737

Bevington, A. and Copland, L. (2014): Characteristics of the last five surges of Lowell Glacier, Yukon, Canada, since 1948. Journal of Glaciology, 60(219), 113-123. doi: 10.3189/2014JoG13J134.

Burgess EW, Larsen CF and Forster RR (2013a) Summer melt regulates winter glacier flow speeds throughout Alaska. *Geophysical Research Letters*, **40**, doi:10.1002/2013GL058228.

Burgess EW, Forster RR and Larsen CF (2013b) Flow velocities of Alaska glaciers. *Nature Communications*, **4**, doi:10.1038/ncomms3146.

Bush E and Lemmen DS (Eds.) (2019) Canada's changing climate report. Government of Canada, Ottawa, ON. 444p. https://changingclimate.ca/CCCR2019

Chen X and 7 others (2017) The increasing rate of global mean sea-level rise during 1993-2014. *Nature Climate Change*, **7**, 492-495. https://doi.org/10.1038/nclimate3325

Ciracì E, Velicogna I and Swenson S (2020) Continuity of the mass loss of the world's glaciers and ice caps from the GRACE and GRACE Follow-On missions. *Geophysical Research Letters*, **47**(9), 1–11. doi: 10.1029/2019gl086926.

Clarke CKC, Schmok JP, Ommanney SL and Collins SG (1986) Characteristics of surge-type glaciers. *Journal of Geophysical Research,* **91**(B7), 7165-7180. doi: 10.1029/JB091iB07p07165.

Clarke GKC (1987) Fast glacier flow: ice streams, surging, and tidewater glaciers. *Journal of Geophysical Research: Solid Earth*, **92**(B9), 8835-8841. doi: 10.1029/JB092iB09p08835.

Clarke GKC and Holdsworth G (2002) Glaciers of the St. Elias Mountains. In R. S. William & J. G. Ferrigno (Eds.). Satellite image atlas of glaciers of the world (pp. J301−J311). North America: U.S. Geological Survey Professional Paper.

Copernicus. (2020) Copernicus Climate Change Service (C3S): ERA5: Fifth generation of ECMWF atmospheric reanalyses of the global climate. https://cds.climate.copernicus.eu Accessed May 2020.

Cowtan K and Way RG (2014) Coverage bias in the HadCRUT4 temperature series and its impact on recent temperature trends. *Quarterly Journal of the Royal Meteorological Society*, **140**, 1935-1944. doi: 10.1002/qj.2297.

Derksen C and 19 others (2012) Variability and change in the Canadian Cryosphere. *Climate Change*, **115**(1), 58-88. doi: 10.1007/s10584-012-0470-0.

Dowdeswell JA, Hamilton GS and Hagen JO (1991) The duration of the active phase on surge-type glaciers: contrasts between Svalbard and other regions. *Journal of Glaciology*, **37**(127): 388–400. doi: 10.3189/S0022143000005827.

ECCC (Environment and Climate Change Canada) (2015) Climate Trends and Variations Bulletin. Government of Canada. Accessed October 04, 2023 https://publications.gc.ca/collections/collection_2016/eccc/En81-23-2015-eng.pdf

ECCC (Environment and Climate Change Canada) (2021) Climate Trends and Variations Bulletin. Government of Canada. Accessed January 27, 2022 https://www.canada.ca/en/environment-climate-change/services/climate-change/science-research-data/climate-trends-variability/trends-variations.html.

Eisen O, Harrison WD, Raymond CF, Echelmeyer KA, Bender GA and Gorda JLD (2005) Variegated Glacier, Alaska, USA: a century of surges. *Journal of Glaciology*, **51**(174), 399-406. doi: 10.3189/172756505781829250

Enderlin EM, Howatt IM, Jeong S, Noh M-J, van Angelen JH and van den Broeke MR (2014) An improved mass budget for the Greenland Ice Sheet. *Geophysical Research Letters*, **41**, 866-72. https://doi.org/10.1002/2013GL059010.

Fowler AC (1987) A theory of glacier surges. *Journal of Geophysical Research: Solid Earth*, **92**(B9), 9111-9120. doi: 10.1029/JB092iB09p09111.

Fox-Kemper B and 17 others (2021) Ocean, Cryosphere and Sea Level Change. In Climate Change 2021: The Physical Science Basis. Contribution of Working Group I to the Sixth Assessment Report of the Intergovernmental Panel on Climate Change [Masson-Delmotte, V., P. Zhai, A.

Pirani, S.L. Connors, C. Péan, S. Berger, N. Caud, Y. Chen, L. Goldfarb, M.I. Gomis, M. Huang, K. Leitzell, E. Lonnoy, J.B.R. Matthews, T.K. Maycock, T. Waterfield, O. Yelekçi, R. Yu, and B. Zhou (eds.)]. Cambridge University Press, Cambridge, United Kingdom and New York, NY, USA, pp. 1211–1362, doi: 10.1017/9781009157896.011.

Foy N, Copland L, Zdanowicz C, Demuth M and Hopkinson C (2011) Recent volume and area changes of Kaskawulsh Glacier, Yukon, Canada. *Journal of Glaciology*, **57**(203), 515–525. doi: 10.3189/002214311796905596

Frappé T-P, and Clarke GKC (2007) Slow surge of Trapridge Glacier, Yukon Territory, Canada. *Journal of Geophysical Research*, **112**(F3), F03S32. doi: 10.1029/2006JF000607.

Furbish DJ and Andrews JT (1984) The use of hypsometry to indicate long-term stability and response of valley glaciers to changes in mass transfer. *Journal of Glaciology*, **30**(105), 199-211. doi: 10.3189/S0022143000005931.

Guillet G, King O, Lv M, Ghuffar S, Benn D, Quincey D and Bolch T (2022) A regionally resolved inventory of High Mountain Asia surge-type glaciers, derived from a multi-factor remote sensing approach. The Cryosphere, 16, 603-623. doi: 10.5194/tc-16-603-2022.

Gutiérrez JM, and 15 others (2021) Atlas. In Climate Change 2021: The Physical Science Basis. Contribution of Working Group I to the Sixth Assessment Report of the Intergovernmental Panel on Climate Change [Masson-Delmotte V, Zhai P, Pirani A, Connors SL, Péan C, Berger S, Caud N, Chen Y, Goldfarb L, Gomis MI, Huang M, Leitzell K, Lonnoy E, Matthews JBR, Maycock TK, Waterfield T, Yelekçi O, Yu R and Zhou B (eds.)]. Cambridge University Press, Cambridge, United Kingdom and New York, NY, USA, pp. 1927–2058, doi:10.1017/9781009157896.021.

Harrison WD, Motyka RJ, Truffer M, Eisen O, Moran MT, Raymond CF, Fahnestock MA and Nolan M (2008) Correspondence. Another surge of Variegated Glacier, Alaska, USA, 2003/04. *Journal of Glaciology*, **54**(184), 192– 194. doi: 10.3189/002214308784409134.

Heid T and Kääb A (2012) Repeat optical satellite images reveal widespread and long term decrease in land-terminating glacier speeds. *The Cryosphere*, **6**, 467-478. doi: 10.5194/tc-6-467-2012.

Hugonnet R and 10 others (2021) Accelerated global glacier mass loss in the early twenty-first century. *Nature*, **592**, 726-731. doi: 10.1038/s41586-021-03436-z.

Huss M and Hock R (2015) A new model for global glacier change and sea-level rise. *Frontiers in Earth Science*, **3**:54. doi:10.3389/feart.2015.00054.

IPCC (2021) Summary for Policymakers. In*: Climate Change 2021: The Physical Science Basis. Contribution of Working Group I to the Sixth Assessment Report of the Intergovernmental Panel on Climate Change* [Masson-Delmotte V, Zhai P, Pirani A, Connors SL, Péan C, Berger S, Caud N, Chen Y, Goldfarb L, Gomis MI, Huang M, Leitzell K, Lonnoy E, Matthews JBR, Maycock TK, Waterfield T, Yelekçi O, Yu R and Zhou B (eds.)]. In Press.

Jiskoot H (2011a) Glacier surging. In Singh VP et al. (eds) Encyclopedia of Snow, Ice and Glaciers, Dordrecht, The Netherlands, Springer, 415-428.

Jiskoot H (2011b) Dynamics of Glaciers. In Singh VP et al. (eds) Encyclopedia of Snow, Ice and Glaciers, Dordrecht, The Netherlands, Springer, 245–256.

Kääb A, Brazilova V, Leclercq PW, Mannerfelt ES and Strozzi T (2023) Global clustering of recent glacier surges from radar backscatter data, 2017-2022. *Journal of Glaciology*, 1-9. doi: 10.1017/ jog.2023.35.

Kamb B and 7 others (1985) Glacier surge mechanism: 1982–1983 surge of the Variegated Glacier, Alaska. *Science,* **227**(4686), 469–479. doi: 10.1126/science.227.4686.469.

Kamb B (1987) Glacier surge mechanism based on linked cavity configuration of the basal water conduit system. *Journal of Geophysical Research*, **92**(B9), 9083–9100. doi: 10.1029/JB092iB09p09083.

Kochtitzky W and 6 others (2019) Terminus advance, kinematics and mass redistribution during eight surges of Donjek Glacier, St. Elias Range, Canada, 1935-2016. *Journal of Glaciology*, **65**(252), 565-579. doi: 10.1017/jog.2019.34

Kochtitzky W and Copland L (2022) Retreat of northern hemisphere marine-terminating glaciers, 2000-2020. *Geophysical Research Letters*, **49**, e2021GL096501. doi: 10.1029/2021GL096501.

Larsen CF, Burgess E, Arendt AA, O'Neel S, Johnson AJ and Kienholz C (2015). Surface melt dominates Alaska glacier mass balance. *Geophysical Research Letters*, **2**(14), 5902-5908. doi: 10.1002/2015GL064349.

Lovell H, Carrivick JL, King O, Sutherland JL, Yde JC, Boston CM and Małecki J (2023) Surge-type glaciers in Kalaallit Nunaat (Greenland): distribution, temporal patterns, and climatic controls. *Journal of Glaciology*, 1-18. doi: 10.1017/jog.2023.61.

Millan R, Mouginot J, Rabatek A and Morlighem M (2022) Ice velocity and thickness of the world's glaciers. *Nature geoscience*, **15**, 124-129. doi: 10.1038/s41561-021-00885-z.

Moon T, Joughin I, Smith B and Howat I (2012) 21st-century evolution of Greenland outlet glacier velocities. *Science*, **336** (6081): 576-578. doi: 10.1126/science.1219985.

Murray T, Strozzi T, Luckman A, Jiskoot H and Christakos P (2003) Is there a single surge mechanism? Contrasts in dynamics between glacier surges in Svalbard and other regions. *Journal of Geophysical Research*, **108** (B52237), 1-15. doi: 10.1029/2002JB001906.

Muskett RR, Lingle CS, Sauber JM, Rabus BT, and Tangbore WV (2008) Acceleration of surface lowering on the tidewater glaciers of Icy Bay, Alaska, U.S.A. from InSAR DEMs and ICESat Altimetry. *Earth and Planetary Science Letters*, **265**: 345-359. doi: 10.1016/j.epsl.2007.10.012.

Nanni U, Gimbert F, Vincent C, Gräff D, Walter F, Piard L, and Moreau L (2020) Quantification of seasonal and diurnal dynamics of subglacial channels using seismic observations on an Alpine glacier. *The Cryosphere*, **14**, 1475–1496. doi: 10.5194/tc-14-1475-2020.

Nolan A, Kochtitzky W, Enderlin EM, McNabb R and Kreutz KJ (2021) Kinematics of the exceptionally-short surge cycles of Sít' Kusá (Turner Glacier), Alaska, from 1983 to 2013. *Journal of Glaciology*, **67**(264), 744-758. doi: 10.1017/jog.2021.29.

Perrin A and Jolkowski D (2022) Yukon climate change indicators and key findings 2022. YukonU Research Centre, Yukon University, 126p. https://www.yukonu.ca/sites/default/files/inline-files/Indicators2022_FinalReport.pdf

Post A (1969) Distribution of surging glaciers in western North America. *Journal of Glaciology* **8**(53): 229- 240. doi: 10.3189/S0022143000031221.

Raymond CF (1987) How do glaciers surge? A review. *Journal of Geophysical Research*, **92**, 9121-9134. doi:10.1029/JB092iB09p09121.

Sevestre H and Benn D (2015) Climatic and geometric controls on the global distribution of surge-type glaciers: implications for a unifying model of surging. *Journal of Glaciology*, **61**(288), 646-663. doi: 10.3189/2015JoG14J136.

Schaffer N, Copland L and Zdanowicz C (2017) Ice velocity changes on Penny Ice Cap, Baffin Island, since the 1950s. *Journal of Glaciology*, **63**(240), 716-730. doi: 10.1017/jog.2017.40.

Tedstone AJ, Nienow PW, Gourmelen N, Dehecq A, Goldberg D and Hanna E (2015) Decadal slowdown of a land-terminating sector of the Greenland Ice Sheet despite warming. *Nature*, **526**, 692-695. doi: 10.1038/nature15722.

Terleth Y, Van Pelt WJJ, Pohjola VA and Pettersson R (2021) Complementary approaches towards a universal model of glacier surges. *Frontiers in Earth Science*, 9:732962. doi: 10.3389/feart.2021.732962

Thomson L and Copland L (2018) Changing contribution of peak velocity events to annual velocities following a multi-decadal slowdown at White Glacier. *Annals of Glaciology*, **58**(75pt2), 145-154. doi: 10.1017/aog.2017.46

Waechter A, Copland L and Herdes E (2015) Modern glacier velocities across the Icefield Ranges, St. Elias Mountains, and variability at selected glaciers from 1959 to 2012. *Journal of Glaciology*, **61**(228), 624-634. doi: 10.3189/2015JoG14J147.

Werder MA, Hewitt IJ, Schoof CG, and Flowers GE (2013) Modeling channelized and distributed subglacial drainage in two dimensions. *Journal of Geophysical Research: Earth Surface*, **118**, 2140–2158. doi: 10.1002/jgrf.20146.

WGMS (2015) Global Glacier Change Bulletin No. 1 (2012-2013). Zemp, M. et al (eds.). World Glacier Monitoring Service, Zurich, Switzerland, 230 pp.

Williamson SN and 9 others (2020) Evidence for elevation-dependent warming in the St. Elias Mountains, Yukon, Canada. *Journal of Climate*, **33**, 3253–3269. doi: 10.1175/JCLI-D-19-0405.

Willis IC (1995) Intra-annual variations in glacier motion: a review. *Progress in Physical Geography: Earth and Environment*, **19**(1), 61–106. doi: 10.1177/030913339501900104.

Yde JC and Paasche Ø (2010) Reconstructing climate change: Not all glaciers suitable. *Eos, Transactions American Geophysical Union*, **91**(21):189–90. doi: 10.1029/2010EO210001

Young EM, Flowers GW, Berthier E and Latto R (2021) An imbalancing act: the delayed dynamic response of the Kaskawulsh Glacier to sustained mass loss. *Journal of Glaciology*, **67**(262), 313-330. doi: 10.1017/jog.2020.107

Zemp M and 10 others (2019) Global glacier mass changes and their contributions to sea-level rise from 1961 to 2016. *Nature* **568**, 382–386. doi: 10. 1038/s41586-019-1071-0

Zheng W, Pritchard ME, Willis MJ and Stearns, LA (2019) The possible transition from glacial surge to ice stream on Vavilov Ice Cap. *Geophysical Research Letters*, **46**(23), 13892-13902. https://doi.org/10.1029/2019GL084948.

Zwally HJ, Abdalati W, Herring T, Larson K, Saba J and Steffen K (2002) Surface melt induced acceleration of Greenland ice-sheet flow. *Science*, **297**, 218-222. doi: 10.1126/science.1072708.

Chapter 2: Characteristics of observed glacier surges in the St. Elias Mountains, Yukon-Alaska

2.1 Introduction

Surge-type glaciers experience cyclical flow instabilities, where prolonged periods of relatively slower flow (quiescence) are interrupted by short periods of rapid flow (active phase) (Post, 1969). The magnitude of ice velocities during a surge, and the timescales that these events can occur over can be highly variable, as can the processes governing the irregular motion (Kääb and others, 2023). Past studies have noted the high proportion of surge-type glaciers in the St. Elias Mountains (Post, 1969; Clarke and others, 1986; Clarke and Holdsworth, 2002), which may be due to the warm-temperate climatic envelope that the region occupies, and as a result most glaciers are likely polythermal (Sevestre and Benn, 2015). It is hypothesized that glaciers within a mean annual air temperature range from -10°C to 0°C, and mean annual precipitation range from 165 mm a^{-1} to 402 mm a^{-1}, provide an optimal climatic zone for surging behaviour by ineffectively discharging enthalpy gains (e.g., from balance velocities) through enthalpy losses (e.g., from heat conduction and meltwater discharge) (Aschwanden and others, 2012; Sevestre and Benn, 2015). As such, these glaciers are unable to maintain a steady state (i.e., a constant geometry and velocity/temperature distribution in balance with the climate), which may result in the storage of basal water in inefficient, distributed systems, a commonly suggested initiation mechanism for Alaskan-style surges (Kamb and others, 1985; Fowler, 1987).

Remote sensing techniques have been used to obtain regional-scale glacier velocities in the St. Elias Mountains (Burgess and others, 2013; Waechter and others, 2015; Abe and Furuya, 2015; Van Wychen and others, 2018), while several detailed studies of individual glacier surges have been undertaken there, including of Variegated Glacier (Kamb and others, 1985; Eisen and others, 2005), Sít' Kusá (Turner Glacier; Nolan and others, 2021), Nàłùdäy (Lowell Glacier; Bevington and Copland, 2014), Dän Zhür (Donjek Glacier; Abe and others, 2016; Kochtitzky and others, 2019, 2020), and Trapridge Glacier (Frappé and Clarke, 2007), among others (Flowers and others, 2016; Main and others, in review). Research on glaciers in this region, particularly Variegated, contributed to the initial development of the hydrological-switch model of glacier surging (Kamb and others, 1985; Kamb, 1987; Fowler, 1987), which focuses on the switch between a channelized and distributed subglacial hydrological network as a mechanism for triggering a surge.

Despite noteworthy research on individual glacier surges in the St. Elias Mountains, there is still a gap in the understanding of which glaciers surge, how often, and if there are any common characteristics between them, including initiation timing and location. Additionally, it is not yet well understood what the impacts of recent decreases in surface mass balance and increasing air temperatures have been on regional glacier velocities and ice dynamics. Glacier thinning in the Alaska-Yukon region is accelerating, accounting for 38% of the increase in mass loss from glaciers outside of the Greenland and Antarctic ice sheets between 2000-04 and 2015-19 (Hugonnet and others, 2021). Young and others (2021) found that from 2007-18 Kaskawulsh Glacier has had a negative mass balance of -0.46 ± 0.17 m w.e. a^{-1}, with a projected ~23 km of terminus retreat and minimum 46 km^3 of future ice loss based on the 2007-18 climate. Larsen and others (2015) reported the mass balance of Kaskawulsh Glacier as -0.35 m w.e. a^{-1} from 1995-2013, and -0.72 m w.e. a^{-1} for all land-terminating glaciers in the southcentral subregion. Similar to other high latitude regions, the Yukon has also been experiencing climatic warming since the mid-1900s, with amplified warming at high elevations at rates ~1.5 times greater than the global average (Williamson and others, 2020), and a further increase of 3.0-3.5°C in mean annual air temperatures predicted by 2099 (Gutiérrez and others, 2021).

This study provides a comprehensive examination of long-term trends in glacier surging across the St. Elias Mountains since 1874, and explores patterns of annual, winter, and summer glacier velocities during surge events from 1985-2023, using a combination of optical and Synthetic Aperture Radar (SAR)-derived velocity datasets. We identify new glacier surges and other flow instabilities, and investigate of common characteristics between surges, including surge initiation location, seasonal timing, duration, and propagation/cessation patterns. In addition, we present an updated inventory of observed surges, to build on inventories previously provided by Post (1969), Clarke and others (1986), and Sevestre and Benn (2015).

2.2 Study Site

Located at the intersection between Alaska, Yukon, and northern British Columbia, the Wrangell-St. Elias Mountains contain ~33 000 km^2 of glacierized terrain. On the eastern side of the region, the climate is characterized as arctic and continental with prevailing low winter temperatures, however the western and southwestern area is considerably warmer and more humid, and can be characterized as subarctic maritime (Newman and others, 2020). Temperatures have been

increasing at all elevations between 2000 - 6000 m since 1979 (Williamson and others, 2020). This region contains land-, lake-, and tidewater-terminating glaciers, as well as the highest concentration of surge-type glaciers in North America: up to 229 surge-type glaciers have been previously identified based on three factors: i) periodic changes in surface velocities, ii) anomalous terminus advance or retreat patterns, and iii) glaciological/geomorphological evidence, such as looped moraines and heavy crevassing (Post, 1969; Clarke and others, 1986; Clarke and Holdsworth, 2002; Sevestre and Benn, 2015). Large glaciers across the range are known to surge periodically, including Bering, Nàłùdäy, Dän Zhür, Tweedsmuir, Fisher, Sít' Kusá, and Variegated glaciers (Kamb and others, 1985; Eisen and others, 2005; Bevington and Copland, 2014; Kochtitzky and others, 2019; Nolan and others, 2021; Sharp, 2021; Partington 2023). On the southwest coast, Sít' Tlein (Malaspina) is formed by the coalescence of Agassiz, Seward, and Marvine tributaries, all of which are known to surge, and which surged near-simultaneously between 1999 and 2002 (Deur and others, 2015; Muskett and others, 2008). Sevestre and Benn (2015) explored the enthalpy model as an explanation of the high percentage of surge-type glaciers in the region, and found that glaciers in this region are more geometrically complex, with more tributaries, compared to non surge-type glaciers.

Past studies have found that glacier velocities are generally faster on the southwestern, seaward side of the St. Elias Mountains compared to the eastern flank, reflecting the higher moisture availability and precipitation on the southwestern side (Waechter and others, 2015; Van Wychen and others, 2018). Non surge velocities reach a peak of ~1500-3600 m a^{-1} near the coast of Alaska, decreasing towards the Yukon continental interior (peak velocity ~150-400 m a^{-1}) (Waechter and others, 2015). Compared to surge-type glaciers in their quiescent phase, non-surging glaciers display less interannual velocity variability (Waechter and others, 2015).

2.3 Methods

2.3.1 Velocity mapping

2.3.1.1 Winter velocities derived from Synthetic Aperture Radar images

We generated winter glacier surface velocities from speckle-tracking of ALOS PALSAR, RADARSAT-2 and RADARSAT Constellation Mission (RCM) image pairs acquired between 2007 and 2023 (Appendix 2-A). Winter velocities from 2007-8 and 2009-10 were obtained from ALOS PALSAR-derived datasets previously published by Van Wychen and others (2018), and

have an image pair separation of 46 days and 10 m resolution. ‘Fine’ and ‘ultra-fine wide’ beam mode images from RADARSAT-2 were utilised to generate 2011-12 velocity mosaics originally published by Waechter and others (2015), using a nested search window approach to accurately measure both high and low velocity regions.

For winters 2014-2020, velocity maps were created from RADARSAT-2 ultra-fine (3 m resolution), and wide-fine (8 m resolution) image pairs acquired by Parks Canada (Appendix 2-A). Most image pairs have 24-day separation (RADARSAT-2 repeat orbit interval), although some have 48-day separation due to acquisition conflicts. Four-day repeat RCM images from winters 2021-2023 were obtained through the EODMS data portal (https://www.eodms-sgdot.nrcan-rncan.gc.ca/), via the Canadian Space Agency, and used to generate velocity mosaics for the region (Van Wychen and others, 2023).

Winter SAR imagery was used to avoid loss of coherence between image pairs caused by melt. Based on co-registered backscatter intensity images, a patch intensity cross-correlation was used to determine displacement in the azimuth and range directions from the offset between corresponding pixel blocks in each image pair (Lu and Veci, 2016). The earlier datasets (ALOS PALSAR from 2007-10; Van Wychen and others, 2018, and RADARSAT-2 from 2011-12; Waechter and others, 2015) were processed using a custom Matlab script, while those from 2014 onwards (RADARSAT-2 2014-20, RCM 2021-23) were processed with GAMMA software. These speckle-tracking methods provide velocity results similar in quality to each other (Schellenberger and others, 2016) and have been previously applied in northern and western Canada (Waechter and others, 2015; Van Wychen and others, 2018, 2023).

Displacements were reprojected into UTM zone 7N, normalized to values of m a^{-1}, and filtered to remove noise and mismatches. Custom R and Matlab scripts, as well as ArcGIS tools, were used to filter and post-process the displacements. Coarse filtering was used to limit magnitudes to between 5 m a^{-1} and 6000 m a^{-1}, which represent the lower detection limit and maximum velocities previously measured in the St. Elias Mountains (Waechter and others, 2015). A Matlab script was used to automatically filter the data based on flow direction, with values which differed by >50° from the mean direction of neighbouring cells discarded. Where multiple image pair results from the same winter existed, overlapping values were averaged to produce a single velocity value, and Inverse Distance Weighted (IDW) interpolation was used to fill minor gaps (<250 m for ultra-fine,

or <500m for fine-wide imagery). The results were clipped to the Randolph Glacier Inventory version 6.0 outline (RGI Consortium, 2017). Velocities for selected glaciers were extracted at 240 m intervals along centrelines provided by Kienholz and others (2015), which were manually modified to match glacier flow patterns. This follows a similar methodology to that used by Waechter and others (2015), with the final results smoothed using a 720 m moving window.

2.3.1.2 Annual and short-term velocities derived from optical images

NASA's Inter-Mission Time Series of Land Velocity and Elevation (ITS_LIVE) program provides annual average surface velocities derived from Landsat 4, 5, 7 and 8 imagery over the period 1985-2018, with a resolution of 240 m (Appendix 2-B). These are based on the auto-RIFT feature tracking processing chain, as described by Gardner and others (2019). The parameter v (velocity magnitude in m a^{-1}) was extracted along the same centrelines of glaciers as described in the previous section, and smoothed over a 720 m (3-pixel) moving window.

In addition, the ITS_LIVE point comparison tool (https://itslive-dashboard.labs.nsidc.org/) was used to download short-term velocities from 2013 to 2022 at point locations along the centreline of selected surge-type glaciers. The point data was limited to between 45 and 245 days separation to focus on short-term and recent velocity peaks. Filtering of data points was completed using the relationship between velocity and provided error estimates: if the velocity errors were 50% or higher than the velocity, the point was excluded (Main and others, in review). This threshold was selected as it adequately represents the range in velocity extremes, but excludes all observations where the velocity error is higher than the measurement itself.

2.3.1.3 Error analysis

For velocities derived from SAR data, poor image co-registration, DEM errors, inconsistencies in the satellite orbital model, cross-correlation errors, and layover or foreshortening effects can cause errors in speckle-tracking results (Schellenberger and others, 2016; Van Wychen and others, 2018). Velocity errors were determined from apparent motion over stable ground, based on a 100 m buffer surrounding the modified RGI 6.0 glacier outlines (Appendix 2-A). The 2007-10 ALOS PALSAR velocities have an error range of 8.5 – 15.0 m a^{-1} (Van Wychen and others, 2018), while the 2011 and 2012 RADARSAT-2 mosaic errors average 16.6 m a^{-1} and 12.7 m a^{-1}, respectively (Waechter and others, 2015). The 2014-20 RADARSAT-2 errors range between 4 and 8 m a^{-1}, and 2021-23 RCM mosaics range between 7 and 13 m a^{-1}.

For velocities derived from optical data, the ITS_LIVE velocity dataset provides the error product *v_error* (error in velocity magnitude in m a^{-1}). Sources of error associated with the ITS_LIVE dataset, including surface skipping and sensor biases, are described in the *Regional Glacier and Ice Sheet Surface Velocities Known Issues* documentation (http://its-live-data.jpl.nasa.gov.s3.amazonaws.com/documentation/ITS_LIVE-Regional-Glacier-and-Ice-Sheet-Surface-Velocities-Known-Issues.pdf). The error values within the RGI v6.0 outlines for the St. Elias Mountains averaged 16 m a^{-1} from 1985-99 and 6 m a^{-1} for 2000-18 (Appendix 2-B).

2.3.2 Statistical analysis

We preformed statistical analysis on a pixel-by-pixel basis on time stacked velocity mosaics, to understand how glacier velocities vary over time, and to identify new glacier surges and other dynamic changes. This was performed on 1985-2018 annual average velocities (ITS_LIVE data), as well as for 2007-23 winter velocity datasets (ALOS PALSAR, RADARSAT-2 and RCM), and finally using all datasets combined. The maximum and minimum velocities recorded at each pixel over the full 38-year period were extracted and then differenced to provide the maximum velocity range. This was used to identify areas of high velocity variability, which can be indicative of glacier surging. In addition, quiescent mean annual average (1985-2018) and winter velocity (2007-23) mosaics were generated by masking glaciers with observed surges for each individual year, and averaging all remaining velocity data on a pixel-by-pixel basis. We also created maximum annual average (1985-2018) and winter velocity (2007-23) mosaics during active surge periods. Finally, we produced a map based on the percentage change between quiescence and maximum active surging velocity on a pixel-by-pixel basis over the entire time period.

Glaciers with known surges, and those with high velocity variability, were selected for further analysis. In particular, centreline profiles were examined if the velocities increased successively for more than 1 year. Descriptive statistics regarding the physical characteristics (e.g., area, slope and elevation) of glaciers in different categories (surge-type, non surge-type, and confirmed surges, see below for definitions) were extracted from the RGI v.6.0 database in ArcGIS.

2.3.3 Surge-type glacier inventory

The surface features and velocity characteristics of all glaciers in the St. Elias Mountains were used to classify them into surge-type and non surge-type. The inventory of Sevestre and Benn (2015), which itself was developed from earlier inventories by Post (1969), Clarke and others

(1986), and Clarke and Holdsworth (2002), among others, identified surge-type and non surge-type glaciers based on periodic changes in glacier velocity (e.g., an observed active phase, often asynchronous compared to neighbouring glaciers), terminus advance (e.g., rapid advance, out of phase with nearby glaciers), and/or the presence of looped moraines, heavy crevassing, or other geomorphological evidence (e.g., presence of potholes or push moraines). If a surge was not directly observed, Sevestre and Benn (2015) stated that a "sufficient combination" of glaciological/geomorphological features was required to confirm a glacier as surge-type, based on an index ranging from i) possible surge-type; ii) very probable surge-type; and iii) confirmed surge-type.

Using the Sevestre and Benn (2015) inventory as a foundation, observed surges identified by recent studies were added to the inventory (e.g., Altena and others, 2019; Kochtitzky and others, 2019; Fu and Zhou, 2020; Samsonov and others, 2021; Nolan and others, 2021; Partington, 2023; Kääb and others, 2023; Van Wychen and others, 2023; Main and others, in review). In addition, our own velocity mosaics and field observations were used to add observed surges to the inventory.

Based on our velocity mosaics we classified a glacier as having undergone an observed surge (i.e., confirmed surge-type) if it met three conditions: i) there was a large range between the observed minimum and maximum velocities; ii) velocities increased substantially over a 2+ year period; and iii) this pattern occurred over a large, and mostly contiguous area of the glacier. Characteristics of all surges identified from 1874 to 2023 were used to determine the repeat frequency and active phase duration of events, and to explore if overall surge behaviour has changed over time. In the Sevestre and Benn (2015) inventory two surge entries were created if rapid flow behaviour of a tributary differed from the main trunk (e.g., in timing), and we adhere to this categorization. Unfortunately, the above set of criteria are necessarily vague, as glaciers in the St. Elias Mountains have displayed a significant variety of velocity behaviours both between glaciers, and even within the same glacier during different surges, rendering a quantitative set of benchmarks elusive. This represents a larger issue in the study of glacier dynamics and surging, as even the most fundamental term, "*surging glacier*", is not yet defined in terms of the difference between quiescent and active velocities, how often a surge must occur, or what proportion of the glacier must be affected, among other characteristics. For example, must a glacier surge more than once to be considered surge-type?

A subset of glaciers were selected for further analysis to quantify the detailed characteristics of surges if the events were both confirmed (i.e., dated), and had clear patterns either from our own data sources, or were well-represented in past literature. This subset was analyzed using velocity values reported in past studies, or velocity records from our 1985-2023 datasets, and was used to examine the common features among surges, including surge initiation timing and location, timing of termination, recurrence interval, active and quiescent phase durations, and percent change between quiescent and peak velocities. The velocity patterns along centrelines of glaciers in this subset were also extracted and further analyzed for patterns during quiescence, acceleration, active, and deceleration phases.

On glaciers where more than one surge was observed, the availability of past studies and our velocity data dictated how individual surge patterns were described: where possible, a synthesis of past studies and observations from our datasets were used. A range of trunk-tributary interactions and velocity behaviours were also examined.

2.4 Results

2.4.1 Long-term surface velocity trends of surge-type glaciers

Analysis of the ITS_LIVE mosaics from 1985-2018 show that average annual velocities of surge-type glaciers during their quiescent phase range from 2 to ~245 m a^{-1}, averaging ~70 m a^{-1} (Fig. 2-1). There is a strong southwest to northeast velocity gradient across the St. Elias Mountains, with surge-type glaciers on the eastern flank averaging 35 m a^{-1} during quiescence, and none over 100 m a^{-1}. In contrast, glaciers located on the south-west corner of the study area near the maritime coast averaged ~130 m a^{-1} during quiescence, with Guyot Glacier having the highest average annual velocity of ~245 m a^{-1}. The overall highest annual velocities during quiescence were found in the south-central region, including Yahtse at ~6000 m a^{-1}, Hubbard at ~5000 m a^{-1} and Seward at ~3500 m a^{-1}.

Analysis of maximum velocities during active surging demonstrates that several surge-type glaciers experience the highest velocities along their main trunk (e.g., Nàłùdäy, Steele, and Klutlan), although on the western side of the range some glaciers experience the highest velocities in the middle and upper sections of their basins (e.g., Chitina, Walsh). Figure 2-3 shows the percentage change in velocity (m a^{-1}) from quiescence to maximum values during active surging, with a lower threshold cut-off of at least 50% increase. For some glaciers, such as Nàłùdäy, Steele,

and Klutlan, the largest change in velocities is concentrated towards the lowest part of the glacier, with surging velocities up to 7500% higher than quiescent. Chitina and Walsh glaciers experience slower velocities near their termini during active surging (Fig. 2-2), which coincides with a much smaller change between their quiescent and active surge velocities (Fig. 2-3) compared to their upper regions, suggesting that there is a zone of dead ice in their lowermost parts that is minimally impacted during surging. While pulse-style glaciers (e.g., Hubbard, Seward, and Agassiz) demonstrate high velocities during surging (Fig. 2-2), they also have consistently lower percentage change in velocities from quiescence to surging (Fig. 2-3), signalling that mean quiescent and active surge phases are not greatly different.

Average winter velocities of surge-type glaciers in quiescence over the period 2007-23 derived from our SAR speckle tracking were slightly higher than average annual velocities, at 80 m a^{-1}, and ranged from 4 to 180 m a^{-1}, although these datasets do not completely overlap in coverage or timing. On the eastern flank, surge-type glaciers averaged 45 m a^{-1} during quiescence, while on the west coast they averaged ~130 m a^{-1}. The fastest flowing glaciers include Hubbard and Seward glaciers at ~2500 m a^{-1} and ~2250 m a^{-1} on average, respectively, although short-lived velocity peaks occasionally doubled these values. During surges, winter-time velocities are typically higher than average annual velocities for Alaskan-style surges (Figs 2-1, 2-4), including during the acceleration, active and deceleration phases. For pulsing glaciers in their active phase, winter velocities are not significantly higher than annual average velocities, and often are lower overall, such as at Agassiz Glacier (Fig. 2-5).

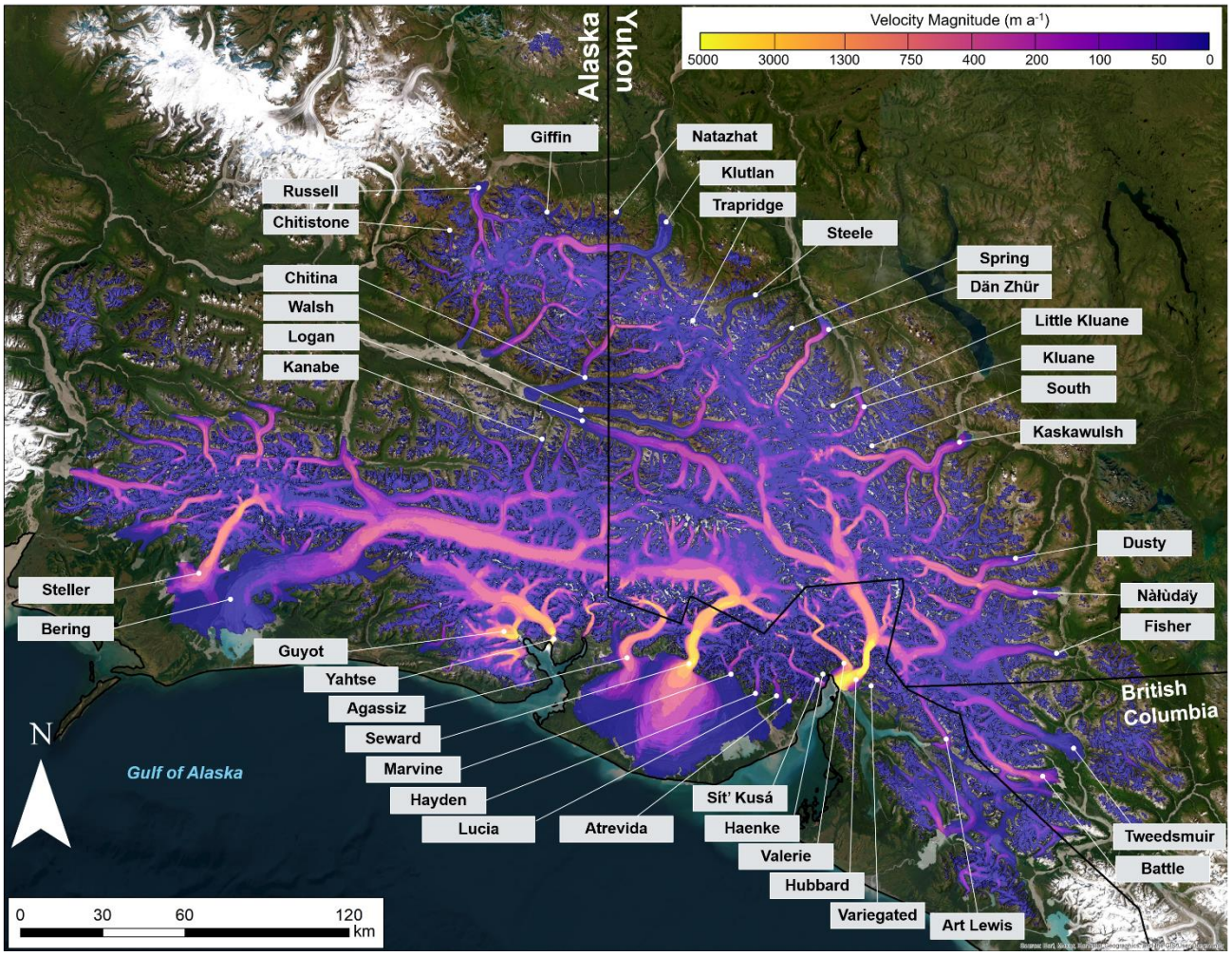

Figure 2-1: Regional map of quiescent glacier velocities over the period 1985-2018, based on analysis of annual ITS_LIVE velocity mosaics of the St. Elias Mountains, Yukon-Alaska, identifying key glaciers and locations mentioned in this study. Glacierized terrain is defined by RGI v6.0. Base image: ESRI World Imagery from 2018-2023, UTM Zone 7N.

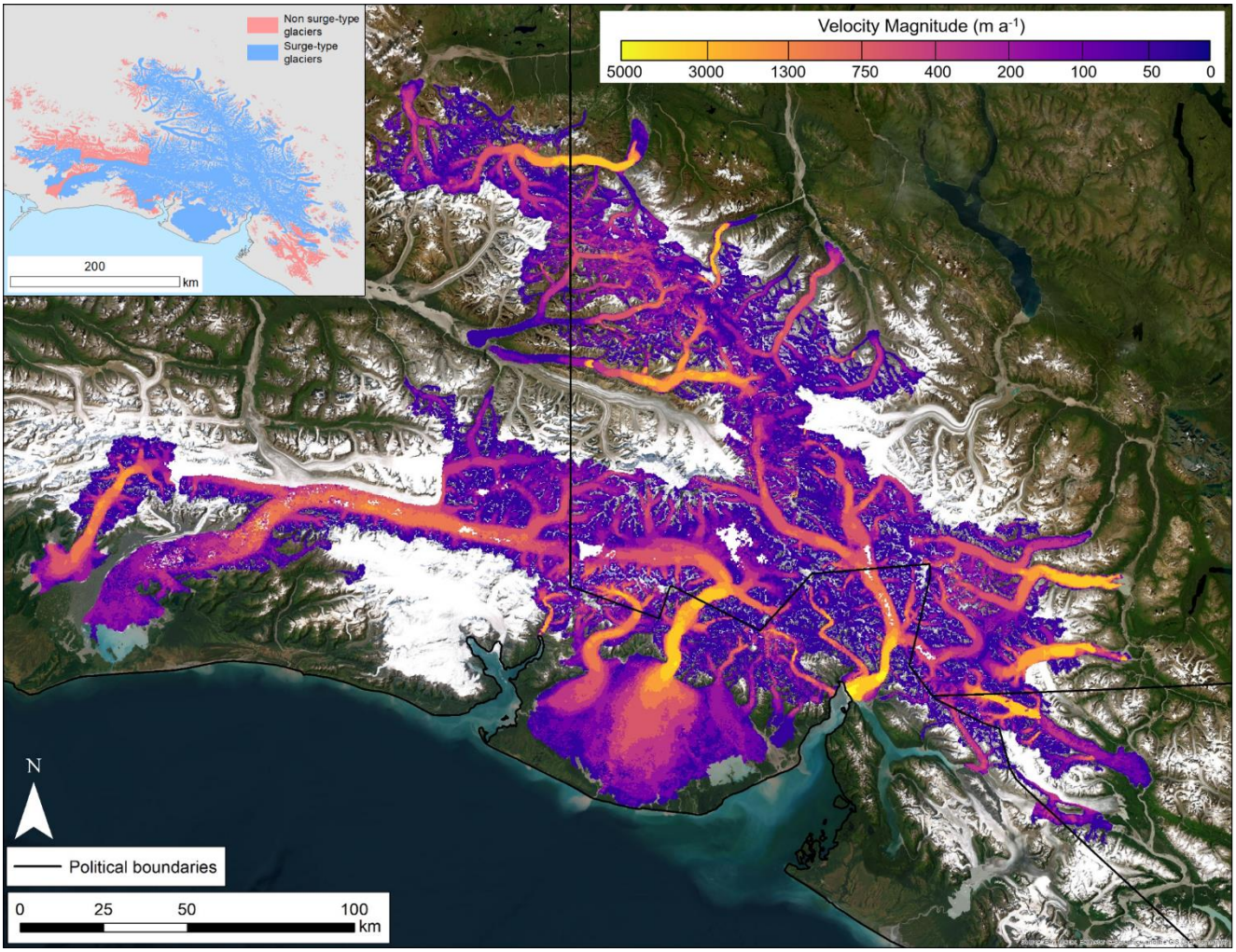

Figure 2-2: Regional map of maximum velocities during active surging, based on derived from mosaics of annual average velocities (1985-2018) and winter-time velocities (2008-2023) of the St. Elias Mountains, Yukon-Alaska. Base image: ESRI World Imagery from 2018-2023, UTM Zone 7N. Inset: Regional distribution of surge-type and non-surge type glaciers; the surge-type glacier category includes glaciers where the main glacier does not surge, but a tributary does (e.g., Kaskawulsh Glacier).

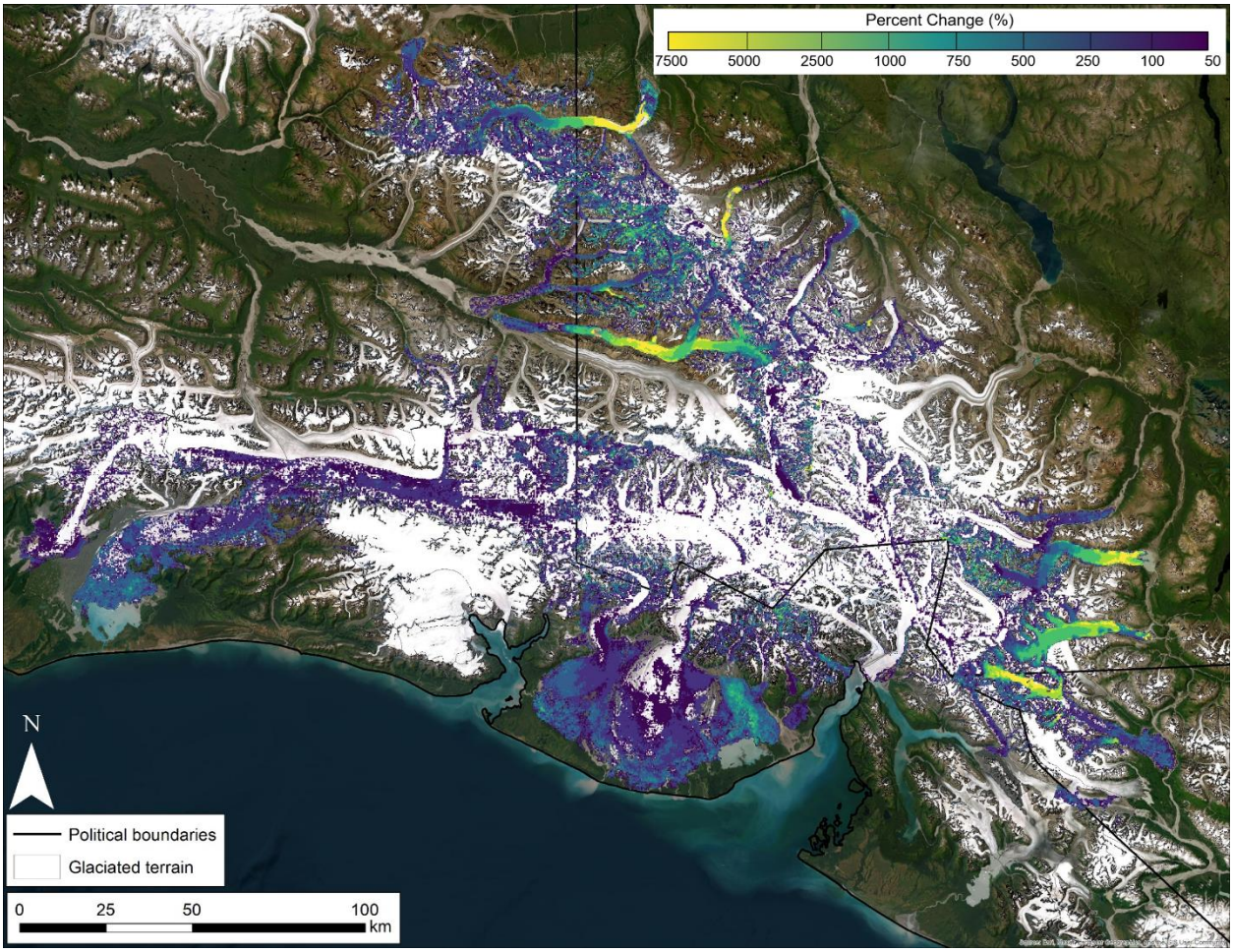

Figure 2-3: Active ice areas during surges, based on the percentage change in velocity magnitude from quiescence to active surging (minimum change of 50% increase shown). Glacierized terrain is defined by RGI v6.0. Base image: ESRI World Imagery from 2018-2023, UTM Zone 7N.

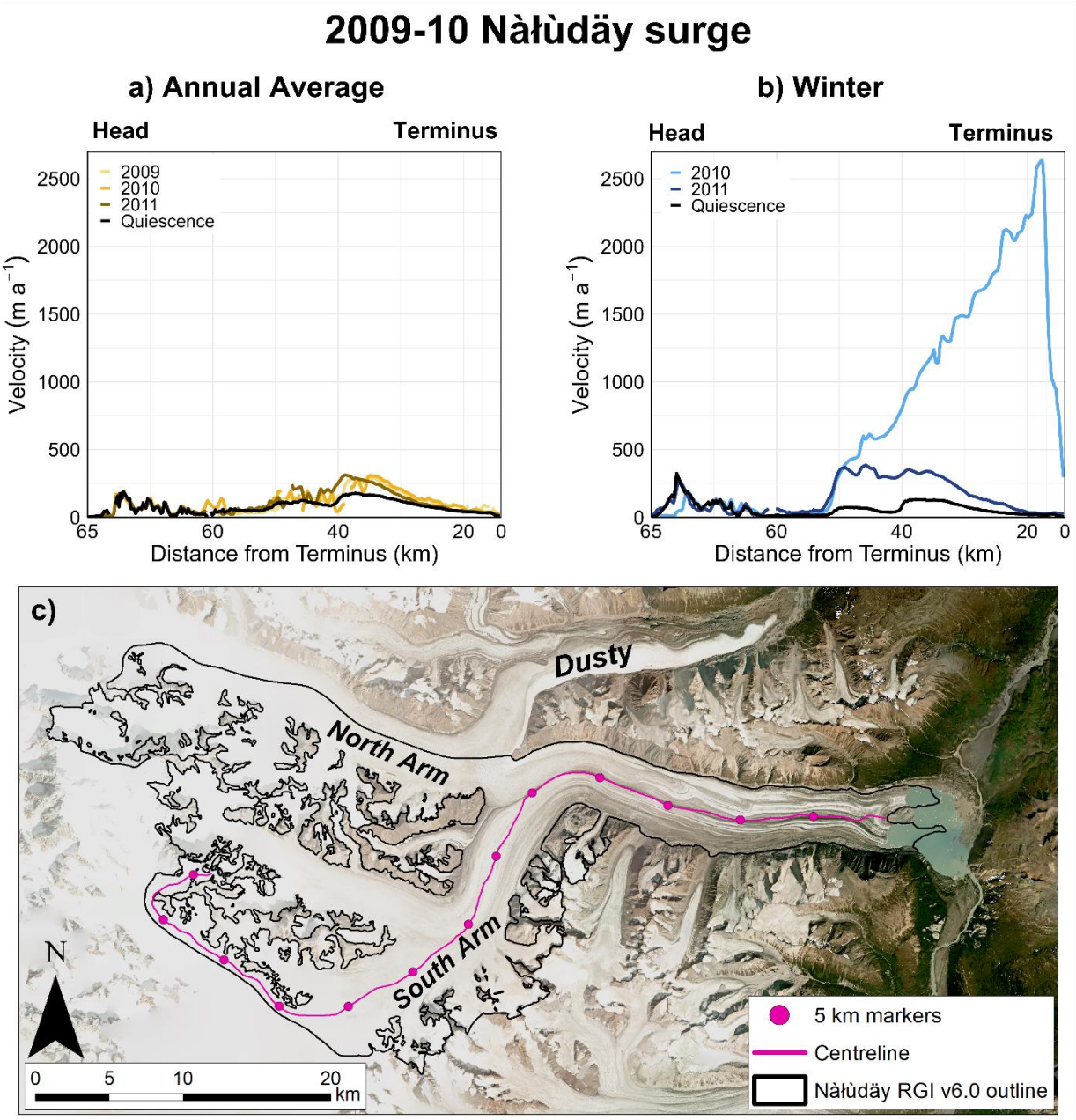

Figure 2-4: Comparison of a) annual average and b) winter velocities during the 2009-2010 surge of Nàłùdäy along the c) south arm centreline. Glacierized terrain is defined by the RGI v6.0. Base image: ESRI World Imagery from 2018-2023, UTM Zone 7N.

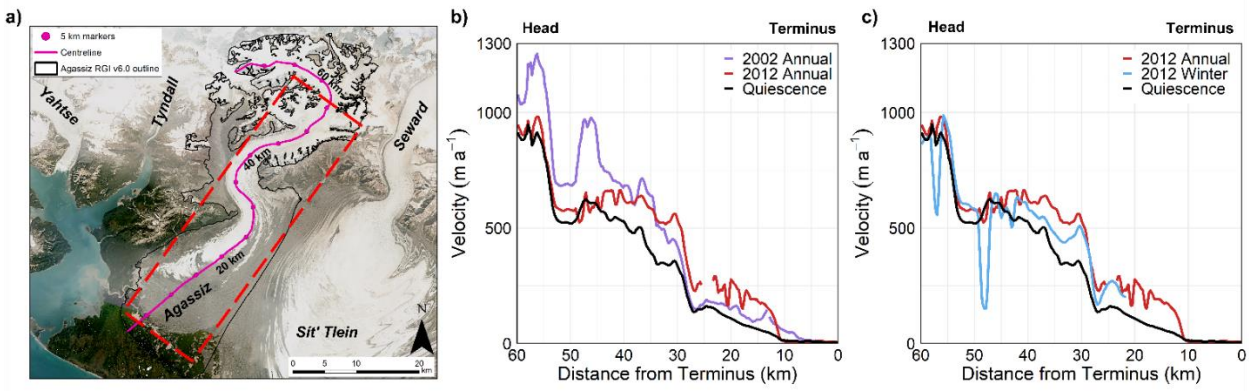

Figure 2-5: Comparison of the 1999-2002 full surge of Agassiz Glacier reported by Muskett and others (2008), compared to the 2011-12 pulse determined in this study. a) map of glacier showing centreline, b) comparison of glacier velocities during the 2002 surge and 2012 pulse, and c) annual average and winter velocities in 2012 compared to quiescent velocities. This demonstrates that opposite to Alaskan-style surges, where peak velocities occur during the winter, glacier pulses instead experience similar velocities on annual and winter timescales. Red dashed box indicates section of centreline presented in b) and c). Glacierized terrain is defined by RGI v6.0. Base image: Planet Fall 2018 basemap, UTM Zone 7N.

2.4.2 Inventory of observed glacier surges

Based on the initial inventory of Sevestre and Benn (2015), other recent studies and our new velocity mapping we categorized a total of 231 glaciers (4.6% of the total glaciers by basin; Appendix 2-C) as surge-type in the St. Elias Mountains. This includes the division of 2 glaciers from the Sevestre and Benn (2015) inventory into 4 glaciers in ours due to their physical separation: Kluane and Little Kluane glaciers; Marvine and Hayden glaciers. There have been a total of 192 observed surges involving 66 individual glaciers since 1874, of which 40 glaciers surged more than once. During the period 1985-2023, 73 surges occurred on 42 individual glaciers, with 21 new surges identified in this study (Appendix 2-D). All glaciers that surged during this period were previously identified as surge-type by previous inventories (e.g., Sevestre and Benn, 2015), however their index classification can now be upgraded to confirmed surge-type, rather than possible or very-probable. In addition, we identified several new surges of tributaries of these glaciers (e.g., upper Hubbard Glacier, Hodgson (tributary of Steele Glacier)).

2.4.3 Characteristics of observed glacier surges

Using our velocity records (1985-2023), four distinct phases can be identified for most glaciers with observed surges in the St. Elias Mountains: acceleration, active, deceleration, and quiescence. Most previous studies in this region and elsewhere have commonly focused on describing characteristics of the active and quiescent phases, but with the enhanced temporal resolution provided by new velocity datasets such as ITS_LIVE used here, it is clear that distinct acceleration and deceleration phases are also often present. The main features of the four phases are as follows:

(a) The acceleration phase (Figs 2-6a, 2-7a) is characterized by progressive increases in glacier velocity over a multi-year to multi-decadal period. Partial or slow surges may only reach the acceleration phase, and not eventually progress to the active phase.

(b) The active phase (Figs 2-6b, 2-7b) is characterized by the highest velocities, which often last from a couple of months to a couple of years. The transition between the acceleration and active phase is characterized by a significant increase in velocities (e.g., Figs 2-7a, 2-7b, *Atrevida Glacier*), however in some instances the active phase is simply represented by the highest velocities (e.g., Figs 2-7a, 2-7b, *Lucia Glacier*). Often, this is accompanied by significant movement of glacier ice from an up-glacier reservoir zone to a down-glacier receiving zone, as well as terminus advance and the formation of new

geomorphological features such as looped moraines and heavy crevassing. Annual average velocities often do not capture the full magnitude of the active phase, meaning that short-term (~ monthly) velocity observations are necessary to properly characterize this signal.

(c) The deceleration phase (Figs 2-6c, 2-7c) occurs after the active phase and is typically shorter in duration than the acceleration phase, occurring over a 1-2 year period (although deceleration periods of up to 7 years have been observed).

(d) A glacier is in quiescence when surface velocities are low and stable for multiple years (Figs 2-6c, 2-7c).

While other studies have observed an acceleration period prior to active phase onset, it has typically not been characterised as a distinct phase, and often there is little distinction between the acceleration and active phases in the literature (e.g., Bevington and Copland, 2014; Fu and Zhou, 2020; Nolan and others, 2021).

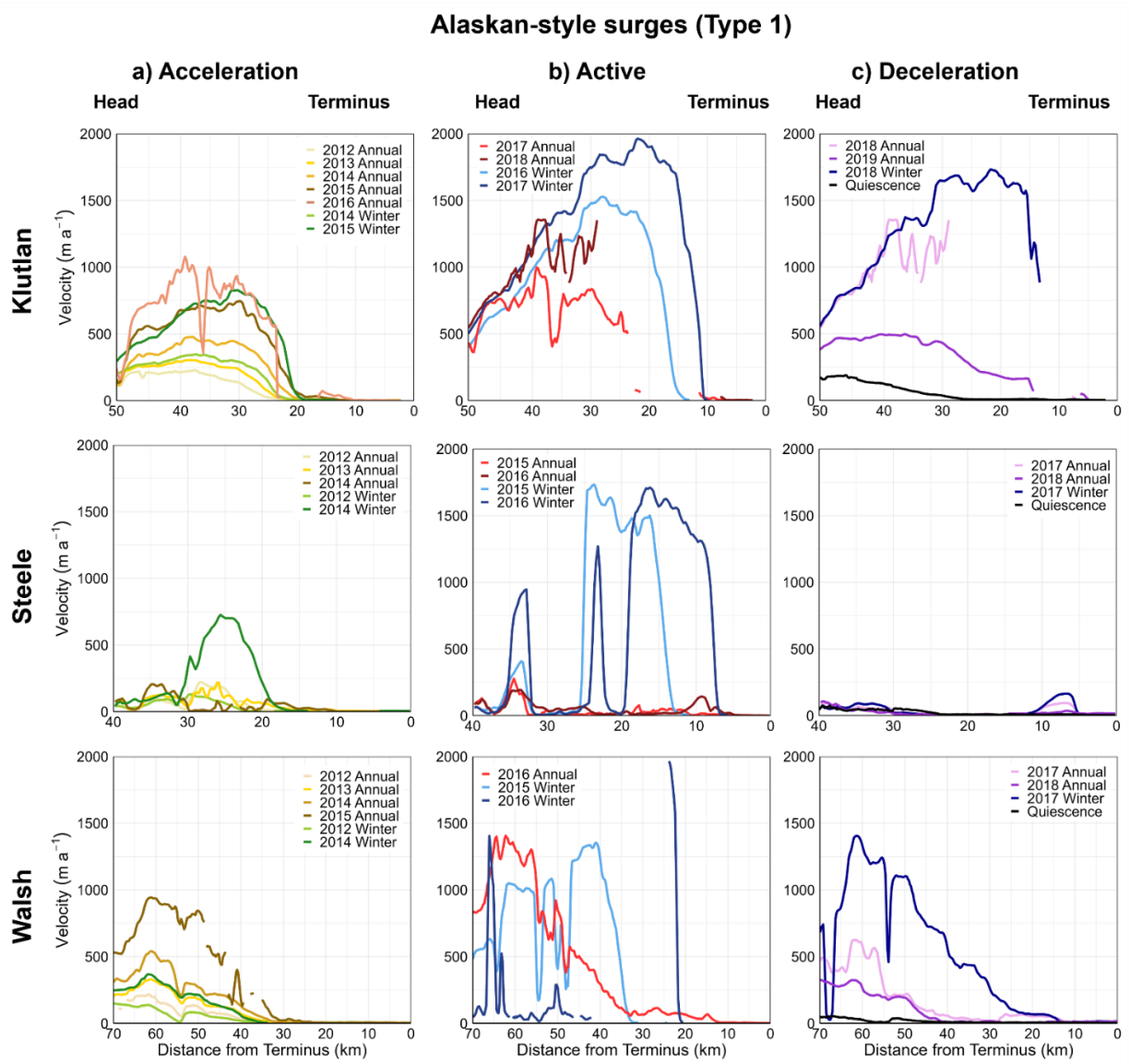

Figure 2-6: Patterns of Alaskan-style glacier surging in the St. Elias Mountains. The a) acceleration, b) active and c) deceleration phases of land-terminating Klutlan, Steele and Walsh glaciers. Glacier head is located on the left side of each plot, and terminus on the right.

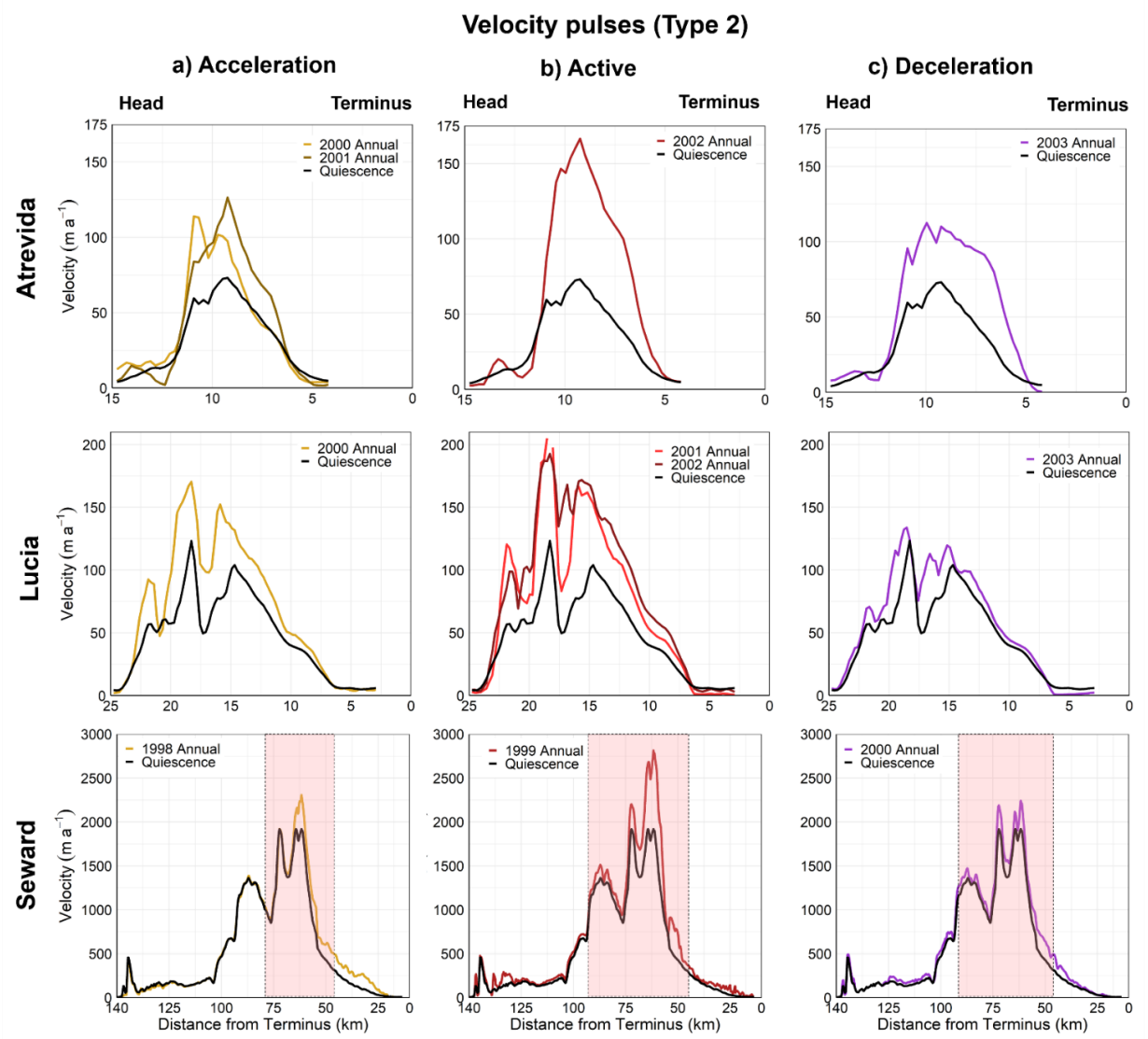

Figure 2-7: Patterns of velocity pulses in the St. Elias Mountains, demonstrating the a) acceleration, b) active, and c) deceleration phases of land-terminating Atrevida and Lucia glaciers, and partially lake-terminating Seward Glacier. Glacier head is located on the left side of each plot, and terminus on the right. The light red box indicates the affected region when a pulse is limited in extent.

2.4.4 Classification of observed surges

The velocity patterns of glaciers observed to have surged since 1985 are further described below to identify their common characteristics, and to categorize them based on similarities in surging behaviour. Due to incomplete data, it is not possible to determine the detailed characteristics of all surges identified in this study, but it is possible to reconstruct the detailed history of 55 surges that occurred on 28 glaciers in the St. Elias Mountains over the period 1985-2023. Based on their physical characteristics and duration of acceleration, active and deceleration phases, as well as the relative changes in velocity between phases, the 55 surges can be grouped into 4 main types (Table 2-1, Figs 2-6, 2-7):

Type 1 - Alaskan-style surge: this is the most common type of glacier surge, during which there is a typical acceleration period of 2-4 years prior to the actual surge (e.g., 4 years for Variegated Glacier for its 1982-83 surge; Kamb and others, 1985), although acceleration periods of over a decade have been observed (e.g., 11 years for Logan Glacier; this study; ~25 years for Fisher Glacier; Partington, 2023). Velocities then peak during the active phase over ~2 months to ~2 years, after which there is a deceleration period lasting for 1-2 years. A total of 16 glaciers (57% of the 28 examined) fell into this category (Table 2-1). These glaciers dominate most of the St. Elias Mountains, including the north, central-west, and the eastern continental portion of the range (Fig. 2-8). Although it is only possible to determine with confidence when surges terminate for 8 glaciers of this type, each of these terminated during the summer. The active phase for Alaskan-style surges averages 2.3 years, and quiescent phase averages 25 years, although there is significant variability in the length of the quiescent phase between individual glaciers, varying from ~5 years (Sít' Kusá; Nolan and others, 2021) to ~40 years (Fisher Glacier; Partington, 2023). Alaskan-style surges experience a range from ~50-7500% change between quiescent and active phase velocities (Table 2-1; Appendix 2-C).

Type 2 - Pulsing: this is the next most frequent style of surge, where 2-3 year velocity increases, often limited in both magnitude and extent, are followed by a return to lower velocities (Table 2-1, Fig. 2-7); a total of 10 (36%) glaciers are categorized as experiencing pulses in our study. The active phase of pulsing glaciers averages 3 years, and quiescent phase averages 8.5 years (Appendix 2-C). Glacier pulses are more commonly found in

faster flowing glaciers (average annual velocity peaks of up to ~5200 m a^{-1} at Hubbard, ~3700 m a^{-1} at Seward, and ~1500 m a^{-1} at Agassiz glaciers during quiescence) (Fig. 2-1), compared to those that flow more slowly, and are geographically clustered in the south-central region close to the Gulf of Alaska (Fig. 2-7). Pulse glaciers experience ~50-150% increase between quiescent and peak velocities (Table 2-1).

Type 3 - Slow surge: there were 2 (7%) glaciers which slowly surged between 1985 and 2023, Trapridge (Frappé and Clarke, 2007) and South (Little Kasa) (De Paoli and Flowers, 2009), although the data available from ITS_LIVE is too low-resolution to create detailed velocity profiles for them. During its slow surge, velocities at Trapridge Glacier reached ~44 m a^{-1}, compared to ~9 m a^{-1} during quiescence, a ~390% increase (Frappé and Clarke, 2007). It was not possible to calculate a meaningful average active or quiescent phase length with only 2 data points, although De Paoli and Flowers (2009) reported the active phase for South Glacier was 30-40 years. Both slowly-surging glaciers are small (~3.5 and 5.7 km^2, respectively) and located on the eastern continental side of the range.

Type 4 - Partial surge: a partial surge occurs when a major mass movement occurs in an upper basin that does not instigate a surge in the main trunk, nor does the terminus advance (Sund and others, 2009; Main and others, in review). There were 4 partial surges identified from 1985-2023, all in the Hubbard Glacier complex (Table 2-1). Main and others (in review) also described a partial surge that occurred from the upper tributaries of Little Kluane Glacier in the 1960s. Due to the short temporal nature and limited spatial extent of these events, it is not possible to accurately determine the length of their active phase (although events at Hubbard Glacier seem to last for ~1 month; Abe and Furuya, 2015), nor is it possible to determine their repeat interval. As partial surges are fundamentally different compared to full surges or pulses (e.g., often occur over a relatively small area of a glacier (e.g., a single tributary), for a significantly shorter time (e.g., one month compared to several years), we categorize some as having both partial surges and other types of surge events.

Table 2-1: Types of glacier surges identified through analysis of velocity patterns and previously published papers during observed rapid velocity events in the St. Elias Mountains from 1985-2023.

Type	Description	Description of velocity profiles for each phase			Glaciers
		Acceleration	Active	Deceleration	
1 Alaskan	Recognizable acceleration, active and deceleration phases over a period of several years, impacting the majority of the glaciers' extent	Velocities increase progressively for several (2+) years to several decades	Velocities increase significantly (over 50% up to 7500%) for 1-2 years, and impact a large area of the glacier	Velocities decrease steadily for 1-2 years before returning to near-quiescent values	Bering, Chitina, Dän Zhür, Dusty, Fisher, Klutlan, Little Kluane (2010s), Logan, Nàłùdäy, Marvine, Russell, Sít' Kusá, Steele, Tweedsmuir, Variegated, Walsh
2 Pulse	Pulsing: short-term (but more than one year), low magnitude speedups, limited in magnitude and geographic extent	No clear acceleration leading up to active phase	Short-term speedups of ~50-150%, over a limited section of the glacier (often in the middle, not impacting terminus). Speedups last more than a single year.	Deceleration between active phase and return to background velocities	Agassiz, Art Lewis, Atrevida, Hayden, Hubbard (main trunk), Kanabe, Seward, Spring, Steller, Valerie
3 Slow	Slow surge	Exceptionally long active phase (up to 40 years), with significantly lower velocities compared to Alaskan-style surges. Similar to Svalbard-stye surges		Velocities decelerate to background levels rapidly	South, Trapridge
4 Partial	Partial surge	A mass movement, often in or near the accumulation area, which does not instigate a full surge in the main glacier trunk			Hubbard (3 upper accumulation area tributaries (2009), and one small tributary (2021))
Not categorizable		Battle, Chitistone, Duktoth, Giffin, Natazhat			

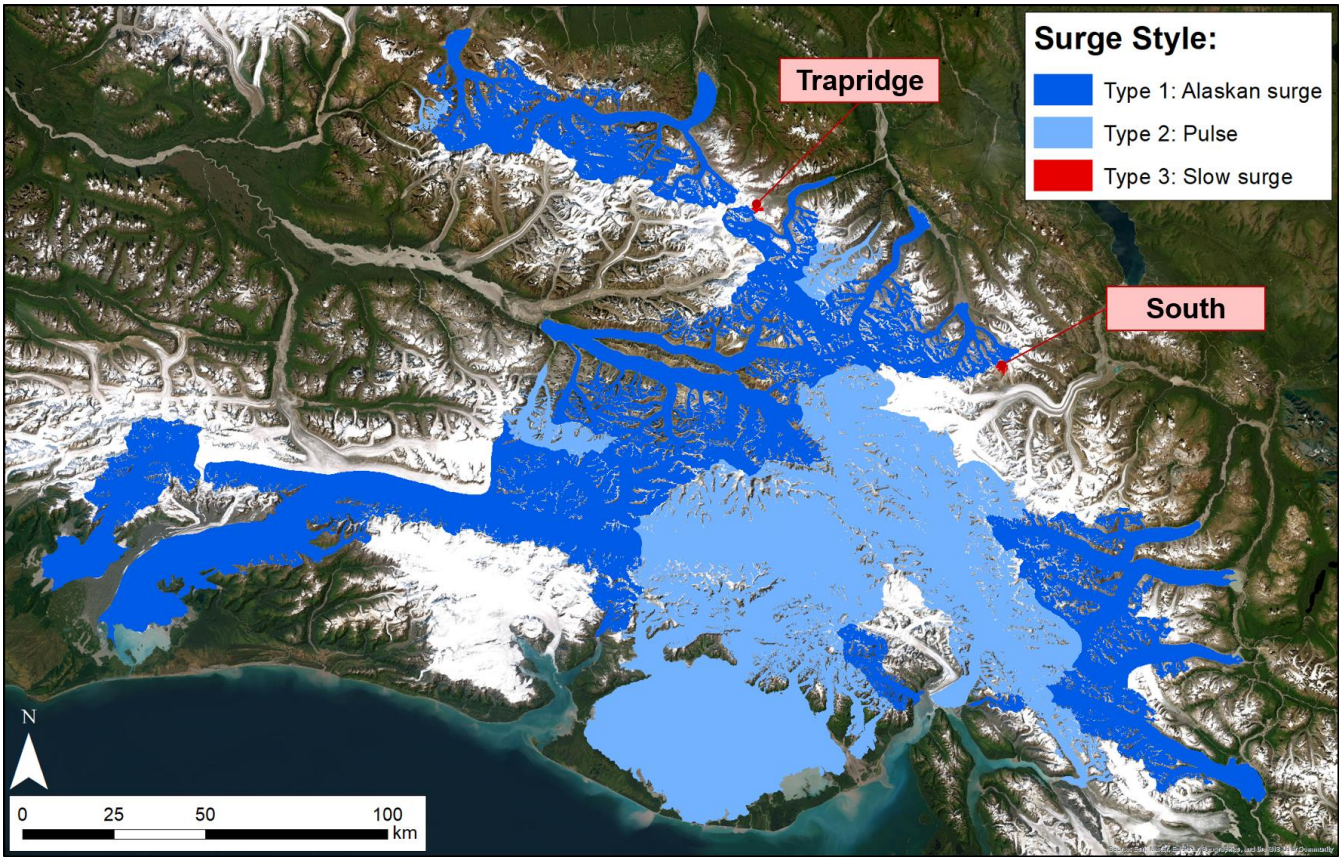

Figure 2-8: Map of the three identified types of dynamic instabilities found in the St. Elias Mountains, with slow surge-type glaciers Trapridge and South/Little Kasa Glaciers labelled due to their small size. Glacierized terrain is defined by RGI v6.0. Base image: ESRI World Imagery from 2018-2023, UTM Zone 7N.

2.4.5 Characteristics of surge-type glaciers

Based on the RGI Inventory, a series of characteristics of surge-type glaciers are synthesized below. It is important to note that these characteristics are obtained from single-snapshots in time, and do not necessarily distinguish between glaciers in active phase or quiescence, and values such as slope are obtained over the entire main trunk. Approximately 77%, or ~25,600 km^2, of the glaciated area of the St. Elias Mountains is classified as surge-type (as defined by the three categories used by Sevestre and Benn, 2015), and 68% of the glaciated area has been observed to surge since 1874, compared to ~7500 km^2 of glaciated area that is non surge-type. Geographically, surge-type glaciers comprise the majority of the area within the centre of the region, whereas non surge-type glaciers are mainly located either on the margins of the icefields, or in the south-east and central-west regions (Fig. 2-4, inset). The majority of the glaciers with observed surges are much larger in area (average ~370 km^2, with glaciers as large as ~3360 km^2) than non surge-type glaciers (average ~1.5 km^2) (Table 2-2). Coinciding with their larger extents, surge-type glaciers have a lower average surface slope (17-20°) compared to non surge-type glaciers (25°), as well as more tributaries. Surge-type glaciers are far more likely to terminate in water, with 11% of observed surges occurring on lake-terminating glaciers, compared to 0.3% of non surge-type glaciers, and 8% vs 0.1% for marine-terminating glaciers (Table 2-2).

2.4.6 Controls and characteristics of glacier surges

In addition to classifying surge events by their velocity patterns, it is also possible to categorize them based on other characteristics, including where on the glacier and at what time of year the initiation of a dynamic instability occurs, when and where on a glacier the surge terminates, recurrence interval and magnitude, and propagation direction. These factors are summarized for up to 30 glaciers with observed glacier surges from 1985-2023 in Table 2-3. The entries for this table were created using a combination of past studies, as well as our own velocity data.

Table 2-2 Main characteristics of surge-type glaciers in the St. Elias Mountains. Glaciers with an observed surge over the period 1985-2023 were further categorized based on surge type as described in Table 2-1. Note: total number of observed surges is not equal to the total of individual types, as categorization was not possible for all glaciers.

Characteristic		**Non surge-type**	**Surge-type**	**Glaciers with observed surges from 1985 to 2023**			
				All	**Alaskan**	**Pulse**	**Slow**
Number		4802	231	63	16	10	2
Average area (km^2)		1.5	110	370	644	822	4.6
Average length (km)		1.2	14.2	37.1	67.2	56.8	3.8
Average median elevation (m asl)		1757	2100	1843	1916	1368	2309
Average surface slope (°)		25	20	17	14	13	20
Terminus Type (% and number)	Lake-terminating	0.3% (16)	3% (7)	11% (7)	31% (5)	0%	0%
	Marine-terminating	0.1% (4)	3.5% (8)	8% (5)	12.5% (2)	20% (2)	0%
	Land-terminating	99.6% (4782)	93% (216)	81% (51)	56% (9)	80% (8)	100% (2)
Average change in velocities from quiescent to active phase (%)		-	-	-	~1000	~60	-

Table 2-3: Characteristics of observed glacier surges from 1985-2023 in the St. Elias Mountains.

Characteristic		**Number (percentage)**	**Glaciers**
Where does the surge initiate?	Upper glacier (accumulation area)	10 (33%)	Agassiz, Art Lewis, Bering, Chitina, Little Kluane, Logan, Marvine, Tweedsmuir, Variegated, Walsh
	Middle section (ELA)	16 (53%)	Battle, Chitistone, Dän Zhür, Dusty, Fisher, Hayden, Kanabe, Klutlan, Lucia, Russell, Seward, Sít' Kusá, South, Spring, Steele, Steller
	Lower glacier (ablation area, terminus)	4 (13%)	Atrevida, Hubbard, Nàłùdäy, Tyndall
When does the surge initiate?	Winter / early spring	13 (81%)	Bering, Chitina, Chitistone, Fisher, Hubbard (partial surges only), Klutlan, Little Kluane, Logan, Sít' Kusá, Steele, Tweedsmuir, Variegated, Walsh
	Late summer / early fall	3 (19%)	Dän Zhür, Nàłùdäy, Tweedsmuir
When does the surge terminate?	Summer	8 (100%)	Fisher, Klutlan, Little Kluane, Nàłùdäy, Steele, Tweedsmuir, Variegated, Walsh
	Unknown	-	All pulsing glaciers

2.5 Discussion

A high percentage (72%) of the glaciers identified as surge-type in the Sevestre and Benn (2015) inventory and our update did not experience a recognizable surge between 1874 and 2023. Based on geomorphic evidence, these glaciers may have surged in the past, but have not shown such activity recently. However, while only a relatively small number of glaciers have undergone an observed surge in the historical record these glaciers account for a disproportionately large area within the St. Elias Mountains.

2.5.1 Comparing classifications of observed surges

Based on the classifications presented in 2.4.4 and detailed studies published about individual surges (footnote c in Appendix 2-C), it is clear that a wide range of fast-flow behaviour is present across the St. Elias Mountains. This necessitates a conceptual shift from older studies which typically present surging as being a distinct two-phase process (i.e., active vs quiescent) (Meier and Post, 1969; Fowler, 1987; Jiskoot, 2011), to a more comprehensive view, where glacier dynamic changes exist on a continuum. While characterization conflicts with the concept of a continuum, it is important to note where patterns do exist, in the hopes of creating benchmarks along a spectrum of behaviour. From the data reviewed here, there are cases where multiple types of surging behaviour can exist on the same glacier, such as at Little Kluane and Hubbard glaciers, which have both experienced partial surges in their accumulation areas, and full surges or pulses at other times, sometimes along different parts of their length. The partial surges of 3 small tributaries in the upper accumulation area of Hubbard Glacier in 2009 each lasted for ~1 month, with their influence limited to a local area, with no clear velocity changes found elsewhere in the majority of the glacier trunk (Abe and Furuya, 2015).

Glacier pulses may exist as a transitional stage between ‘normal’ and surging glaciers, and it may be possible for some glaciers, such as Agassiz, to exist at the boundary between full surges (1999-2002) and pulsing behaviour (2011-12) (Fig. 2-5). Muskett and others (2008) describe the 1999-2002 changes of Agassiz Glacier as a full surge based on ice surface elevation lowering (loss of up to 40 m) and a terminus advance of 1.6 km, although they did not present any velocity data. While they indicate that this was a full surge, our data indicates only a maximum ~60% increase in ITS_LIVE annual average velocities between 1998 and 2002, although velocities are higher in 2002 compared to 2012 (Fig. 2-5b). For comparison, during the 2011-12 pulse, Agassiz

experienced ~25% increase in annual average velocities, and up to 80% increase in winter velocities, mainly in the terminus region (Fig. 2-5c). Agassiz Glacier has been described as having "pulse-like flow" prior to the 1999-2002 surge (Muskett and others, 2003), although there is limited quantitative evidence to support this. Despite earlier reports of Agassiz Glacier experiencing full Alaskan-style surges, we have decided based on our velocity observations, particularly the change in glacier velocities between quiescence and active surging, to classify it as a pulse-type glacier.

The incremental acceleration stage prominent in Alaskan-style surges reflects a progressive increase in basal sliding, and suggests that the active phase might be the culmination of this acceleration (Frappé and Clarke, 2007; Sund and others, 2009; Jay-Allemand and others, 2011). This progressive increase in basal sliding over several years has been found at glaciers such as Klutlan (Altena and others, 2019), Variegated (Kamb and others, 1985) and Fisher (Partington, 2023). Fisher Glacier, for example, experienced an abnormally long (~25 year), but gradual (a few metres per year) acceleration phase which started in the middle of the glacier and eventually transitioned into a traditional Alaskan-style surge (Partington, 2023). At Sít' Kusá, acceleration begins directly after the most recent 2020-2021 surge (Liu and others, in press). Little Kluane Glacier also experienced a relatively long (~5 year) acceleration period which initially looked similar to a 1970s partial surge, but eventually transitioned into a full surge in 2017-18. Main and others (in review) suggested that this may be due to the change from a normal to a reverse surface slope due to the transfer of mass from the tributary to the main trunk, and, as a result, changes in hydrologic organization, including ponding of surface water and rapid drainage to the bed. In contrast, pulse-type glaciers may not reach this final active phase, as demonstrated by their relatively low active phase velocities compared to the acceleration phase (Figs 2-2b, 2-4), and often subdued winter velocities, compared to those of Alaskan-style surges (Figs 2-6c, 2-7c). Turrin and others (2014) determined that there were 5 low magnitude pulses at Ruth Glacier in the nearby Alaska Range from 1973-2012, with peaks occurring every ~7 years. They suggest this behaviour is due to enhanced basal motion due to incomplete drainage of the underlying till and subsequent deformation, followed by recharge and a repeat of the cycle, but without the glacier transitioning into a full active phase. While only providing findings for this particular glacier, the authors suggested that major surges are avoided as the basal roughness is great enough to restrict ice flow (Turrin and others, 2014). Pulse-style glaciers are also found to have the highest quiescent

phase velocities, which may suggest a modulating effect: since ice flow is relatively high, this may modulate against significant ice build-up in the reservoir zone, and therefore relatively small ice mass gains are released during surge events compared to Alaskan-style surges. This is demonstrated by the consistently small percentage change increase in velocities from quiescence to surging, which does not impact most of the glacier length, differing from Alaskan-style surges (Fig. 2-3).

2.5.2 Contextualization of surge styles within seasonal velocity variations

There are well-studied examples of seasonal velocity variations in the Yukon-Alaska region, including seasonal speed-ups of land-terminating glaciers (Burgess and others, 2013b). Transient water storage in an inefficient subglacial distribution network can increase glacier velocities for a short period due to increased basal motion (Bartholomaus and others, 2008). For example, during the spring early inputs of meltwater can overwhelm the undeveloped subglacial system and instigate short periods of acceleration (Burgess and others, 2013b). Eventually the subglacial drainage network develops, increases in efficiency as the channels enlarge, and the meltwater is evacuated quickly, decreasing basal motion (Bartholomaus and others, 2008). Similarly, accelerations can occur during the autumn through winter, suggesting that existing water at the bed can become pressurized and induce flow even without additional water inputs (Abe and Furuya, 2014). Burgess and others (2013a) established an inverse relationship between summer melt and ice velocities in the following winter for major glaciers in Alaska: for every additional metre of summer melt, there was an 11% reduction in winter velocity regardless of glacier size, geometry, climate, and bed type. This study suggested that higher summer melt rates lowered the amount of meltwater retained in the subglacial system during winter, and therefore did not provide an adequate film of water at the bed to enhance winter basal sliding (Burgess and others, 2013a).

Although Herreid and Truffer (2016) suggest that the difference between glacier surges and pulses is arbitrary, our results show that there is a clear, quantitative distinction between the two types: specifically, Alaskan-style surges experience significantly higher increases in velocity from quiescence to active phases (up to 7500%), whereas pulses are limited to up to 500% increase in velocity. Additionally, these pulses are unique compared to hydrologically forced seasonal speed-ups, as these increased velocities last more than one season at a time, which the seasonal speed-ups are by definition, limited to a single year.

2.5.3 Geographical distribution of different types of surging glaciers

Our analyses indicate that Alaskan-style and slowly surging glaciers are located primarily on the eastern continental climate zone of the St. Elias range, as opposed to the maritime climate in the south-west (Fig. 2-8). Pulsing glaciers are most commonly located in the south-west corner close to the Gulf of Alaska, while partial surges have thus far only been found in tributary basins in the upper accumulation area of Hubbard, Chitina, and Little Kluane glaciers (Abe and Furuya, 2015; Main and others, in review). It appears that the types of glacier surging are associated with precipitation patterns, with the highest clustering of pulse-type glaciers occurring where annual average precipitation levels are also highest (over 5000 mm a^{-1}), whereas Alaskan-style surges are more frequently found in drier regions (~300 to 500 mm a^{-1}), although more work is needed to refine this (Newman and others, 2020).

2.5.4 Timing of surge initiation and termination

The analysis of velocities from 1985-2023 indicates that 81% of observed surges begin in the winter, with the other 19% initiating during the late summer/early fall (Table 2-3). This is consistent with winter initiation reported by other studies on individual glaciers, such as at Variegated (Eisen and others, 2005), Little Kluane (Main and others, in review), and Fisher (Partington, 2023). Meanwhile, surges at a few glaciers (19%) such as Dän Zhür, Nàłùdäy and Tweedsmuir have initiated during the late summer or early fall (Kochtitzky and others, 2019; Bevington and Copland, 2014; Van Wychen and others, 2023).

Our finding that the majority of Alaskan-style surges initiate in the winter supports existing evidence that these events are hydrologically controlled and rely on a switching mechanism between an efficient, channelized subglacial drainage system during quiescence, to an inefficient, distributed network, which encourages fast glacier flow (Kamb and others, 1985). The linked-cavity theory suggests that a rapid change between these systems may trigger a surge due to enhanced basal sliding under certain geometric conditions (Kamb, 1987). In a surge-type glacier, the main subglacial channel may initially remain open due to frictional heating, despite water pressure being out of equilibrium with ice overburden pressure; however, this conduit may eventually weaken and collapse due to the weight of overlying ice which has accumulated due to inefficient ice flow during the quiescent phase (Kamb, 1987; Jiskoot, 2011). Once the main channel collapses, the subglacial network transforms into a distributed linked-cavity system,

whereby small openings remain connected due to high water pressure, reducing basal shear stress and increasing basal sliding. As most Alaskan surge-type glaciers are thought to be underlain by a layer of deformable till, high water pressure and shear stress may also destroy the subglacial networks present within the sediment (Harrison and Post, 2003; Jiskoot, 2011). There is not enough winter velocity data to distinguish when glacier pulsing begins, although increased annual average velocities are apparent during successive years (Fig. 2-7ab).

Where the timing of surge termination could be determined, all 8 examples occurred during the summer (Table 2-3). This timing again suggests that there is a relationship between meltwater availability and the size and distribution of subglacial channels in regulating velocity. The termination of Alaskan-style surges is likely related to two factors: i) the decrease in driving stress and overburden pressure driven by the change in glacier morphology (e.g., down-glacier redistribution of mass which had accumulated in the reservoir zone during quiescence), and ii) a rapid, large increase in frictional heating due to large volumes of subglacial water, which can re-establish the efficient channelized subglacial drainage network (Kamb, 1987; Jiskoot, 2011). Once an efficient system is re-established, a drop in meltwater production (e.g., through cooling air temperatures), can cause a rapid reduction in the amount of water at the bed, basal sliding to slow or cease, and the surge to terminate (Jiskoot, 2011). This interpretation agrees with past studies (e.g., Main and others, in review; Samsonov and others, 2019), including at Variegated Glacier where this interpretation originated, where an abnormally warm period and subsequent record levels of surface meltwater may have caused the 1995 surge to finish prematurely (Eisen and others, 2005).

2.5.5 Changes in surge magnitude and recurrence over time

For the 38 glaciers in this study that have multiple observed surges (Appendix 2-C), there is evidence that the magnitude of Alaskan-style surges is decreasing over time, demonstrated by decreasing maximum surge terminus extent. For example, Bevington and Copland (2014) found that each maximum surge extent of Nàłùdäy was shorter than during the previous event, decreasing by up to 2.8 km over 5 surges between 1948 and 2010. Van Wychen and others (2023) confirmed that this trend has continued for the latest 2020-22 surge, where the maximum extent was ~1.65 km less than during the previous 2009-10 surge. The maximum surge extent has also decreased by a total of ~1.5 km over the last 8 surges of Dän Zhür between ~1947 and 2014 (Kochtitzky and others, 2019). Another glacier which is advancing less now than in the past is Fisher Glacier, which increased in terminus area by 7.88 ± 0.04 km^2 during its 2014-16 surge, compared to 15.86 ± 0.06 km^2 during its 1963-1972 surge (Partington, 2023).

Trends in glacier velocities during repeat surges are inconclusive compared to changes in terminus extent, partly due to less frequent image coverage in the past, which makes it difficult to determine accurate short-term velocities for older surges. At Nàłùdäy, peak velocities derived from remote sensing reached ~2600 m a^{-1} during the 2009-10 surge, compared to maximum values of 2050 m a^{-1} during the 2021-22 surge, although Bevington and Copland (2014) found similar surface velocities between surges in 1983, 1997 and 2010. During the 2012-14 surge of Dän Zhür, Kochtitzky and others (2019) found generally lower velocities (1150 m a^{-1}) compared to those during the 2000-02 surge (1700 m a^{-1}). However, at Steele Glacier, peak velocities increased between surges, from 5840 m a^{-1} in 1960s to 10950 m a^{-1} in 2014-16 (Dutnall and others, in prep). At Sít' Kusá, Nolan and others (2021) did not find a trend of decreasing or increasing peak velocities over the last 5 surges between 1983 and 2013.

Overall, there are too few data points to fully characterize the surge recurrence interval for most surge-type glaciers, although there are a few glaciers which surge regularly enough to provide useful information. The shortest surge recurrence interval occurs at Sít' Kusá, which fully surges every ~5 years, while other glaciers averaged a surge every ~20 years (Appendix 2-C). The recurrence interval of Nàłùdäy has generally decreased over the past 5 surges, from ~18 years after the 1948 surge to ~11 years after the 2010 surge (Bevington and Copland, 2014; Van Wychen and others, 2023). During the intervening periods, this glacier experienced both thinning (ranging

between 2.2 - 3.7 m a^{-1}) and loss of both relative area and length (Bevington and Copland, 2014). In contrast, the repeat cycle at Dän Zhür has remained mostly consistent at ~12 years over 8 surges from ~1935 to 2016 (Kochtitzky and others, 2019). In the maritime zone, Seward Glacier had previously undergone surges in the early 1930s and 1954-56, and analysis of folded moraines suggested the next surge would occur around 1970 (Sharp, 1958; Jones and others, 1989). Instead, the next surge developed in 1987-88, 1.5 times the predicted recurrence interval (Muskett and others, 2008).

2.5.6 Surge propagation

The location of surge initiation and termination, propagation, and how tributaries and trunks interact with each other can vary significantly between glaciers and the type of surge. Slow surges have been shown to initiate in the middle of the glacier and propagate down-glacier (De Paoli and Flowers, 2009). Alaskan-style surges have been shown to propagate both up- and down-glacier from their initiation zones. Some glacier surges initiate in the middle, and spread both up- and down-glacier, such as Klutlan and Fisher (Altena and others, 2019; Partington, 2023). Surges at other glaciers have initiated at the terminus and propagated up-glacier, such as Nàłùdäy (Van Wychen and others, 2023). There are some glaciers where only a section of the glacier surges, such as Dän Zhür, where only the lower 21 km surges (Fig. 2-3), out of a total length of 65 km (Kochtitzky and others, 2019).

Commonly, Alaskan-style surges propagate down-glacier far enough to cause the terminus to advance, including at Dän Zhür, Fisher, and Nàłùdäy (Appendix 2-C). However, some glaciers do not experience an advance, such as at Walsh and Steele glaciers (Fu and Zhou, 2020; Dutnall and others, in prep). In these instances, the termini have a very long, heavily debris covered zone, and annual velocities there are very low (<10 m a^{-1}). Although the termini do not advance, the surges propagate into the nearly stagnant termini (Fig. 2-3).

Past studies have identified one of the key regional controls on surge-type glaciers as ‘branchiness’, with glaciers with more tributaries more likely to experience surges (Kienholz and others, 2013; Sevestre and Benn, 2015). However, there has been limited work to explore the relationships between glacier tributaries and main trunks in this region, such as if tributaries surge consistently, if tributary surges instigate a surge in the main trunk, or if surges are initiated near the confluence of a tributary and trunk. There is an assortment of trunk-tributary behaviour in the

St. Elias Mountains, including independently surging tributaries, partial surges of tributaries, and surges in the main trunk which propagate up- and down-glacier, entraining tributaries. For example, Little Kluane Glacier's 2017-18 surge initiated in the upper accumulation area of the north arm, and later initiated a surge in the main trunk over a period of several years, entraining ice in the south arm (Main and others, in review).

Glaciers with tributaries that surge independently of the main trunk include Dän Zhür (Kochtitzky and others, 2019), Kaskawulsh (Foy and others, 2011), and sometimes Chitina (Altena and others, 2019). The lower section of Seward Glacier is further subdivided into east and west lobes, which are known to surge independently of each other (Muskett and others, 2008). While Little Kluane's upper north tributary has been shown to surge (e.g., 1960s) without entraining the full glacier (Main and others, in review), other Alaskan-style surges have initiated in the main trunk and propagated up-glacier, entraining tributaries, including Klutlan, Walsh and Fisher (Altena and others, 2019; Fu and Zhou, 2019; Partington, 2023). Finally, at Steele Glacier, the surge of the main trunk occurs ~5-7 years prior to the surge of an upper tributary, known as Hodgson Glacier (Dutnall and others, in-prep). In 2014-16, a surge initiated in the ablation region of the main trunk, affecting the central and western upper tributaries, but did not initiate a surge in Hodgson (Dutnall and others, in-prep). However, 5 years later, in 2021, Hodgson began to surge independently, likely driven by the reduction in backstress caused by the lowering of Steele Glacier, as was also reported during the 1960s surge (Fig. 2-9) (Stanley, 1969; Dutnall and others, in prep).

The factors which may influence whether a tributary is influenced by fast flow in the main trunk, or the inverse, can include the relative size and volume of the tributary compared to the main glacier trunk, and the location on the main trunk where the tributary enters (e.g., accumulation zone vs. ablation zone). Jiskoot and others (2017) suggest that if the flux of a tributary glacier is at least one third of the main trunk flux, the blocking that the tributary provides may contribute to a flow restriction (so long as there is no icefall at the junction), and therefore may be conducive to surging. Tributaries which are relatively small compared to their main trunks may not induce a surge in the main trunk, as has been suggested for a tributary of Dän Zhür, which surged independently in 1974 and 2010 (Abe and others, 2016; Kochtitzky and others, 2019). Similarly, a surge occurred on a tributary of Kaskawulsh Glacier at some point between 1977 and 1994, but

this did not have a major impact or induce a surge in the main trunk of Kaskawulsh Glacier (Foy and others, 2011).

The location of a tributary relative to the main trunk may also influence the relative impact that a tributary surge has on the rest of the glacier. For example, if a tributary enters the main glacier in the ablation zone it may simply cut off the trunk, such as during the 1968 surge of Anderson tributary, which did not cause a surge of adjacent Chitina Glacier (Clarke and Holdsworth, 2002). However, this blocking effect might create enough of a barrier to slow flow and enable mass to rebuild, thus increasing surge propensity. Similarly, the slope of the tributary and the trunk, and the velocity of the ice in this zone, may play a role. For example, if a tributary and a trunk confluence in a wide, flat region close to the terminus, and both have low velocities or dead ice, this might not have a strong impact in reducing overall flow and enabling pre-surge mass build-up.

2.5.7 Study limitations

Despite providing an updated inventory of glacier surges in this region, and further identifying glacier surge characteristics, there are key limitations with our study, including a lack of winter velocity data from 1985-2007, as well as restrictions imposed by the structure of the RGI database. As our study demonstrates, often winter velocities are necessary to detect surge initiation in the St. Elias Mountains, as annual glacier velocity signals can be averaged over too long of a period to produce a strong recognizable surge signal. Slow surges are also difficult to characterize as there are only two current examples from the region, and their areas are small and velocities relatively low, which makes them difficult to observe via remote sensing techniques. We suggest that slowly surging glaciers are likely under-reported (including in our study) for these reasons. In addition, the RGI is not divided into separate tributaries, meaning that if a tributary surges the entire glacier is assumed to have surged. This likely overestimates the area of ice that is surge-type and increases the difficulty of analyzing tributary-trunk surging interactions on a regional level.

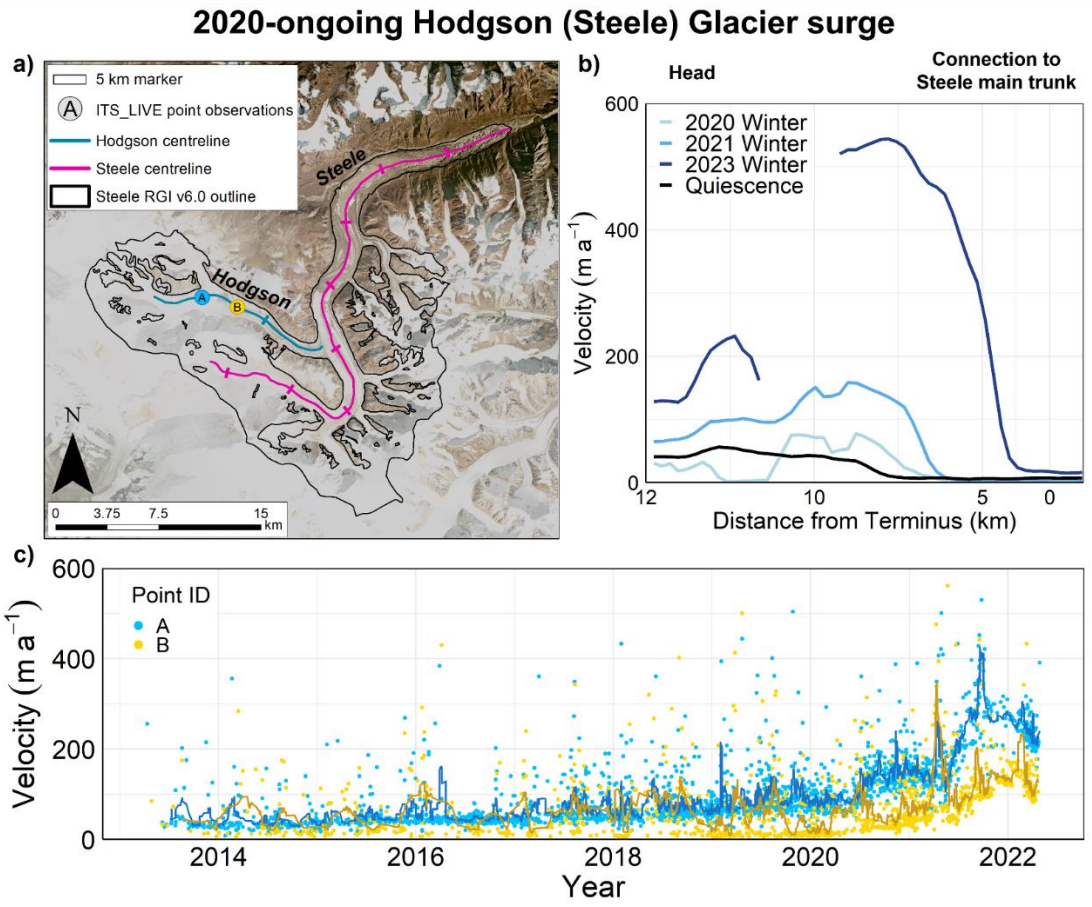

Figure 2-9: Ongoing surge of Hodgson Glacier, a tributary of Steele Glacier, demonstrating one example of tributary-trunk interactions, whereby a tributary surge began several years after the surge of the main trunk; a) Map of the glacier complex. Glacierized terrain is defined by RGI v6.0. Base image: Planet Fall 2018 basemap, UTM Zone 7N; b) winter velocities during the 2020-ongoing glacier surge. Winter velocities from 2007-19 are averaged to provide quiescent velocities for comparison; c) ITS_LIVE point measurements from two locations on Hodgson Glacier from mid-2013 until mid-2022.

2.6 Conclusions

This study presents an updated inventory of surge-type glaciers and surge events in the St. Elias Mountains, adding 21 previously undescribed surge events since 1985. We determine that there are 231 surge-type glaciers in this region, which includes two glaciers that are no longer attached to previous tributaries compared to the inventory of Sevestre and Benn (2015), and should therefore be considered as four separate entities. Surge-type glaciers represent 4.6% of the number of glaciers in the region, and 77% of the glaciated area. Surge-type glaciers are larger, more centrally located in the mountain range, have more tributaries and are more likely to be marine- or lake-terminating, compared to non surge-type glaciers.

In the first comprehensive study of the characteristics of observed glacier surges in this region, we find that there is a progressive increase in annual average velocities for several years prior to the peak surge phase across almost all Alaskan-style surges, as well as a deceleration phase after the peak. In the majority of instances surges initiate during the winter months, and the most common type of dynamic instability in this region is the Alaskan-style surge, although there is a diverse spectrum of behaviours within this category which require further detailed analysis. This work underscores the necessity for additional high resolution (both temporally and spatially) velocity data, as well as for further studies of individual surges.

Only 40 glaciers are responsible for ~86% of observed (active) glacier surges or pulses in the St. Elias Mountains. This suggests that those glaciers with a high propensity to surge are maintaining their surge behaviour in the current climate, although at a lower magnitude than before, as demonstrated through smaller maximum surge extents and smaller mass transfers towards present day (Bevington and Copland, 2014). This presents an opportunity to focus ice dynamics research on these glaciers, including surge initiation location, timing, and to install sensors at the glacier bed to better connect remotely sensed velocities with hydrology processes. Surge initiation location is somewhat variable, with just over half of the glaciers studied initiating in their central region, near the ELA. Rapid velocities then propagate from this surge nucleus, moving both up- and down-glacier, although this process is very limited in pulsing glaciers. There is significant variability in terms of tributary-trunk interactions, although this may be related to both the relative size of both the tributary and the main trunk, and the location of the junction between the tributary and the trunk.

While recognizing that ‘surge’ is the most widely used and accepted term to describe the rapid velocity events presented in this study, this term may be a misnomer: it can be ambiguous, as it can currently refer to any type of rapid velocity event, despite the wide spectrum of behaviours and mechanisms which have been observed. The use of ‘surge’ as a comprehensive label should perhaps therefore be reconsidered, and instead rapid velocity events could be classified based on the relative change in velocities over time.

2.7 Data Availability

The RADARSAT-2 wintertime glacier velocities generated for this study are available from the Polar Data Catalogue under CCIN reference number 13316. Original RADARSAT-2 data is available through MDA Geospatial Services (https://www.asc-csa.gc.ca/eng/satellites/radarsat2/order-contact.asp). All satellite imagery (Landsat, Sentinel-2, Rapid-Eye, and Planet), air photos, and ITS_LIVE velocity products are publicly available from data sources listed in the methods.

References

Abe T and Furuya M (2015) Winter speed-up of quiescent surge-type glaciers in Yukon, Canada. *The Cryosphere*, **8**, 1183-1190. doi: 10.5194/tc-9-1183-2015.

Abe T, Furuya M and Sakakibara D (2016) Brief communication: twelve-year cyclic surging episodes at Donjek Glacier in Yukon, Canada. *Cryosphere*, **10**(4), 1427-1432. doi: 10.5194/tc-10-1427-2016.

Altena B, Scambos T, Fahnestock M and Kääb A (2019) Extracting recent short-term glacier velocity evolution over southern Alaska and the Yukon from a large collection of Landsat data. *The Cryosphere*, **13**(3), 795-814. doi: 10.5194/tc-13-795-2019.

Aschwanden A, Bueler E, Khroulev C and Blatter H (2012) An enthalpy formulation for glaciers and ice sheets. *Journal of Glaciology*, **58**(209), 441-457. doi: 10.3189/2012JoG11J088.

Bartholomaus TC, Anderson RS and Anderson SP (2008) Response of glacier basal motion to transient water storage. *Nature Geoscience*, **1**, 33-37. doi:10.1038/ngeo.2007.52

Bevington A and Copland L (2014) Characteristics of the last five surges of Lowell Glacier, Yukon, Canada, since 1948. *Journal of Glaciology*, **60**(219), 113-123. doi: 10.3189/2014JoG13J134.

Burgess EW, Larsen CF, & Forster RR (2013a) Summer melt regulates winter glacier flow speeds throughout Alaska. *Geophysical Research Letters*, **40**, doi:10.1002/2013GL058228.

Burgess, EW., Forster, RR. and Larsen CF (2013b) Flow velocities of Alaska glaciers. *Nature Communications*, **4**, 2146 . doi:10.1038/ncomms3146.

Clarke CKC, Schmok JP, Ommanney SL and Collins SG (1986) Characteristics of surge-type glaciers. *Journal of Geophysical Research*, **91**(B7), 7165-7180. doi: 10.1029/JB091iB07p07165.

Clarke GKC and Holdsworth G (2002) Glaciers of the St. Elias Mountains. In R. S. William & J. G. Ferrigno (Eds.). Satellite Image Atlas of Glaciers of the World (pp. J301−J311). North America: U.S. Geological Survey Professional Paper

Commission for Environmental Cooperation (2021) North American Atlas - Political Boundaries, 2021. Montreal, Quebec, Canada: http://www.cec.org/north-american-environmental-atlas/political-boundaries-2021/

De Paoli L and Flowers GE (2009) Dynamics of a small surge-type glacier using one-dimensional geophysical inversion. *Journal of Glaciology*, **55**(194):1101-12. doi: 10.3189/002214309790794850.

Deur D, Thornton T, Lahoff R, and Hebert J (2015) Yakutat Tlingit and Wrangell-St. Elias National Park and Preserve: An ethnographic overview and assessment. *Anthropology Faculty Publications and Presentations*. Retrieved from https://pdxscholar.library.pdx.edu/anth_fac/99.

Dutnall S, Kochtitzky W and Copland L (in-prep) Surging of Steele Glacier, Yukon, Canada, 1930s-2020.

Eisen O, Harrison WD, Raymond CF, Echelmeyer KA, Bender GA and Gorda JLD (2005) Variegated Glacier, Alaska, USA: a century of surges. *Journal of Glaciology*, **51**(174), 399-406. doi: 10.3189/172756505781829250.

Flowers G, Jarosch A, Belliveau P and Fuhrman L (2016) Short-term velocity variations and sliding sensitivity of a slowly surging glacier. *Annals of Glaciology* **57**(72), 71-83. doi:10.1017/aog.2016.7.

Fowler AC (1987) A theory of glacier surges. *Journal of Geophysical Research: Solid Earth*, **92**(B9), 9111-9120. doi: 10.1029/JB092iB09p09111.

Foy N, Copland L, Zdanowicz C, Demuth M and Hopkinson C (2011) Recent volume and area changes of Kaskawulsh Glacier, Yukon, Canada. *Journal of Glaciology,* **57**(203), 515–525. doi: 10.3189/002214311796905596

Frappé TP and Clarke GKC (2007) Slow surge of Trapridge Glacier, Yukon Territory, Canada. *Journal of Geophysical Research Earth Surface,* **112**(3), 1–17. doi: 10.1029/2006JF000607

Fu X and Zhou J (2020) Recent surge behavior of Walsh Glacier revealed by remote sensing data. *Sensors*, **20**(3), p.716. doi:10.3390/s20030716.

Gardner AS, Fahnestock MA and Scambos TA (2019) [accessed Jan. 2022] ITS_LIVE Regional Glacier and Ice Sheet Surface Velocities. Data archived at National Snow and Ice Data Center; doi: 10.5067/6II6VW8LLWJ7.

Gutiérrez JM, and 15 others (2021) Atlas. In Climate Change 2021: The Physical Science Basis. Contribution of Working Group I to the Sixth Assessment Report of the Intergovernmental Panel on Climate Change [Masson-Delmotte, V., P. Zhai, A. Pirani, S.L. Connors, C. Péan, S. Berger, N. Caud, Y. Chen, L. Goldfarb, M.I. Gomis, M. Huang, K. Leitzell, E. Lonnoy, J.B.R. Matthews, T.K. Maycock, T. Waterfield, O. Yelekçi, R. Yu, and B. Zhou (eds.)]. Cambridge University Press, Cambridge, United Kingdom and New York, NY, USA, pp. 1927–2058, doi:10.1017/9781009157896.021.

Herreid S., and M. Truffer (2016) Automated detection of unstable glacier flow and a spectrum of speedup behavior in the Alaska Range. *Journal of Geophysical Research, Earth Surface*, **121**, 64–81, doi:10.1002/2015JF003502.

Harrison WD and Post AS (2003) How much do we really know about glacier surging? *Annals of Glaciology*, **36**, 1–6. https://doi.org/10.3189/172756403781816185

Hugonnet R and 10 others (2021) Accelerated global glacier mass loss in the early twenty-first century. *Nature*, **592**, 726-731. doi: 10.1038/s41586-021-03436-z.

Jay-Allemand M, Gillet-Chaulet F, Gagliardini O and Nodet M (2011) Investigating changes in basal conditions of Variegated Glacier prior to and during its 1982-1983 surge. *The Cryosphere,* **5**, 659-672. doi:10.5194/tc-5-659-2011.

Jiskoot H (2011) Glacier surging. In Singh VP et al. (eds) Encyclopedia of Snow, Ice and Glaciers. Dordrecht, The Netherlands, Springer, 415-428.

Jiskoot H, Fox TA and Van Wychen W (2017) Flow and structure in a dendritic glacier with bedrock steps. *Journal of Glaciology,* **63**(241), 912-928. doi: 10.1017/jog.2017.58.

Jones JE, Molnia BF, and Schoonmaker JW Jr (1989) The Malaspina Glacier radar study: a SLAR investigation of glacier and periglacial features. USGS Year Book, 34–40.

Kääb A, Brazilova V, Leclercq PW, Mannerfelt ES and Strozzi T (2023) Global clustering of recent glacier surges from radar backscatter data, 2017-2022. *Journal of Glaciology*, 1-9. doi: 10.1017/ jog.2023.35.

Kamb B and 7 others (1985) Glacier surge mechanism: 1982–1983 surge of the Variegated Glacier, Alaska. *Science*, **227**(4686), 469–479. doi: 10.1126/science.227.4686.469.

Kamb B (1987) Glacier surge mechanism based on linked cavity configuration of the basal water conduit system. *Journal of Geophysical Research: Solid Earth*, **92**(B9), 9083-9100. doi: 10.1029/JB092iB09p09083.

Kienholz C, Herreid S, Rich JL, Arendt AA, Hock R and Burgess EW (2015) Derivation and analysis of a complete modern-date glacier inventory for Alaska and northwest Canada. *Journal of Glaciology*, **61**(277). doi: 10.3189/2015JoG14J230.

Kochtitzky W and 6 others (2019) Terminus advance, kinematics and mass redistribution during eight surges of Donjek Glacier, St. Elias Range, Canada, 1935-2016. *Journal of Glaciology*, **65**(252), 565-579. doi: 10.1017/jog.2019.34

Kochtitzky W and 10 others (2020) Climate and surging of Donjek Glacier, Yukon, Canada. *Arctic, Antarctic, and Alpine Research*, **52**:1, 264-280, doi: 10.1080/15230430.2020.1744397

Larsen CF, Burgess E, Arendt AA, O'Neel S, Johnson AJ and Kienholz C (2015). Surface melt dominates Alaska glacier mass balance. *Geophysical Research Letters*, **2**(14), 5902-5908. doi: 10.1002/2015GL064349

Lu J and Veci L (2016) Offset Tracking Tutorial: Sentinel-1 Toolbox. Array Systems Computing Inc.

Liu J and others (in-press) Propagating speedups during quiescence escalate to the 2020-2021 surge of Sít' Kusá, southeast Alaska. *Journal of Glaciology*.

Main B and 11 others (2022) Terminus change of Kaskawulsh Glacier, Yukon, under a warming climate: retreat, thinning, slowdown and modified proglacial lake geometry. *Journal of Glaciology*, **69**(276), 1-17. doi: 10.1017/jog.2022.114.

Main B, and 6 others (in review) Little Kluane Glacier: varying dynamic instabilities in a medium-sized glacier, Yukon, Canada. *Journal of Glaciology*

Meier MF and Post A (1969) What are glacier surges? *Canadian Journal of Earth Sciences*, **6**(4), 807-817. doi: 10.1139/e69-081.

Muller EH and Fleisher PJ (1995) Surging history and potential for renewed retreat: Bering Glacier, Alaska U.S.A. *Arctic and Alpine Research*, **27**(1), 81-88. doi: 10.1080/00040851.1995.12003099

Muskett RR, Lingle CS, Tangborn WV and Rabus BT (2003) Multi-decadal elevation changes on Bagley Ice Valley and Malaspina Glacier, Alaska. *Geophysical Research Letters*, **30**(16), 1857. doi:10.1029/2003GL017707

Muskett RR, Lingle CS, Sauber JM, Post AS, Tangborn WV and Rabus BT (2008) Surging, accelerating surface lowering and volume reduction of the Malaspina Glacier system, Alaska, USA, and Yukon, Canada, from 1972-2006. *Journal of Glaciology*, **54**(1888), https://doi.org/10.3189/002214308787779915

Newman AJ, Clark MP, Wood AW and Arnold JR (2020) Probabilistic spatial meteorological estimates for Alaska and the Yukon. *Journal of Geophysical Research: Atmospheres,* **125**(22), e2020JD032696. doi: 10.1029/2020JD032696.

Nolan A, Kochtitzky W, Enderlin EM, McNabb R and Kreutz KJ (2021) Kinematics of the exceptionally-short surge cycles of Sít' Kusá (Turner Glacier), Alaska, from 1983 to 2013. *Journal of Glaciology*, **67**(264), 744-758. doi: 10.1017/jog.2021.29.

Partington G (2023) Reconstructing the Surge History and Dynamics of Fisher Glacier, Yukon, 1948-2022. MSc thesis, University of Ottawa. doi: 10.20381/ruor-29290

Planet Team (2017) Planet Application Program Interface: In Space for Life on Earth. San Francisco, CA. https://api.planet.com.

Post A (1969) Distribution of surging glaciers in western North America. *Journal of Glaciology* **8**(53): 229- 240. doi: 10.3189/S0022143000031221.

RGI Consortium (2017). Randolph Glacier Inventory - A Dataset of Global Glacier Outlines, Version 6 [Data Set]. Boulder, Colorado USA. National Snow and Ice Data Center. doi: 10.7265/4m1f-gd79.

Samsonov S, Tiampo K, and Cassotto R (2021) Measuring the state and temporal evolution of glaciers in Alaska and Yukon using synthetic-aperture-radar-derived (SAR-derived) 3D time series of glacier surface flow. *The Cryosphere*, **15**(9), 4221-4239. doi: 10.5194/tc-15-4221-2021.

Schellenberger T, Van Wychen W, Copland L, Kääb A and Gray L (2016) An Inter-Comparison of Techniques for Determining Velocities of Maritime Arctic Glaciers, Svalbard, Using Radarsat-2 Wide Fine Mode Data. *Remote Sensing*, **8**(9), 785. doi: 10.3390/rs8090785.

Sevestre H, and Benn D (2015) Climatic and geometric controls on the global distribution of surge-type glaciers: implications for a unifying model of surging. *Journal of Glaciology*, **61**(288), 646-663. doi: 10.3189/2015JoG14J136.

Sharp M (2021) Amplification of surface topography during surges of Tweedsmuir Glacier [Unpublished master's thesis]. University of Calgary, Calgary, AB. http://hdl.handle.net/1880/113988.

Sharp RP (1958) Malaspina Glacier, Alaska. *Geol. Soc. Am. Bull.*, **69**(2), 617–646. doi:10.1130/0016-7606(1958)69[617:MGA]2.0.CO;2.

Stanley AD (1969) Observations of the surge of Steele Glacier, Yukon Territory, Canada. *Canadian Journal of Earth Sciences*, **6**(4), 819–830. doi: 10.1139/e69-082.

Sund M, Eiken T, Hagen JO and Kääb A (2009) Svalbard surge dynamics derived from geometric changes. *Annals of Glaciology* **50**(52), 50-60. doi: 10.3189/172756409789624265.

Turrin JB, Forester RR, Larsen C and Sauber J (2013) The propagation of a surge front on Bering Glacier, Alaska, 2001-2011. *Annals of Glaciology*, **54**(63), 221-229. doi: 10.3189/2013AoG63A341.

Turrin JB, Forester RR, Sauber JM, Hall DK and Bruhn RL (2014) Effects of bedrock lithology and subglacial till on the motion of Ruth Glacier, Alaska, deduced from five pulses from 1973 to 2012. Journal of Glaciology, 60(222), 771-781. doi: 10.3189/2014JoG13J182.

Van Wychen W, Copland L, Jiskoot H, Gray L, Sharp M and Burgess D (2018) Surface velocities of glaciers in western Canada from speckle-tracking of ALOS PALSAR and RADARSAT-2 data. *Canadian Journal of Remote Sensing*, **44**(1), 57-66. doi: 10.1080/07038992.2018.1433529.

Van Wychen W, Bayer C, Copland L, Brummell E and Dow C (2023) Radarsat Constellation Mission derived winter glacier velocities for the St. Elias Icefield, Yukon/Alaska: 2022 and 2023. *Canadian Journal of Remote Sensing*, **49**(1), 1-10. doi: 10.1080/07038992.2023.2264395.

Waechter A, Copland L and Herdes E (2015) Modern glacier velocities across the Icefield Ranges, St. Elias Mountains, and variability at selected glaciers from 1959 to 2012. *Journal of Glaciology*, **61**(228), 624-634. doi: 10.3189/2015JoG14J147.

Williamson SN and 9 others (2020) Evidence for elevation-dependent warming in the St. Elias Mountains, Yukon, Canada. *Journal of Climate*, **33**, 3253–3269. doi: 10.1175/JCLI-D-19-0405.

Young EM, Flowers GW, Berthier E and Latto R (2021) An imbalancing act: the delayed dynamic response of the Kaskawulsh Glacier to sustained mass loss. *Journal of Glaciology*, **67**(262), 313-330. doi: 10.1017/jog.2020.107.

Appendix 2-A: Summary of SAR imagery used to derive surface ice velocities in this study. FBS = ALOS PALSAR Fine-beam single polarisation (HH); UF = RADARSAT-2 Ultra-fine single polarisation (HH); M = HR = RADARSAT Constellation Mission High Resolution mode. Dates are in YYYY-MM-DD.

Beam Path/ Swath	Date 1	Date 2	Resolution (m)	Mode	Velocity error (m yr^{-1})
ALOS-PALSAR Imagery (originally published in Van Wychen and others, 2018)					
245	2007-12-21	2008-02-05	10	FBS	8.5 – 15.0
243	2008-01-02	2008-02-17			
241	2008-01-14	2008-02-29			
242	2009-12-21	2010-02-05			
240	2010-01-02	2010-02-17			
244	2010-01-24	2010-03-11			
RADARSAT-2 Imagery					
2011 (originally published in Waechter and others, 2015)					
F2F	2011-01-10	2011-02-03	8	F	16.6
	2011-02-27	2011-03-23			
F2	2011-01-17	2011-02-10			
F6	2011-01-03	2011-01-27			
	2011-02-20	2011-03-16			
F23F	2011-02-14	2011-03-10			
2012 (originally published in Waechter and others, 2015)					
U1W2	2012-02-17	2012-03-12	3	UF	12.7
U2W2	2012-02-24	2012-03-19			
	2012-03-19	2012-04-12			
U9W2	2012-02-21	2012-03-16			
U10W2	2012-02-28	2012-03-23			
U24W2	2012-02-18	2012-03-13			
	2012-03-13	2012-04-06			
2014					
U4W2	2014-02-06	2014-03-02	3	UF	7
	2014-03-02	2014-03-26			
U5W2	2014-02-13	2014-03-09			
	2014-03-09	2014-04-02			
U6W2	2014-02-20	2014-03-16			
	2014-03-16	2014-04-09			
U7W2	2014-02-03	2014-02-27			
	2014-02-27	2014-03-23			
U10W2	2014-02-17	2014-03-13			
	2014-03-13	2014-04-06			
U17W2	2014-02-24	2014-03-20			
	2014-03-20	2014-04-13			
U24W2	2014-02-21	2014-03-17			
	2014-03-17	2014-04-10			
2015					
U4W2	2015-02-01	2015-02-25	3	UF	8
	2015-02-25	2015-03-21			

U5W2	2015-02-08	2015-03-04			
	2015-03-04	2015-03-28			
U6W2	2015-02-15	2015-03-11			
	2015-03-11	2015-04-04			
U7W2	2015-01-29	2015-02-22			
	2015-02-22	2015-03-18			
U10W2	2015-02-12	2015-03-08			
	2015-03-08	2015-04-01			
U17W2	2015-02-19	2015-03-15			
	2015-03-15	2015-04-08			
2016					
U4W2	2016-01-27	2016-02-20			
U5W2	2016-02-03	2016-02-27			
U6W2	2016-02-10	2016-03-05			
	2016-03-05	2016-03-29			
U7W2	2016-01-24	2016-02-17			
	2016-02-17	2016-03-12	3	UF	7
U10W2	2016-02-07	2016-03-02			
	2016-03-02	2016-03-26			
U17W2	2016-02-14	2016-03-09			
U24W2	2016-02-11	2016-03-06			
	2016-03-06	2016-03-30			
2017					
U4W2	2017-01-21	2017-02-14			
	2017-02-14	2017-03-10			
U5W2	2017-01-28	2017-02-21			
U6W2	2017-01-11	2017-02-04			
	2017-02-04	2017-02-28			
U7W2	2017-01-18	2017-02-11			
	2017-02-11	2017-03-07	3	UF	7
U10W2	2017-01-08	2017-02-01			
	2017-02-01	2017-02-25			
U17W2	2017-01-15	2017-02-08			
	2017-02-08	2017-03-04			
U24W2	2017-01-12	2017-02-05			
	2017-02-05	2017-03-01			
2018					
U4W2	2018-01-16	2018-02-09			
	2018-02-09	2018-03-05			
	2018-03-05	2018-03-29			
U6W2	2018-01-06	2018-03-19	3	UF	4
U7W2	2018-01-13	2018-03-02			
U10W2	2018-01-03	2018-02-20			
U24W2	2018-01-07	2018-02-24			
2019					
U4W2	2019-02-04	2019-03-24			
	2019-03-24	2019-04-17			
U5W2	2019-03-31	2019-04-24	3	UF	6
U6W2	2019-04-07	2019-05-01			

U10W2	2019-04-04	2019-04-28			
U17W2	2019-04-11	2019-05-05			
U24W2	2019-04-08	2019-05-02			
2020					
U4W2	2020-01-06	2020-01-30	3	UF	6
	2020-01-30	2020-02-23			
U5W2	2020-01-13	2020-02-06			
U6W2	2020-01-20	2020-02-13			
U7W2	2020-01-27	2020-02-20			
U17W2	2020-01-24	2020-02-17			
U6W2	2020-01-27	2020-02-20			
RADARSAT CONSTELLATION MISSION					
2021					
RCM Beam Mode	Date 1	Date 2	Resolution (m)	Velocity error (m yr^{-1})	
5MCP1	2021-01-02	2021-01-14	5	13: average error over stable terrain	
5MCP8	2021-01-03	2021-01-15			
	2021-01-15	2021-01-27			
5MCP9	2021-01-05	2021-01-29			
5MCP15	2021-01-02	2021-01-14			
	2021-01-03	2021-01-15			
	2021-01-15	2021-01-27			
5MCP18	2021-01-02	2021-01-14			
5MCP21	2021-01-01	2021-01-25			
	2021-01-04	2021-01-16			
	2021-01-16	2021-01-28			
2022 (originally published in Van Wychen and others, 2023)					
5MCP1	2022-01-05	2022-01-09	5	6.6: average absolute displacement 0.3: minimum absolute difference 36.1: maximum absolute difference	
5MCP5	2022-01-15	2022-01-19			
5MCP8	2022-01-06	2022-01-10			
5MCP18	2022-01-05	2022-01-09			
5MCP20	2022-01-02	2022-01-06			
5MCP22	2022-01-20	2022-01-24			
5MCP23	2022-01-15	2022-01-19			
5MCP5	2022-01-04	2022-01-08			
2023 (originally published in Van Wychen and others, 2023)					
5MCP23	2023-01-02	2023-01-06	5	Value unavailable until 2023 GPS station displacements are calculated, but are assumed to be similar to 2022 values	
5MCP20	2023-01-12	2023-01-16			
5MCP16	2023-01-04	2023-01-08			
5MCP12	2023-01-29	2023-02-02			
5MCP11	2023-01-07	2023-01-11			
5MCP10	2023-01-12	2023-01-16			
5MCP9	2023-01-14	2023-01-31			
5MCP6	2023-01-10	2023-01-14			
5MCP6	2023-01-27	2023-01-31			
5MCP2	2023-01-04	2023-01-08			
5MCP19	2023-01-09	2023-01-13			

Appendix 2-B: List of ITS_LIVE annual velocity mosaics (pixel resolution 240 m) used in this study, and their associated error averaged over the St. Elias Mountains.

Year	Mean velocity error (m yr^{-1})
1985	16
1986	22
1987	42
1988	23
1989	18
1990	26
1991	15
1992	12
1993	10
1994	10
1995	10
1996	6
1997	7
1998	8
1999	10
2000	7
2001	6
2002	6
2003	7
2004	5
2005	7
2006	8
2007	8
2008	9
2009	8
2010	7
2011	9
2012	10
2013	2
2014	2
2015	2
2016	2
2017	1
2018	7

Appendix 2-C: Inventory of surge-type glaciers in the St. Elias Mountains, updated from Sevestre and Benn (2015). Latitude/longitude values are based on WGS84 datum. 'Surge date' indicates that a glacier surged at some point during the years listed, although the surge did not necessarily last for that entire period. Names in brackets indicate an unofficial or unpublished name. See end of table for guide to shorthand references.

Glacier name	GLIMS ID	Long.	Lat.	Surge Index[a]	Description	Surge Date(s)[b]	References[c]
Agassiz	G219116 E60102N	-140.884	60.102	3	M03: has a pulse like flow; surface lowered up to 100 m from 1973-2000. W87: Surge type B: Active phase: velocity of 2-8 m d^{-1}, horizontal displacement 2-5km, vertical displacement 10-30m, duration 1-4 years. OS: during 1999-2002 surge, annual average velocities peaked at 815 m a^{-1}, and quiescent at 520 m a^{-1}; during 2011-2012 pulse, active velocities peaked at 545 m a^{-1}, and quiescent at 350 m a^{-1}	1965 1990-1993 1999-2002 2011-2012	M03; MS08; OS; W87
Art Lewis	G221141 E59910N	-138.859	59.91	2	W87: Surge type E; Active phase: very high velocity, >15 m d^{-1}, calving rate high. Horizontal displacement large but small relative to size. Vertical displacement difficult to discern. Duration <2 years. M08: A surge of Art Lewis glacier in the middle 1960s resulted in a temporary advance of the terminus of East Nunatak to tidewater during 1966. OS: during 2000-2002 surge, annual average velocities peaked at 230 m a^{-1}, and quiescent at 130 m a^{-1}; during 2011-2013 pulse, active velocities peaked at 145 m a^{-1}, and quiescent at 60 m a^{-1}	1964-1966 2000-2002 2011-2013	M08; P69; W87
Atrevida	G220169 E59934N	-139.831	59.934	2	W87: Surge type B; Active phase velocity of 2-8 m d^{-1}, horizontal displacement 2-5 km, vertical displacement 10-30m, duration 1-4 years.	1905-1906 1963 1973 1984-1985 1987-1989 2000-2003 2011-2015	H69; W87
Barnard	G218563 E61248N	-141.437	61.248	2	W87: Surge type C.	-	W87
Battle	G221646 E59667N	-138.354	59.667	2	C86: Tributary to B001. OS: Velocity increase over lower terminus region in winter 2019, surging likelihood uncertain/low.	2019-2021	C86; OS
Bering	G217928 E60461N	-142.072	60.461	2	P72: links deformation of medial debris to surging frequency. W87: Surge type A; Active phase: <1-8 m d^{-1}, horizontal displacement small but 10-30% of size. Vertical displacement: little observable depression, but great extension. Duration <1-4 years. F98: Active phase 1 velocities: 1-7.4 m d^{-1}, phase 2 velocities 1-2 m d^{-1}. Pressurized subglacial water outburst between active phase 1 and 2. S15: Terminus advances 4-13 km during surges (1960, 1966)	1874 ~1900 ~1920 ~1938 1957-1959 1966-1968 1993-1995 2008-2011	BF12; F98; H97; L97; M94; M95; P72; S15; T13; T18; W87

Butler	G220950 E59943N	-139.05	59.943	2	H69: Listed as surge type glacier. P69: From Map: observed surging or display evidence of surging. W87: Surge type A; Active phase: velocity >15 m d^{-1}, annually to >50 m d^{-1} for short periods. Horizontal displacement large > 5km. Vertical displacement: large >50 m. Duration 2 to 6 years	1946-1948 1964-1969 1986	H69; P69; W87
Cement D	G220054 E61345N	-139.946	61.345	1	C86: Two tongues, part joins t032; uncertain surge characteristics. W87: Surge type D	-	C86; W87
Chitina	G219155 E61116N	-140.845	61.116	3	H69: surge in the late 1960s W87: Surge type A. M08: impacted the central Chitina glacier in the early 1970s." C02: "The approximate 1968 surge of Anderson Glacier truncated the terminus of Chitina glacier, another surging glacier." VW23: shows surge progression of velocities from 250 m a^{-1} to >400 m a^{-1}.	1912 1951-1952 1967-1968 1986 1995-2003 2010 2015-2016 2021-2023	A19; C02; H69; M08; VW23; W87
Chitistone	G217961 E61427N	-142.039	61.427	2	H69: Listed as surge type glacier W87: Surge type B; Active phase: velocity of 2-8 m d^{-1}, horizontal displacement 2-5 km, vertical displacement 10-30 m, duration 1-4 years. OS: lowermost 25 km affected by velocity increases, from 45 m a^{-1} to 105 m a^{-1} (max change).	1910-1911 1966 2017-2020	H69; OS; W87
Dän Zhür (Donjek)	G220176 E60979N	-139.824	60.979	3	P69: From Map: observed surging or display evidence of surging. W87: Surge type B. K19: reconstructs surge history from 1935 - 2016. Active phase velocities highest in lower 10 km, up to 1500 m a^{-1}. (4.5 m d^{-1}). Quiescent velocities 0.5 m d^{-1}. Glacier surges only in lower 21 km. Surface lowering of 9.6 m a^{-1} in last active phase. Surge magnitude decreasing in max terminus extent. K20: cumulative accumulation of 15.5 ± 1.46 or 16.6 ± 2 m w.e. between surges.	~1935 1947 1958 1969 1974 (trib.) 1977-1980 1987-1989 2000-2002 2012-2014	A16; K19; K20; P69
Dusty	G221265 E60410N	-138.735	60.41	3	C86: moraine shows large recession. W87: Surge type B; Active phase: velocity of 2-8 m d^{-1}, horizontal displacement 2-5 km, vertical displacement 10-30 m, duration 1-4 years.	1964-1968 2000-2002	C02; M71; W87
Ewe	G218707 E61059N	-141.293	61.059	3	W87: Surge type C.	-	W87
Fisher	G221417 E60065N	-138.583	60.065	3	C86: Tributary to E001, surges with E001. W87: Surge type B. P23: Active phase velocities 5.5 m d^{-1}, quiescent velocities 0.1-0.4 m d^{-1}. Several decades of increasing velocities prior to surge, has both Alaskan and Svalbard style surge characteristics. Propagates up and down glacier from initiation.	1934-1935 1968-1972 2014-2016	C86; P23, W87
Galiano	G220289 E59979N	-139.711	59.979	2	W87: Surge type C; Active phase: <1-8 m d^{-1}, horizontal displacement small but 10-30% of size. Vertical displacement: little observable depression, but great extension. Duration <1-4 years. 87: 1974 surge: 20-40% of glacier effected.	1899-1900 1974	W87

					Degree of Transformation: localized "abnormal activity" no advance		
Giffin	G218538 E61570N	-141.462	61.57	2	W87: Surge type B; Active phase: velocity of 2-8 m d^{-1}, horizontal displacement 2-5 km, vertical displacement 10-30 m, duration 1-4 years. >80% of glacier affected. Degree of transformation: entire glacier broken up, riven with crevasses, entire upper basin active, probable terminus advance.	1948 (trib.) 1986	W87
Guyot	G218236 E60214N	-141.764	60.214	2	Published velocity data.	-	B12; S15
Haenke	G220324 E60088N	-139.676	60.088	3	P69: Listed as surge type glacier. W87: Surge type B; Active phase: velocity of 2-8 m d^{-1}, horizontal displacement 2-5 km, vertical displacement 10-30m, duration 1-4 years. M08: Tarr and Martin 1914 reported that it underwent a rapid advance, thickened, became crevassed and advanced nearly 1km between 1905 and 1906.	1905-1906 1930 1960 1986	H69; M08; P69; W87
Hidden	G220934 E59702N	-139.066	59.702	3	H69: Listed as surge type glacier. W87: Surge type B; Active phase: velocity of 2-8 m d^{-1}, horizontal displacement 2-5 km, vertical displacement 10-30 m, duration 1-4 years. M08: In the 3 year period between Tarr's 1906 visit and 1909, Hidden Glacier's terminus advanced 3.2 km	1906-1907	H69; M08; W87
Hubbard	G220499 E60427N	-139.501	60.427	3	W87: Surge type B; Active phase: very high velocity, >15 m d^{-1}, calving rate high. Horizontal displacement large but small relative to size. Vertical displacement difficult to discern. Duration <2 years. C02: in 1981, a surge was observed in one of the glaciers on the side of Mt Queen Mary and a surge bulge moved out onto Hubbard Glacier. W93: Weak surge or pulse of the Valerie Glacier (tributary of Hubbard Glacier) and a pulse of the Hubbard Glacier caused a rapid advance of the calving terminus in the spring of 1986. OS: during 2002 surge, annual average velocities peaked at 2290 m a^{-1}, and quiescent at 1700 m a^{-1}	1986 2002 2009 (3 tribs.) 2021 (trib.)	A15; C02; M07; OS; W87; W93
Kaskawulsh	G220886 E60666N	-139.114	60.666	1	C86: Very probable surger, looped medials; Surge index 4, strong surface evidence. F11: tributary surged between 1977 and 1994.	~1977 (trib.)	C02; C86, F11
Kluane	G220578 E60873N	-139.422	60.873	2	P69: From Map: observed surging or display evidence of surging. W87: Surge type B; Active phase: velocity of 2-8 m d^{-1}, horizontal displacement 2-5 km, vertical displacement 10-30 m.	1941 1960-1961 1972 (trib.) 1986	C86, H69; P67; P69; W87
Klutlan	G218909 E61392N	-141.091	61.392	3	H69: Listed as surge type glacier. P69: From Map: observed surging or display evidence of surging. C86: possible surge, tongue much crevassed A19: surge initiates in central arm, then propagates up and down glacier; entrains western most basin, and the easternmost basin to a smaller extent.	1940-1944 (trib.) 1946-1951 (trib.) 1951-1957 (tribs.) 1961-1963 1965-1967 (tribs.) 1973-1974 (trib.) 1980 (trib.) 1985-1987 (tribs.)	A19; C86, M08 P69, S15; OS; W87

					S15: glacier terminus advanced 4 km 1963 surge OS: Winter velocities peak during surge at 1950 m a^{-1}, annual averages peak at 1350 m a^{-1}; quiescent velocities 200 m a^{-1}	2012-2018	
Little Kluane	G220578 E60873N	-139.542	60.910	3	Partial surge possible in 1970's. Observed glacier surge, peak active phase velocities up to 3600 m a^{-1} compared to 20 m a^{-1} during quiescence. Acceleration phase from 2013-16, active phase 2017-18. Advance of 2.2 km.	1970s 2017-2018	M23
Logan	G219297 E60730N	-140.703	60.73	3	W87: Surge type B; Active phase: velocity of 2-8 m d^{-1}, horizontal displacement 2-5 km, vertical displacement 10-30 m, duration 1-4 years. C02: Logan glacier is not included in Post's 1969 catalog of surging glaciers, the moraine loops near its confluence with Walsh glacier indicate variations in flow velocity, but these may be in response to surges of Walsh glacier. OS: Winter velocity peaks of 390 m a^{-1}; quiescent annual average velocities 120 m a^{-1}. Long acceleration (2000-2011) active phase 1 year, deceleration from 2013-2018.	1912 1940 1957-1965 ~2005-2012	C02; H69; OS; P69; W14; W87
Lucia	G220103 E60023N	-139.897	60.023	3	H69: Listed as surge type glacier. During 1990s active phase velocities: W87: Surge type B; Active phase: velocity of 2-8 m d^{-1}, horizontal displacement 2-5 km, vertical displacement 10-30 m, duration 1-4 years. OS: during 1992-1995 pulse, annual average velocities peaked at 155 m a^{-1}, and quiescent at 95 m a^{-1}; during 2000-2002 pulse, active velocities peaked at 190 m a^{-1}, and quiescent at 125 m a^{-1}	1908-1909 1966 1992-1995 2000-2002	H69; OS; W87
Martin River	G216127 E60550N	-143.873	60.55	2	Surge type B; Active phase: velocity of 2-8 m d^{-1}, horizontal displacement 2-5 km, vertical displacement 10-30 m, duration 1-4 years.	1910 1964-1965 1984	W87
Marvine	G219820 E59978N	-140.18	59.978	2	H69: listed as surge type glacier W87: Surge type B; Active phase: velocity of 2-8 m d^{-1}, horizontal displacement 2-5 km, vertical displacement 10-30 m, duration 1-4 years. M03: surface lowered up to 100 m from 1973-2000 MS08: glacier surged between 1986 and1987. S58: surged between 1954 and 1956.	1905-1906 1954-1956 1965 1984-1988 2015-2018	H69; M03; MS08; S59; W87
Miles	G215853 E60631N	-144.147	60.631	3	H69: listed as surge type K73: "Major surge advanced along 30km long southeast terminus between 1957 and 1960 with an advance of up to 5km; smaller surge occurred in late 1965 and early 1966 moving glacier terminus slightly in advance of the 1960 surge. S15: advance of 5 km during 1960 surge	1909-1910 1957-1960 1965-1966	H69; K73; PS67; S15
Miller	G220402 E60097N	-139.598	60.097	3	W87: Surge type B; Active phase: <1-8 m d^{-1}, horizontal displacement small but 10-30% of size. Vertical displacement: little observable depression, but great extension. Duration <1-4 years.	1899-1901 1966 1986	H69; M08; P67; W87

					P67: underwent small surge in 1966, advanced 2 km.		
Nàłùdäy (Lowell)	G221355 E60283N	-138.645	60.283	3	W87: Surge type B. B14: Multiple observed surges. Active phase velocities up to 10 m d^{-1} quiescent velocities of 0.2 m d^{-1}. Surge magnitude decreasing between surges: Net active phase advance has decreased from 2.89 (1983-84), 2.38 (1998-99) to 2.07 (2009-10); time between surges decreased from 18-12 years. VW23: surge initiates at the terminus and propagates up-glacier.	1920 1948-1950 1968-1970 1983-1984 1997-1998 2009-2010 2021-2023	C86; B14; H69; OS; P69; VW23; W87
Natazhat	G218962 E61517N	-141.038	61.517	3	W87: Surge type C; Active phase: <1-8 m d^{-1}, horizontal displacement small but 10-30% of size. Vertical displacement: little observable depression, but great extension. Duration <1-4 years.	1986	C86, W87
Ram	G218719 E61120N	-141.281	61.12	2	Surge type B; Active phase: velocity of 2-8 m d^{-1}, horizontal displacement 2-5 km, vertical displacement 10-30 m, duration 1-4 years.	1985	P69; W87
Russell	G218192 E61498N	-141.808	61.498	3	W87: Surge type B; Active phase: velocity of 2-8 m d^{-1}, horizontal displacement 2-5km, vertical displacement 10-30m, duration 1-4 years. M08: beginning to surge in 1986. OS: glacier velocities increase in eastern arm (annual average) from 90 m a^{-1} to 275 m a^{-1}. Acceleration period: 2000-2003; active phase: 2004-2006; Deceleration: 2007-2013	1948 1979 1986 2004-2006	M08; P69; OS; W87
Seward	G219572 E60177N	-140.428	60.177	3	W87: Surge type B: Active phase: velocity of 2-8 m d^{-1}, horizontal displacement 2-5km, vertical displacement 10-30m, duration 1-4 years. M03: surface lowered up to 120 m from 1973-2000. Surges periodically, most recently 1987-88. OS: during 1986-1987 surge, annual average velocities peaked at 3615 m a^{-1}, and quiescent at 2955 m a^{-1}; during 1999-2000 pulse, active velocities peaked at 2870 m a^{-1}, and quiescent at 2320 m a^{-1}	1906 1930s 1954-1956 1987-1988 1999	M03; MS08; OS; S58; W87
Sít' Kusá (Turner)	G220204 E60098N	-139.796	60.098	3	W87: Active phase: very high velocity, >15 m d^{-1}, calving rate high. Horizontal displacement large but small relative to size. Vertical displacement difficult to discern. Duration <2 years. N21: peak velocities 25 m d^{-1}, quiescent velocities, <1 m d^{-1}, surge nucleus middle of glacier; initiation winter/early spring	1963-1965 1974 1983-1986 1991-1993 1999-2002 2006-2008 2012-2013 2020-2021	N21; P69; W87
Spring	G220030 E61076N	-139.97	61.076	3	W87: Surge type B; Active phase: velocity of 2-8 m d^{-1}, horizontal displacement 2-5 km, vertical displacement 10-30 m, duration 1-4 years. P69: From Map: observed surging or display evidence of surging. OS: during 2007-2015 pulse, annual average velocities peaked at 110 m a^{-1}, and quiescent at 55 m a^{-1}	1951 2007-2012	C86; OS; P69; W87
Steele	G219819 E61242N	-140.181	61.242	3	C86: "surface streams, recent retreat" W87: Active phase: velocity of 2-8 m d^{-1}, horizontal displacement 2-5 km, vertical	1940 1965-1968 2012-2017 2020-2023 (trib.)	C86, D00; OS; W87

					displacement 10-30 m, duration 1-4 years. C02: surge in 1960s, ice advanced 9.5 km D00: Active phase up to 30 m d^{-1}, quiescent velocities <0.4 m d^{-1}. No terminus advance. Features of both Alaskan and Svalbard style surges. OS: Hodgson Glacier began to surge in 2020-23 as a result of surface lowering of main glacier trunk from 2012-2017		
Steller	G216487 E60497N	-143.513	60.497	3	W87: Surge type B; Active phase: velocity of 2-8m d^{-1}, horizontal displacement 2-5 km, vertical displacement 10-30 m, duration 1-4 years. M08: In early 2000, a small surge began that caused a readvance of the terminus of Steller glacier. Continued through the fall of 2001.	1984 1995 2000-2001	M08; W87
Tsaa	G218272 E60103N	-141.728	60.103	2	S15: Published velocity data. No other info provided.	-	B12; S15
Tweedsmuir	G221531 E59902N	-138.469	59.902	3	W87: Surge type B. C86: Tributary to C001, out of phase; medial moraines show surge, past record. S21: Surged from 1969-1974, elevation change of 13 m a^{-1} in receiving area. Surge in 2000s produced elevation change of +8.5 m a^{-1} in receiving area.	1933-1935 1952-1954 1973-1974 2006-2009	C86; B13; P69; S21; W87
Tyndall	G218857 E60196N	-141.143	60.196	3	M03: major surge in 1964 (Post, per. comm). W87: Surge type E; Active phase: very high velocity, >15 m d^{-1}, calving rate high. Horizontal displacement large but small relative to size. Vertical displacement difficult to discern. Duration <2 years. OS: velocities in 2008 up to 1550 m a^{-1}, compared to ~800 m a^{-1}, limited to only ~15 km, lower glacier	1964 2008	M03; OS; W87
Valerie	G220560 E60074N	-139.44	60.074	3	W87: Surge type E; Active phase: very high velocity, >15 m d^{-1}, calving rate high. Horizontal displacement large but small relative to size. Vertical displacement difficult to discern. Duration <2 years. W93: A weak surge or pulse of the Valerie Glacier (tributary of Hubbard Glacier) and a pulse of the Hubbard Glacier caused a rapid advance of the calving terminus in the spring of 1986.	1986	W87; W93
Variegated	G220833 E59999N	-139.167	59.999	3	E05: connection between high air temperatures, large outburst of meltwater and end of surging, leading to uncompleted surge in 1995. K85: 1982 surge peak velocities of 10 m d^{-1}, quiescent velocities of 0.1-0.5 m d^{-1}. 2 active phases during surge. Surge in 1965 advanced terminus by 6 km, but did not advance as much during 1980s surge. KE87: Mini-surges, velocity increases from 55 cm d^{-1} to 100-300 cm d^{-1} prior to full surge, uplift of surface (6-11 cm) due to basal cavitation and high subglacial water pressure. W87: Surge type A.	1905-1906 ~1920 1933 1946-1947 1964-1965 1982-1983 1995-1996 2003-2004	E05; J11; K85; K87; KE87; L97; M08; P69; W87
Walsh	G219611 E60880N	-140.389	60.88	3	W87: Surge type A; Active phase: velocity of 2-8 m d^{-1}, horizontal displacement 2-5 km, vertical displacement 10-30 m, duration 1-4 years.	1920 1948-1952 1960-1965 1988-1992	C02; F20; M08; M69; OS; P69; W87

					M08: Between 1961 and 1966 the glacier underwent a surge (Paige 1965, Post 66, 67b) that resulted in ice displacement of approximately 11.5 km F20: max ice velocity 14 m d^{-1}, thickening of 140 m, summer and winter speed ups. Surge initiated at connection between east and north branches (upper glacier). Spring/winter initiation, summer termination. OS: peak winter velocities reach 1950 m a^{-1}; annual average = 1400 m a^{-1}	2012-2017	
Yahtse	G218284 E60329N	-141.716	60.329	2	W87: Surge type E B12: Unpublished velocity data.	-	B12; S15 W87
(Ahnkattie)	G222217 E59703N	-137.783	59.703	2	W87: Surge type B.	-	W87
(Alberta)	G219180 E60941N	-140.82	60.941	2	W87: Active phase: velocity of 2-8 m d^{-1}, horizontal displacement 2-5 km, vertical displacement 10-30 m, duration 1-4 years.	1920 1948-1951	W87
(Alki)	G222495 E59766N	-137.505	59.766	2	C86: tributary to a064, probable surger. W87: Surge type B.	-	C86; W87
(Backe Jackal)	G219665 E61212N	-140.335	61.212	3	W87: Surge type D; Active phase: very slow, <1 m d^{-1}, horizontal displacement: small but 10-30% of size. Vertical displacement little observable depression, but great extension. Duration <4-20 years.	1961	C86; P69; W87
(Brabazon A)	G219408 E61380N	-140.592	61.38	1	C86: toe debris-covered, was tributary to f027. W87: Surge type D	-	C86; W87
(Brabazon B)	G219426 E61373N	-140.574	61.373	1	C86: Was tributary to f024, possibly has surged. W87: Surge type D	-	C86; W87
(Brooke)	G219073 E61517N	-140.927	61.517	3	C87: Tributary to f068, surges, very narrow. W87: Surge type C	-	C86; W87
(Cement A)	G219918 E61325N	-140.082	61.325	3	C86: Possible past surges shown in toe. W87: Surge type D; Active phase: very slow, <1 m d^{-1}, horizontal displacement: small but 10-30% of size. Vertical displacement little observable depression, but great extension.	1951	C86, W87
(Cement B)	G219959 E61324N	-140.041	61.324	2	C86: Possible surge, surface drainage. WS87: Surge type B.	-	C86; P69; W87
(Cement C)	G220007 E61330N	-139.993	61.33	1	C86: Shows recent advance, toe bulges. W87: Surge type D	-	C86; W87
(Chitina South Trib 2)	G218954 E60955N	-141.046	60.955	2	W87: Surge type B; Active phase: velocity of 2-8 m d^{-1}, horizontal displacement 2-5 km, vertical displacement 10-30 m, duration 1-4 years.	1950-1951	P69; W87
(Chitina South trib)	G218798 E60961N	-141.202	60.961	3	W87: Surge type B	-	P69; W87
(Congruent C)	G219995 E61245N	-140.005	61.245	2	W87: Surge type D	-	W87
(Congruent D)	G220043 E61222N	-139.957	61.222	2	C86: "may show surge features in tongue" W87: Surge type D; <1 m d^{-1}, horizontal displacement: small but 10-30% of size. Vertical displacement little observable depression, but great extension.	1951	C86, W87
(Congruent E)	G220100 E61229N	-139.9	61.229	2	C86: "high laterals show retreat" W87: Surge type D; Active phase: very slow, <1 m d^{-1}, horizontal displacement: small but 10-30% of size. Vertical displacement little observable depression, but great extension.	1966	C86, W87

(Congruent F)	G220155 E61251N	-139.845	61.251	2	C86: "very steep profile" W87: Surge type D.	-	C86; W87
(Congruent G)	G220163 E61264N	-139.837	61.264	1	C86: surged 1966. W87: Active phase: very slow, <1 m d^{-1}, horizontal displacement: small but 10-30% of size. Vertical displacement little observable depression, but great extension. Duration <4-20 years.	1966	C86
(Count North)	G219444 E61415N	-140.556	61.415	2	C86: very steep, probable surger W87: Surge type D	-	C86; P69; W87
(Count South)	G219477 E61387N	-140.523	61.387	2	C86: joins f024, no contribution, possible surger. W87: Surge type D.	-	C86; P69; W87
(Detour)	G222476 E59860N	-137.524	59.86	2	C86: looped moraines, debris covered tongue. W87: Surge type B.	-	C86; W87
(Duktoth)	G217831 E60335N	-142.169	60.335	2	W87: Surge type B; Active phase: velocity of 2-8 m d^{-1}, horizontal displacement 2-5 km, vertical displacement 10-30m, duration 1-4 years.	1986	W87
(Dyke)	G222139 E59820N	-137.861	59.82	2	C86: over-extended stagnant tongue. W87: Surge type B.	-	C86; W87
(Fdetsak)	G221299 E60659N	-138.701	60.659	2	C86: crevassed tongue may be surging. W87: Surge type B.	-	C86, W87
(Gibson)	G219913 E61232N	-140.087	61.232	1	C86: shear planes show probable past surge. W87: Surge type D; Active phase: very slow, <1 m d^{-1}, horizontal displacement: small but 10-30% of size. Vertical displacement little observable depression, but great extension.	1961-1962	C86, P69; W87
(Hayden)	G219820 E59978N	-140.020	60.051	3	W87: Surge type B M03: surface lowered up to 100 m from 1973-2000 OS: increase during pulse from 40 m a^{-1} to 115 m a^{-1}, limited to lower glacier.	2012-2014	M03; OS; W87
(Kanabe)	G218609 E60691N	-141.391	60.691	2	W87: Surge type B; Active phase: velocity of 2-8 m d^{-1}, horizontal displacement 2-5 km, vertical displacement 10-30 m, duration 1-4 years. OS: during 2013-2020 surge, annual average velocities peaked at 95 m a^{-1}, and quiescent at 60 m a^{-1}.	1966-1970 2015-2020	OS; P69; W87
(Kluane (lil) West)	G220522 E61029N	-139.478	61.029	2	W87: Surge type B	-	C86; W87
(Kluane 2nd east)	G220940 E60907N	-139.06	60.907	2	P69: From Map: observed surging or display evidence of surging. C86: tributary to n107, surges out of phase. W87: Surge type B; Active phase: velocity of 2-8 m d^{-1}, horizontal displacement 2-5 km, vertical displacement 10-30m, duration 1-4 years.	1951-1954	C86; P69; W87
(Lambart)	G219040 E61500N	-140.96	61.5	2	C86: stagnant toe, looped moraines, surges. W87: Surge type C; Active phase: <1-8 m d^{-1}, horizontal displacement small but 10-30% of size. Vertical displacement: little observable.	1951	C86, W87
(Leloo)	G222355 E60035N	-137.645	60.035	2	C86: looped medial moraines show five probably surges. W87: Surge type C.	-	C86, W87
(Little Chitistone 1)	G217952 E61569N	-142.048	61.569	2	W87: Surge type D.	-	W87

(Little Chitistone 2)	G217927 E61547N	-142.073	61.547	2	W87: Surge type D; Active phase: very slow, <1 m d^{-1}, horizontal displacement: small but 10-30% of size. Vertical displacement little observable depression, but great extension. duration <4-20 years.	1956-1958	W87
(Little Duktoth)	G217716 E60305N	-142.284	60.305	2	W87: Surge type C	-	W87
(Little Goat)	G218339 E60742N	-141.661	60.742	2	W87: Surge type B; Active phase: velocity of 2-8 m d^{-1}, horizontal displacement 2-5 km, vertical displacement 10-30 m, duration 1-4 years.	1985-1986	W87
(Little Hawkins)	G218173 E61288N	-141.827	61.288	2	W87: Surge type D.	-	W87
(Little Huberts)	G218493 E61046N	-141.507	61.046	2	W87: Surge type D; Active phase: very slow, <1 m d^{-1}, horizontal displacement: small but 10-30% of size. Vertical displacement little observable depression, but great extension. Duration <4-20 years.	1984	W87
(Marble A East)	G218438 E60872N	-141.562	60.872	2	W87: Surge type B; 40-80% of glacier effected. Degree of transformation: where active: considerable, quite often surge does not reach terminus. Most of main trunk affected, some upper ice streams not affected. Terminus characteristics: minor surface rise, slight bulge, moderately crevassed, not all stagnant ice activated. Marginal characteristics; considerable shearing, but with regions without noticeable activity, tributaries not wholly sheared. Reservoir characteristics: crevassing confined to certain tributaries and certain regions, parts of upper basin look "normal". Duration 1 to 3 years.	1986	W87
(Moffat)	G219971 E61216N	-140.029	61.216	2	C86: "lateral moraines at toe" W87: Surge type D; Active phase: very slow, <1 m d^{-1}. Horizontal displacement: small but 10-30% of size. Vertical displacement little observable depression, but great extension.	1951-1963	C86, W87
(Mount Sulzer North)	G218368 E61627N	-141.632	61.627	2	W87: Surge type B; Active phase: velocity of 2-8 m d^{-1}, horizontal displacement 2-5 km, vertical displacement 10-30 m, duration 1-4 years.	1947-1948 1986	W87
(Mount Wood)	G219484 E61307N	-140.516	61.307	2	C86: was tributary to f024, receded. W87: Surge type B; Active phase: very slow, <1 m d^{-1}. horizontal displacement: small but 10-30% of size. Vertical displacement little observable depression, but great extension. duration <4-20 years.	1972	C86; W87
(Nouse creek)	G221577 E60001N	-138.423	60.001	3	C86: Surged in 1960. W87: Surge type B; Active phase: velocity of 2-8 m d^{-1}, horizontal displacement 2-5 km, vertical displacement 10-30 m, duration 1-4 years.	1960-1963	C86, W87
(Range)	G222232 E59826N	-137.768	59.826	2	C86: "much recent recession" W87: Surge type B.	-	C86, W87
(Russell east trib)	G218263 E61598N	-141.737	61.598	3	P69: From Map: observed surging or display evidence of surging. W87: Surge type B.	-	P69; W87
(Rusty/Fox)	G219698 E61200N	-140.302	61.2	3	W87: Active phase: very slow, <1 m d^{-1}, horizontal displacement: small but 10-30% of size. Vertical displacement little observable	1951	C86; W87

					depression, but great extension. Duration <4-20 years.		
(Sheep)	G218396 E61641N	-141.604	61.641	2	W87: Active phase: <1-8 m d^{-1}, horizontal displacement small but 10-30% of size. Vertical displacement: little observable depression, but great extension. Duration <1-4 years.	1948-1949 1963-1967 1974	P69; W87
(South/ Little Kasa)	G220869 E60822N	-139.131	60.822	3	W87: Surge type C: Active phase: 0.05 – 0.10 m d^{-1}, recurrence interval: 30-40 years; surge nucleus: Middle of Glacier. Slow surge.	1951 1986-1987	C86, D09 W87
(St Clare 3)	G219587 E61301N	-140.413	61.301	3	From Map: observed surging or display evidence of surging.	-	P69
(St Clare 4)	G219646 E61285N	-140.354	61.285	3	C86: possible surgers, has heavy moraine. W87: Surge type D.	-	C86; W87
(Taylor)	G218423 E60785N	-141.577	60.785	2	W87: Surge type B.	-	W87
(Trapridge)	G219646 E61222N	-140.354	61.222	3	W87: Surge type D. F07: Active phase: 0.12 m d^{-1}, quiescent phase: 0.025 m d^{-1}. Active phase duration: ~20 years, recurrence interval ~30 years.	1939-1949 1977-2005	C86; F07; W87
(Wolverine Creek A)	G219924 E61409N	-140.076	61.409	2	W87: Surge type D; Active phase: very slow, <1 m d^{-1}. horizontal displacement: small but 10-30% of size. Vertical displacement little observable depression, but great extension. duration <4-20 years.	1951	W87
(Wolverine Creek B)	G219880 E61424N	-140.12	61.424	2	W87: Surge type D.	-	W87
(Yukon A)	G218890 E60997N	-141.11	60.997	2	W87: Surge type D.	-	W87
(Yukon C)	G218928 E60997N	-141.072	60.997	2	W87: Surge type D.	-	W87
-	G220130 E61242N	-139.87	61.242	1	C86: Surge index 1; Tributary to s048, surged 1966.	-	C86
-	G222006 E59939N	-137.994	59.939	1	C86: Surge index 2; Medial moraines show surge possible.	-	C86
-	G221723 E60439N	-138.277	60.439	1	C86: Surge index 1; Looped medials, truncated tributaries.	-	C86
-	G218973 E61495N	-141.027	61.495	2	C86: Surge index 3; very steep, probable surger.	-	C86
-	G221543 E60517N	-138.457	60.517	2	C86: Surge index 4; Looped moraines may show surge.	-	C86
-	G222264 E60041N	-137.736	60.041	2	C86: Surge index 4; Surface drainage, stranded lateral moraines.	-	C86
-	G219636 E61240N	-140.364	61.24	3	C86: Surge index 5; Retreated, surface drainage.	-	C86
-	G222235 E59923N	-137.765	59.923	2	C86: Surge index 4; Tongue stagnant, looped medials.	-	C86
-	G222264 E60106N	-137.736	60.106	1	C86: Surge index 2; Looped medials, debris covered tongue.	-	C86
-	G222396 E59895N	-137.604	59.895	1	C86: Surge index 1; Crevassed tongue, quite steep.	-	C86
-	G219545 E61310N	-140.455	61.31	1	C86: Surge index 1; Surger, surface streams dissecting tongue. P69: From Map: observed surging or display evidence of surging.	-	C86, P69
-	G219568 E61274N	-140.432	61.274	1	C86: Surge index 1; Many surge features, surged 1968.	-	C86
-	G222251 E59747N	-137.749	59.747	1	C86: Surge index 1; Probably surger, has thick stagnant tongue.	-	C86
-	G219581 E61248N	-140.419	61.248	2	C86: Surge index 3; Surged 1951, tributary to s100 after.	-	C86

-	G219481 E61356N	-140.519	61.356	2	C86: Surge index 3; Possible surger, moraine shows recession. C08: Listed from WGMS and NSIDC (1989, updated 2009) based on WGMS (various regions)	-	C08; C86
-	G221972 E59952N	-138.028	59.952	1	C86: Surge index 1; Tributary to D057	-	C86
-	G221803 E60227N	-138.197	60.227	1	C86: Surge index 1; LGE moraine, much recession.	-	C86
-	G221737 E60860N	-138.263	60.86	1	C86: Surge index 2; Tributary to and truncated by k005.	-	C86
-	G222357 E59762N	-137.643	59.762	1	C86: Surge index 1; Probable surger, multiple surge features.	-	C86
-	G221125 E60884N	-138.875	60.884	1	C86: Surge index 1; Stranded laterals lead to m018.	-	C86
-	G221748 E59787N	-138.252	59.787	1	C86: Surge index 1; Tributary to B019, probably no contributor.	-	C86
-	G219961 E61389N	-140.039	61.389	2	C86: Surge index 3; Surface drainage, depression.	-	C86
-	G221416 E60637N	-138.584	60.637	1	C86: Surge index 2; Tributary j045 truncated by main glacier.	-	C86
-	G221656 E59919N	-138.344	59.919	1	C86: Surge index 1; Tributary to D007.	-	C86
-	G221691 E60902N	-138.309	60.902	1	C86: Surge index 1; Tributary, has pushed into main glacier c044.	-	C86
-	G220972 E61004N	-139.028	61.004	1	C86: Surge index 2; Tributary to m212 probable surges.	-	C86
-	G221584 E60447N	-138.416	60.447	2	C86: Surge index 3; Tributary to h062, may surge.	-	C86
-	G221133 E60899N	-138.867	60.899	1	C86: Surge index 1; Long proterminal moraine probable ice cored.	-	C86
-	G221060 E60936N	-138.94	60.936	1	C86: Surge index 2; Probably receding.	-	C86
-	G220015 E61260N	-139.985	61.26	1	C86: Surge index 1; Hanging tongue, elongated cirque.	-	C86
-	G219767 E61327N	-140.233	61.327	1	C86: Surge index 1; Crevassed, probable surger, tributary to e029.	-	C86
-	G220189 E61266N	-139.811	61.266	1	C86: Surge index 1; Tributary to s048, active tongue.	-	C86
-	G220041 E61341N	-139.959	61.341	2	C86: Surge index 4; Surface drainage. C08: Listed from WGMS and NSIDC (1989, updated 2009) based on WGMS (various regions)	-	C08; C86
-	G219756 E61313N	-140.244	61.313	1	C86: Surge index 1; Possible surger, has heavy moraine.	-	C86
-	G222266 E60077N	-137.734	60.077	2	C86: Surge index 4; Looped laterals, debris covered tongue.	-	C86
-	G221798 E60337N	-138.202	60.337	1	C86: Surge index 1; Tributary to g038, probably surges with g038.	-	C86
-	G221615 E60520N	-138.385	60.52	1	C86: Surge index 2; Tributary to i029, surged into main stream.	-	C86
-	G222334 E59810N	-137.666	59.81	1	C86: Surge index 1; Crevassed, active tongue.	-	C86
-	G222332 E60068N	-137.668	60.068	2	C86: Surge index 3; Moraine joins that of m007.	-	C86
-	G220506 E60951N	-139.494	60.951	1	C86: Surge index 1; Recent retreat.	-	C86
-	G220022 E61250N	-139.978	61.25	1	C86: Surge index 1; Sml slide, thrust planes, on tongue.	-	C86
-	G220594 E61245N	-139.406	61.245	1	C86: Surge index 2; Thinned tongue has surface streams.	-	C86

-	G220650 E60900N	-139.35	60.9	1	C86: Surge index 1; Tributary to o001, likely surger.	-	C86
-	G220859 E60905N	-139.141	60.905	1	C86: Surge index 2; Probable surges with n107 (tributary).	-	C86
-	G221026 E60812N	-138.974	60.812	1	C86: Surge index 2; 2 main branches with large snowfields.	-	C86
-	G220440 E61088N	-139.56	61.088	2	C86: Surge index 3; Joins p048, has own flow pattern.	-	C86
-	G220505 E61036N	-139.495	61.036	2	C86: Surge index 3; Probable surger, high stranded lateral moraines.	-	C86
-	G220176 E61169N	-139.824	61.169	1	C86: Surge index 2; Tributary to r048, surges, ogive waves.	-	C86
-	G221481 E60894N	-138.519	60.894	1	C86: Surge index 1; Irregular medials show possible surge.	-	C86
-	G220803 E60983N	-139.197	60.983	1	C86: Surge index 2; High stranded laterals.	-	C86
-	G220915 E60817N	-139.085	60.817	1	C86: Surge index 2; Crevassed tongue shows possible surge.	-	C86
-	G220812 E61015N	-139.188	61.015	2	C86: Surge index 3; Joins n047, in surge.	-	C86
-	G221722 E59903N	-138.278	59.903	1	C86: Surge index 1; Steep profile, much crevassing.	-	C86
-	G221030 E60928N	-138.97	60.928	2	C86: Surge index 3; Wasted tongue, looped medials. P69: From Map: observed surging or display evidence of surging.	-	C86, P69
-	G221691 E60355N	-138.309	60.355	2	C86: Surge index 3; Has surge history.	-	C86
-	G220157 E61168N	-139.843	61.168	1	C86: Surge index 1; Appears advancing, may surge.	-	C86
-	G220763 E60789N	-139.237	60.789	1	C86: Surge index 1; Tributary to l050, probably surges.	-	C86
-	G222101 E59860N	-137.899	59.86	2	C86: Surge index 3; Extreme recession, prob after surge.	-	C86
-	G222492 E59824N	-137.508	59.824	2	C86: Surge index 3; Looped medials, other surge features.	-	C86
-	G222325 E60004N	-137.675	60.004	1	C86: Surge index 2; Looped medials, wasted tongue.	-	C86
-	G221844 E59934N	-138.156	59.934	1	C86: Surge index 1; Advance possible, tongue crevassed.	-	C86
-	G222157 E60102N	-137.843	60.102	1	C86: Surge index 1; Heavy crevassing may show surge.	-	C86
-	G220534 E61010N	-139.466	61.01	3	From Map: observed surging or display evidence of surging.	-	P69
-	G220780 E61022N	-139.22	61.022	2	C86: Surge index 3; Joins n056.	-	C86
-	G220027 E61147N	-139.973	61.147	3	From Map: observed surging or display evidence of surging.	-	P69
-	G219258 E61381N	-140.742	61.381	1	C86: Surge index 1; Probable surger, possible beginning surge.	-	C86
-	G219889 E61237N	-140.111	61.237	1	C86: Surge index 2; Moraines show 3 retreat stages.	-	C86
-	G219789 E61301N	-140.211	61.301	2	C86: Surge index 3; Possible surger, surface drainage, cold ice.	-	C86
-	G219496 E61342N	-140.504	61.342	2	C86: Surge index 3; Possible surge features, large recession.	-	C86
-	G222516 E59884N	-137.484	59.884	1	C86: Surge index 1; Long debris-covered lower tongue.	-	C86
-	G222447 E60035N	-137.553	60.035	1	C86: Surge index 2; Formerly trib to b034, receded.	-	C86

-	G220541 E60958N	-139.459	60.958	1	C86: Surge index 1; Could be surger.	-	C86
-	G220809 E60806N	-139.191	60.806	1	C86: Surge index 2; Tongue appears active.	-	C86
-	G219985 E61228N	-140.015	61.228	1	C86: Surge index 1; Very steep and narrow tongue.	-	C86
-	G221057 E60901N	-138.943	60.901	1	C86: Surge index 1; Strong retreat indicated.	-	C86
-	G221665 E60221N	-138.335	60.221	1	C86: Surge index 1; Tributary to G016, flow may be irregular.	-	C86
-	G221380 E60604N	-138.62	60.604	2	C86: Surge index 3; Looped moraine, probable surger.	-	C86
-	G221343 E60689N	-138.657	60.689	2	C86: Surge index 4; Strong recession indicated.	-	C86
-	G220944 E61063N	-139.056	61.063	1	C86: Surge index 1; Receding, may surge.	-	C86
-	G221203 E60826N	-138.797	60.826	1	C86: Surge index 1; Tributary to l115, truncated.	-	C86
-	G220954 E60974N	-139.046	60.974	2	C86: Surge index 4; Greatly extended, snowline approximative. C08: Listed from WGMS and NSIDC (1989, updated 2009) based on WGMS (various regions)	-	C08; C86
-	G221369 E60650N	-138.631	60.65	1	C86: Surge index 1; Long proterminus moraine shows recession.	-	C86
-	G221083 E60895N	-138.917	60.895	1	C86: Surge index 1; Stranded laterals lead to m018.	-	C86
-	G221389 E60570N	-138.611	60.57	2	C86: Surge index 4; Tributary to j033, truncated.	-	C86
-	G221011 E60884N	-138.989	60.884	1	C86: Surge index 1; Tributary to m018, surged after main glacier.	-	C86
-	G220990 E60829N	-139.01	60.829	1	C86: Surge index 2; Probably surger, long wasted tongue.	-	C86
-	G220471 E60996N	-139.529	60.996	2	C86: Surge index 3; C08: Listed from WGMS and NSIDC (1989, updated 2009) based on WGMS (various regions)	-	C08; C86
-	G221183 E60823N	-138.817	60.823	1	C86: Surge index 1; Rapid retreat indicated.	-	C86
-	G220479 E60945N	-139.521	60.945	1	C86: Surge index 1; Surged with o099 before 1951.	-	C86
-	G220402 E61052N	-139.598	61.052	3	From Map: observed surging or display evidence of surging.	-	P69
-	G221059 E61033N	-138.941	61.033	1	C86: Surge index 1; Has truncated tributary.	-	C86
-	G219944 E61391N	-140.056	61.391	1	C86: Surge index 1; Crevasses show advance of tongue.	-	C86
-	G220927 E61049N	-139.073	61.049	1	C86: Surge index 2; High stranded laterals.	-	C86
-	G222443 E60004N	-137.557	60.004	1	C86: Surge index 1; Looped medials, stranded laterals.	-	C86
-	G221324 E60729N	-138.676	60.729	1	C86: Surge index 2; Probable surger.	-	C86
-	G220203 E61078N	-139.797	61.078	2	C86: Surge index 3; Probable surger, wasted tongue.	-	C86
-	G221022 E60855N	-138.978	60.855	2	C86: Surge index 4; Looped moraines in tongue probably show surge.	-	C86
-	G221694 E60149N	-138.306	60.149	1	C86: Surge index 2; Joins E001, does not contribute.	-	C86
-	G219544 E61284N	-140.456	61.284	2	C86: Surge index 4; Was tributary to f024, receded.	-	C86

-	G221458 E60531N	-138.542	60.531	2	C86: Surge index 4; Has looped medial moraines, probably surger.	-	C86
-	G219236 E61384N	-140.764	61.384	1	C86: Surge index 1; Was tributary to f024, possible surger.	-	C86
-	G219457 E61327N	-140.543	61.327	1	C86: Surge index 1; Tributary to f024, surge history.	-	C86
-	G219737 E61148N	-140.263	61.148	1	C86: Surge index 1; Tributary to s068, surface drainage.	-	C86
-	G219064 E61496N	-140.936	61.496	1	C86: Surge index 2; Very steep, probable surger.	-	C86
-	G218802 E61546N	-141.198	61.546	3	+3.5 km advance between 1950 and 2009.	-	A12
-	G219250 E61325N	-140.75	61.325	2	C86: Surge index 4; Was tributary to f024, tongue debris-covered.	-	C86
-	G219413 E61394N	-140.587	61.394	1	C86: Surge index 1; Tributary to f001, has surge history.	-	C86
-	G219935 E61396N	-140.065	61.396	1	C86: Surge index 2; Probably surged recently.	-	C86
-	G219866 E61327N	-140.134	61.327	1	C86: Surge index 2; Tributary to u018.	-	C86
-	G219213 E61313N	-140.787	61.313	1	C86: Surge index 1; Tributary to f031, probably surges with main glacier.	-	C86
-	G219200 E61396N	-140.8	61.396	1	C86: Surge index 1; Tributary to f001, surges.	-	C86
-	G219860 E61308N	-140.14	61.308	1	C86: Surge index 1; Lateral moraines show recession, surface drainage.	-	C86
-	G219104 E61497N	-140.896	61.497	2	C86: Surge index 3; Stagnant toe, surface drainage, surger.	-	C86
-	G219442 E61362N	-140.558	61.362	2	C86: Surge index 3; Was tributary to f024, much receded.	-	C86
-	G219642 E61233N	-140.358	61.233	2	C86: Surge index 3; Probably past surge induced by lateral moraines.	-	C86
-	G220955 E60941N	-139.045	60.941	1	C86: Surge index 1; May surge.	-	C86
-	G221930 E59893N	-138.07	59.893	1	C86: Surge index 1; Heavily crevassed tongue.	-	C86
-	G220149 E61058N	-139.851	61.058	2	C86: Surge index 3; Recently surged pre-1951.	-	C86
-	G220781 E60996N	-139.219	60.996	1	C86: Surge index 1; Joins n056, non-contributing.	-	C86
-	G219719 E61296N	-140.281	61.296	1	C86: Surge index 1; Possible surger, has heavy moraine.	-	C86
-	G219505 E61317N	-140.495	61.317	1	C86: Surge index 1; Possible surge features, large recession.	-	C86
-	G220067 E61343N	-139.933	61.343	1	C86: Surge index 2; Surface drainage.	-	C86
-	G221573 E60496N	-138.427	60.496	2	C86: Surge index 4; Trib to i029, flow out of phase.	-	C86
-	G220443 E61106N	-139.557	61.106	1	C86: Surge index 2; Probably surges, has stranded lateral.	-	C86
-	G220576 E60975N	-139.424	60.975	1	C86: Surge index 1; Possible surger, high terminal moraine.	-	C86
-	G221618 E60478N	-138.382	60.478	3	C86: Surge index 5; Looped medials in stagnant toe.	-	C86
-	G222541 E59844N	-137.459	59.844	1	C86: Surge index 1; Probable surger, possibly advance in progress.	-	C86
-	G220191 E61109N	-139.809	61.109	1	C86: Surge index 1; Tributary to r048, flow out of phase.	-	C86
-	G221573 E60227N	-138.427	60.227	2	C86: Surge index 4; Tributary to g016, flow may be irregular. C08: Listed from WGMS and NSIDC (1989,	-	C08; C86

					updated 2009) based on WGMS (various regions)		
-	G219954 E61398N	-140.046	61.398	1	C86: Surge index 1: Stranded laterals, surface stream.	-	C86

[a] Surge Index: 1= Possible, 2= Likely, 3= Confirmed (from Sevestre and Benn, 2015).

[b] Where the surge date has (trib.) beside it, this refers to the surge of a tributary, but not the main glacier trunk.

[c] References to previously published descriptions/inventories: A12 = Arendt and others (2012); A14 = Abe and others (2014); A15 = Abe and Furuya (2015); A16 = Abe and others (2016); A15 = Abe and Furuya (2015); A19 = Altena and others (2019); B12 = Burgess and others (2012); B13 = Burgess and others (2013); BF12 = Burgess and others (2012); B14 = Bevington and Copland (2014); C02 = Clarke and Holdsworth (2002); C08 = Cogley (2008); C86 = Clarke and others (1986); D00 = Dutnall and others (in-prep); D09 = De Paoli and Flowers (2009); D77 = Denton and Karlen (1977); E05 = Eisen and others (2005); F11 = Foy and others (2011); F20 = Fou and Zhou (2020); F98 = Fleisher and others (1998); H69: Horvath and Field (1969); J11 = Jay-Allemand and others (2011); K85 = Kamb and others (1985); K87 = Kamb (1987); KE87 = Kamb and Engelhardt (1987); K19 = Kochtitzky and others (2019); K20 = Kochtitzky and others (2020); K73 = Kasser (1973); L97 = Lawson (1997); L97 = Lingle and others (1997); M03 = Muskett and others (2003); M07 = Motyka and Truffer (2007); M08 = Molnia (2008); MS08 = Muskett and others (2008); M69 = Meier and Post (1969); M71 = Miller (1971); M95 = Molina and others (1994); M95 = Muller and Fleisher (1995); N21 = Nolan and others (2021); OS = our study; P67 = Post (1967); P69 = Post (1969); P72 = Post (1972); S15 = Sevestre and Benn (2015); S21 = Sharp (2021); S58 = Sharp (1958); T13 = Turrin and others (2013); T18 = Trantow and Herzfeld (2018); VW23 = Van Wychen and others (2023); W14 = Waechter and others (2014); W87 = Wilbur and Post (1987); W93 = WGMS (1993).

Appendix 2-D: Glacier surges added to the inventory of Sevestre and Benn (2015) through the analyses undertaken for this study.

Name	GLIMS ID	Surge Period	Confidence Level	Notes:
Agassiz	G219116E60102N	1990 – 1993 2011 – 2012	Medium	Pulse.
Art Lewis	G221141E59910N	2000 – 2002 2011 – 2013	Medium	Pulse.
Atrevida	G220169E59934N	1987 – 1989 2000 – 2003 2011 – 2015	Medium	Pulse. Note: Continuing to reach approximately the same magnitude as earlier pulsing events.
Battle	G221646E59667N	2019 – 2021	Low	A mini surge or limited surge, terminus only.
Chitina	G219155E61116N	2021 – ongoing	High	Noted in Kääb and others (2023) and Van Wychen and others (2023).
Chitistone	G217961E61427N	2017 – 2020	Low	Potentially a pulse.
Hubbard	G220499E60427N	2009	High	3 partial surges of north, central and south upper tributaries observed near Icefield Discovery Camp. Noted in Abe and Furuya (2015).
Kanabe	G218609E60691N	2013 – 2020	Low	Potentially a slow surge that is still speeding up, a partial surge of a tributary, or a pulse.
Lucia	G220103E60023N	1992 – 1995 2000 – 2002	Medium	Pulse.
Marvine	G219820E59978N	2015 – 2018	Medium	Glacier velocity more than doubles.
Hayden	G219820E59978N	1986 – 1987 2012 – 2014	Medium	This glacier is no longer connected to Marvine Glacier. Pulse.
Russell	G218192E61498N	1999 – 2006	High	Impacts both the east and south tributaries, with the south beginning first.
Spring	G220030E61076N	2007 – 2012	Medium	Potentially a pulse or slow surge.
Steele (tributary)	G219819E61242N	~2020 – 2023	High	Full surge, but limited in impact on main glacier trunk.
Tyndall	G218857E60196N	2008	Medium	Very short event, only lasting 1 year. Impacts terminus only.

References

Abe, T., M. Furuya, and D. Sakakibara. 2016. Brief Communication: Twelve-year cyclic surging episodes at Donjek Glacier in Yukon, Canada. *The Cryosphere*, **10** (4):1427–32. doi: 10.5194/tc-10-1427-2016.

Burgess EW, Forster RR, Larsen CF and Braun M (2012) Surge dynamics on Bering Glacier, Alaska, in 2008-2011. *The Cryosphere*, **54**(63), 158-170. doi: 10.3189/2013AoG63A348.

Burgess EW, Forster RR and Larsen CF (2013) Flow velocities of Alaskan glaciers. *Nature Communications*, **4**, 2146-2154. doi: 10.1038/ncomms3146.

Cogley G (2008) World glacier Inventory from WGMS and NSIDC (1989, updated 2009) based on WGMS (various regions) WGMS and NSIDC. 1989, updated 2012.: Compiled and made available by the World Glacier Monitoring Service, Zurich, Switzerland, and the National Snow and Ice Data Center, Boulder CO, U.S.A.

Denton GH and Karlen WK (1977) Holocene Glacial and Tree-Line Variations in the White River Valley and Skolai Pass. Alaska and Yukon Territory. *Quaternary Research*, **7**(1), 63-111. doi: 10.1016/0033-5894(77)90014-X.

Fleisher JP, Cadwell DH and Muller EH (1998) Tsivat Basin Conduit System persists through two surges, Bering Piedmont Glacier, Alaska. *GSA Bulletin*, **110** (7): 877–887. doi: 10.1130/0016-7606(1998)110<0877:TBCSPT>2.3.CO;2

Herzfeld UC and Mayer H (1997) Surge of Bering Glacier and Bagley Ice Field, Alaska: an update to August 1995 and an interpretation of brittle-deformation patters. *Journal of Glaciology*, **43**(145) 427-434. doi:10.3189/S0022143000035012.

Horvath EV and Field WO (1969) References to glacier surges in North America. *Canadian Journal of Earth Sciences*, **6**, 845-851.

Kamb B and Englehardt H (1987) Waves of accelerated motion in a glacier approaching surge: the mini-surges of Variegated Glacier, Alaska, U.S.A. *Journal of Glaciology*, **33**(113), 27-46. doi: 10.3189/S0022143000005311.

Kasser P (ed.) (1973) Fluctuations of Glaciers 1965-70, Zurich, Switzerland: Permanent Service on Fluctuations on Glaciers.

Lawson W (1997) Spatial, temporal and kinematic characteristics of surges of Variegated Glacier, Alaska. *Annals of Glaciology*, **24,** 95-101. doi: https://doi.org/10.3189/S026030550001199X.

Lingle CS, Fatland DR, Voronina V, Ahlnäs K and Troshina E (1997) Dynamic behaviour of the Bering Glacier–Bagley Ice Field system during a surge, and other measurements of Alaskan glaciers with ERS imagery. In Third ERS Scientific Symposium, Noordwijk, 17–21 March 1997, Florence, Italy. Proceedings. European Space Agency, 995–1000. (ESA Spec. Pub. SP-414.)

Miller MM (1971) Glaciological and Geological Investigations on the 1965 Mount Kennedy, Yukon, Expedition. National Geographic Society Research Reports, 161-179 (http://crevassezone.org/reports/JIRP/32-MtKennedyStudies.pdf)

Molina 1994 Molnia, B. F., Post, A., and Fleisher, P. J., 1994, Abrupt glacio-hydrologic change, Bering Glacier, AK: *Eos (Transactions, American Geophysical Union),* v. 75, p. 63.

Molnia BF (2008) Glaciers of Alaska. In: Williams JRS and Ferrigno JG (eds.) Satellite Image Atlas of Glaciers of the World. U.S. Geological Survey Professional Paper

Motyka RJ and Truffer M (2007) Hubbard Glacier, Alaska: 2002 closure and outburst of Russell Fjord and postflood conditions at Gilbert Point. *Journal of Geophysical Research: Earth Surface*, **11**(F02004), 1-15. doi: 0.1029/2006JF000475.

Muller EH and Fleisher PJ (1995) Surging history and potential for renewed retreat: Bering Glacier, Alaska U.S.A. *Arctic and Alpine Research,* **27**(1), 81-88. doi: 10.1080/00040851.1995.12003099

Post A (1967) Walsh Glacier surge, 1966 observations. *Journal of Glaciology*, **6**, 763-765. doi: 10.3189/S0022143000020049.

Post A (1972) Periodic surge origin of folded medial moraines on Bering Piedmont Glacier: *Journal of Glaciology*, **11**, p. 219–226. doi: 10.3189/S0022143000022218.

Sharp RP (1958) Malaspina Glacier, Alaska. Bulletin of the Geological Society of America, 69, 617-646.

Sharp M (2021) Amplification of surface topography during surges of Tweedsmuir Glacier [Unpublished master's thesis]. University of Calgary, Calgary, AB. http://hdl.handle.net/1880/113988.

Trantow T and Herzfeld UC (2018) Crevasses as indicators of surge dynamics in the Bering Bagley Glacier System, Alaska: Numerical experiments and comparison to image data analysis. *Journal of Geophysical Research: Earth Surface*, **123**, 1615-1637. doi: 10.1029/2017JF004341.

WGMS: Haeberli W and Hoelzle M (eds.) (1993) Fluctuations of Glaciers 1985-1990, Zurich, Switzerland: World Glacier Monitoring Service.

Chapter 3: Little Kluane Glacier: varying dynamic instabilities in a medium-sized glacier, Yukon, Canada

3.1 Introduction

Surge-type glaciers are typically characterized by short periods of rapid flow (active phase), interspersed with extended periods of slow or near-stagnant flow (quiescence) (e.g., Benn and Evans, 2010). During the quiescent phase, ice mass builds up in the reservoir zone, often located in the glacier's accumulation area, while mass is lost in the receiving zone, usually located in the ablation area. When a surge occurs, ice mass is rapidly redistributed to the receiving zone, often resulting in thinning in the reservoir zone, thickening in the receiving zone, and an advance of the glacier front (e.g., Jiskoot, 2011; Benn and Evans, 2010). Although surge-type glaciers comprise only ~1% of glaciers globally, they tend to concentrate in specific regions such as Alaska-Yukon, where at least 322 surge-type glaciers have been identified through direct observation of physical changes such as increased velocity and rapid terminus advance, or due to the occurrence of indicative features such as looped surface moraines (Post, 1969; Clarke and others, 1986; Clarke and Holdsworth, 2002; Sevestre and Benn, 2015).

Theories of surge initiation in temperate glaciers have focused on hydrologic triggers based on transformation of the subglacial water drainage system from channelized to distributed (Kamb and others, 1985; Kamb, 1987; Fowler, 1987; Murray and others, 2003). While the duration of surge events and their recurrence interval are unique to each glacier, surges of temperate glaciers typically last for ~1-2 years, with an intervening quiescent phase of a decade or longer (e.g., Eisen and others, 2001, 2005; Bevington and Copland, 2014; Sevestre and Benn, 2015; Kochtitzky and others, 2019). However, growing evidence suggests that glacier flow instabilities exist with a spectrum of characteristics and on variable timescales, making a simple definition of surging challenging (e.g., Herreid and Truffer, 2016; Truffer and others, 2021). For example, the term "mini-surges" has been used to describe short-term velocity pulses over a period of hours, followed by a gradual decline in velocity throughout the following day, which occur prior to a glacier surge after the reservoir has refilled with sufficient mass (e.g., Variegated Glacier; Harrison and others, 1986; Kamb and Engelhardt, 1987). Sund and others (2009) also describe partial or "invisible" surges, whereby there is a major mass movement in an upper basin, which does not result in a surge of the main trunk of a glacier, and does not result in a terminus advance.

Recently, studies have attempted to reconcile existing surging theories into an over-arching enthalpy theory, which suggests that surging exists where enthalpy gains (e.g., from balance velocities) cannot be effectively discharged through enthalpy losses (e.g., from heat conduction and meltwater discharge) (Aschwanden and others, 2012; Benn and others, 2019; Benn and others, 2023). However, there are still variations in surging behaviour that are not fully explained by this theory, and further data is needed to test it.

It is therefore useful to investigate surge-type glaciers to advance our understanding of dynamic ice-flow instabilities, and to better disentangle glacier-climate responses from internal variability (e.g., Yde and Paasche, 2010; Flowers and others, 2011). Additionally, on a local scale, glacier surges can be hazardous to communities and infrastructure due to their rapid mass redistribution, increased calving, and potential for the formation of ice dams and associated downstream flooding (Harrison and others, 2015; Painter and others, 2023). For example, Kochtitzky and others (2020) report how repeated surges of Dań Zhùr (Donjek) Glacier, located ~30 km downstream of the terminus of Little Kluane Glacier, have blocked the Dań Zhùr River and led to the formation of several ice-dammed lakes and associated glacial lake outburst floods. While overall a limited impact, oral histories attest to glacier outburst floods having had fatal consequences for members of local indigenous communities in the past (Cruikshank, 2001, 2005).

Here we provide the first report of a 2013-18 surge of "Little Kluane Glacier", Yukon, to expand upon knowledge of glacier surges and other ice-flow instabilities in the St. Elias Mountains. No official name exists for the glacier, but historical air photo surveys completed by Austin Post in 1963 and 1965 identified it as Little Kluane Glacier, so we use that name here. We describe the surge from beginning to end to quantify the initiation location and subsequent progression, using a variety of datasets including digital elevation models (DEMs), temporally dense records of ice velocity, and observations of changes in surface characteristics and terminus location. These observations are placed in the context of the behaviour of Little Kluane Glacier since the late 1940s, including the likelihood of a previous partial surge.

3.2 Study Area

Located on the eastern side of the St. Elias Mountains in the traditional territory of Kluane and White River First Nations (Fig. 3-1), Little Kluane Glacier (60°45'N, 139°08'W) is ~20 km long and up to ~1.5 km wide, and ranges in surface elevation from ~1400–3500 m asl (Morin and others,

2023). The glacier was previously classified as a tributary of Kluane Glacier in the Randolph Glacier Inventory (RGI 6.0), but from recent satellite imagery and historical air photos it is clear that these glaciers have not been connected since at least 1963 (Post, 1963).

Little Kluane Glacier is land-terminating, with a section of dead ice in front of the terminus. There are extensive looped moraines on the glacier surface, in particular on the northern side of the main trunk in the ablation area. There is limited debris cover on the glacier outside of the dead ice zone and moraines. In historical air photos, and until the 1990s, a northern tributary was connected to Little Kluane Glacier (Fig. 3-1), but since the early 2000s it has retreated significantly. The uppermost section of the glacier is divided into three main arms (here referred to as north, upper and south), all of which have several smaller cirque tributaries (Fig. 3-1). The upper and south arms converge approximately 14 km from the terminus. Ice-penetrating radar measurements at the confluence of the north arm and main trunk in July 2021 show a maximum ice thickness of ~173 m (Appendix 3-A). While no direct meteorological measurements exist within the glacier catchment, the climate on the eastern side of the St. Elias Mountains is generally characterized as arctic and continental, with prevailing low winter temperatures (Newman and others, 2020), although since 1970 temperatures have increased at all elevations between 2000 – 6000 m (Williamson and others, 2020).

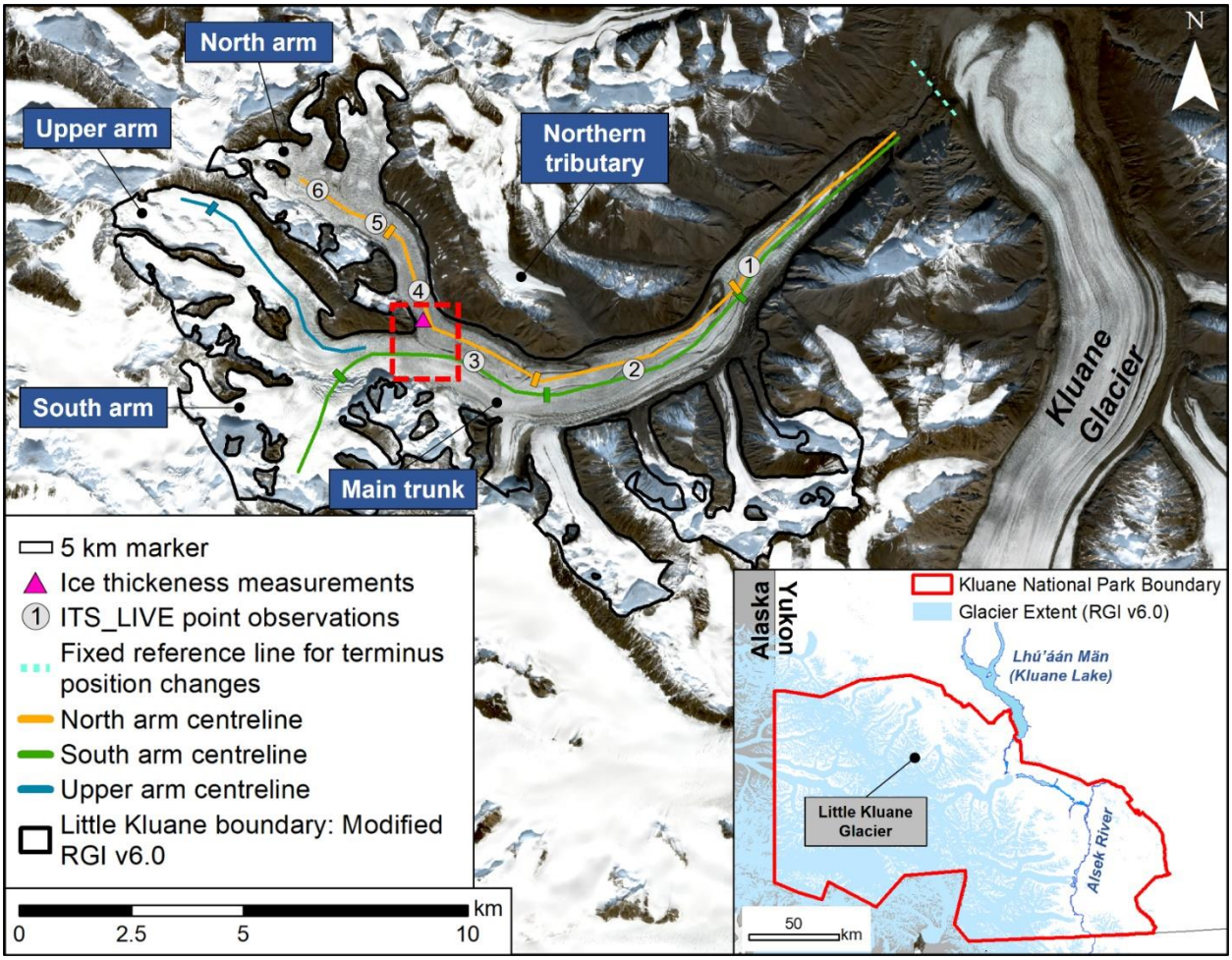

Figure 3-1: Little Kluane Glacier showing main locations referred to in the text. Red dashed box indicates region of interest in Figure 3-7. Note that the northern tributary disconnected from Little Kluane Glacier in the 1990s. Base image: Sentinel-2, 03-08-2019, UTM Zone 7N. Inset: Regional map of Kluane National Park and Reserve within the St Elias Mountains, with location of Little Kluane Glacier highlighted. Background Map: Yukon Geological Survey.

3.3 Methods

3.3.1 Data sources

To capture long-term changes in glacier geometry and surface features, historical air photos (1947-77), and optical satellite images from Landsat, Sentinel-2, RapidEye and PlanetScope (1972-2022) were obtained (Appendices 3-B and 3-C). The Royal Canadian Air Force (RCAF) acquired nadir photos during reconnaissance flights in 1947, 1951, 1972, and 1977, with the originals held in the National Air Photo Library, Ottawa; copies for this study were obtained from the University of Ottawa Map Library (https://www.uottawa.ca/library/collections/find-format/geospatial-data-maps) and the Yukon's Department of Energy, Mines and Resources Library (https://yukon.ca/en/science-and-natural-resources/research-and-monitoring/find-yukon-maps-energy-mines-and-resources) in Whitehorse. In addition, Austin Post flew a number of air photo surveys that captured Little Kluane Glacier in 1963 and 1965; these oblique images were obtained from the University of Washington Special Collections (https://www.lib.washington.edu/specialcollections/).

Landsat imagery was obtained from the United States Geological Survey Earth Explorer (https://earthexplorer.usgs.gov/) and downloaded in Level 1 GeoTIFF format. Sentinel-2 imagery was obtained from the ESA Copernicus Open Access hub and downloaded in Level-1C format (https://scihub.copernicus.eu/dhus/#/home). Images were preferentially selected from summer months under cloud-free conditions, with Landsat 1-3 (60 m resolution) and Landsat 5 (30 m resolution) imagery obtained in approximately 5-year intervals from 1972 to 2000, although suitable imagery during this time is sparse. Through an Education and Research Agreement with Planet Labs, RapidEye imagery (5 m resolution) was acquired from 2012-19, along with PlanetScope Level 3B Analytic MS imagery (3 m resolution) for summer 2018 (Planet Team, 2017). Some of the Planet imagery required further georectification, so it was aligned with the same August 30, 2021, Sentinel-2 scene used for the nadir air photos.

Glacier surface elevation changes before, during, and after the 2013-18 surge were characterized using DEMs from a variety of sources. DEMs were generated from SETSM WorldView imagery and ASTER Level 1A reconstructed unprocessed instrument data using the MMASTER software package (Girod and others, 2017; Appendix 3-D). Co-registration to the ASTER GDEM version 3 was completed using overlapping bedrock elevations (Shean and others, 2016). The produced

ASTER DEMs have a 10 m vertical and 2 m horizontal uncertainty (Girod and others, 2017). The SPOT DEM used in this study is 30 m resolution, and available in L1A Level (radiometric equalization, no geometric correction) from the SPOT World Heritage Data Search (https://regards.cnes.fr/user/swh/modules/60), and has an estimated uncertainty of 6 m. A 2 m-resolution DEM produced from WorldView stereo pairs was obtained from the University of Minnesota Polar Geospatial Center (PGC), and has 3 m vertical accuracy (Noh and Howat, 2015). All DEMs were further co-registered to each other using the method outlined by Nuth and Kääb (2011).

Glacier velocities were used to characterize behaviour prior to and after the 2013-18 surge. NASA's Inter-Mission Time Series of Land Velocity and Elevation (ITS_LIVE) program provides surface velocity mosaics derived from Landsat 4, 5, 7 and 8 imagery over the period 1985-2018, with a resolution of 240 m, created via the auto-RIFT feature tracking processing chain explained by Gardner and others (2019) (Appendix 3-E). Velocity magnitude in m a^{-1} (parameter v) was extracted along the centrelines of Little Kluane Glacier (Fig. 3-1). The ITS_LIVE velocity dataset provides the error product v_error (error in velocity magnitude in m a^{-1}). Errors associated with the ITS_LIVE dataset, including surface skipping and sensor biases, are presented in the Regional Glacier and Ice Sheet Surface Velocities Known Issues documentation (http://its-live-data.jpl.nasa.gov.s3.amazonaws.com/documentation/ITS_LIVE-Regional-Glacier-and-Ice-Sheet-Surface-Velocities-Known-Issues.pdf). To calculate errors, the error values within the modified Little Kluane Glacier RGI v6.0 outline were extracted and averaged to provide an overall value (Appendix 3-E). The ITS_LIVE point comparison tool (https://itslive-dashboard.labs.nsidc.org/) was used to download velocities at specific locations along the glacier's surface (Fig. 3-1). The separation time was limited to between 0 and 200 days to focus on short-term velocity peaks. Winter (January-May) RADARSAT-2 ultra-fine image pairs were acquired by Parks Canada to generate surface velocity maps (Appendix 3-F). The majority of the image pairs have 24-day separation (RADARSAT-2 repeat orbit interval), although a few sets have 48-day separation due to acquisition conflicts.

Multiple field visits were made to Little Kluane Glacier between 2018 and 2022 to observe surface conditions and the evolution of the glacier during and after the 2013-18 surge. This included validation of the terminus and moraine positions identified in satellite imagery, ground-based

surveys to measure ice thickness, and observations of the changes in crevassing, supraglacial hydrology and surface elevation over time.

3.3.2 Terminus length and position

Terminus positions were mapped from 1947 to 2021 using a combination of historical air photos (1947-77) and optical satellite imagery (1972-2021) (Appendices 3-B and 3-C). These nadir photos were georectified to a Sentinel-2 base image acquired on August 30, 2021, using distinctive bedrock and topographic features as tie points. A minimum of 20 tie points were used to align each of the historical photos, although more were used if the image covered a larger area. Based on a comparison of fixed landmarks with cloud-free, snow-free Sentinel-2 imagery, the estimated georectification error averaged 13 m.

A combination of satellite imagery was used to track changes in the terminus position of Little Kluane Glacier from 1972-2021 (Appendix 3-C). Terminus positions were traced manually, and the distance of the glacier terminus to a fixed reference line at the valley mouth close to Kluane Glacier was measured (Fig. 3-1). The maximum terminus extent was measured in each image, rather than an average across the glacier's width, as the terminus is narrow and typically well defined. However, there were limiting factors in the terminus position mapping, including the relatively low resolution of early imagery (1972-2000), shadowing from surrounding mountains, and extensive debris cover over the lowermost glacier. To maintain consistency, the same person manually created all termini outlines, with uncertainties determined using the method described by Paul and others (2013). It is assumed that outline errors are equal to at least one pixel, resulting in a range in uncertainty from 3 – 60 m, with an average of 16.5 m as imagery is heavily skewed towards newer observations from higher resolution imagery.

3.3.3 Supraglacial hydrology and surface features

The surface morphology of Little Kluane Glacier, including crevassing, supraglacial hydrology, and moraine positions, was characterized using the georectified nadir air photos and optical satellite imagery from 1951-2020 (Appendices 2-B and 2-C). These were used to identify and measure temporally consistent supraglacial hydrologic features such as surface channels and lakes, and how supraglacial drainage patterns evolved before, during and after a surge. The supraglacial lakes were outlined in RapidEye imagery in 2016 using the same process as the terminus positions,

and area uncertainty was assumed to be as high as 5%, ranging from 276 – 1628 m^2, as determined using the Paul and others (2013) method (Appendix 3-G).

The location and evolution of a series of looped moraines along the surface of Little Kluane Glacier were mapped in ~10-year intervals during quiescent periods, and as often as monthly during surge periods when suitable imagery was available. During quiescence, moraine positions were mapped from May to September, as snow often obscures the features at other times of the year. However, during surge periods it was possible to also map changes in moraines during the winter months. Changes in moraine position were quantified in relation to a set point up-glacier of the initial position of each moraine loop. Uncertainties in moraine locations are assumed to be within one pixel in the imagery used to map their position, following the methodology used for the terminus outlines (Paul and others, 2013), equating to 10 – 60 m during quiescent periods and 3 – 10 m during surge periods.

3.3.4 Digital Elevation Model (DEM) Analysis

To compute surface elevation change over the period 2001-2019, the earliest ASTER DEM was subtracted from the most recent post-surge DEM to generate a DEM of Difference (DoD). Glacier surface elevation change was extracted at 10 m intervals along south and north arm centrelines (Fig. 3-1), and smoothed using a 300 m moving window to reduce noise. Mountains surrounding the glacier are steep, leading to data gaps and high comparative errors in these regions, although relative patterns on the glacier surface are clear. Changes in surface slope during the most recent surge were examined using a SPOT DEM (03-09-2010), and WorldView DEM (17-07-2016) (Table S4). Ice rim heights were estimated by extracting and analyzing elevation points from the 22-08-2020 DEM.

3.3.5 Winter velocity mapping

Knowledge of winter velocities was required as glacier surges often initiate in the late winter or early spring in the study region. These were derived from SAR imagery as feature-tracking velocities computed from optical imagery, such as those provided through ITS_LIVE, are unreliable over short periods in the winter when visible features on the glacier surface are obscured by snow, shadow, and/or low light levels. SAR imagery also delivers accumulation-area velocities, which can be difficult to detect in optical imagery. Speckle-tracking was performed on winter (January-May) RADARSAT-2 ultra-fine image pairs to generate surface velocity maps (Table S5).

GAMMA software was used to process the SAR image pairs, as it provides velocity results similar to other speckle-tracking methods previously applied in northern and western Canada (Waechter and others 2015; Van Wychen and others 2018). Based on co-registered backscatter intensity images, a patch intensity cross-correlation was used to determine displacement in the azimuth and range directions from the offset between corresponding pixel blocks in each image pair (Lu and Veci, 2016).

Displacements were reprojected into UTM zone 7N, normalized to values of m a^{-1}, and progressively filtered to remove noise and mismatches. Custom R and Matlab scripts, as well as ArcGIS tools, were used to filter and post-process the displacements. Coarse filtering was used to retain values between 5 m a^{-1} and 5000 m a^{-1}, which represented the lower detection limit and maximum velocities previously measured in the St. Elias Mountains, respectively (Waechter and others, 2015). A custom Matlab script was used to automatically filter the data based on flow direction, where values that differed by >50° from the mean direction of neighbouring cells were discarded (Main and others, 2022). Where multiple image pair results from the same winter existed, overlapping values were averaged to produce a single velocity value, and Inverse Distance Weighted (IDW) interpolation was used to fill minor gaps (<250 m). The results were clipped to a modified Randolph Glacier Inventory version 6.0 outline, with Little Kluane Glacier separated from Kluane Glacier. Following a similar methodology to that used by Waechter and others (2015), velocities were extracted at 50 m intervals along centrelines (Fig. 3-1) and smoothed using a 100 m moving window.

Variations in the satellite orbital model, poor image co-registration, DEM/cross-correlation errors, and layover or foreshortening effects in SAR imagery can create errors in speckle-tracking results (Schellenberger and others, 2016; Van Wychen and others, 2018). To quantify these errors, the apparent motion over stable ground was determined outside of a buffer of 100 m around the modified RGI v6.0 outline. The apparent motion is the average speed of all stable ground pixels, irrespective of x or y direction. We assume that this represents the uncertainty, with values ranging between 3 and 6 m a^{-1} for the 2014-20 RADARSAT-2 data (Table S5).

3.4 Results

Results from this study are presented both chronologically and by dataset, from the earliest available results to the most recent.

3.4.1 Terminus position

The oldest available imagery of Little Kluane Glacier, a RCAF photo from 1947, indicates that the glacier terminus once pushed into Kluane Glacier, displacing the adjacent ice, and creating a slight bulge (Fig. 3-2a). This photograph only includes the lowermost section of the terminus of Little Kluane Glacier, with the bulge appearing to contain mainly dead ice as demonstrated by significant debris cover, potholes in the surface, and a lake and river near the valley mouth. This suggests that the last surge of Little Kluane Glacier occurred some years before the image was acquired.

From 1947-63, the terminus retreated by up to ~2 km. From 1963 until the late 1990s, the terminus retreated gradually, with a total retreat of ~300 ± 50 m (~5.7 ± 1.5 m a^{-1}) (Figs. 3-2b and 3-2d). From 1998-2013, the rate of terminus retreat increased significantly, with a total loss of ~1600 ± 20 m (~107 ± 1.3 m a^{-1}). The terminus advanced ~240 ± 15 m between 2015 and mid-August 2017 then remained stable until the end of May 2018, when thickening at the terminus began. After this, the terminus advanced by 2.2 km, stagnating by September 2018 (Fig. 3-2c). Following surge termination in 2018, the terminus position was ~2.9 ± 0.013 km short of its maximum position in 1947. From 2018-22, the terminus remained mostly stagnant, with minor variations (within 70 m), although debris cover and shadowing made it difficult to detect small scale changes.

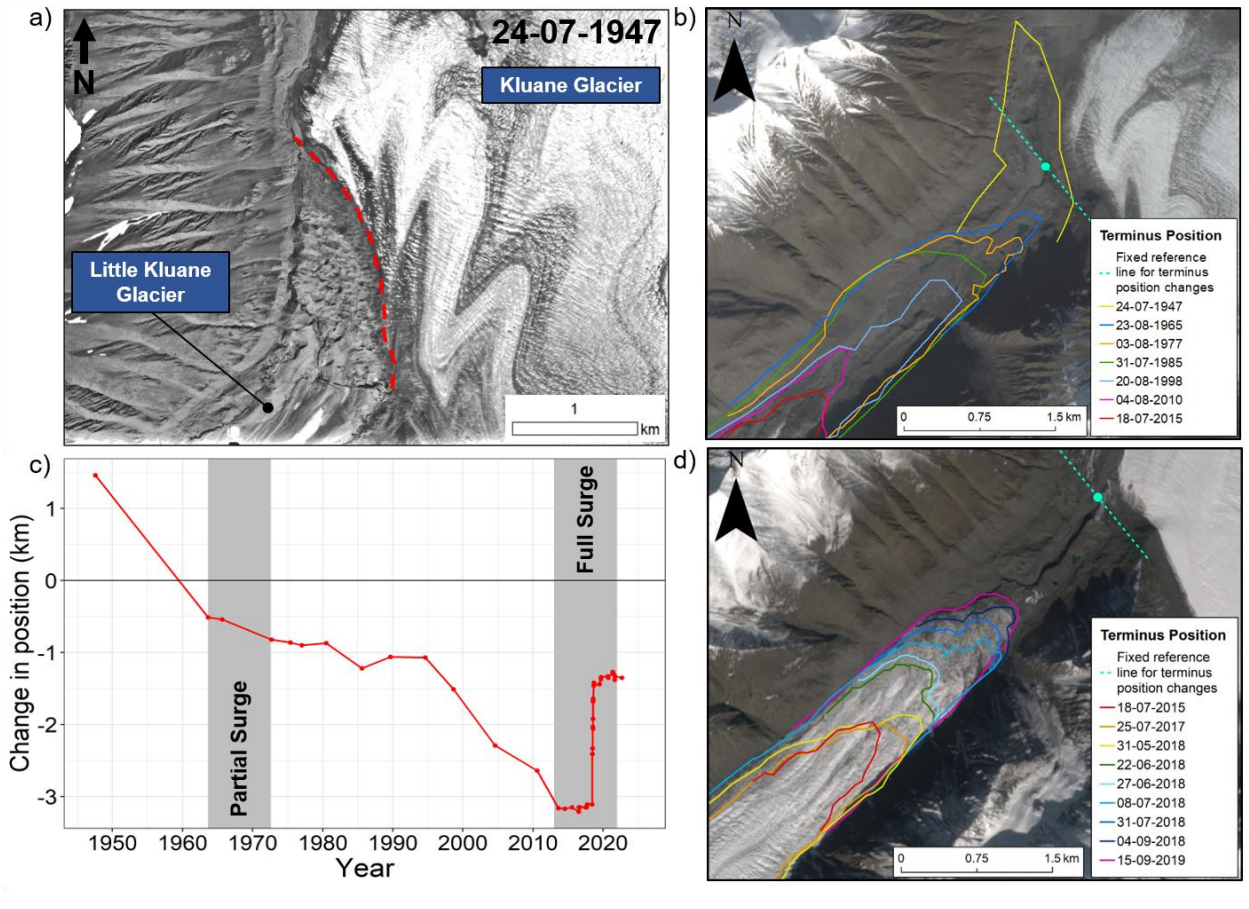

Figure 3-2: a) RCAF air photo from 24-07-1947, demonstrating how Little Kluane Glacier previously pushed into Kluane Glacier (image ID A11014-275). Red dashed line indicates the separation between Little Kluane and Kluane glaciers; b) Terminus positions of Little Kluane Glacier from 1947-2015. Projection: UTM 7N. Base image: Sentinel-2, 24-09-2016; c) Change in relative terminus position from 1947-2021 in relation to distance from valley mouth. Timing of partial surge (possible initiation range) and recent full surge are highlighted in grey; d) Terminus advance between 2015-2019, during recent surge. Base image: Sentinel-2, 30-08-2021.

3.4.2 Surface features

There were distinct changes in the crevassing and supraglacial hydrology of Little Kluane Glacier over the study period (Appendix 3-H). From 1977 until 2012 the surface was relatively smooth, with a ~1 km long supraglacial channel and small supraglacial lakes present on the surface of the north arm in the accumulation zone (Figs. 3-3a and 3-3b). This supraglacial channel remained in approximately the same position over several decades, as it was visible in the August 3 1977 air photo, as well as in later imagery up to 2013.

In 2013 crevasses were present over a small area of the upper north arm, as was the supraglacial channel (Appendix 3-Hc). By 2015, significant crevassing had appeared (Appendix 3-Hd) in an area where, in 2012, the surface was smooth and uniform with a dome-like accumulation of snow and ice (Appendix 3-Hb). There was a progressive increase in the intensity of crevassing from 2015 to 2016 (Appendix 3-Hd and e), and by mid-June 2016 the supraglacial channel had been interrupted near its head by new, larger crevasses. Extensive crevassing covered nearly the entire surface of the upper north arm (i.e., accumulation zone) to the connection with the main glacier trunk by June 2016. Crevassing in the south and upper arms was delayed by approximately a year compared to the north arm: in 2013-14 there was limited crevassing in the south and upper arms, followed by an increase in intensity from 2016-17, and finally a peak in crevassing intensity and extent by September 2018. Crevassing in the main glacier trunk began to increase in intensity between February and June 2018, was extensive by July 2018 (Fig. 3-3), and peaked in September 2018.

Starting in June 2016 two supraglacial lakes (Fig. 3-3) formed below the north arm-main trunk connection, in an area where no lakes were observed in prior imagery. The lakes reached a maximum size of ~17400 ± 860 m^2 on June 18, 2016, and ~32600 ± 1630 m^2 on June 29, 2016, and had almost completely drained by late July that year. Heavy cloud cover in May and June 2017 made it difficult to monitor the lakes during this period, and only the west lake was observed to redevelop. By July 2017, the glacier morphology had significantly changed, and the east lake did not develop. From mid-July until mid-August 2017 the west lake decreased in area, although due to its small size the uncertainty estimates are too high to produce reliable quantitative estimates of its area. By September 2017, the west lake had completely drained. In 2018 the lakes again formed in approximately the same positions, but were surrounded by significant crevassing and additional

ice from the north arm (Fig. 3-3c). RapidEye imagery from July 27 and 28, 2018, show that the east lake drained entirely within a single day (Fig. 3-3b-c).

There were four teardrop-shaped moraines visible in the 1951 air photos, which can be interpreted as the product of past surges (Fig. 3-4a) (Meier and Post, 1969; Young and others, 2022): these features were located on the north side of the glacier, were relatively evenly spaced apart, and had similar structural appearances. Between 1972 and 1977, a new looped moraine (E) was created (Fig. 3-4b, 3-5). The oldest looped moraine, 'A', was visible in the record until 1994 (Fig. 3-4c), when it reached the terminus. The three moraine loops (C, D and E) moved a maximum of ~1 km over the 43-year period from 1972-2015 (Fig. 3-4e), with higher velocities up-glacier and an average of 25 m a^{-1}.

After 2015, a new moraine loop (F) was formed via the transfer of ice from the north arm to the main glacier trunk between October 2015 and February 2016 (Figs. 3-4d, 3-5). Due to poor image quality during the winter it is difficult to pin-point exact timing, but movement of the new bulge (moraine F) continued until September 2016 (Fig. 3-5f), and then slowed for most of 2017 (Fig. 3-5g). The largest displacement occurred between November 2017 and June 2018 (Fig. 3-5h-k), slowing in August 2018 to background velocities through 2019 (Fig. 3-5j-l). Existing moraine loops C, D and E were each transported approximately 1.7 km down-glacier during this period (Fig. 3-4e). Loop B (the second oldest moraine visible beginning in 1951) was no longer visible on the glacier after 2019.

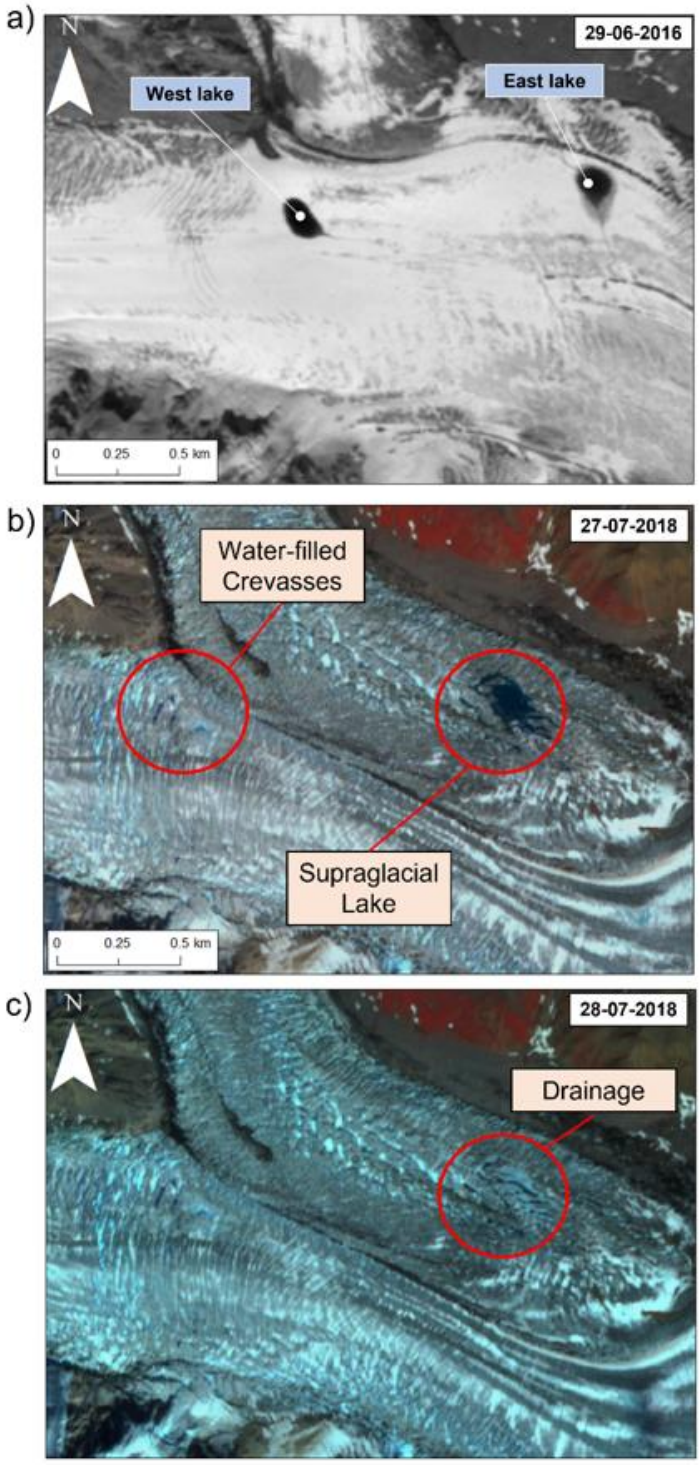

Figure 3-3: a) Supraglacial lake locations in 2016 (Fig. 3-7), on the surface of Little Kluane Glacier on 29-06-2016, during the active surge; b) Location of water-filled crevasses and supraglacial lake, on 27-07-2018; c) One day later on 28-07-2018, showing partial drainage of these features. Satellite images courtesy of Planet Labs.

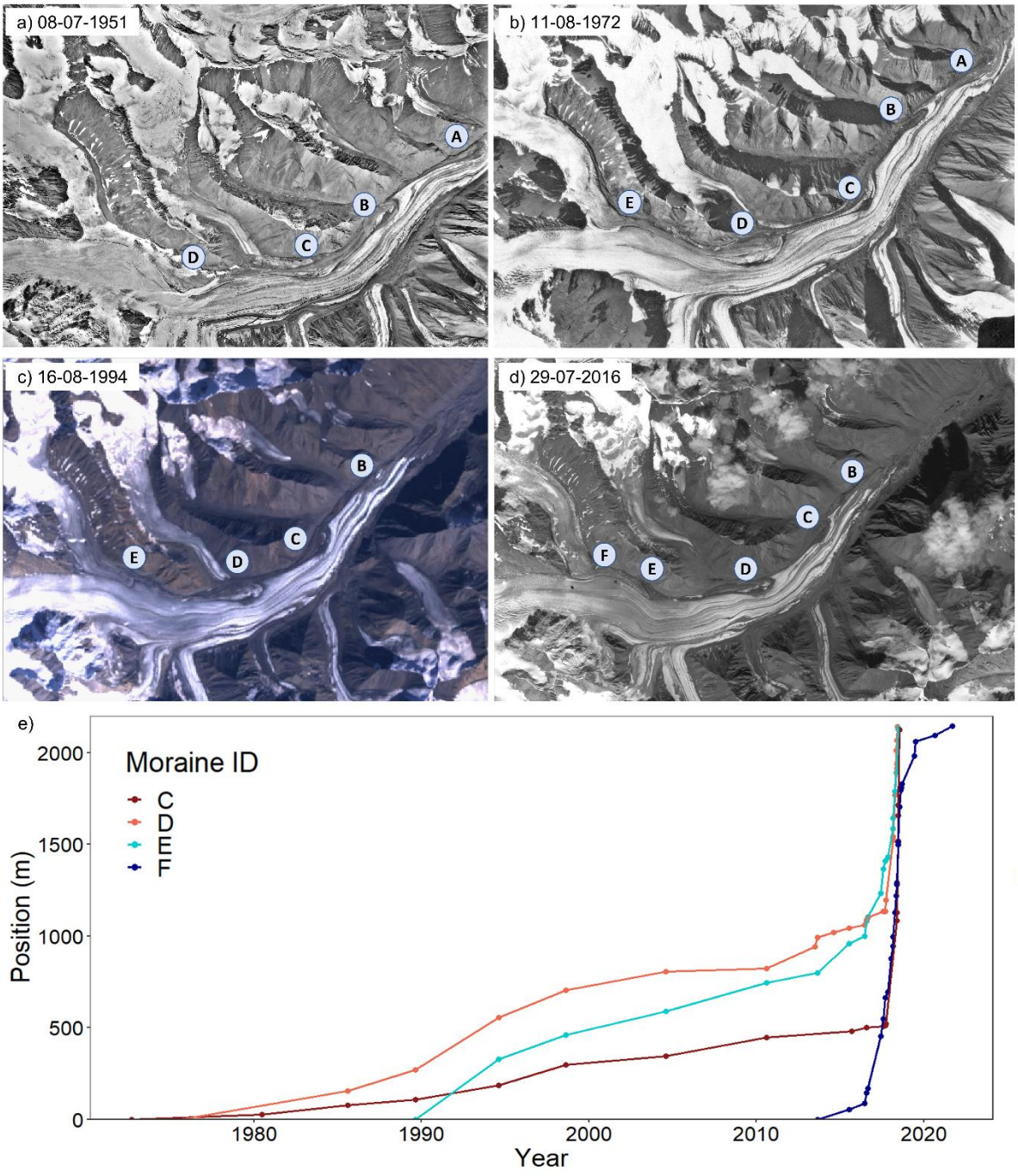

Figure 3-4: Looped moraine positions for each decade at Little Kluane Glacier in historical air photos (a-b) and satellite imagery (c-d) (listed in Table S1); a) 08 July, 1951; b) 11 August 1972; c) 16 August 1994; d) during surge initiation, 29 July 2016. Air photos are courtesy of the National Air Photo Library, Ottawa; e) Looped moraine movement from 1972-2021. Moraines A and B are not included as they disappear before the recent surge.

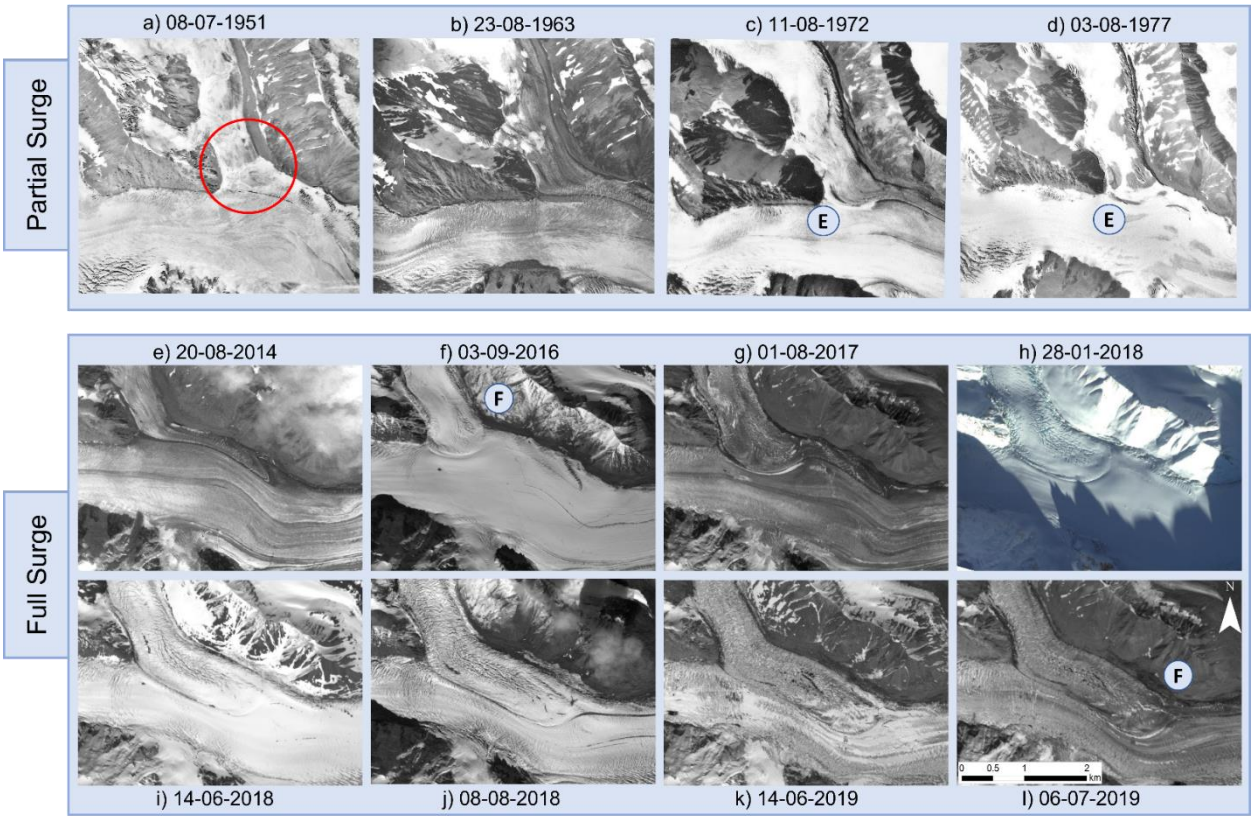

Figure 3-5: a-d) Comparison of air photos of the medial moraine at the junction of the north arm and main trunk of Little Kluane Glacier, showing the movement of mass during the partial surge. a) Prior to the partial surge on 8 July, 1951, with red circle indicating area of interest; b) A similar moraine pattern to that in 1951, still prior to the partial surge, 23 August, 1963; c) After partial surge, 11 August, 1972. Label E shows the initial formation of looped moraine from the partial surge; d) After partial surge, with minimal change and lack of initiation into full surge, 3 August, 1977.

e-l) Comparison of RapidEye satellite imagery of the medial moraine separating the north arm from the main trunk of Little Kluane Glacier, showing the movement of mass during the 2013-2018 full surge. Label F shows the initial formation of looped moraine F and its location at the end of this timeseries. e) Prior to the surge on 20 August, 2014; f) During surge initiation on 3 September, 2016; g) 1 August, 2017; h) 28 January, 2018; i) 14 June, 2018; j) 8 August, 2018; k) 14 June, 2019; l) After full surge, 6 July, 2019. Images are courtesy of Planet Labs.

3.4.3 Surface elevation changes

Changes in the surface elevation of Little Kluane Glacier between 2001 and 2019 indicate a transfer of mass from the top of the north arm and the main glacier trunk (over an area of ~27.5 km^2) into the terminus region, resulting in an overall thickening of ~100 to 170 m in the lower 2.5 km of the glacier over an area of ~7.3 km^2 (Fig. 3-6). There was a corresponding thinning of up to ~90 m in the upper north arm basin (Fig. 3-6), which is evident from a stranded ice rim that remained attached to valley walls (Appendix 3-I). In contrast, the upper arm and the uppermost region of the south arm (12-17.5 km up-glacier) remained relatively stable, with the main mass movement occurring from the main glacier trunk (~15-11 km from terminus) (Fig. 3-6b). Thinning of the south arm was more limited in area and intensity, with losses up to 70 m along the south arm centreline (Fig. 3-6b). There is also evidence of localized thickening where the valley narrows, such as at the confluence between the north arm and the main glacier trunk.

Over the period 2010-16 there were localized changes to the glacier surface slope. Specifically, the slope in the confluence region of the north arm with the main trunk reversed between 2010 and 2016 (Fig. 3-7a). In 2010, the slope of line A-A' was 4.5%, and B-B' was 5.2%, while in 2016 the reversed slope section of the survey line (Figs. 3-7c and 3-7d) had a slope of 2.5% and -9.3%, respectively. The reverse slope created a ~0.13 km^2 basin (west lake).

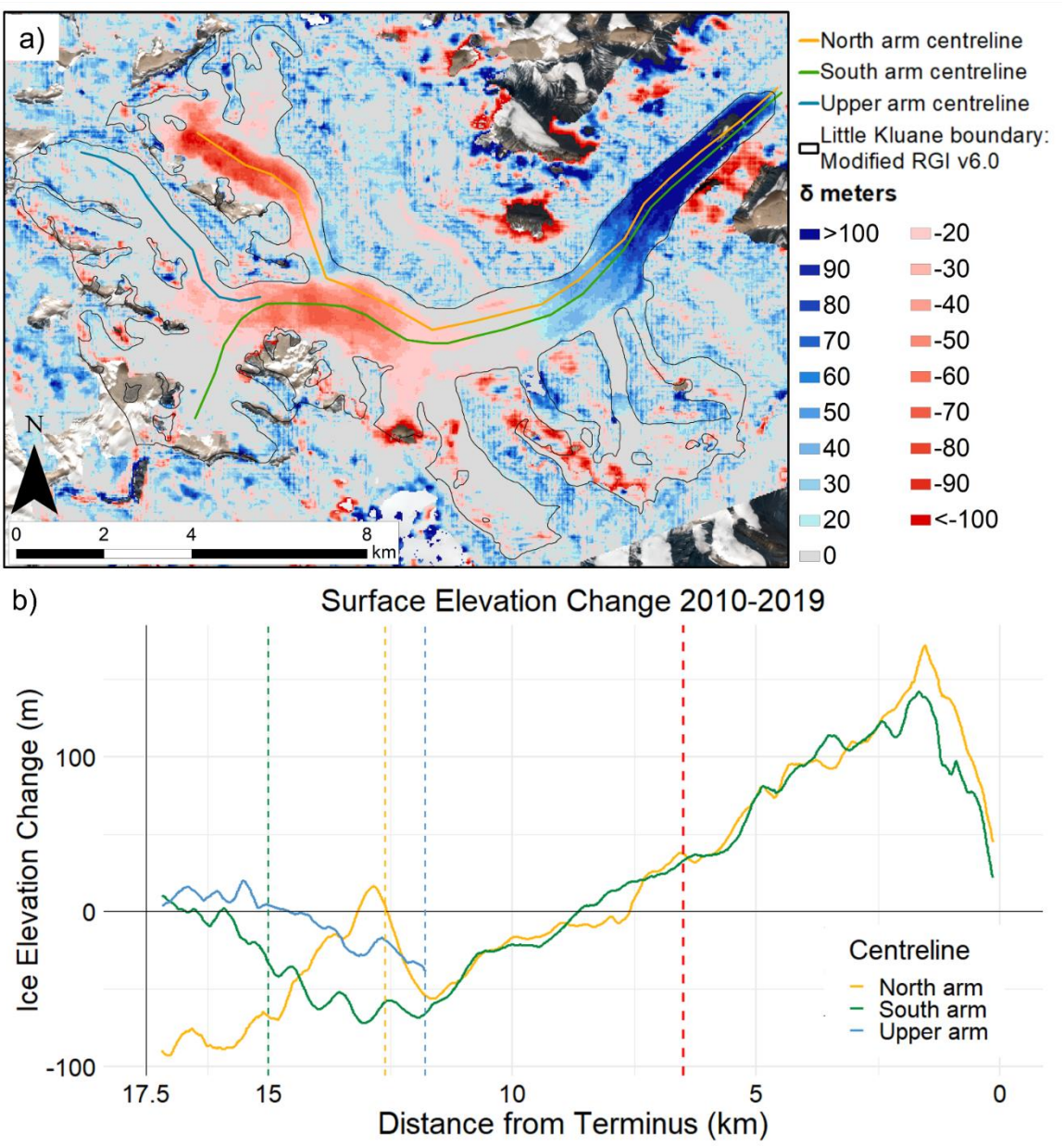

Figure 3-6: a) Elevation change across Little Kluane Glacier between 2010 and 2019, with overlain modified RGI 6.0 glacier outline and 2018 terminus extent. Projection: UTM 7N. Base image: Sentinel-2, 3 August, 2019; b) Little Kluane surface elevation change derived from a DEM of Difference between 2010 and 2019; dashed blue, green and yellow lines indicate where the respective arm connects to the main glacier trunk. Dashed red line indicates the location of the Dynamic Balance Line (DBL).

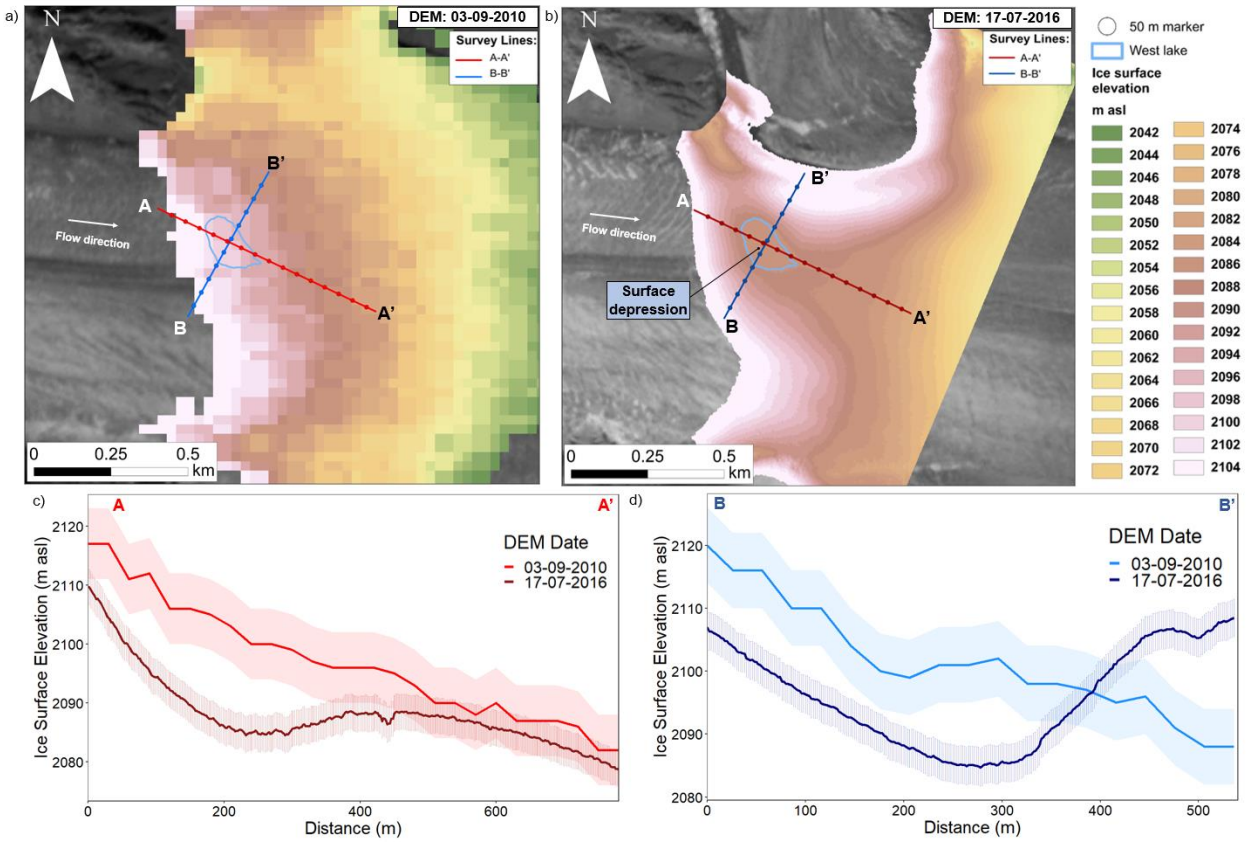

Figure 3-7: Changes in glacier surface topography after surge initiation. General location is indicated by red dashed box on Figure 1. a) SPOT DEM of glacier surface on 03-09-2010 prior to surge initiation. Background image: RapidEye, 06-08-2013; b) WorldView DEM of glacier surface on 17-07-2016, as mass moves from the north arm to the main trunk of Little Kluane Glacier, demonstrating a reverse slope and resulting depression; c) ice elevation profiles of survey line A-A' in 2010 and 2016; d) ice elevation profiles of survey line B-B' in 2010 and 2016. Satellite images courtesy of Planet Labs. The relationship between ice elevation and supraglacial lake location is only shown for the west lake, as DEM coverage does not extend to the east lake.

3.4.4 Surface velocities

Annual average velocities obtained from the ITS_LIVE dataset (Fig. 3-8) revealed three main dynamic phases over the period 1985-2013. First, there was a higher velocity period from 1985-96, where velocities in the main trunk ranged from ~40-70 m a^{-1}, with lower (<25 m a^{-1}) velocities in the north arm. This was followed by a lower velocity period from 1997-2012, when velocities across the glacier centreline averaged 10 m a^{-1}, and never exceeded 50 m a^{-1}. Finally, during the third period from 2013-18 maximum annual average velocities progressively increased, beginning at ~40 m a^{-1} in 2013, ~70 m a^{-1} in 2014, ~100 m a^{-1} in 2015, ~260 m a^{-1} in 2016, ~375 m a^{-1} in 2017, and finally ~830 m a^{-1} in 2018 (Fig. 3-8 and Appendix 3-J). Velocities increased first in the north arm, followed by the main glacier trunk (Appendix 3-Ja). Both the upper and south arms of the glacier retained relatively stable velocity patterns compared to the north arm and main trunk, with modest increases occurring mainly from 2016-18.

Point measurements from ITS_LIVE image pairs (Fig. 3-1) indicate increasing velocities from 2016 through 2018 (Appendix 3-J). Mean velocity of points located in the north arm (Appendix 3-Ja) showed steady increases through 2016, followed by slight decreases in 2017, before peaking in fall 2018. Velocities in the main trunk increased progressively towards the terminus, with a point ~12 km up-glacier from the terminus (point 3) increasing in speed approximately one year prior to a point ~8 km up-glacier from the terminus (point 2), and two years prior to a point ~4 km up-glacier from the terminus (Point 1) (Appendix 3-Jb). Mean velocities in the main trunk were steady from 2014-16 (<100 m a^{-1}), increased in 2017, and peaked at ~3600 m a^{-1} near the terminus in fall 2018 (Appendix 3-Jb).

RADARSAT-2 wintertime velocities indicate increased ice motion along the north arm centreline from 2014-20 (Fig. 3-9). In the upper accumulation zone of the north arm, velocities increased over 4 years, from 2014-17 (Fig. 3-9b). In the main glacier trunk, velocities remained stable (~40 m a^{-1}) through 2014-15, then increased in 2016 and 2017, before decreasing to background levels in 2020 (Fig. 3-9a). The highest winter velocities (~1000 m a^{-1}) were recorded ~5 km up-glacier from the terminus in early 2018 (Fig. 3-9a).

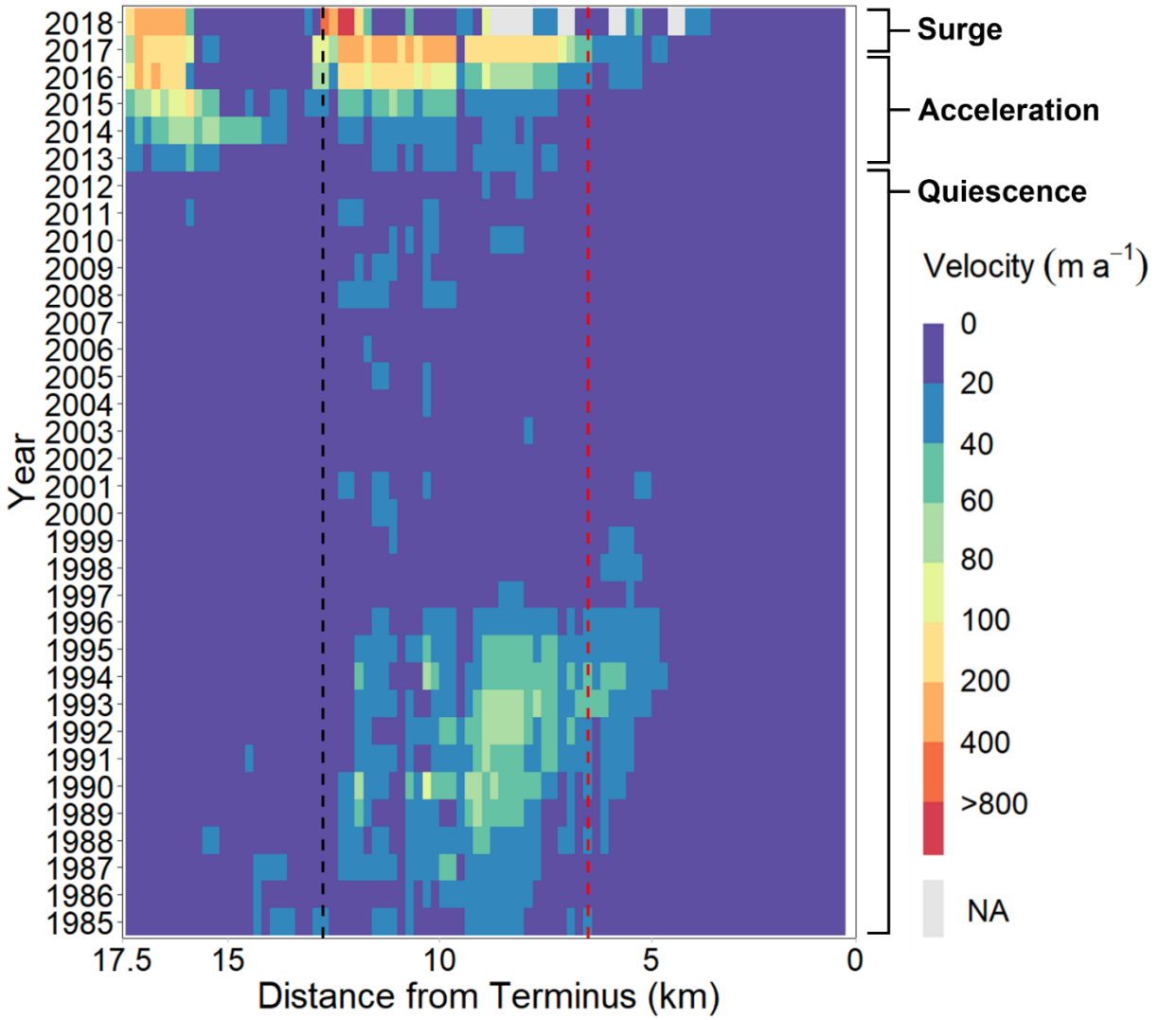

Figure 3-8: ITS_LIVE velocities along the north arm centreline of Little Kluane Glacier from 1985-2018 (see Fig. 3-1 for location). Dashed black lines indicate where the north arm joins the main glacier trunk. Dashed red line indicates location of the Dynamic Balance Line (DBL).

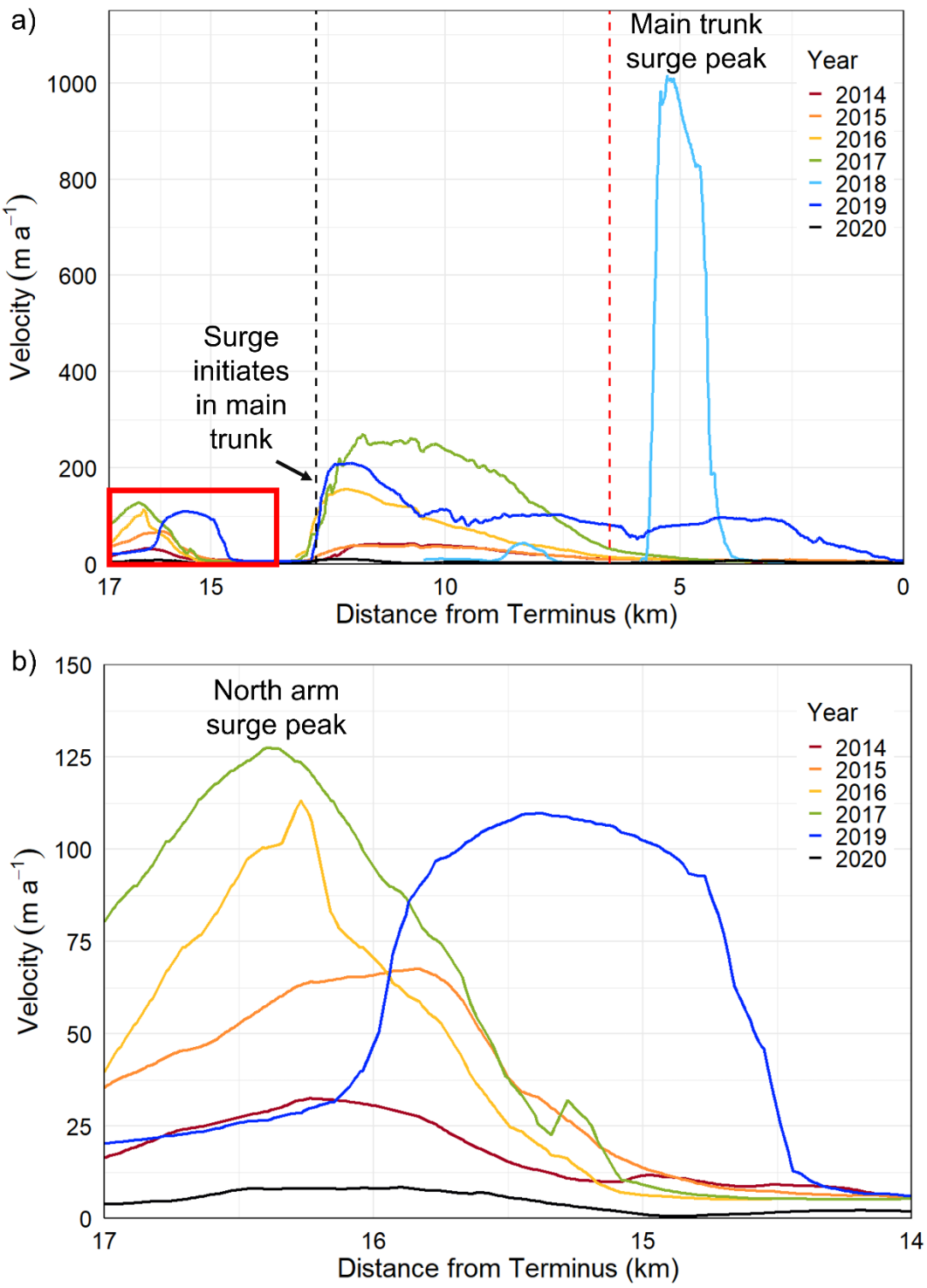

Figure 3-9: a) Winter (January-May) velocities from RADARSAT-2 data along the north arm centreline of Little Kluane Glacier, 2014-20. Red box indicates location of zoomed in section in part b). Dashed black lines indicate where the north arm joins the main glacier trunk. Dashed red line indicates the location of the Dynamic Balance Line (DBL); b) Zoom-in to show velocity details for the north arm of Little Kluane Glacier from 2014-19. Note: there is no data from 2018.

3.5 Discussion

Our measurements indicate that Little Kluane Glacier underwent a full surge over the period 2013-18, with substantial relative changes in terminus position, supraglacial hydrology, crevassing, surface elevation and ice velocities. Another full surge did not occur during our observation period between 1947 and 2013, although there is evidence that a partial surge occurred during the 1960s-70s, and that multiple surges occurred prior to 1947. We review the evidence for these events chronologically below.

3.5.1 Pre-1947 surges

The presence of large, looped moraines on the glacier surface suggest that at least 4 surges occurred prior to 1947. The spacing between each looped moraine increases from the terminus through the main trunk, from ~1100 m between loops B and C, to ~2500 m between loops D and E in 2013, reflecting a more compressive flow regime toward the terminus. The distance between the moraines has remained mostly consistent since 1972, with only a slight decrease in distance (~200 m) between moraines closer to the terminus. Observations from the 1960-70's partial surge (section 5.2) and 2013-18 full surge (section 5.3) indicate that these looped moraines form from the episodic movement of mass from the north arm into a slower moving main glacier trunk (Fig. 3-5). A similar but increasing distance occurs between each loop, suggesting a regularity in the occurrence of past surges. From 1989 to 2010, moraine loop B flowed down-glacier at an average rate of ~35 m a^{-1}, loop C at ~15 m a^{-1}, and loop D at ~25 m a^{-1}. If we take the average of this motion of 25 m a^{-1}, and use a contemporary glacier length of 17 km, this means that at least 4 partial or full surges must have occurred in the ~70 years prior to 1947 to produce them, assuming that mass balance and velocity conditions have remained relatively constant.

Studies from other glaciers have shown that potholes begin to form on the ice surface as early as 4 years after surge termination (Sturm, 1987; Partington, 2023). If we assume that the last full surge prior to 1947 behaved similarly to the 2013-18 full surge, then by comparing the development of the surge bulge with the well-developed pothole and surface channels covering the dead ice zone at the glacier terminus in 1947 (Fig. 3-2a), we suggest that the pre-1947 surge likely occurred within the prior decade. This means that there was a period of at least 70 years between the two most recent full surges. In Figure 3-2a, the terminus extends ~2.5 km further than

the most recent advance; this might have been caused by a greater pre-surge extent, a larger pre-1947 surge, or a combination of both scenarios.

3.5.2 1960-70's partial surge of Little Kluane Glacier

Although no full surge occurred between 1947 and 2013, there is still evidence of dynamic variability during this time. Historical air photos demonstrate that the north arm pushed into the main trunk of Little Kluane Glacier between 1963 and 1972 (Fig. 3-5), although the terminus did not advance during this time, instead following the long-term pattern of >4 km retreat between 1947 and 2013 (Fig. 3-2d). This mass movement created moraine E (Fig. 3-4b, 3-5c), although it is smaller and more elongated compared to the other moraine loops, such as loop D.

Partial surges are described by Sund and others (2009) as a phenomenon when a mass movement occurs but does not instigate a terminus advance. In terms of their proposed surge stages, this refers to when a surge does not develop past stage 2, where there is surface lowering in major parts of the reservoir zone and thickening in the receiving zone, but there is no pronounced acceleration across most of the glacier surface, nor is there a terminus advance. Sund and others (2009) hypothesize that surge-type glaciers may oscillate between weaker, partial surges and more developed, full surges, and that this behaviour may explain the long build-up phase of some glaciers. They argue that while small and partial mass movements from the reservoir zone may initially delay a full surge, they could also promote a large surge through the slower, more stable, and potentially enhanced buildup of ice mass.

Between 1963 and 1972, there was a mass movement originating from the north arm to the main trunk of Little Kluane Glacier that displaced the medial moraine by ~250 m (Fig. 3-5); however, this did not develop into a full surge by 1977, with the bulge remaining in essentially the same position and no evidence of glacier acceleration or terminus advance (Fig. 3-5d). Changes in glacier surface morphology, including curved or displaced medial moraines have been used to identify partial surges in Svalbard (Sund and others, 2009, 2014) and the Pamirs (Kotlyakov and others, 2008; Shangguan and others, 2016). We therefore interpret this as being a partial surge of Little Kluane Glacier. This event formed a new moraine loop (loop E, Fig. 3-5b-d).

3.5.3 Characteristics of the 2013-18 surge

The 2013-18 surge of Little Kluane Glacier was driven primarily by the transfer of a large mass of ice from the north arm that prompted a surge in the main trunk. The extensive photographic,

velocity and elevation records for this glacier provide insights into surge-related processes, including the interplay between surface topography and hydrology. Increased velocities in 2013 provided the first signal of the impending surge, followed by intensifying crevassing through 2015 and 2016, which interrupted a prominent supraglacial channel near the head of the north arm (Appendix 3-H). As velocities and strain rates increase at the start of a surge, the larger stress results in intense crevassing, enhancing distributed water access to the glacier bed that may further increase velocities due to the reduction in basal friction, thereby establishing a positive feedback (Dunse and others, 2015; Gong and others, 2018). For Little Kluane Glacier, this increased crevassing appears to have caused the supraglacial hydrological network to change from a concentrated to a distributed system (Appendix 3-H), which over time may have influenced the englacial and subglacial hydrologic networks, as surface water was no longer entering the glacier interior and bed from a single point (Shepherd and others, 2009), but instead through multiple locations (Colgan and others, 2011). As there is a delay between the increased velocities beginning in 2013 and the mass movement in 2016, we hypothesize that the evolution of the surficial hydrological network resulted in an increasing volume of water at the glacier bed, thereby increasing basal sliding, and enhancing the movement of mass from the north arm to the main trunk of the glacier.

At Little Kluane Glacier, changes in surface slope and supraglacial hydrology at the junction between the north arm and main trunk may also play a role in defining whether a partial surge of the north arm develops into something closer to a glacier-wide surge. Glacier velocities in the main trunk began to increase noticeably in 2015, a year after velocities increased in the north arm (Fig. 3-8 and Appendix 3-J). Beginning in early winter 2016, movement of a large ice mass occurred from the north arm to the main trunk. The addition of this mass changed the surface topography of the main trunk above the confluence with the north arm, and created a reverse surface slope, allowing surface water to pool and form supraglacial lakes in 2016, which reformed and drained throughout 2017 and 2018 (Figs. 3-3, 3-7). The following winter (2018), the glacier entered the fast, active phase (Appendix 3-Jb), first increasing in velocity near the confluence with the north arm (Appendix 3-Jb, point #3), with the surge then propagating down-glacier. The formation and drainage of these lakes over several years, combined with incrementally increasing glacier velocities (~155 m a^{-2}) over a 3-year period suggest that there may have been a slow, and then rapid, shift between subglacial drainage configurations, whereby significant, localized water input

to the bed over multiple seasons may have eventually overwhelmed the subglacial drainage network and provoked acceleration, until an efficient drainage network was able to form and evacuate the water (Kamb and others, 2015). Sund and others (2014) suggested that a tributary is able to initiate a surge in the main trunk only if the main trunk was already in stage 1 or 2, and thus ready to reach the final surge stage. However, at Little Kluane Glacier, we hypothesize that the main trunk becomes topographically and hydrologically primed for the final surge stage over a period of several years prior to the secondary surge initiation. In the absence of subglacial hydrological observations, we cannot definitively show that the change in surface morphology or hydrology (e.g., formation of supraglacial lakes and water-filled crevasses) drove the main trunk into a surge, although this may be a process that could be observed during tributary-trunk surges on other glaciers.

In 2018 the surge front reached the glacier terminus region, and surface velocities peaked at ~1000 m a^{-1} during the winter (Fig. 3-9) and ~2200 m a^{-1} near the end of summer (Appendix 3-Jb). The terminus began to advance in May 2018, which coincided with the highest recorded point velocity of ~3600 m a^{-1} approximately 4.5 km up-glacier from the terminus (Figs. 3-2, Appendix 3-Jb). The terminus underwent a total advance of ~2.2 km over spring and summer 2018 (Fig. 3-2c), at a mean rate of 18 m d^{-1}. Similar to other glaciers in the region including Klutlan, Variegated and Bering (Altena and others, 2019; Jay-Allemand and others, 2011; Burgess and others, 2012), Little Kluane displayed a winter initiation, with the highest velocities occurring for a short period during the summer, and the surge terminated abruptly toward the end of the melt season. Considering the above characteristics, along with the already-discussed evidence of subglacial hydrological processes, we suggest that Little Kluane Glacier most closely resembles surges controlled by changes in basal water pressure, at least when considering the main trunk.

After the surge event, it is possible to classify zones of the glacier based on changes in surface elevation: we consider the region >10 km up-glacier from the terminus to be the reservoir zone (Fig. 3-6), and the zone from ~6 km to the terminus the receiving zone. The zone of minimal net surface elevation change, known as the dynamic balance line, occurs ~6 km up-glacier from the terminus. While the surge was mainly driven by ice movement from the north arm, ice mass from the south and upper arms was pulled along as the full surge developed in the main trunk, further suggesting that the main trunk was not in a surge phase prior to input from the north arm. The

minor role of the south and upper arms in the surge is demonstrated by the relatively small changes in ice surface elevation above the south arm-main trunk confluence compared to the north arm basin (Fig. 3-6), and the minor change in ice surface elevation in the upper arm (Fig. 3-7a-b).

From the data presented above, we suggest that the surging behaviour of Little Kluane Glacier follows these main phases:

1. Due to a constriction at the connection between the north arm and the main trunk (a narrow valley which is quite steep, with a trough at the bed (Appendix 3-A)), the glacier is unable to efficiently transfer mass from the north arm to the main trunk, resulting in mass accumulation within the basin during quiescence.
2. After decades of accumulation, the ice mass in the north arm becomes thick enough that glacier velocities increase. Velocities increase over a period of 2-3 years, and crevasses begin to appear, disrupting persistent supraglacial drainage channels and routing water to the glacier bed in a distributed fashion.
3. Eventually the north arm ice mass is able to overcome the resistive forces acting upon it from the valley walls, bed, and abutment with the main trunk, resulting in a large mass movement from the tributary to the main trunk. In one instance (~1963-72) this did not initiate a full surge (Fig. 3-5).
4. Instigation of a full surge of the glacier may be facilitated by mass transfer from the north arm altering the surface slope below the junction of the north arm and main trunk, as occurred around 2016 (Fig. 3-7). A surface slope reversal allows water to pool and then drain into the glacier (Fig. 3-4), possibly overwhelming the subglacial drainage system of the main trunk and initiating a surge there.
5. The surge front then propagates down-glacier, causing the terminus to advance, and driving enhanced ice motion in the south and upper arms due to a combination of longitudinal coupling with faster-flowing downstream ice, a steepening in surface slope, and a reduction in backpressure where they meet the main trunk.
6. Active surging ends as ice mass reaches the lower part of the glacier, lowering the driving stress and reducing glacier velocities to ~10 m a^{-1}. For Little Kluane Glacier, this coincided with the end of the melt season in September 2018.

7. The quiescent stage begins, and ice mass starts accumulating again in the north arm and along the main glacier trunk above the dynamic balance line.

3.5.4 Comparison of the 2013-18 surge of Little Kluane Glacier with others in the St. Elias Mountains

Surging glaciers can be difficult to characterize due to lack of high-frequency temporal data from surge initiation through termination, resulting in uncertainties concerning where surges initiate, how they progress, the length of active/quiescent cycles, and whether a surge bulge is present. In Alaska-Yukon region, 322 surge-type glaciers have been previously identified (Sevestre and Benn, 2015), with 151 in the St. Elias Mountains of Yukon alone (Clarke and others, 1986). When compared to surges of some of the other glaciers in the region with comprehensive records (Dań Zhùr, Sít' Kusá, Nàłùdäy, and Variegated), the surge of Little Kluane Glacier has a longer quiescent phase (~45 years compared to ~5-20 years for the others), and a long initiation phase (~5 years of initiation then ~1 year of intense surging, compared to 1-2 years of total active surging for the others). Several glaciers to the southeast, however, have quiescent phases exceeding 30 years. The most recent surges of Dusty Glacier (~80 km away) and Tweedsmuir Glacier (~140 km away) were <3 years in duration and preceded by quiescent intervals of ~36 years (Young, 2023) and ~34 years (Sharp, 2021), respectively. Fisher Glacier (~110 km away) had a quiescent phase of ~40 years, and an active phase of ~2.5 years, with a slow multidecadal increase in velocity between the mid-1980s and 2013 (Partington, 2023). Several smaller polythermal glaciers in the region, including Trapridge Glacier (Clarke and Blake, 1991; Frappé and Clarke, 2007) and "South Glacier" (De Paoli and Flowers, 2009), formerly surged in a manner similar to the glaciers above with multidecadal quiescent intervals, but more recently underwent prolonged "slow surges" where the high velocities associated with typical surges failed to develop.

3.5.5 Impact of geometric restrictions on glacier surging

Other studies (Jiskoot, 2011; Abe and others, 2016; Kochtitzky and others, 2019; Nolan and others, 2021) have suggested that restriction of ice flow is crucial in influencing surging behaviour of specific glaciers. The restrictions affecting glaciers can take a number of forms, including bedrock sills and overdeepenings (Jiskoot, 2011; Flowers and others, 2011; Lovell and others, 2018), constrictions in valley width (Kochtitzky and others, 2019), trunk-tributary interactions (Kotlyakov and others, 2008; Sund and others, 2009; Jiskoot and others, 2017) and icefalls (Nolan

and others, 2021). For some glaciers, these features may act as a potential barrier to efficient ice flow due to increased friction during quiescence, and hence may encourage mass (and thus, energy/enthalpy) to build up in the reservoir zone (Sevestre and Benn, 2015). For example, Eisen and others (2001) found that cumulative mass balance played a role in the duration of the surge cycle of temperate Variegated Glacier, which was influenced by the location of a bedrock sill.

At Little Kluane Glacier, we suggest that the narrow connection between the north arm and the main glacier trunk acts as a flow constriction that, along with the backstress of the much larger main trunk, restricts ice flow, allowing ice mass to build. Eventually, the ice mass accumulates sufficiently to steepen the surface slope and overcome the frictional forces at this constriction, inducing a mass movement. The size of this ice flux (either relatively small, as in 1960s-1970s, or large, as in 2013-18) results in either a partial or a full surge, which may be dependent on several factors, including the cumulative mass balance between surges, and/or the state of the subglacial hydrological network of the main trunk.

3.6 Conclusions

Little Kluane Glacier experienced a progressive increase in glacier velocities in the north arm basin from 2013-17, prior to the initiation of a full surge which occurred in 2018. A total of 6 previous dynamic instabilities were identified based on the presence of looped moraines, which includes one full and one partial surge documented here. A partial surge was identified in the mid-1960s to early-1970s, whereby mass movement was observed from the north arm tributary to the main trunk, but did not initiate a full surge and was smaller than the mass displacements that occurred during the 2013-18 surge. It appears that the narrow connection between the north arm tributary and the main trunk is important in defining the nature and extent of surges through the creation of a flow restriction. Evidence for this is provided by the initiation of the 2013-18 surge at the very top of the tributary through increased crevassing, then a mass movement from the tributary to the main trunk 2 years later, followed by a full surge in the main trunk. Additional data are needed to determine whether topographic or geometric factors are underpinning glacier surges at other locations in the St. Elias Mountains, and therefore detailed valley and bed elevation profiles are necessary to fully understand the role that geometry plays in glacier surging in this region.

This study demonstrates that unstable flow of Little Kluane Glacier depends on a number of factors which are not yet fully understood. These could include glacier geometry, whereby a partial surge

may delay a full surge by dissipating a portion of the stored energy, and therefore appear to promote conditions that favour more gradual reservoir growth. Another hypothesis is that the initial mass movement from a tributary to the main glacier trunk could initiate a full surge by producing a reverse slope that establishes the necessary conditions for water to pool on the surface, which eventually drains and overwhelms the subglacial drainage network. This may act as the trigger that enables a partial surge to evolve into a full surge affecting most of the glacier area. This study underlines the importance of data frequency and resolution when describing dynamic instabilities, and highlights that there are a variety of intersecting behaviours that can occur during a surge.

3.7 Data availability

The RADARSAT-2 glacier velocities generated for this study are available from the Polar Data Catalogue under CCIN reference number 13309. Original RADARSAT-2 data is available through MDA Geospatial Services (https://www.asc-csa.gc.ca/eng/satellites/radarsat2/order-contact.asp). All satellite imagery (Landsat, Sentinel-2, RapidEye, and Planet), air photos, and ITS_LIVE velocity products are publicly available from data sources listed in the methods.

References

Abe T, Furuya M and Sakakibara D (2016) Brief communication: twelve-year cyclic surging episodes at Donjek Glacier in Yukon, Canada. *The Cryosphere* **10**(4), 1427-1432. doi: 10.5194/tc-10-1427-2016

Altena B, Scambos T, Fahnestock M and Kääb A (2019) Extracting recent short-term glacier velocity evolution over southern Alaska and the Yukon from a large collection of Landsat data. *The Cryosphere* **13**(3), 795-814. doi: 10.5194/tc-13-795-2019

Aschwanden A, Bueler E, Khroulev C and Blatter H (2012) An enthalpy formulation for glaciers and ice sheets. *Journal of Glaciology* **58**(209), 441-457. doi: 10.3189/2012JoG11J088

Benn DI, and Evans DJA (2010) *Glaciers and Glaciation*, 2nd Edition. London, UK: Hodder Education, 789pp.

Benn DI, Fowler AC, Hewitt I and Sevestre H (2019) A general theory of glacier surges. *Journal of Glaciology* **65**(253), 701-716. doi: 10.1017/jog.2019.62

Benn DI, Hewitt IJ and Luckman AJ (2023) Enthalpy balance theory unifies diverse glacier surge behaviour. *Annals of Glaciology* **63**(87-89), 88-94. doi: 10.1017/aog.2023.23

Bevington A and Copland L (2014) Characteristics of the last five surges of Lowell Glacier, Yukon, Canada, since 1948. *Journal of Glaciology* **60**(219), 113-123. doi: 10.3189/2014JoG13J134

Burgess EW, Forster RR, Larsen CF and Braun M (2012) Surge dynamics on Bering Glacier, Alaska, in 2008-2011. *The Cryosphere* **6**, 1251-1262. doi: 10.5194/tc-6-1251-2012

Clarke GKC and Blake EW (1991) Geometric and thermal evolution of a surge-type glacier in its quiescent state: Trapridge Glacier, Yukon Territory, Canada, 1969–89. *Journal of Glaciology* **37** (125), 158–169. doi: 10.3189/S002214300004291X

Clarke GKC, Schmok JP, Ommanney SL and Collins SG (1986) Characteristics of surge-type glaciers. *Journal of Geophysical Research: Solid Earth* **91**(B7), 7165-7180. doi: 10.1029/JB091iB07p07165

Clarke GKC and Holdsworth G (2002) Glaciers of the St. Elias Mountains. In: Williams RS Jr. & Ferrigno JG (eds). *Satellite Image Atlas of Glaciers of the World* (pp. J301−J311). North America: U.S. Geological Survey Professional Paper 1386.

Colgan W and 7 others (2011) An increase in crevasse extent, West Greenland: hydrologic implications. *The Cryosphere* **38**(18), L18502. doi: 10.1029/2011GL048491

Cruikshank J (2001) Glaciers and climate change: perspectives from oral tradition. *Arctic* **54**(4), 377-393. https://www.jstor.org/stable/40512394

Cruikshank, J (2005) *Do Glaciers Listen?: Local Knowledge, Colonial Encounters, and Social Imagination*. Vancouver, Canada: UBC Press. 288 pp.

De Paoli L and Flowers GE (2009) Dynamics of a small surge-type glacier using one-dimensional geophysical inversion. *Journal of Glaciology* **55**(194), 1101-1112. doi: 10.3189/002214309790794850

Dunse T, Schellenberger T, Hagen JO, Kääb A, Schuler TV and Reijmer CH (2015) Glacier-surge mechanisms promoted by a hydro-thermodynamic feedback to summer melt. *The Cryosphere* **9**, 197–215. doi: 10.5194/tc-9-197-2015

Eisen O, Harrison WD and Raymond CF (2001) The surges of Variegated Glacier, Alaska, U.S.A., and the connection to climate and mass balance. *Journal of Glaciology* **47**(158), 351-358. doi: 10.3189/172756505781829250

Flowers GE, Roux N, Pimentel S and Schoof CG (2011) Present dynamics and future prognosis of a slowly surging glacier. *The Cryosphere* **5**(1), 299-313. doi: 10.5194/tc-5-299-2011

Flowers G, Jarosch A, Belliveau P and Fuhrman L (2016) Short-term velocity variations and sliding sensitivity of a slowly surging glacier. *Annals of Glaciology* **57**(72), 71-83. doi:10.1017/aog.2016.7

Fowler AC (1987) A theory of glacier surges. *Journal of Geophysical Research: Solid Earth* **92**(B9), 9111-9120. doi: 10.1029/JB092iB09p09111

Frappé TP and Clarke GKC (2007) Slow surge of Trapridge Glacier, Yukon Territory, Canada. *Journal of Geophysical Research: Earth Surface* **112**(3), 1–17. doi: 10.1029/2006JF000607

Gardner AS, Fahnestock MA and Scambos TA (2019) [accessed Jan. 2022] ITS_LIVE Regional Glacier and Ice Sheet Surface Velocities. Data archived at National Snow and Ice Data Center; doi: 10.5067/6II6VW8LLWJ7.

Girod L, Nuth C, Kääb A, McNabb R and Galland O (2017) MMASTER: Improved ASTER DEMs for Elevation Change Monitoring. *Remote Sensing* **9**(7), 704. doi: 10.3390/rs9070704

Gong, Y and 6 others (2018) Simulating the roles of crevasse routing of surface water and basal friction on the surge evolution of Basin 3, Austfonna ice cap. *The Cryosphere*, **12**, 1563-1577. https://doi.org/10.5194/tc-12-1563-2018

Harrison W, Raymond C and MacKeith P (1986) Short period motion events on Variegated Glacier as observed by automatic photography and seismic methods. *Annals of Glaciology* **8**, 82-89. doi: 10.3189/S0260305500001191

Harrison WD and 9 others (2015) Chapter 13: Glacier Surges. In Shroder JF, Haeberli W and Whiteman C (eds) Hazards and Disaster Series, Snow and Ice-Related Hazards, Risks and Disasters, Academic Press, 437-485. doi: 10.1016/B978-0-12-394849-6.00013-5

Herreid S and Truffer M (2016) Automated detection of unstable glacier flow and a spectrum of speedup behaviour in the Alaska Range. *Journal of Geophysical Research: Earth Surface* **121**(1), 64-81. doi: 10.1002/2015JF003502

Jay-Allemand M, Gillet-Chaulet F, Gagliardini O and Nodet M (2011) Investigating changes in basal conditions of Variegated Glacier prior to and during its 1982-1983 surge. *The Cryosphere* **5**(3), 659-672. doi: 10.5194/tc-5-659-2011

Jiskoot H. (2011) Glacier surging. In: Singh VP, Singh P and Haritashya UK (eds) *Encyclopedia of Snow, Ice and Glaciers*. Dordrecht, The Netherlands, Springer, 415-428.

Jiskoot H, Fox TA and Van Wychen W (2017) Flow and structure in a dendritic glacier with bedrock steps. *Journal of Glaciology* **63**(241), 912-928. doi: 10.1017/jog.2017.58

Kamb B and 7 others (1985) Glacier surge mechanism: 1982–1983 surge of Variegated Glacier, Alaska. *Science* **227**(4686), 469–479. doi: 10.1126/science.227.4686.469

Kamb B (1987) Glacier surge mechanism based on linked cavity configuration of the basal water conduit system. *Journal of Geophysical Research: Solid Earth* **92**(B9), 9083–9100. doi: 10.1029/JB092iB09p09083

Kamb B and Engelhardt H (1987) Waves of accelerated motion in a glacier approaching surge: the mini-surges of Variegated Glacier, Alaska, U.S.A. *Journal of Glaciology* **33**(113), 27-46. doi:10.3189/S0022143000005311

Kochtitzky W and 6 others (2019) Terminus advance, kinematics, and mass redistribution during eight surges of Donjek Glacier, St. Elias Range, Canada, 1935 to 2016. *Journal of Glaciology* **65**(252), 565-579. doi: 10.1017/jog.2019.34

Kochtitzky W, Copland L, Painter M and Dow C (2020) Draining and filling of ice-dammed lakes at the terminus of surge-type Dań Zhùr (Donjek) Glacier, Yukon, Canada. *Canadian Journal of Earth Sciences* **57**(11), 1337-1348. doi: 10.1139/cjes-2019-0233

Kotlyakov VM, Osipova GB and Tsvetkov DG (2008) Monitoring surging glaciers of the Pamirs, central Asia, from space. *Annals of Glaciology* **48**, 125-134. doi: 10.3189/172756408784700608

Lovell AM, Carr RJ and Stokes CR (2018) Topographic controls on the surging behaviour of Sabche Glacier, Nepal (1967 to 2017). *Remote Sensing of Environment* **210**, 434-443. doi: 10.1016/j.rse.2018.03.036

Lu J and Veci L (2016) Offset Tracking Tutorial: Sentinel-1 Toolbox. Array Systems Computing Inc.

Main B and 11 others (2022) Terminus change of Kaskawulsh Glacier, Yukon, under a warming climate: retreat, thinning, slowdown and modified proglacial lake geometry. *Journal of Glaciology* **69**(276), 936-952. doi: 10.1017/jog.2022.114

Meier MF and Post A (1969) What are glacier surges? *Canadian Journal of Earth Sciences* **6**(4), 807-817. doi: 10.1139/e69-081

Mingo and Flowers (2010). An integrated lightweight ice-penetrating radar system. Journal of Glaciology, 56(198), 709-714. https://doi.org/10.3189/002214310793146179

Morin A, Flowers GE, Nolan A, Brinkerhoff D and Berthier E (2023) Exploiting high-slip flow regimes to improve inference of glacier bed topography. *Journal of Glaciology* **69**(275), 658-664. doi: 10.1017/jog.2022.121

Murray T, Strozzi T, Luckman A, Jiskoot H, and Chrisakos P (2003) Is there a single surge mechanism? Contrasts in dynamics between glacier surges in Svalbard and other regions. *Journal of Geophysical Research: Solid Earth* **108**(B5), 2237. doi:10.1029/2002JB001906

Newman AJ, Clark MP, Wood AW and Arnold JR (2020) Probabilistic spatial meteorological estimates for Alaska and the Yukon. *Journal of Geophysical Research: Atmospheres* **125**(22), e2020JD032696. doi: 10.1029/2020JD032696

Noh M and Howat I (2015) Automated stereo-photogrammetric DEM generation at high latitudes: surface extraction from TIN-based search minimization (SETSM) validation and demonstration over glaciated regions. *GIScience and Remote Sensing* **52**(2), 198-217. doi: 10.1080/15481603.2015.1008621

Nolan A, Kochtitzky W, Enderlin EM, McNabb R and Krutz KJ (2021) Kinematics of the exceptionally short surge cycles of Sít' Kusá (Turner Glacier), Alaska, from 1983 to 2013. *Journal of Glaciology* **67**(264), 744–758. doi: 10.1017/ jog.2021.29

Nuth C and Kääb A (2011) Co-registration and bias corrections of satellite elevation data sets for quantifying glacier thickness change. *The Cryosphere* **5**(1), 271-290. doi:10.5194/tc-5-271-2011

Painter M, Copland L, Dow C, Kochtitzky W and Medrzycka D (2023) Patterns and mechanisms of repeat drainages of glacier-dammed Dań Zhùr (Donjek) Lake, Yukon. *Arctic Science,* 1-13. doi: 10.1139/AS-2023-0001

Partington G (2023) Reconstructing the surge history and dynamics of Fisher Glacier, Yukon, 1948-2022. MSc thesis, University of Ottawa. doi: 10.20381/ruor-29290

Paul F and 19 others (2013) On the accuracy of glacier outlines derived from remote-sensing data. *Annals of Glaciology* **54**(63), 171-182. doi:10.3189/2013AoG63A296

Planet Team (2017) Planet Application Program Interface: In Space for Life on Earth. San Francisco, CA. https://api.planet.com.

Post A (1963) Austin Post Photographs. PH Coll 734 Box 39. University of Washington Libraries, Special Collections. Available from: https://www.lib.washington.edu/specialcollections

Post A (1969) Distribution of surging glaciers in western North America. *Journal of Glaciology* **8**(53), 229-240. doi: 10.3189/S0022143000031221

Schellenberger T, Van Wychen W, Copland L, Kääb A and Gray L (2016) An inter-comparison of techniques for determining velocities of maritime Arctic glaciers, Svalbard, using Radarsat-2 Wide Fine mode data. *Remote Sensing* **8**(9), 785. doi: 10.3390/rs8090785

Sevestre H and Benn D (2015) Climatic and geometric controls on the global distribution of surge-type glaciers: implications for a unifying model of surging. *Journal of Glaciology* **61**(288), 646-663. doi: 10.3189/2015JoG14J136

Shangguan D and 6 others (2016) Characterizing the May 2015 Karayaylak Glacier surge in eastern Pamir Plateau using remote sensing. *Journal of Glaciology* **62**(235), 944-953. doi: 10.1017/jog.2016.81

Sharp M (2021) Amplification of surface topography during surges of Tweedsmuir Glacier. MSc thesis, University of Calgary. doi: 10.11575/PRISM/39300

Shean DE and 6 others (2016) An automated, open-source pipeline for mass production of digital elevation models (DEMs) from very-high-resolution commercial stereo satellite imagery. ISPRS

Journal of Photogrammetry and Remote Sensing **116**, 101–117. doi: 10.1016/j.isprsjprs.2016.03.012

Shepherd A, Hubbard A, Nienow P, King M, McMillan M and Joughin I (2009) Greenland Ice Sheet motion coupled with daily melting in late summer. *Geophysical Research Letters* **36**, L01501. doi:10.1029/2008GL035758

Sturm, M (1987) Observations on the distribution and characteristics of potholes on surging glaciers. *Journal of Geophysical Research: Solid Earth* **92**(B9), 9015-9022. doi: 10.1029/JB092iB09p09015

Sund M, Eiken T, Hagen JO and Kääb A (2009) Svalbard surge dynamics derived from geometric changes. *Annals of Glaciology* **50**(52), 50-60. doi: 10.3189/172756409789624265

Sund M, Lauknes TR and Eiken T (2014) Surge dynamics in the Nathorstbreen glacier system, Svalbard. *The Cryosphere* **8**, 623-638. doi: 10.5194/tc-8-623-2014

Truffer M and 10 others (2021) Chapter 13 - Glacier surges. In: Haeberli W and Whiteman C (eds.). *Snow and Ice-Related Hazards, Risks, and Disasters* (Second Edition), 417-466.

Van Wychen W, Copland L, Jiskoot H, Gray L, Sharp M and Burgess D (2018) Surface velocities of glaciers in western Canada from speckle-tracking of ALOS PALSAR and RADARSAT-2 data. *Canadian Journal of Remote Sensing* **44**(1), 57-66. doi: 10.1080/07038992.2018.1433529

Waechter A, Copland L and Herdes E (2015) Modern glacier velocities across the Icefield Ranges, St. Elias Mountains, and variability at selected glaciers from 1959 to 2012. *Journal of Glaciology* **61**(228), 624-634. doi: 10.3189/2015JoG14J147

Williamson SN and 9 others (2020) Evidence for elevation-dependent warming in the St. Elias Mountains, Yukon, Canada. *Journal of Climate* **33**, 3253–3269. doi: 10.1175/JCLI-D-19-0405

Yde JC and Paasche Ø (2010) Reconstructing climate change: Not all glaciers suitable. *Eos, Transactions American Geophysical Union* **91**(21), 189–90. doi: 10.1029/2010EO210001

Young EM, Flowers GE, Jiskoot H, Gibson HD (2022) Kinematic evolution of kilometre-scale fold trains in surge-type glaciers explored with a numerical model. *Journal of Structural Geology* **161**(2022), 104644. doi: 10.1016/j.jsg.2022.104644

Young EM (2023) Reconstructing the mass balance, ice flow, and structural glaciology of a non-surge-type and surge-type glaciers in the continental St. Elias Mountains. PhD thesis, Simon Fraser University.

Appendix 3-A: a) Location of ground-based ice-penetrating radar data collected with BSI IceRadar system (Mingo and Flowers, 2010) on 18 July 2021, just upstream of the confluence where the surge initiated. Base image: Sentinel-2, 30-08-2021. b) Radargram from the GPR survey, with a maximum ice depth of 173 m. Vertical and horizontal scales are approximate. General location is indicated by pink triangle on Fig. 3-1.

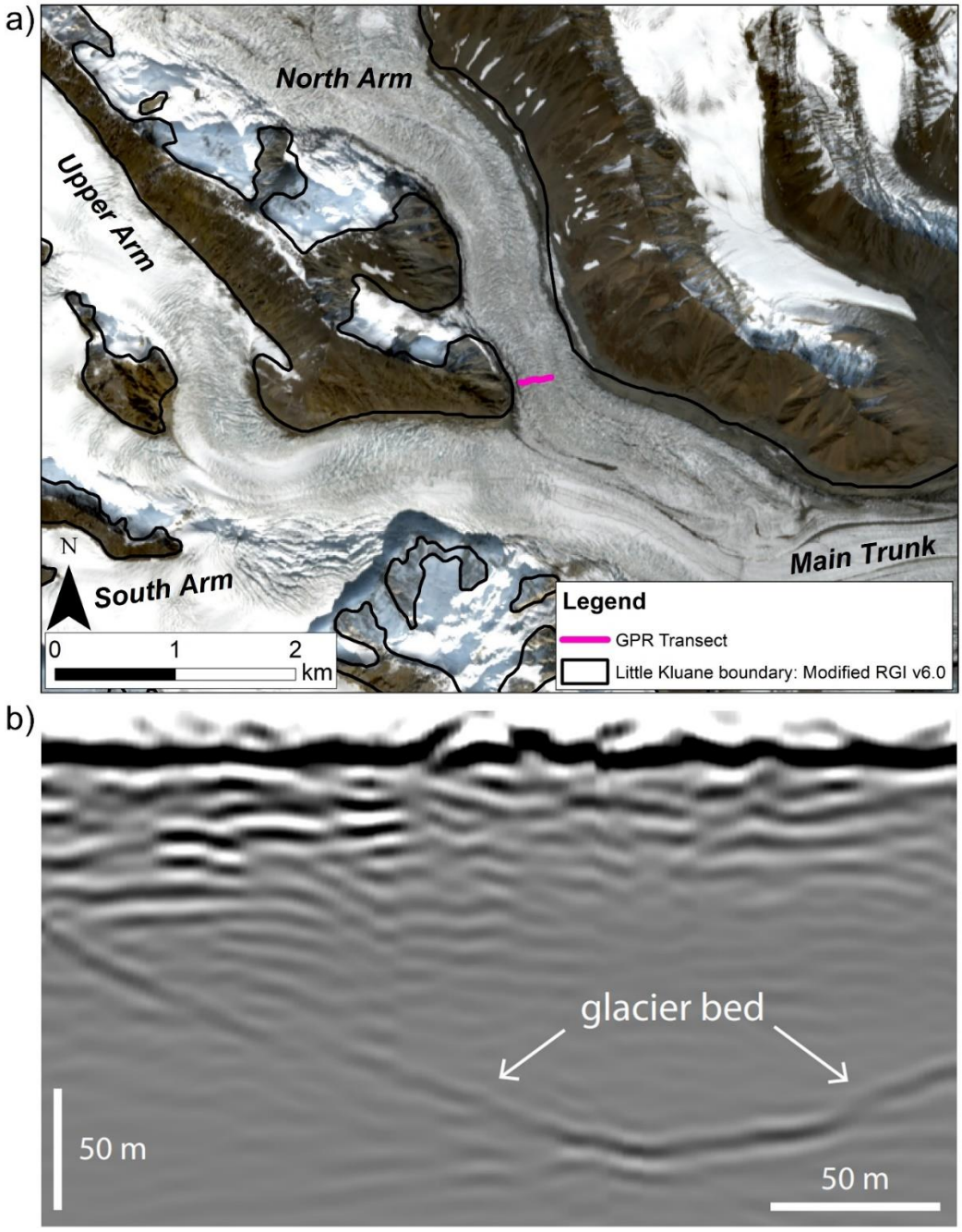

Appendix 3-B: List of air photos used in this study. Dates are in DD-MM-YYYY. RCAF = Royal Canadian Air Force.

Collection ID	Survey Date	Surveyor	Photo IDs	Exposure #	Roll ID	Altitude or scale
A-11014 (2 photos)	24-07-1947	RCAF	275 to 276	N/A	A11014	20000 ft
A-13132 (4 photos)	08-07-1951	RCAF	3 to 6	N/A	A13132	35000 ft
A-13132 (2 photos)	08-07-1951	RCAF	40, 41	N/A	A13132	1:70000
PH734 (9 photos)	28-08-1963	Austin Post	734. YD-145 to 734. YD-153	241-249	V634	18000 ft
PH734 (4 photos)	23-08-1965	Austin Post	734. YD-154 to 734. YD-157	109, 110, 113, 117	V652	13400 ft
A-22998 (8 photos)	11-08-1972	RCAF	190 to 193, 220 to 222	NA	A22998	1:80000
A-22999 (8 photos)	11-08-1972	RCAF	11 to 14; 37 to 40	NA	A22999	1:80000
A-24763 (4 photos)	03-08-1977	RCAF	130 to 133	N/A	A24763	1:80000

Appendix 3-C: List of optical satellite imagery used in this study, organized by platform. Dates are in DD-MM-YYYY.

Platform	Date	Path, Row	Resolution (m)
Landsat-1	02-09-1972	067, 017	60
Landsat-1	18-05-1975	067, 017	60
Landsat-2	25-06-1980	067, 017	60
Landsat-3	31-07-1985	061, 018	60
Landsat-5	27-08-1989	061, 018	30
Landsat-5	16-08-1994	061, 018	30
Landsat-5	20-08-1998	061, 018	30
Landsat-7	03-08-2004	062, 017	15
Landsat-7	04-08-2010	062, 017	15
Landsat-8	13-08-2013	061, 017	15
Landsat-8	15-07-2014	061, 017	15
Landsat-8	18-07-2015	061, 017	15
Landsat-8	04-07-2016	061, 017	15
Landsat-8	07-07-2017	061, 017	15
Landsat-8	08-07-2018	063, 017	15
Landsat-8	24-07-2018	063, 017	15
Landsat-8	26-07-2018	061, 017	15
Landsat-8	27-08-2018	061, 018	15
Landsat-8	03-09-2018	062, 017	15
Landsat-8	10-09-2018	063, 017	15
Landsat-8	26-09-2018	063, 017	15
Sentinel-2	17-07-2016	T07VEH	10
Sentinel-2	08-09-2016	T07VEH	10
Sentinel-2	04-11-2017	T07VEH	10
Sentinel-2	17-07-2017	T07VEH	10
Sentinel-2	25-07-2017	T07VEH	10
Sentinel-2	04-08-2017	T07VEH	10
Sentinel-2	16-08-2017	T07VEH	10
Sentinel-2	18-09-2017	T07VEH	10
Sentinel-2	30-09-2017	T07VEH	10
Sentinel-2	18-01-2018	T07VEH	10
Sentinel-2	25-02-2018	T07VEH	10
Sentinel-2	04-03-2018	T07VEH	10
Sentinel-2	13-04-2018	T07VEH	10
Sentinel-2	16-05-2018	T07VEH	10
Sentinel-2	18-05-2018	T07VEH	10
Sentinel-2	23-05-2018	T07VEH	10
Sentinel-2	31-05-2018	T07VEH	10
Sentinel-2	12-06-2018	T07VEH	10
Sentinel-2	22-06-2018	T07VEH	10
Sentinel-2	25-06-2018	T07VEH	10
Sentinel-2	22-07-2018	T07VEH	10
Sentinel-2	30-07-2018	T07VEH	10
Sentinel-2	29-08-2018	T07VEH	10
Sentinel-2	13-05-2019	T07VEH	10

Sentinel-2	30-06-2019	T07VEH	10
Sentinel-2	29-08-2019	T07VEH	10
Sentinel-2	15-09-2019	T07VEH	10
Sentinel-2	30-08-2020	T07VEH	10
Sentinel-2	19-09-2020	T07VEH	10
Sentinel-2	07-05-2021	T07VEH	10
Sentinel-2	24-06-2021	T07VEH	10
Sentinel-2	30-08-2021	T07VEH	10
Sentinel-2	12-09-2021	T07VEH	10
Sentinel-2	30-08-2022	T07VEH	10
RapidEye	28-07-2012	767218	5
RapidEye	29-06-2013	767218	5
RapidEye	27-08-2013	767218	5
RapidEye	20-08-2014	767218	5
RapidEye	03-08-2015	767218	5
RapidEye	08-09-2015	767218	5
RapidEye	18-06-2016	767218	5
RapidEye	29-06-2016	767218	5
RapidEye	29-07-2016	767218	5
RapidEye	03-09-2016	767218	5
RapidEye	04-06-2017	767218	5
RapidEye	01-08-2017	767218	5
RapidEye	14-06-2018	767218	5
RapidEye	11-08-2018	767218	5
RapidEye	09-09-2018	767218	5
RapidEye	07-06-2019	767218	5
RapidEye	14-06-2019	767218	5
RapidEye	06-07-2019	767218	5
PlanetScope	27-06-2018	190350_103f	3
PlanetScope	20-07-2018	200444_1035	3
PlanetScope	25-07-2018	200326_1021	3
PlanetScope	27-07-2018	200414_1013	3
PlanetScope	28-07-2018	200526_0f31	3
PlanetScope	31-07-2018	200416_1044	3
PlanetScope	04-09-2018	200320_0e13	3

Appendix 3-D: List of DEMs used in this study. Dates are in DD-MM-YYYY. The SPOT 03-09-2010 and ASTER 04-08-2019 DEMs were also used in DEM Differencing.

Date	Resolution (m)	Vertical Uncertainty (m)	Purpose
ASTER DEMs			
28-09-2001	30	10	Determination of glacier ice elevation change and ice volume loss
26-05-2002	30		
04-08-2019	30		
22-08-2020	30		
SPOT DEM			
03-09-2010	30	6	Surface slope and hydrology analysis
Worldview DEM			
17-07-2016	2	3	Surface slope and hydrology analysis

Appendix 3-E: List of ITS_LIVE velocity mosaics (pixel resolution 240 m) used in this study, and their associated error.

ITS_LIVE Glacier Velocities (Gardner et al., 2019)		
Product	**Year**	**Mean velocity error (m yr^{-1})**
Annual Mosaic	1985	6
Annual Mosaic	1986	6
Annual Mosaic	1987	5
Annual Mosaic	1988	6
Annual Mosaic	1989	7
Annual Mosaic	1990	7
Annual Mosaic	1991	5
Annual Mosaic	1992	4
Annual Mosaic	1993	4
Annual Mosaic	1994	4
Annual Mosaic	1995	3
Annual Mosaic	1996	3
Annual Mosaic	1997	3
Annual Mosaic	1998	3
Annual Mosaic	1999	4
Annual Mosaic	2000	3
Annual Mosaic	2001	2
Annual Mosaic	2002	2
Annual Mosaic	2003	2
Annual Mosaic	2004	2
Annual Mosaic	2005	2
Annual Mosaic	2006	2
Annual Mosaic	2007	2
Annual Mosaic	2008	2
Annual Mosaic	2009	2
Annual Mosaic	2010	2
Annual Mosaic	2011	3
Annual Mosaic	2012	3
Annual Mosaic	2013	1
Annual Mosaic	2014	1
Annual Mosaic	2015	1
Annual Mosaic	2016	1
Annual Mosaic	2017	1
Annual Mosaic	2018	8

Appendix 3-F: Summary of RADARSAT-2 SAR imagery used to derive surface ice velocities in this study. UF denotes Ultra-fine single polarisation (HH) images. Dates are in YYYY-MM-DD.

Beam Path/ Swath	Date 1	Date 2	Resolution (m)	Mode	Velocity error (m yr^{-1})
U7W2	2014-02-03	2014-02-27	3	UF	4
	2014-02-27	2014-03-23			
U17W2	2014-02-24	2014-03-20			
	2014-03-20	2014-04-13			
U7W2	2015-01-29	2015-02-22	3	UF	4
	2015-02-22	2015-03-18			
U17W2	2015-02-19	2015-03-15			
	2015-03-15	2015-04-08			
U7W2	2016-01-24	2016-02-17	3	UF	3
	2016-02-17	2016-03-12			
U17W2	2016-02-14	2016-03-09			
U7W2	2017-01-18	2017-02-11	3	UF	3
	2017-02-11	2017-03-07			
U17W2	2017-01-15	2017-02-08			
	2017-02-08	2017-03-04			
U7W2	2018-01-13	2018-03-02	3	UF	3
U6W2	2019-04-07	2019-05-01	3	UF	6
U17W2	2019-04-11	2019-05-05			
U17W2	2020-01-24	2020-02-17	3	UF	3
U6W2	2020-01-27	2020-02-20			

Appendix 3-G: Measurements of the area of supraglacial lakes located below the confluence between the north arm and main trunk of Little Kluane Glacier, mapped from RapidEye imagery. Locations can be found in Figure 3-3.

Date	**Lake 1 area (m^2)**	**Lake 2 area (m^2)**
18-06-2016	17145 ± 857	32552 ± 1628
29-06-2016	17428 ± 871	27333 ± 1367
29-07-2016	6651 ± 333	5519 ± 276

Appendix 3-H: Surface hydrology of the north arm of Little Kluane Glacier during the quiescent period in: a) 1977 air photo, and b) 2012 RapidEye image, showing a persistent supraglacial channel and ponding which is visible over multiple decades. RapidEye imagery from c) 2013, d) 2015, and e) 2016 showing transverse crevasse development during surge initiation which interrupts the supraglacial channel.

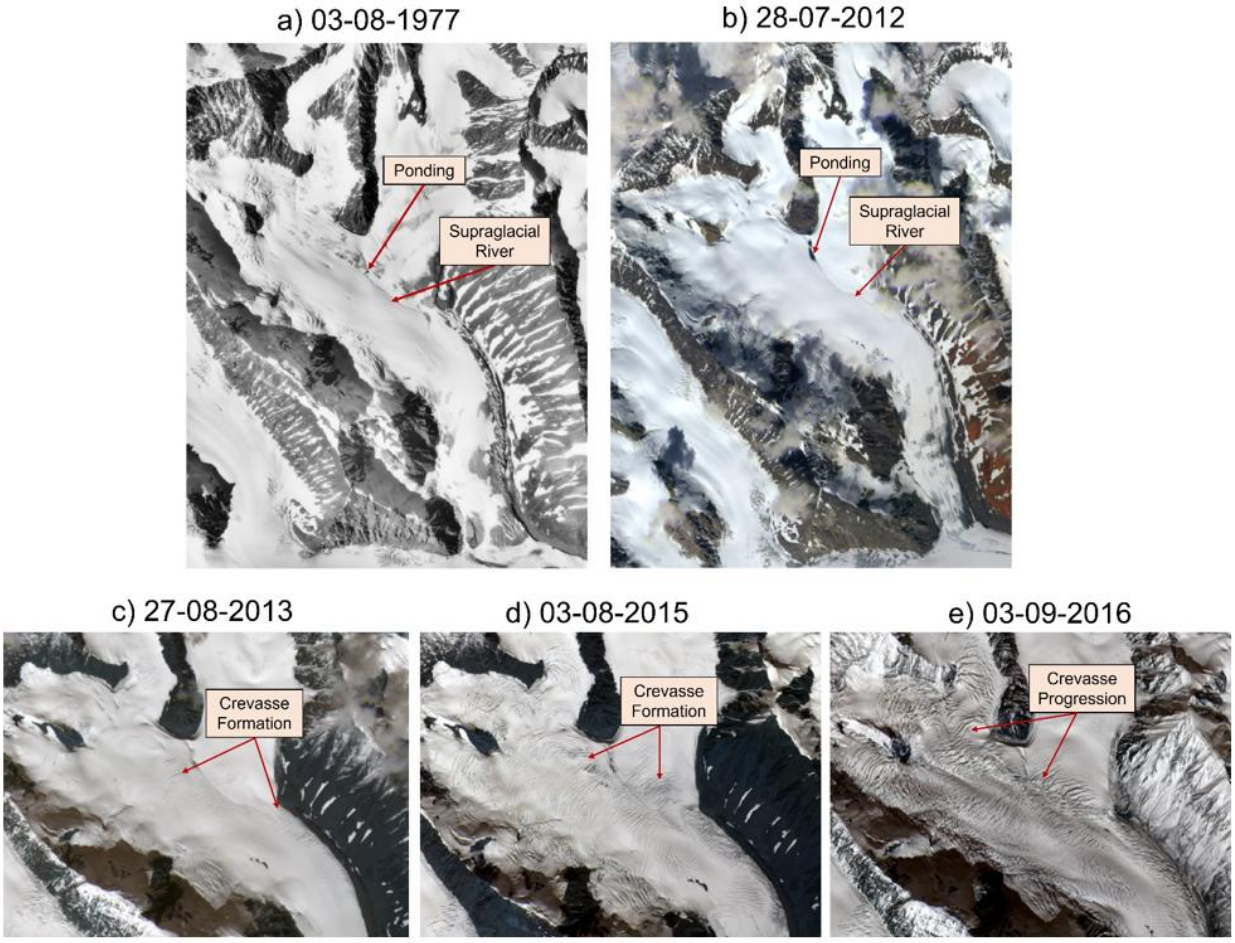

Appendix 3-I: a) View down-glacier in May 2019, showing the stranded ice rim and lowered ice basin in the north arm of Little Kluane Glacier; b) View near the confluence of the north arm and main trunk in August 2021: stranded ice indicates the previous ice surface elevation 5 years post-surge.

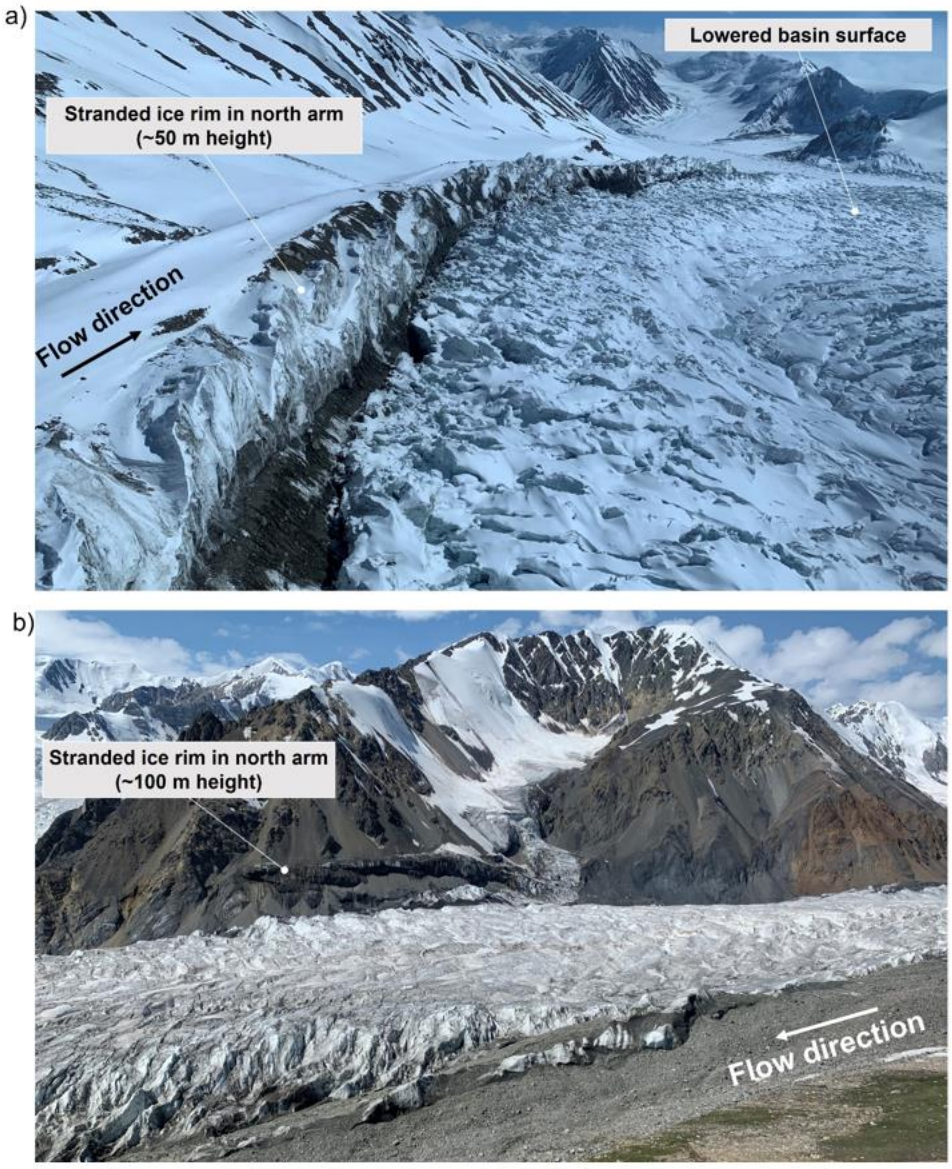

Appendix 3-J: a) ITS_LIVE velocities at upper points 4, 5 and 6 along the north arm centreline of Little Kluane Glacier from 2013-2022; and b) ITS_LIVE velocities at lower points 1, 2 and 3 along the north arm centreline of Little Kluane Glacier from 2013-2022. See Fig. 3-1 for point locations. Solid line represents the 20-point running mean for each set of points.

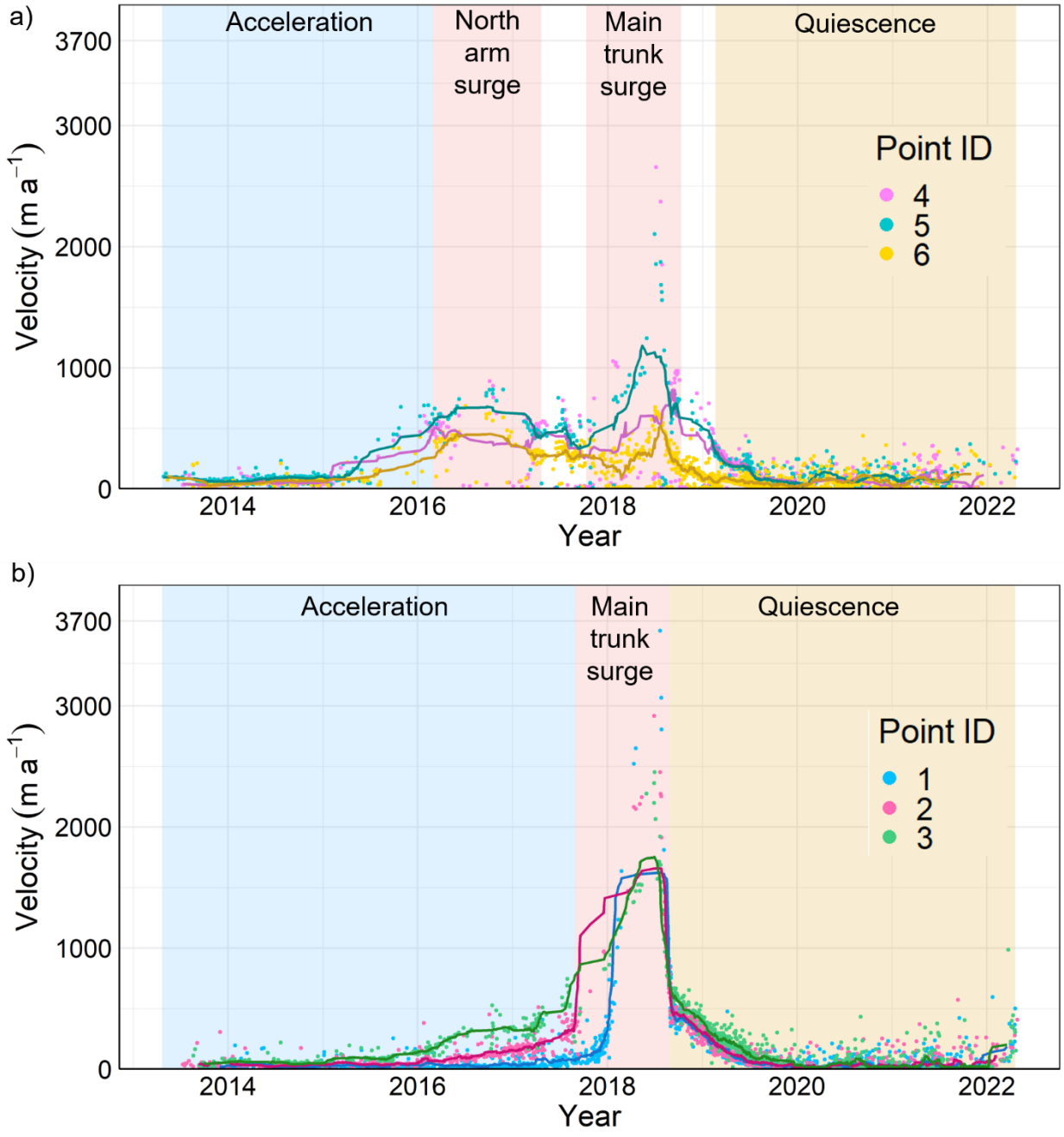

Chapter 4: Terminus change of Kaskawulsh Glacier, Yukon, under a warming climate: retreat, thinning, slowdown and modified proglacial lake geometry

4.1 Introduction

Melt from mountain glaciers accounted for nearly one third of global sea level rise over the period 2000-19 due to their strongly negative mass balance, despite representing only 1% of global glacier ice volume (Hugonnet and others, 2021). In the Alaska-Yukon region, glaciers experienced a total mass loss of approximately 3000 Gt, or 8 mm sea-level equivalent (s.l.e.), from 1961 to 2016 (Zemp and others, 2019). Alaska-Yukon is currently equal with the Canadian Arctic for the region with the largest total glacier mass loss globally, with an average rate of 73 ± 17 Gt a^{-1} from 2002-19 from both satellite gravimetry observations and geodetic mass balance measurements (Zemp and others, 2019; Ciracì and others, 2020). Ciracì and others (2020) also measured an acceleration in mass loss of 2.8 ± 0.5 Gt a^{-2} for Alaska-Yukon over the period 2002-19.

The glaciers of the St. Elias Mountains in Alaska-Yukon cover an area of ~25 000 km^2. Past studies have determined their thinning rate to average ~0.78 ± 0.34 m a^{-1} w.e. over the period 1958 to 2008, with increasing losses in low elevation regions, and negligible thinning in the accumulation area at higher elevations (Barrand and Sharp, 2010; Foy and others, 2011; Kienholz and others, 2015; Larsen and others, 2015; Young and others, 2020). In addition, this region will continue to contribute significantly to sea-level rise beyond the current century, as the large volume of ice will ensure that glaciers persist, unlike other regions, such as Central Europe and the Caucasus, which are expected to lose most of their glacier cover by the second half of this century (Zemp and others, 2019).

The St. Elias region has experienced an accelerated, elevation-dependent warming since 1979, with elevations between 5500 and 6000 m above sea level (asl) warming at a rate ~1.6 times greater than the global average over the period 1970-2015 (Williamson and others, 2020). Furthermore, mean annual air temperatures are expected to increase by an additional 3.0 to 3.5°C for the region by 2099 (Solomon and others, 2007). With all these factors considered, there is a significant committed ice loss from this region, as glacier losses are not in balance with the present climate (Zemp and others, 2019; Young and others, 2020). For example, Young and others (2020) estimate a committed terminus retreat of ~23 km and ice loss of 46 km^3 for Kaskawulsh Glacier based on the 2007-18 climate.

As Kaskawulsh Glacier (Fig. 4-1) has lost mass, terminus retreat has opened space for two proglacial lakes to form and grow, particularly since the start of the 21st century. However, in May 2016 the largest of these, Slims Lake (Fig. 4-1), drained rapidly through an ice-walled channel, lowering the lake level by 17 m (Shugar and others, 2017). This re-routed meltwater away from Ä'äy Chù (Slims River), through the new channel and into the Kaskawulsh River and then Alsek River, with significant impacts to the regional drainage system, including changes in sediment transport, fish populations and ice conditions for local communities (Bachelder and others, 2020). Studies elsewhere suggest that the presence of a large glacial lake can initiate terminus floatation, which even at a localised level, can reduce basal friction and increase velocities (Benn and others, 2007). Nothing is known of how these proglacial lake changes have impacted the dynamics of Kaskawulsh Glacier, but considering that proglacial lake volume has increased recently in the Alaska-Yukon region and is likely to continue to increase globally, this information is important to inform ice flow models, sea level rise predictions, and how glaciers will respond to a warming climate (Field and others, 2021).

This paper undertakes the first century-scale analysis of changes of the terminus (lowermost 10 km) of Kaskawulsh Glacier, one of the largest outlet glaciers in the St. Elias Mountains, containing ~9% of total glacier ice volume in the Yukon (Farinotti and others, 2019). We build on previous studies to extend the terminus position record back to the late 1800's, undertake an analysis of long-term changes in ice thickness, and examine how surface velocities have evolved through the growth and drainage of proglacial lakes at the terminus since the 1980s.

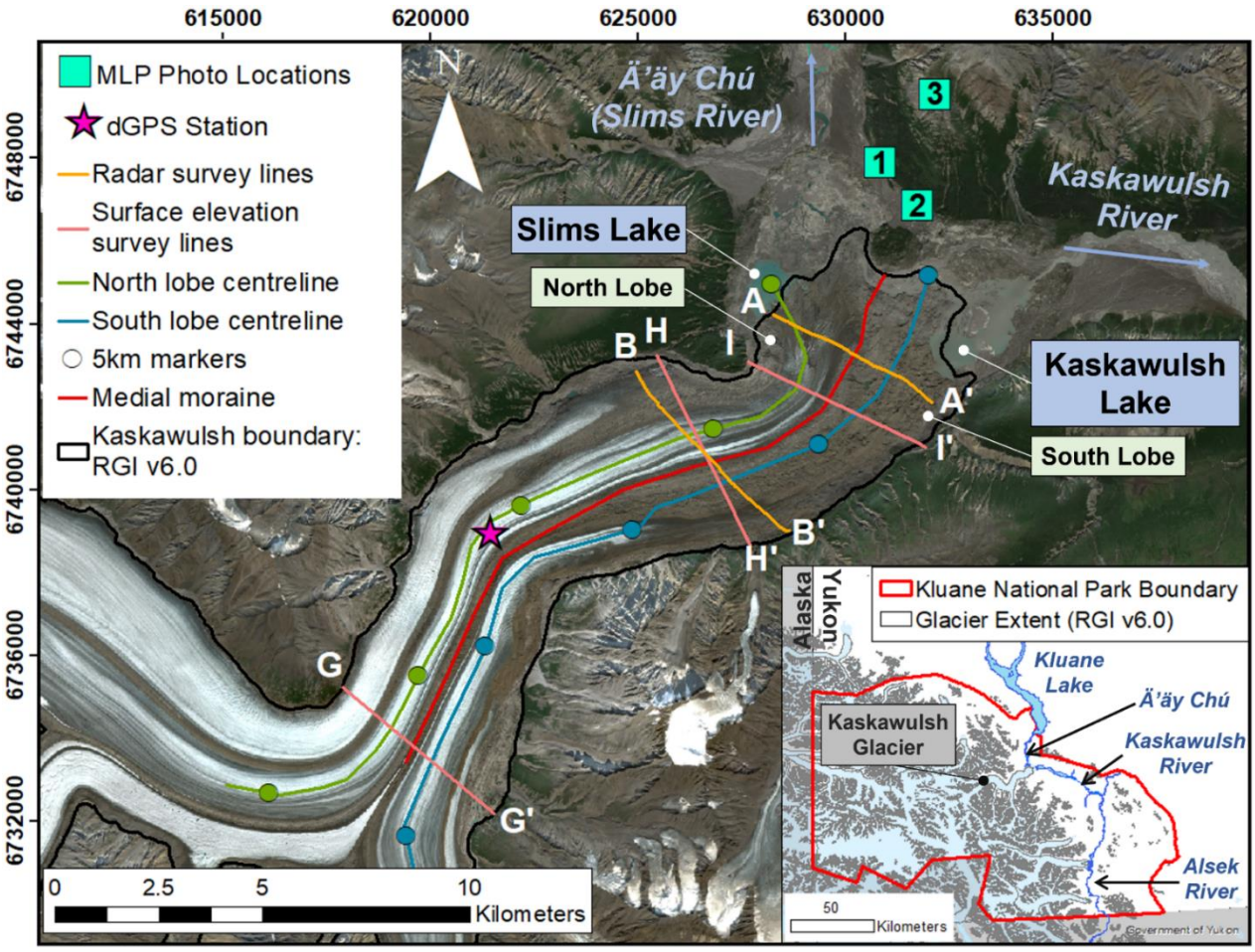

Figure 4-1: Kaskawulsh Glacier terminus region showing main locations referred to in the text. Base image: Sentinel-2, 3 August 2019, UTM Zone 7N. Inset: Regional map of Kluane National Park within the St Elias Mountains (red outline), with location of Kaskawulsh Glacier highlighted (black box); source: Yukon Geological Survey, with glacier outlines from RGI v. 6.0 (RGI Consortium 2017). MLP = Mountain Legacy Project. Transects G-G', H-H', and I-I' are identical to those in Waechter and others, 2015.

4.2 Study Site

Kaskawulsh Glacier (60°45′ 00″N, 139°08′ 37″W), or Tänshį in the Southern Tutchone language, is located on the eastern flank of the St. Elias Mountains in the Donjek Range, Yukon (Fig. 4-1). Covering an area of 1096 km^2, this valley glacier measures ~70 km in length and is up to 6 km wide (Young and others, 2020). Kaskawulsh Glacier is divided into three main arms. The North and Central Arms are supplied by the Kluane Icefields, with an accumulation area bordering Sít' Tlein (Hubbard Glacier) at ~2500 m asl, while the South Arm is sustained by a separate, more southerly catchment (Foy and others, 2011; Flowers and others, 2014). The glacier terminates at ~760 m asl, and radiocarbon dating of trees exposed at the terminus, along with the time required for Picea glauca (white spruce) to re-establish after ice retreat (Denton and Stuiver, 1967), suggests that the Little Ice Age maximum extent was reached between the early- to mid-1700s (Reyes and others, 2006) and 1836 (Borns and Goldthwait, 1966).

Kaskawulsh Glacier is one of only a few large glaciers on the eastern flank of the St. Elias Mountains not known to surge (Young and others, 2020), with Waechter and others (2015) showing that it had undergone few significant changes in velocity over most of its length from 1960-2012 except for a slowdown in the lowermost ablation area, ~10 km from the terminus. The glacier thinned at an average rate of 0.20-0.46 m a^{-1} over the period 1977-2007, for an overall volume loss of 3.27-5.94 km^3 $w.e.^{-1}$, which was mainly expressed as a reduction in surface height at lower elevations in the ablation area, below ~1200 m asl (Foy and others, 2011). Furthermore, thinning dramatically increased in the terminus region from 2007-18, to a maximum of 7.5 m w.e. a^{-1} over the lowermost 5-10 km of the glacier (Young and others, 2020).

The terminus of Kaskawulsh Glacier (Fig. 4-1) is divided into two lobes and accompanying proglacial lakes, which have formed on either side of a bedrock outcrop. The south lobe feeds Kaskawulsh Lake, which drains into Kaskawulsh River and then Alsek River, and ultimately to the Gulf of Alaska. Meanwhile, meltwater from the north lobe has historically flowed into Slims Lake and Ä'äy Chú, and then Lhú'áán Män (Kluane Lake), before eventually flowing into the Bering Sea (Flowers and others, 2014; Shugar and others, 2017). However, when Slims Lake drained in spring 2016, meltwater which previously flowed into Ä'äy Chú was diverted southward to the Kaskawulsh River and ultimately into the Gulf of Alaska (Shugar and others, 2017). This shift caused water levels of Lhú'áán Män to drop by 1.7 m below the long-term mean, resulting in

more frequent dust storms in the Ä'äy Chú valley since the drainage diversion, impacting local economies, air quality and fish and animal habitats (Shugar and others, 2017; Bachelder and others, 2020). A previous study has analysed connections between an ice marginal lake and englacial hydrology near the equilibrium line of Kaskawulsh Glacier (Bigelow and others, 2020), but no previous study has analysed connections between the changing proglacial lakes and glacier dynamics.

4.3 Methods

4.3.1 Changes in terminus length, area and surface characteristics

A range of oblique historical terrestrial photos, nadir air photos and nadir satellite images were used to map changes in the terminus position of Kaskawulsh Glacier for a total of 26 periods from 1899-2020. Additionally, the 1717 glacial limit was obtained from the dendroglaciological study by Reyes and others (2006).

The earliest known photos of the glacier terminus and adjacent outwash plains were taken by the geologist Alfred Hulse Brooks in summer 1899 (Fig. 4-2a), during an expedition on horseback to map the geology and landscape between Haines, Alaska and Wrangell St. Elias National Park. He travelled northwards up the present day Kaskawulsh River and down Ä'äy Chù and named Kaskawulsh Glacier, 'OConnor Glacier' in Brooks (1905; Plate XXIII), the only record of the glacier with that name. Approximately 6 photos cover the glacier terminus (stations 1 and 2 in Fig. 4-1), which were obtained from Library and Archives Canada, Ottawa, and are currently archived by the Mountain Legacy Project (https://explore.mountainlegacy.ca/stations/show/2375 and https://explore.mountainlegacy.ca/stations/ show/2376; Trant and others, 2015).

In summer 1900, James Joseph McArthur travelled along the eastern edge of the St. Elias Mountains as part of a reconnaissance to map the border between Yukon and Alaska as part of the International Boundary Commission. He took photos (Fig. 4-3a) in a panorama across the terminus of Kaskawulsh Glacier from a ridge to the north of the terminus (station 3 in Fig. 4-1). These were obtained from scans of glass plates held by Library and Archives Canada, Ottawa (McArthur, 1900), and are also archived by the Mountain Legacy Project (https://explore.mountainlegacy. ca/stations/show/2321).

A field visit was made on 30 July and 1 August 2012, to take repeat terrestrial photos from the sites of the original 1899 and 1900 photos (Figs 4-2b, 4-3b). Based on the alignment of features in the foreground and background of the historical photos, together with the discovery of historical markers on the ground such as carved sticks and small cairns, we have high confidence that the exact locations of the original photos were found. To place the terminus extent recorded in McArthur's, 1900 photos on a projected map, a total of twenty distinctive landmarks, including bedrock hills and terminal moraines, were identified and matched with a Sentinel-2 image from 8 August 2017.

Historical aerial imagery collected on 10 September 1956, at a flight altitude of 3400-4900 m asl by the Royal Canadian Air Force was used to determine the 1956 terminus position. These images were obtained from the National Air Photo Library, Ottawa, Canada, and scanned at 150 dots per inch, resulting in a pixel resolution of ∼10 m (Foy and others, 2011). Eleven aerial photographs, each covering a 15.2 × 15.2 km area were mosaicked to fully cover the terminus region, and here we use the orthomosaics initially processed by Foy and others (2011).

From 1972-99, Landsat 1-5 imagery was obtained in approximately 5-year intervals, with preferential selection from the summer months (1 June - 30 September) to minimise the impact of snow cover; similarly, images with significant cloud cover were avoided. From 2000-20, optical images from a variety of satellite sensors (Landsat 5, 7, 8; Sentinel 2: Appendix 4-A) were obtained on an annual basis, following the same selection criteria. Images were mosaicked together for 2006, 2008-10 and 2012 to reduce missing data due to the 2003 failure of the Landsat 7 Scan Line Corrector. Imagery was selected from the United States Geological Survey Earth Explorer website (https://earthexplorer.usgs.gov/) and downloaded as Level 1 GeoTIFF.

The satellite imagery was projected into Universal Transverse Mercator (UTM) zone 7N (NAD1983 datum, GRS80 ellipsoid), and colour corrected to provide the best distinction between ice and surrounding bedrock. For later satellite imagery (post-2000), red-green-blue (RGB) channels were assigned to Landsat bands 5, 4 and 2, respectively, while for earlier imagery (1972-99) RGB values were assigned to Landsat bands 3, 2 and 1. The terminus positions were traced manually using the 'draw' tool in ArcGIS (version 10.7) and converted to polygons using the same up-glacier bounding points to determine area change. Change in terminus extent since 1900 was measured for each period along 26 planes in the direction of ice flow and then averaged to provide

a mean value for the terminus, adhering to the methodology of Foy and others (2011). This also allowed for the characterisation of glacier retreat for each of the terminus lobes (north and south). Crevassing on the glacier surface in 2000 and 2015 was visually examined using two Landsat 7 band 8 images (15 m resolution, panchromatic band), which were both obtained during the late summer.

All termini outlines were either created or examined manually by the same person to maintain consistency between outlines. The methodology described by Krumwiede and others (2014) was used to determine the uncertainties. Using the assumption that the outlines are within half of a pixel of the actual terminus outline, there is an average uncertainty of 1.2 m, with a range from 0.05-15.5 m. This method has also been used by Haritashya and others (2018) and Kochtitzky and others (2020).

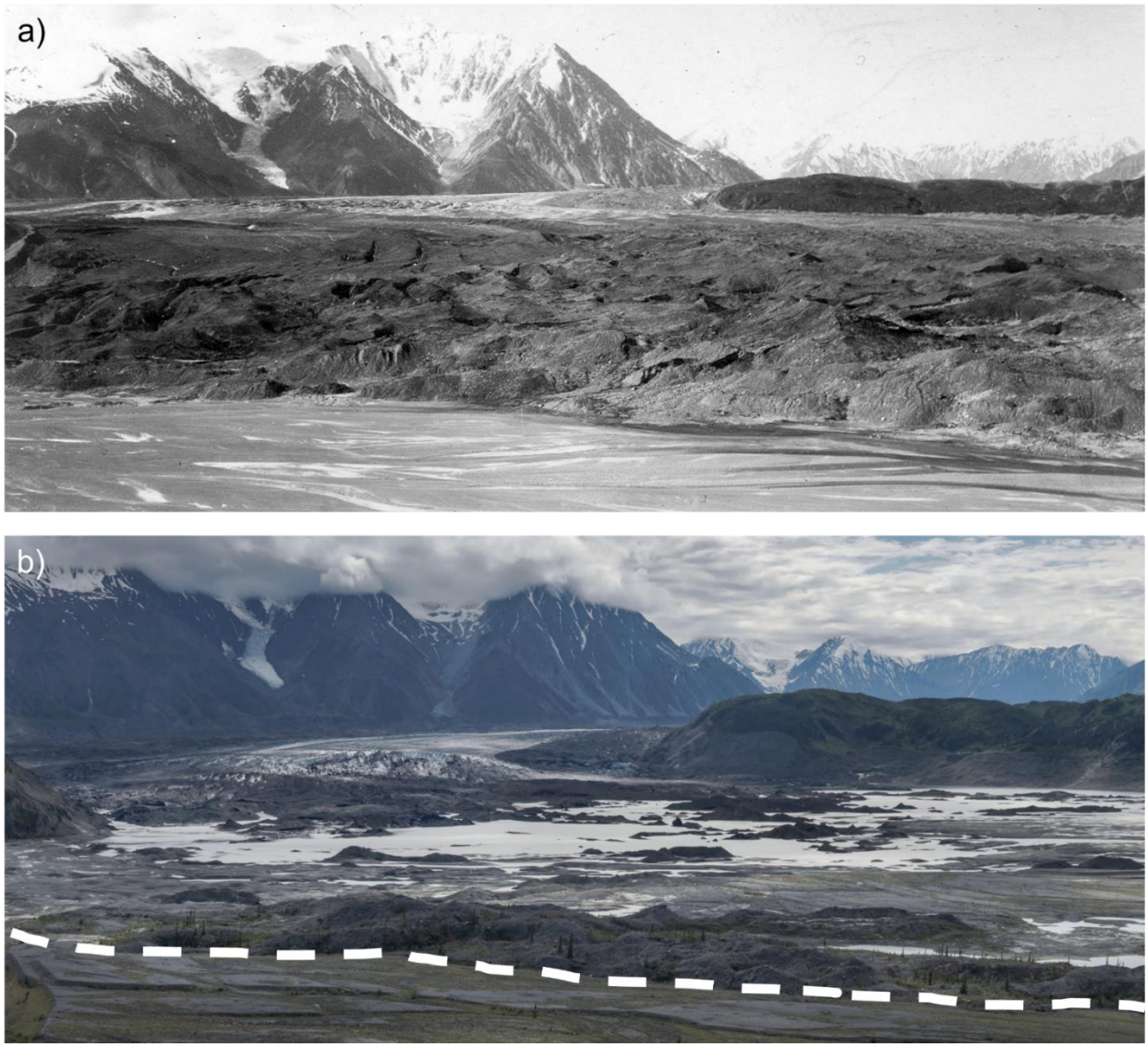

Figure 4-2: Photo comparison of Kaskawulsh Glacier terminus taken from Mountain Legacy Project (MLP) station 1 on Figure 4-1: (a) Summer 1899, taken by Alfred Hulse Brooks; and (b) 31 July 2012, taken by the MLP (image ID A0006335). The dashed white line represents the approximate terminus position in 1899. Photos are courtesy of the MLP and Library and Archives Canada / Bibliothèque et Archives Canada.

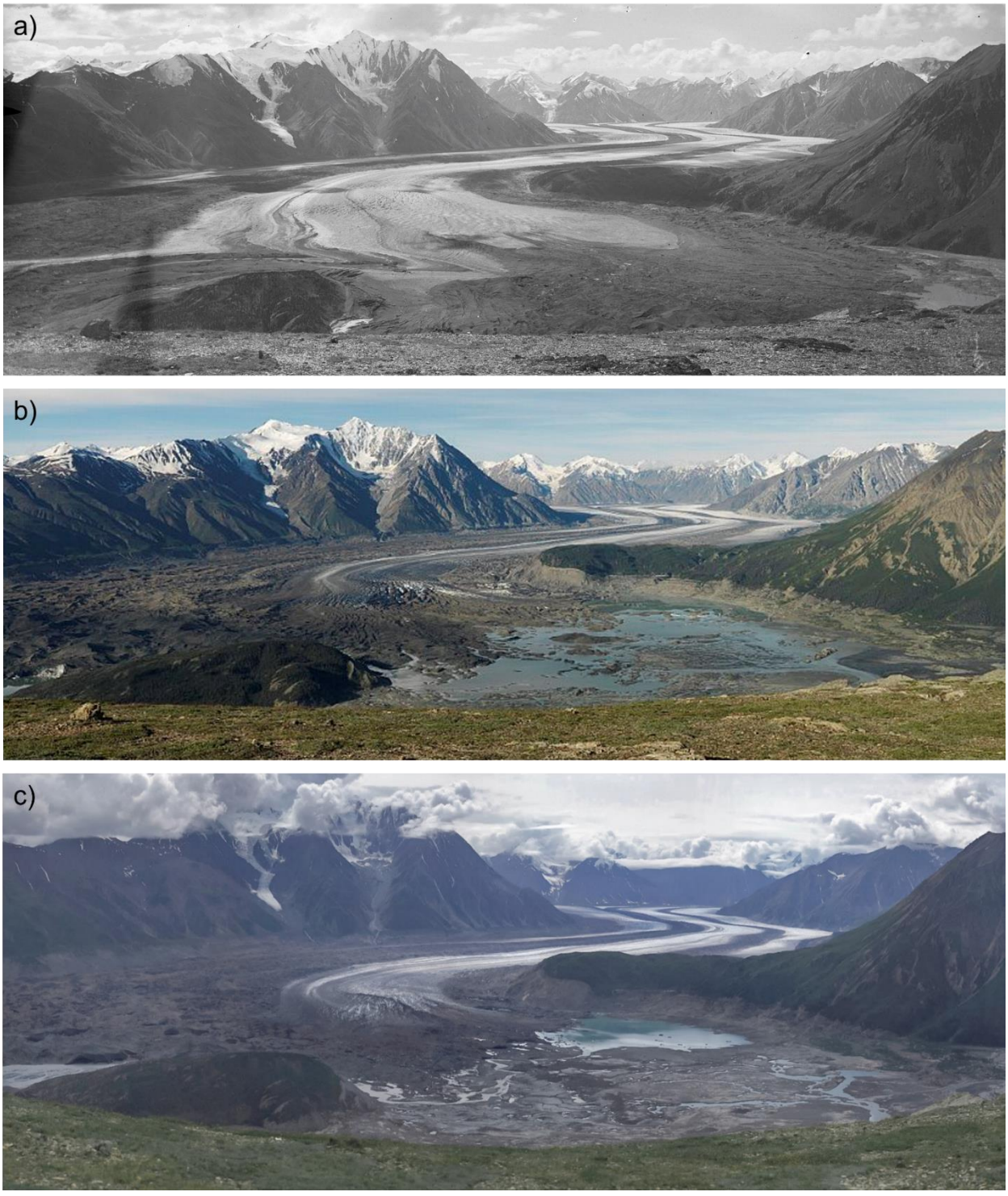

Figure 4-3: Photo comparison of Kaskawulsh Glacier terminus taken from Mountain Legacy Project (MLP) station 3 on Figure 4-1: (a) Summer 1900, taken by James Joseph McArthur; (b) 1 August 2012, taken by the MLP (image ID A0006385); and (c) 24 July 2021, taken by Luke Copland. Photos (a) and (b) are courtesy of the MLP and Library and Archives Canada / Bibliothèque et Archives Canada.

4.3.2 Digital elevation model analysis

4.3.2.1 Changes in ice volume and surface height of glacier terminus

To determine changes in glacier surface elevation over time, digital elevation models (DEMs) were created from SETSM WorldView imagery and ASTER Level 1A reconstructed unprocessed instrument data using the MMASTER software package (Girod and others, 2017). DEMs with sufficient quality and coverage were available for 2003, 2006, 2012, 2014, 2016, 2018 and 2020 (Appendix 4-B). These DEMs have a 10 m vertical and 2 m horizontal uncertainty (Girod and others, 2017). The SETSM and ASTER DEMs were co-registered (Shean and others, 2016) to the ASTER GDEM version 3 using overlapping bedrock elevations. We used the ASTER GDEM for co-registration as it has better coverage and consistency than the ArcticDEM or other products.

A DEM of difference (DoD) was created by subtracting the earliest ASTER DEM (2003) from the latest ASTER DEM (2020). Glacier volume change was calculated by summing the DEM difference for each 30 × 30 m pixel over the terminus region. To convert ice volume to water equivalent ice volume, the result was multiplied by near-surface density, assumed to be 917 kg m^{-3} for the ablation zone, where the entirety of this study is located. Elevation profiles were extracted and smoothed using a 300 m moving window to reduce noise.

Structure from Motion (SfM) was used to create a DEM of the Kaskawulsh terminus region from aerial photo surveys on 28 July and 1 August 2021 (Appendix 4-B). The survey was completed using a nadir-pointing Nikon D850 camera with 24 mm lens (AF-S NIKKOR 24 mm f/1.8 G ED), which took photos through an open port in the floor of a Helio Courier fixed-wing aircraft. The plane maintained an elevation of ∼700 m above ground level, with ∼250 m horizontal distance between adjacent flight lines, at an average velocity of 55 m s^{-1}. Images were captured automatically every 3 s using an intervalometer. A Trimble R7 dual-frequency GPS receiver attached to an Antcom 42GNSSA-XT-1 antenna mounted on top of the aircraft logged positions at a rate of 10 Hz. The camera flash mount was used to trigger a Trimble Event Input Marker and 1 PPS Output device, which inserted a marker in the Trimble R7 GPS record each time that a photo was taken, following the methodology of Nolan and others (2015). Camera positions were derived using a custom R script (version 4.0.5) based on linear interpolation between the recorded 10 Hz GPS positions and the timing of the event marker, which included compensation for the offset between the GPS antenna and camera sensor inside the aircraft. Camera positioning errors were

computed by combining the standard deviations of coordinates calculated with the Natural Resources Canada Precise Point Positioning solution and uncertainties in the lever arm position. The effects of aircraft attitude variability on the lever arm orientation (and therefore on the camera position in relation to the antenna) were approximated by considering variations in the pitch, yaw and roll angles typically reached during normal flight (±15°, ± 15° and ± 30°, respectively).

The survey photos were taken in RAW format and corrected to remove chromatic aberrations and compensate for vignetting, before conversion to TIFFs in Adobe Lightroom (version 5). Images were then imported into Agisoft Metashape software (version 1.6) and re-aligned several times to create a sparse cloud, optimising each alignment to compensate for reprojection errors. A dense cloud was created using high quality and mild filtering. The dense cloud segments were imported into CloudCompare (version 2.11.1), duplicate points were removed, and segments were filtered using the M3C2 algorithm to clean the noisy cloud surface (Lague and others, 2013). The filtered point cloud represents the median elevation within a 0.25 m radius around each point. Points further than 1 m away were considered outliers and excluded from the median computation. Each block was exported into both DEM and RGB orthomosaic rasters at 0.5 m resolution, where each pixel represents the average elevation or RGB values, respectively, of all points within the 0.5 m cell.

Glacier ice surface elevation in 1899/1900 was obtained by first aligning historical imagery (Figs 4-1, 4-2) with the SfM-derived 2021 orthomosaic via prominent features around the glacier margin such as trim lines. The approximated ice position in 1899/1900 was outlined, and the DEM elevation was extracted at ~30 m intervals. The 2021 surface elevation was then subtracted from the 1899/1900 elevation to obtain the change in ice thickness.

4.3.2.2 Change in area, surface elevation, volume and depth of proglacial lakes

The areal extents of the two proglacial lakes at the terminus of Kaskawulsh Glacier were outlined as often as possible from 1956-2021 to quantify area change using Sentinel-2, Landsat and ASTER imagery (Fig. 4-1, Appendix 4-C). Error analysis of the outlines followed the same methodology as the termini outlines (Section 4-3.1, Appendix 4-C). There is an average uncertainty of 0.2 km^2 for Slims Lake area, and 0.2 km^2 (12.8%) for Kaskawulsh Lake.

Images were preferentially chosen from June and July for consistency, although imagery from May, August and September was used when no June/July imagery was available. Comparison of

a sample of lake areas between June and September in the same year demonstrated a difference in lake area of <10% Water surface elevation in 2021 was obtained from the mean of elevations extracted around the 2021 lake margins in the SfM DEM. A 5 m internal buffer was added to the 2021 lake outline, to ensure that the water surface elevation was captured rather than glacier ice, and a visual inspection was performed with the orthomosaic to discard any points which intersected an iceberg or island. Mean water surface elevations in 2015 and 2016 were extracted from the 2021 SfM DEM based on the location of the shoreline in photos from those years. The 2021 SfM DEM was used to estimate the change in volume of the north proglacial lake (Slims Lake) after its May 2016 drainage.

4.3.2.3 Glacier ice thickness and terminus floatation

To assess floatation at the glacier terminus provided by the proglacial lakes, the ratio of ice thickness to water depth was used to compute H_b, the thickness of ice in excess of floatation:

$$H_b = H_M - \frac{\rho_w}{\rho_i} H_{w,} \qquad (1)$$

where H_M is ice front thickness, ρ_w is the density of water (1000 kg m^{-3}), ρ_i is the density of glacier ice (917 kg m^{-3}) (Shumskiy, 1960), and H_w is water depth. If H_b approaches 0, or is negative, floatation would occur.

Ice thickness across the glacier terminus was obtained via two helicopter radar surveys in July 2021 (Fig. 4-4a). The airborne system design stems from past radar surveys with an uncrewed-aerial vehicle (Briggs and others, 2020) and is adapted from the current IceRadar Variant 3, and the original IceRadar setup (Mingo and Flowers, 2010) used in other studies (Rabatel and others, 2018; Pelto and others, 2020; Magnússon and others, 2021). The radar was mounted on a slung platform, 30 m below the helicopter (Fig. 4-4b) and was equipped with an integrated L1 5 Hz Garmin GNSS, and with two versions (Bennest Enterprises Ltd.) of a Narod transmitter (Narod and Clarke, 1994) producing 512 Hz and 5 kHz repeat pulse, respectively. A 7.6 m half-length dipole antenna set was used for the survey and radar data were acquired with stacking set to 5000, a 125 MS s^{-1} sampling rate, and use of a 20 MHz low-pass input filter. The platform was flown at a nominal 30 m above the ice surface with a speed of ∼10 to 15 m s^{-1} during data collection. The air wave and reflected ice-bed wave were picked from each trace using Radar Tools (modified

from release 0.4; github ID: njwilson23/irlib). Ice thickness was determined using a velocity of radar waves in ice of 1.68×108 m s^{-1} (Fujita and others, 2000).

The glacier bed elevation was calculated by subtracting the 2021 ice thickness from the 2021 ice surface elevation. To determine ice thickness in 2015 and 2016, a thinning rate of 1 m a^{-1} (lower bound) and 2 m a^{-1} (upper bound) was applied to account for surface melt and ice thinning between those years and 2021, based on the measurements of Young and others (2020). As the land adjacent to the glacier terminus has been consistently covered by water since at least 2000 (Shugar and others, 2017), it was not possible to directly measure the land's elevation, and therefore this had to be inferred. Water depth of Slims Lake in 2015 and 2016 was calculated by subtracting ice depth from the lake surface elevation for each year. These water depth values and resulting floatation calculations are presented as a range to account for spatial variability in surface mass loss.

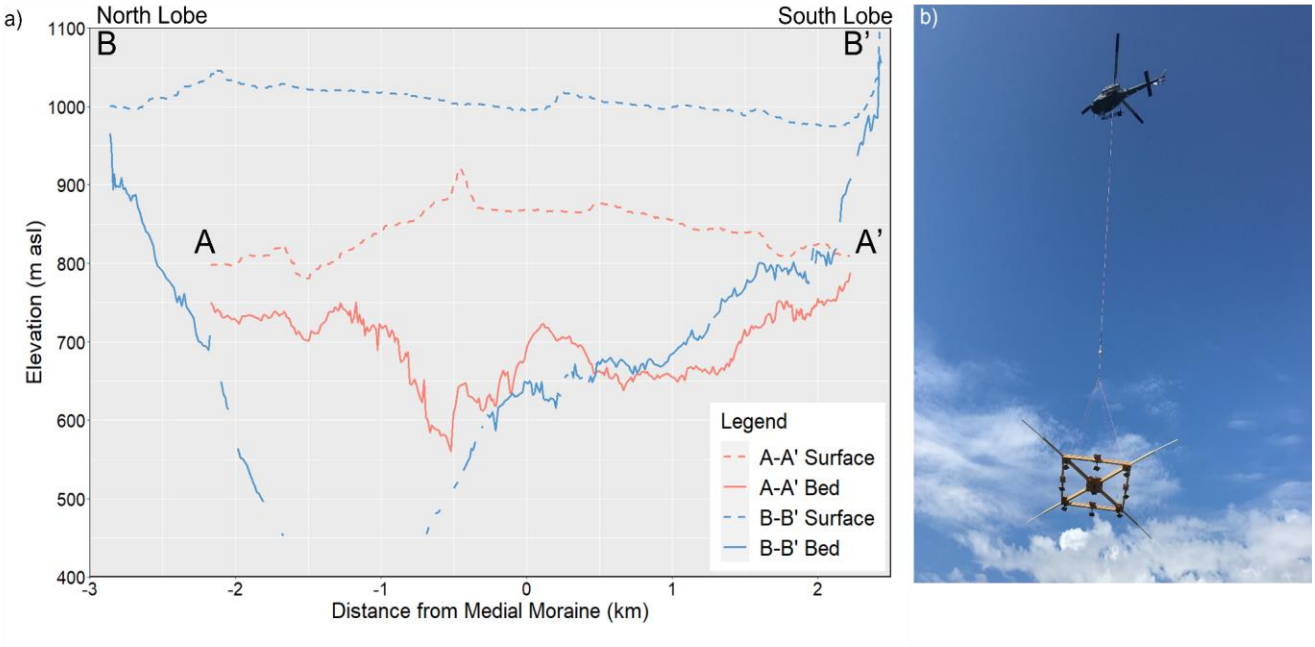

Figure 4-4: (a) Bed elevation and surface elevation (m asl) of Kaskawulsh Glacier across radar survey lines A-A' (near terminus) and B-B' (~6 km up-glacier) (See Fig. 4-1 for locations). (b) Photo of the IceRadar Variant 3 (Blue Systems Integration Ltd.) used for the ice depth surveys, mounted on a helicopter-slung platform. A 512 Hz transmitter and 5 MHz antennae mounted in a 'X' formation were used.

4.3.3 Velocity Mapping

Glacier surface velocities were determined between 2007 and 2021 from speckle tracking of pairs of ALOS PALSAR, RADARSAT-2 and RADARSAT Constellation Mission (RCM) data (Appendix 4-D). The winter 2007-08 and 2009-10 ALOS PALSAR datasets were originally published by Van Wychen and others (2018), while the 2011 and 2012 RADARSAT-2 datasets were originally published by Waechter and others (2015). Velocity maps for winters 2014-2020 (typically January through April annually) were created for this study from RADARSAT-2 ultra-fine (3 m resolution) and fine-wide (8 m resolution) image pairs acquired by Parks Canada, most with 24-day separation defined by the RADARSAT-2 repeat orbit interval, although some had 48-day separation (Appendix 4-D). RCM data from winter 2021 had a 12-day separation and 3 m resolution. Winter imagery was used to avoid melt that can cause loss of coherence between SAR image pairs collected at other times of the year, and is considered most suitable to quantify long-term velocity trends as it is not influenced by short-term melt and rain events that are common in summer (Waechter and others, 2015).

The RADARSAT-2 and RCM data were processed with GAMMA software, which has been demonstrated to provide velocities comparable to other speckle tracking methods in Canada and Svalbard (Waechter and others, 2015; Schellenberger and others, 2016; Van Wychen and others, 2018). The SLC images were then used to create multi-look images, which through averaging reduces the amount of speckle (noise), and ultimately produces backscatter intensity. Pairs of backscatter intensity images were then co-registered, and a patch intensity cross-correlation used to search for a block of pixels selected from the first image in the second image. The offset between the matched pixel blocks indicates displacement in both the azimuth and range directions over the time period between the images (Lu and Veci, 2016). Image chip sizes of ~500 m were used in the azimuth and range directions, with ~50% overlap between image blocks for images from 2012-20. Imagery from 2011 required a smaller image chip size (~250 m) due to the lower spatial resolution of those scenes.

Post-processing of the displacements was undertaken using custom scripts and tools in R, Matlab and ArcGIS. Magnitudes were first coarse filtered to remove any values less than 5 m a^{-1} (the lower limit of detection), and anything greater than 5000 m a^{-1} (maximum velocities previously recorded at the terminus are ~200 m a^{-1}; Waechter and others, 2015). The outputs were reprojected into

UTM zone 7N to match the optical satellite imagery. The data were then automatically filtered based on flow direction, using the assumption that glaciers follow the general orientation of surrounding topography (e.g., valley walls), the orientation of medial moraines, and flow in a generally downslope direction. In addition, single cells that deviated by >45° in flow direction from the mean of surrounding cells were removed using a custom Matlab script. Once fine-filtering was complete, the velocities were clipped to the Randolph Glacier Inventory (RGI) version 6.0 outline of Kaskawulsh Glacier (RGI Consortium, 2017) and overlapping values from multiple image pair dates within the same winter were averaged to provide a single value. Finally, an Inverse Distance Weighting (IDW) algorithm with fixed geographic point influence limits of either 500 or 250 m (based on input image resolution) was then applied to the filtered velocity point dataset to produce a continuous raster surface of ice velocities.

Velocities were extracted at 50 m intervals along centrelines for the north and south lobes of the terminus of Kaskawulsh Glacier (Fig. 4-1) and smoothed using a 300 m moving window. Velocities were also extracted at 50 m intervals along cross-profiles G-G′ and H-H′ (Fig. 4-1) and smoothed using a 300 m moving window, with the medial moraine located at 0 km. This is similar to the methodology used by Waechter and others (2015).

4.3.3.1 Additional velocity datasets

NASA's Inter-Mission Time Series of Land Velocity and Elevation (ITS_LIVE) programme provides mean annual surface velocities derived from Landsat 4, 5, 7 and 8 imagery over the period 1995-2018, at 240 m resolution. These are based on the auto-RIFT feature tracking processing chain, as described by Gardner and others (2022). The parameter v (velocity magnitude in m a^{-1}) was extracted along the north and south lobe centrelines of Kaskawulsh Glacier (Fig. 4-1) in ArcGIS version 10.7 across the same profiles as our SAR datasets, using the same procedure described in the previous section.

4.3.3.2 Velocity error analysis

Errors in speckle-tracking methods can arise from several sources, including poor image co-registration, DEM errors, inconsistencies in the satellite orbital model, cross-correlation errors, and layover or foreshortening effects in the radar imagery (Schellenberger and others, 2016; Van Wychen and others, 2018). For the imagery used in this study, Van Wychen and others (2018) provide errors of 9-15 m a^{-1} for the 2007-10 ALOS PALSAR data, while Waechter and others

(2015) list errors of 17 m a^{-1} for the 2011 RADARSAT-2 fine-beam imagery, and 13 m a^{-1} for the 2012 ultrafine imagery (Appendix 4-D). A buffer of 100 m was created surrounding the RGI 6.0 outlines on the images processed for this study to define stable ground. The mean apparent velocity over these regions was used to define the velocity error, which ranged between 3 and 13 m a^{-1} for the 2014-2020 RADARSAT-2 data, and was 15 m a^{-1} for the 2021 RCM data.

Errors associated with the ITS_LIVE dataset, including surface skipping and sensor biases, are presented in the ITS_LIVE Regional Glacier and Ice Sheet Surface Velocities Known Issues documentation (http://its-live-data.jpl.nasa.gov.s3.amazonaws.com/documentation/ITS_LIVE-Regional-Glacier-and-Ice-Sheet-Surface Velocities-Known-Issues.pdf). ITS_LIVE provides the error product v_error (error in velocity magnitude in m a^{-1}), which was averaged over the Kaskawulsh Glacier RGI 6.0 outline.

4.3.3.3 dGPS validation

A dual frequency Global Positioning System (dGPS) system installed on the terminus of Kaskawulsh Glacier was used to validate both DEM generation and SAR velocity results (Fig. 4-1). A Trimble R7 receiver was used between May 2008 and May 2015, and a Trimble NetR9 receiver between August 2017 and July 2021. These units recorded their position at 15 s intervals, typically for 24 h day^{-1} in the summer (May-August) and 2 h day^{-1} for the remainder of the year. The data was postprocessed using Natural Resources Canada's Precise Point Positioning Service, which enables positioning to an accuracy of ~1-2 cm in the horizontal dimension and ~5 cm in the vertical (Waechter and others, 2015).

4.4 Results

4.4.1 Changes in area and extent of terminus

The area and extent of the terminus of Kaskawulsh Glacier have both dramatically decreased over the past ~120 years, as shown in the comparisons between the 1899/1900 and recent photos (Figs 4-2, 4-3). The average terminus retreat between 1900 and 2020 was 1380 ± 36 m, with similar amounts at both lobes, corresponding to a total loss in ice area of 16 ± 0.5 km^2 (Fig. 4-5). The average rate of retreat over the entire period since 1900 is 22 ± 0.5 m a^{-1}. Since 2000, when annual observations are available, the greatest rate of terminus retreat occurred from 2015-16, when the glacier receded by an average of 93 m. There have also been instances of short-term terminus advance, such as from 1975-80 (26 ± 1.5 m), 2010-11 (87 ± 3.8 m), and 2014-15 (36 ± 1.0 m), but

these were dominated by local changes across only ~3 of the 26 planes used to measure terminus change, with near stagnation along the majority of the glacier front. Aside from 1975-80, these advances were not sustained over multiple years, and are likely due to seasonal variability associated with the timing of satellite images, local terminus instability, glacier dynamics and melt variability.

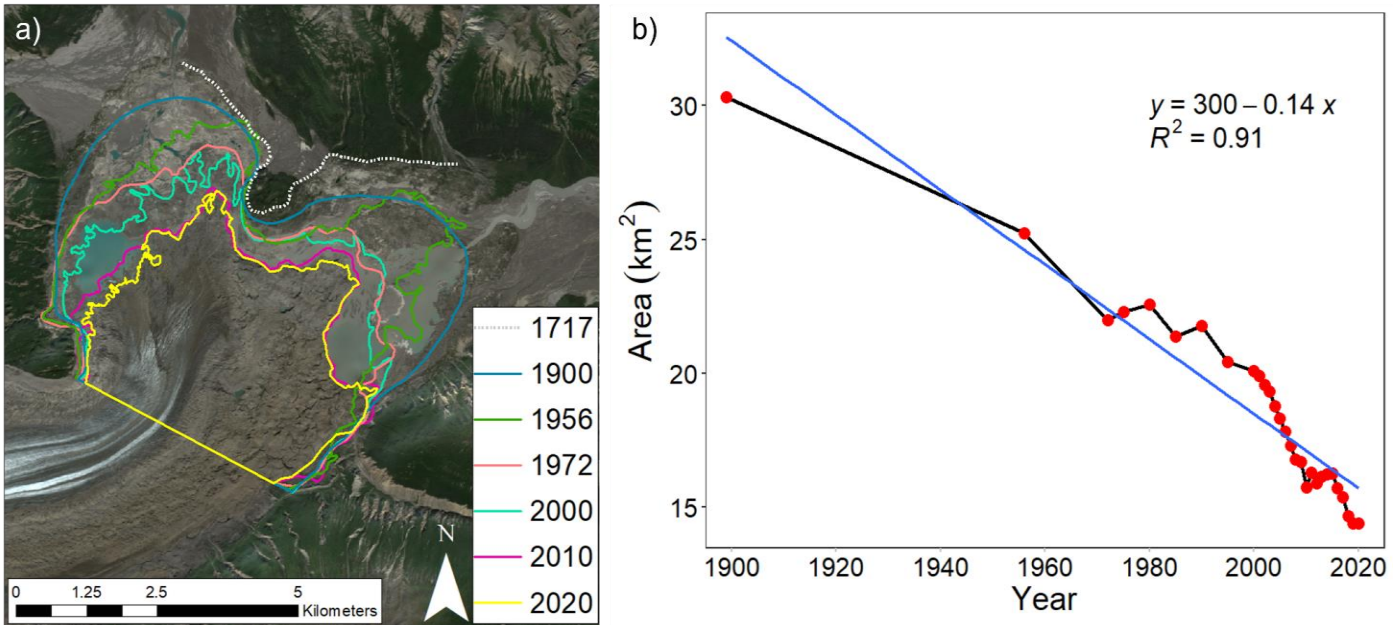

Figure 4-5: (a) Selected terminus positions of Kaskawulsh Glacier, 1717-2020. Base image: Sentinel-2, August 3 2019, UTM Zone 7N; (b) Area of the terminus of Kaskawulsh Glacier from 1900-2020, computed from the polygons shown in (a).

4.4.2 Change in terminus lakes extent

Historical images illustrate that there were no proglacial lakes present in 1899 and 1900 (Figs 4-2a and 4-3a), indicating that the modern lakes formed at some point between 1900 and the first available air photo in 1956. From 1956 to 1980 Slims Lake was no larger than 1 km^2, and then it fully drained by 1990 (Appendix 4-C). Over the mid and late-1990s, the lake reformed and increased in size until the most recent drainage event in 2016 (Fig. 4-6). Kaskawulsh Lake increased in size from 1956 to 1972, then remained mostly stable until 2000, after which it grew rapidly. Its size peaked in 2016, then decreased in extent until 2021 (Appendix 4-C). Kaskawulsh Lake has been consistently larger than Slims Lake in all available observations, except for air photos and satellite imagery from 1956, 2015 and 2021.

Slims Lake drained in May 2016, after reaching a peak area of 3.7 ± 0.2 km^2 in summer 2015. The drainage occurred due to the formation of a meltwater channel in an area of dead ice near the terminus, which allowed water to flow from Slims Lake into Kaskawulsh Lake, along a channel that followed the outer edge of the terminus. The outlet at the head of the new channel is now 17 m lower than the outlet which previously fed Ä'äy Chù (Shugar and others, 2017), indicating that the switch in drainage will persist. The loss of water volume during the 2016 drainage was 0.056 ± 0.01 km^3 equal to an average reduction in water depth of at least 15.35 m over the 2015 lake surface. The area of Kaskawulsh Lake peaked in 2016 at 3.4 ± 0.1 km^2, shortly after the drainage of Slims Lake into it. Since the drainage event in 2016, the areal extent of Slims Lake has been ~1 km^2, with a slight increase in size to 1.3 ± 0.1 km^2 by 2021 (Appendix 4-C). This recent increase in lake size has primarily occurred through terminus retreat, with the lake expanding into new ice-free regions; it has not re-occupied the former lakebed close to Ä'äy Chù.

Observations of seasonal area change in 2021 showed differential response of the two lakes (Appendix 4-C). Kaskawulsh Lake was ~1 ± 0.1 km^2 in mid-May, increased during the summer months to over 3 ± 0.2 km^2 by 31 July 2021, and then decreased to 0.99 ± 0.1 km^2 by 12 September 2021 as meltwater supply lessened (Appendix 4-C). In contrast, Slims Lake showed only minor changes between seasons, increasing from 1.23 ± 0.1 km^2 in May 2021 to 1.36 ± 0.1 km^2 in late July, then decreasing to 1.20 ± 0.1 km^2 in September.

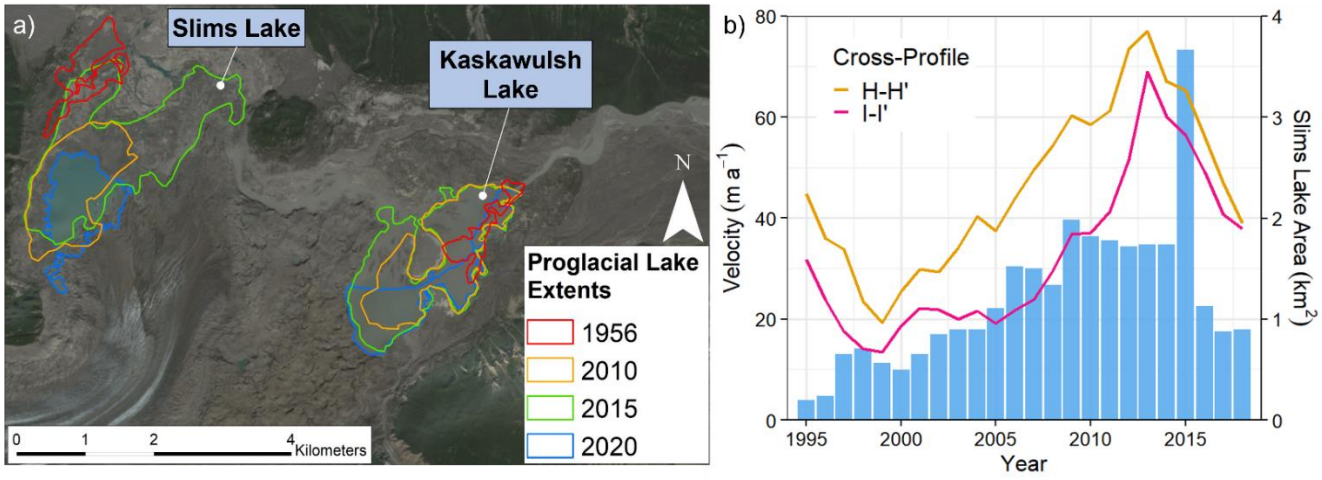

Figure 4-6: (a) Proglacial lake extents for select periods from 1956-2020. Base image: Sentinel-2, August 3 2019, UTM Zone 7N; (b) ITS_LIVE mean velocity at two cross-profiles (purple and yellow lines; left axis, m a^{-1}) compared to Slims Lake area (blue columns; right axis, km^2). H-H' is furthest cross-profile from glacier terminus, I-I' is closest to the terminus front (Fig. 4-1).

4.4.3 Ice thickness changes

Ice thickness transects across the terminus of Kaskawulsh Glacier show that there is consistently thicker ice in the north lobe (>600 m) compared to the south lobe (up to 400 m) (Fig. 4-4a). A comparison of bed and surface elevations along radarlines A-A′ and B-B′ (location in Fig. 4-1) show that there is a reverse slope along the north lobe of the glacier, with the greatest difference between bed elevations (>200 m) occurring at -1.5 km along the survey profile. As there were missing bed returns in this area, it is likely that the difference between the bed elevations in this zone are underestimated. In contrast, the south lobe does not have a reverse slope aside from within 0.5 km of the medial moraine. Instead, average bed elevations at 1-2 km along the profile are higher up-glacier at B-B′ (760 m asl) compared to A-A′ (705 m asl). It appears that ice in the north lobe is increasingly constricted to a narrow region as the ice approaches the terminus. This, along with the velocity patterns shown in Figure 4-7, suggest that ice is primarily funnelled through the north lobe of the terminus, which feeds into Slims Lake.

The terminus of Kaskawulsh Glacier has lost substantial thickness since 1899, with the ice surface sitting approximately 227 m lower at the western edge of the glacier at location I (Fig. 4-1) in 2020 compared to 1899/1900, with a range of ice loss from 186 to 279 m. Thinning rates have been particularly high over the past two decades, with losses exceeding 70 m at some locations across the terminus between 2003 and 2020 (Fig. 4-8). The mean total surface elevation loss from 2003-20 was 26.6 ± 1.7 m, or 1.56 m a^{-1} over the terminus region as a whole. The loss was greatest for the south (Kaskawulsh Lake) lobe, thinning at an average rate of 2.1 ± 0.1 m a^{-1}, compared to the north (Slims Lake) lobe at 1.1 ± 0.1 m a^{-1} (Fig. 4-8).

Elevation change profiles along the H-H′ cross-section (Fig. 4-1), ~6.5 km up-glacier from the terminus (Fig. 4-9a), also demonstrate a marked reduction in glacier surface height from 2003-20. Losses at this location have been most pronounced along the north (Slims Lake) side, with average elevation loss of 22 ± 1.7 m (1.3 m a^{-1}) north of the medial moraine on H-H′. On the south side of the medial moraine the average elevation loss was 13.3 ± 1.7 m (0.78 m a^{-1}). The I-I′ cross section (Fig. 4-9b), which is within 2.5 to 4 km from the terminus, experienced a loss of 25-30 m (1.47-1.76 m a^{-1}) across most of the glacier from 2003-20, aside from a narrow region of elevation increase north of the medial moraine.

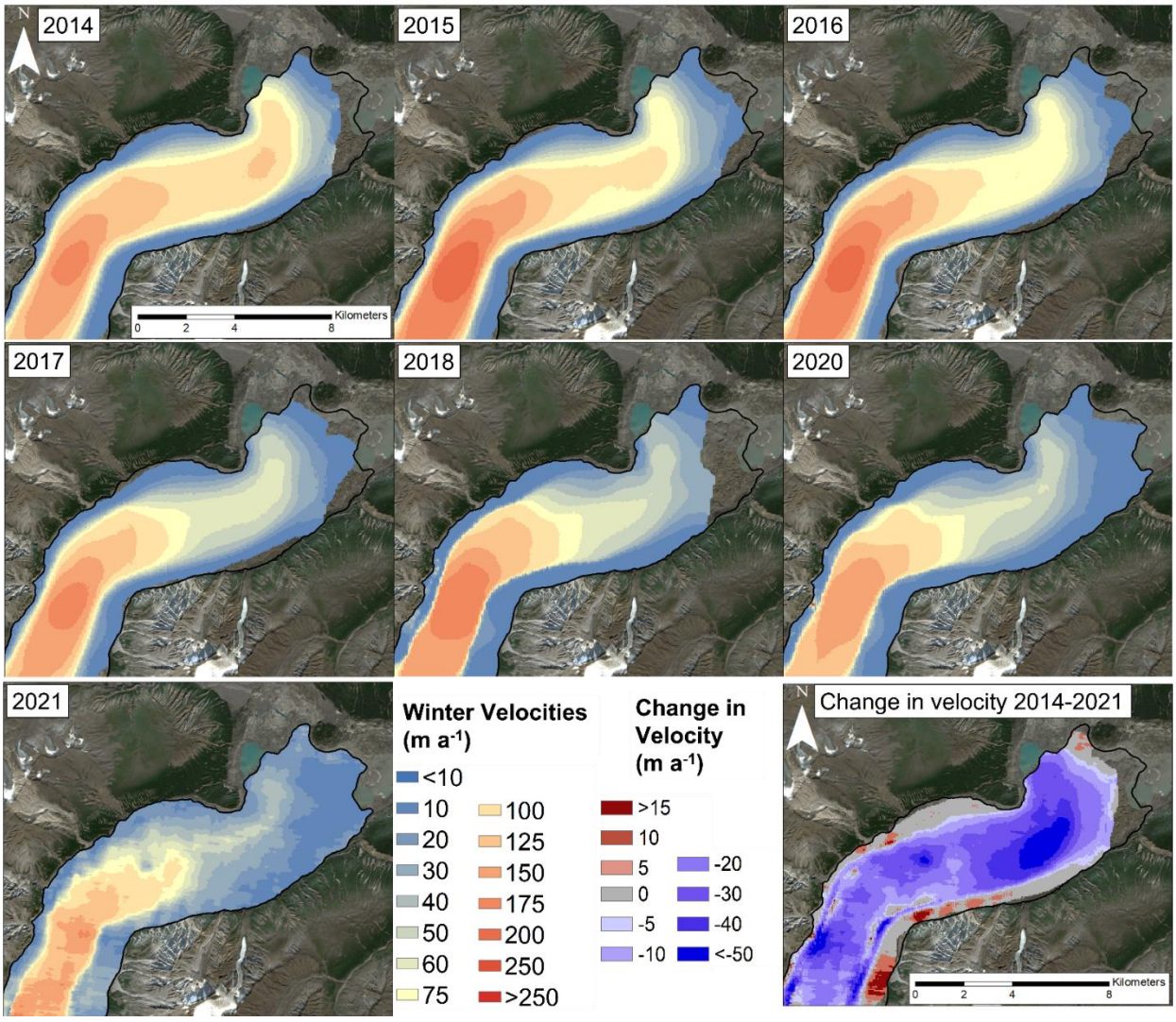

Figure 4-7: Surface velocities across the terminus of Kaskawulsh Glacier for each winter from 2014-2021 derived from SAR speckle tracking, together with the long-term change in velocity from 2014-2021. The change in velocity was calculated on a cell-by-cell basis using Cell Statistics tool in ArcGIS between the 2014/2015 and 2020/2021 mean. Note different scale for positive vs negative changes. Projection: UTM 7N, base image: Sentinel-2 image, August 3 2019.

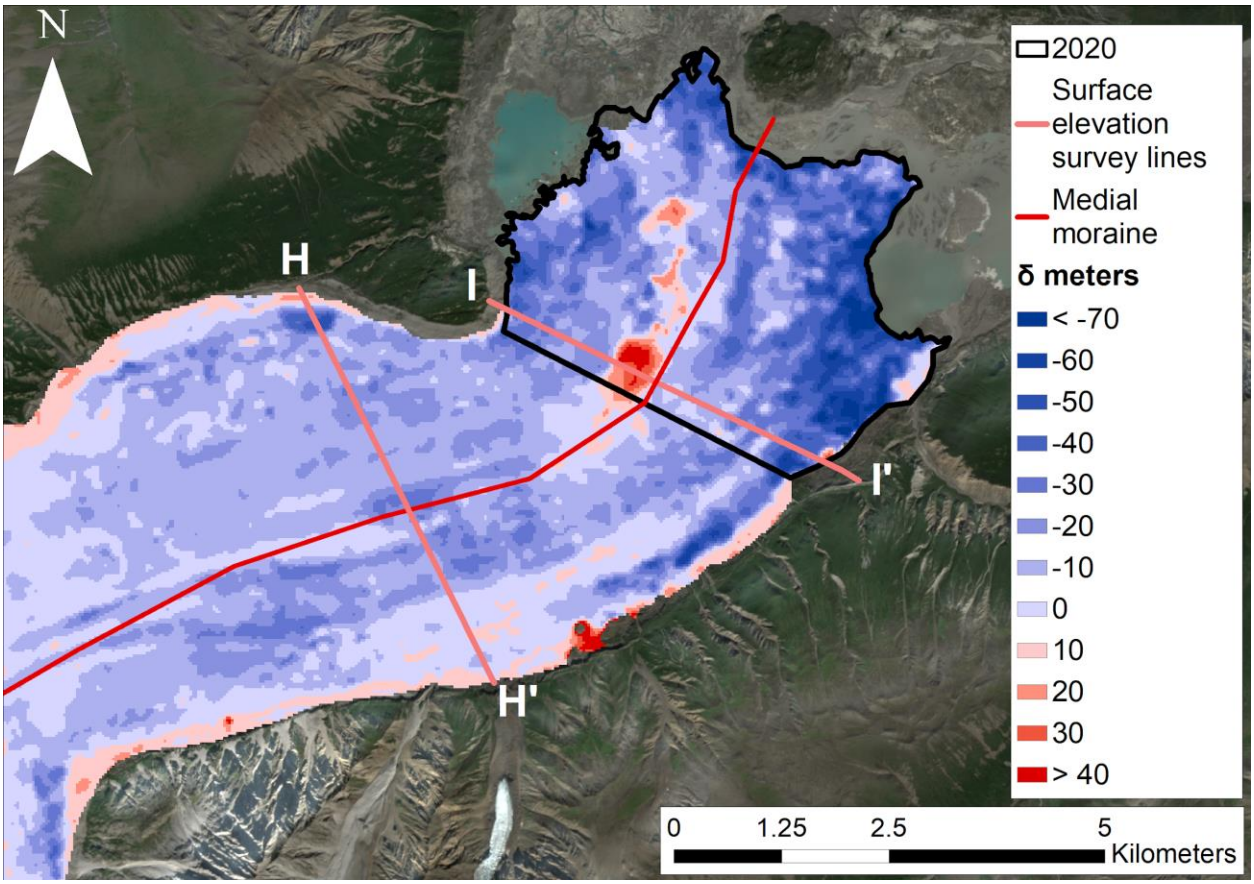

Figure 4-8: Elevation change across the terminus of Kaskawulsh Glacier between 2003 and 2020, clipped to the 2020 glacier outline. The black 2020 polygon delineates the terminus region, where a total ice loss value was calculated. Projection: UTM 7N, base image: Sentinel-2 image, August 3 2019.

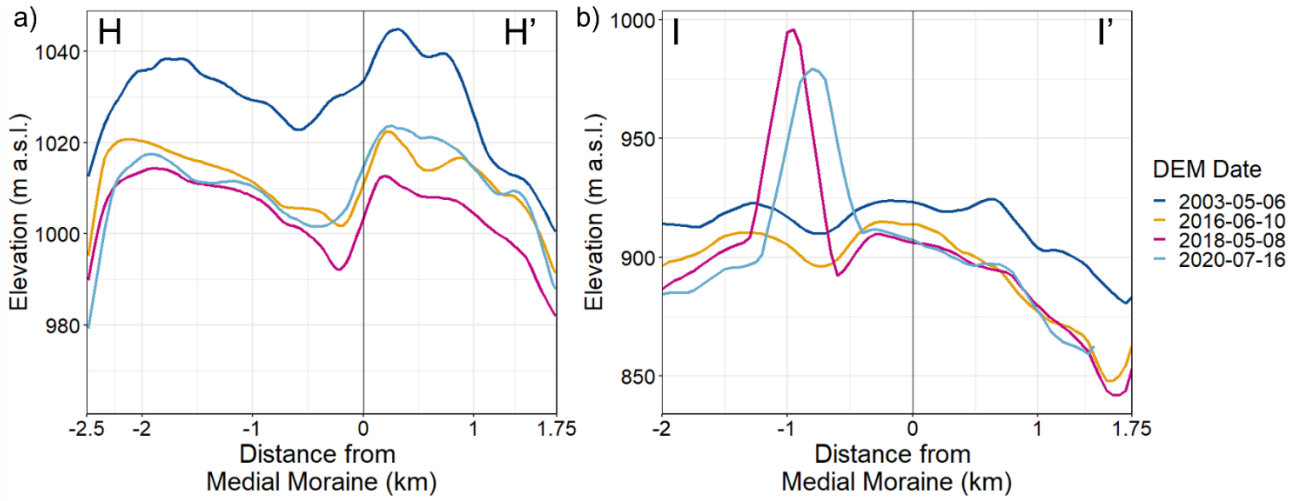

Figure 4-9: Elevation change along cross-profile (a) H-H' and (b) I-I' from 2003-2020. Note: negative values on the x-axis represent the northern side of the glacier, corresponding to Slims Lake. See Figs 4-1 and 4-8 for profile locations.

4.4.4 Terminus velocities

A comparison of the glacier velocities derived from the dGPS record and RADARSAT-2 speckle-tracking for the same dates found generally strong agreement between the two methods, in terms of both magnitude and direction of motion (Fig. 4-10). The RADARSAT-2 velocities were often slightly lower than the point velocities derived from the dGPS station, likely due to the ~500 m averaging area that the speckle-tracking velocities are derived from. However, the magnitudes only varied by < 0.001.

Long-term (1995-2018) annual velocities from the ITS_LIVE dataset point to variations which occur over multi-year periods, particularly for the north lobe (Fig. 4-11a) compared to the south (Fig. 4-11b). For the north lobe, highest velocities occurred a distance of 8-10 km from the terminus. From 1995-99, glacier velocities at this location for the north lobe reduced from ~120 to ~90 m a^{-1}, then increased through the 2000's, peaking in 2012 at ~160 m a^{-1}, after which they dropped from ~155 m a^{-1} in 2015 to ~120 m a^{-1} in 2018. While the velocity signal is dominated by the high velocities up-glacier, there is also a clear signal in the lowermost ~3 km of the terminus, where average velocities ranged from a low of ~20 m a^{-1} in 1998/99, and increased dramatically through the 2000's to a peak of ~125 m a^{-1} in 2013. They then decreased from 105 m a^{-1} in 2015 to 55 m a^{-1} in 2018, a 48% loss at a rate of 12.5 m a^{-2}. While the south lobe exhibits a weaker signal (Fig. 4-11b), average glacier velocities followed a similar pattern to the north lobe.

From the detailed patterns provided by the RADARSAT-2 data since 2014 it is clear that the north and south lobes behaved differently (Fig. 4-7), with the centerline profiles indicating that the north lobe experienced the largest velocity changes at ~3 km up-glacier from the terminus (Fig. 4-12a). Velocities decreased from ~100 m a^{-1} in 2014-2015, to 75 m a^{-1} in 2016-2017 and finally to 50 m a^{-1} in 2017-21. The south lobe experienced the largest change in velocities at 5-7 km up-glacier from the terminus, where they decreased from ~100 m a^{-1} in 2014, to ~75 m a^{-1} in 2015/16, 50 m a^{-1} in 2017 and finally to 25 m a^{-1} in 2021 (Fig. 4-12b). Velocity data in 2021 is more noisy than other years due to the change in data source from RADARSAT-2 to RCM, and associated change in spatial resolution and reduction in number of scenes available for averaging (Appendix 4-D).

At the cross-profiles since 2014, velocities are consistently higher up-glacier near cross-profile G-G′ (16-18 km up-glacier from the terminus; Fig. 4-12c), and have shown little recent slowdown. In comparison, velocities at profiles H-H′ and I-I′ (within 7 km of the terminus; Figs 4-12d, 4-12e)

are lower and have slowed dramatically over 2014-21, with the highest velocities decreasing from ~90 to 50 m a^{-1} near the glacier centreline, and to near stagnation at the glacier margins.

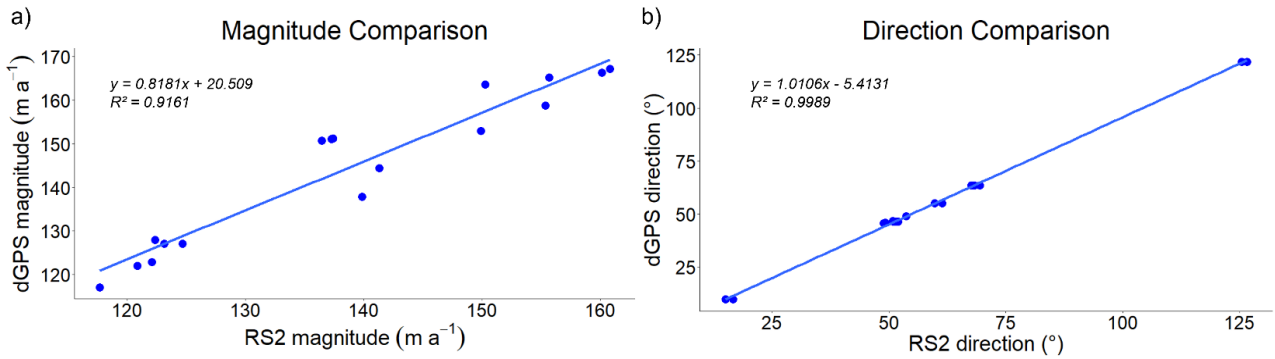

Figure 4-10: Comparison of RADARSAT-2 derived ice motion (a) magnitude and (b) direction values with in-situ velocities from the Kaskawulsh dGPS Station (location shown in Fig. 4-1). Solid blue line shows the 1:1 relationship between the two measurement methods.

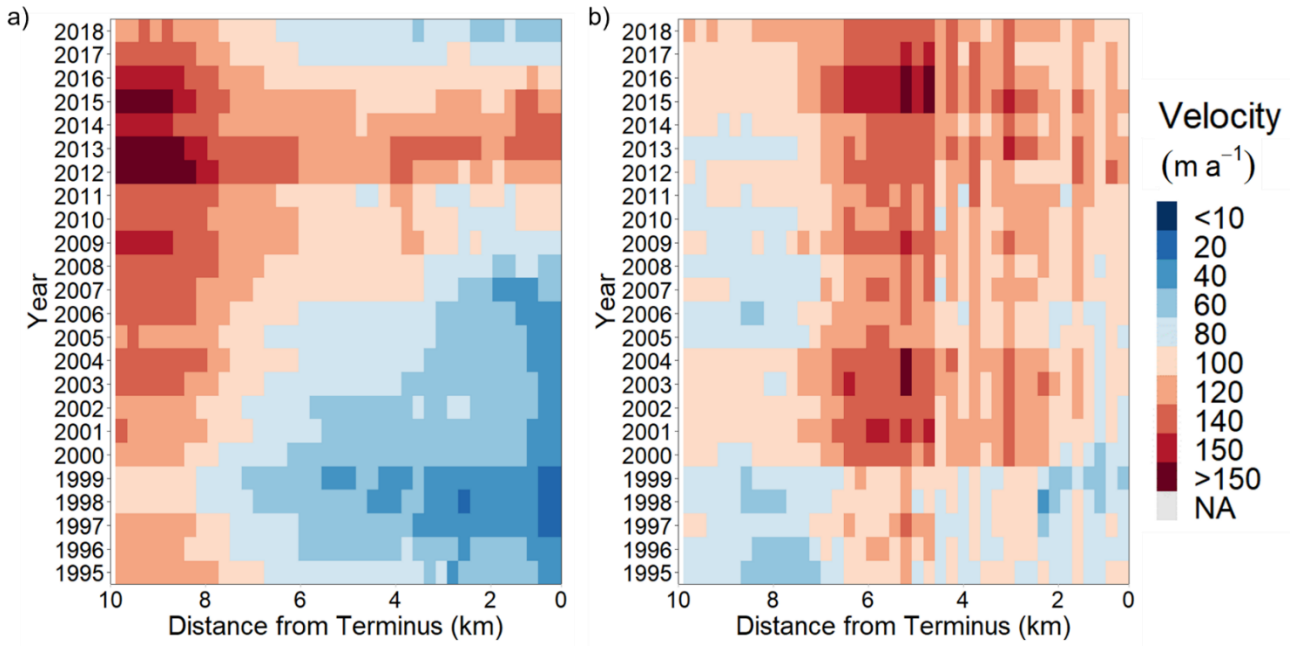

Figure 4-11: Annual average velocity profiles in m a^{-1} created from ITS_LIVE data along the (a) north and (b) south lobe centrelines of Kaskawulsh Glacier, 1995-2018. See Figure 4-1 for location of centrelines and distance markers.

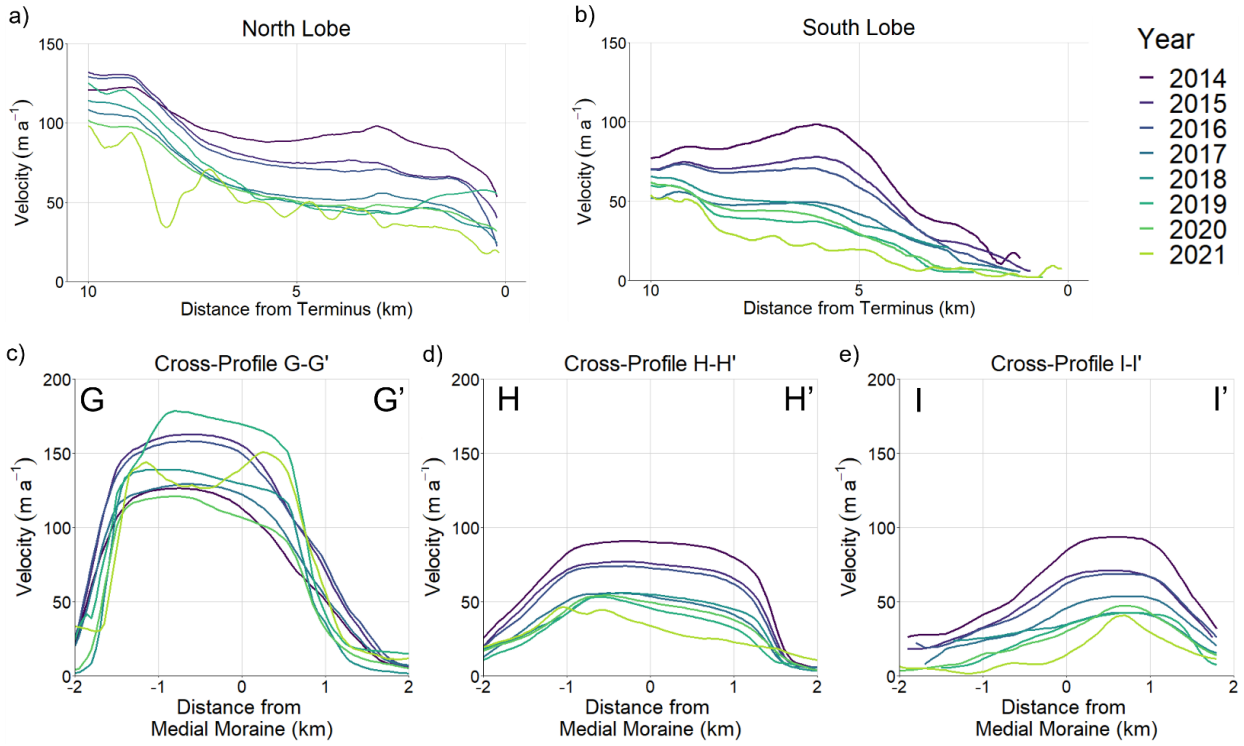

Figure 4-12: Velocity profiles in m a^{-1} derived from speckle-tracking of Radarsat-2 data for centrelines along the (a) north and (b) south lobes of Kaskawulsh Glacier, 2014-2021. Cross-profiles of velocity measurements in m a^{-1} at cross-profiles (c) G-G', (d) H-H' and (e) I-I’ on Kaskawulsh Glacier from 2014-2021. Locations for all centrelines, cross-profiles and distance markers are shown in Fig. 4-1.

4.4.5 Terminus Floatation

Comparison of the ratio of ice thickness to water depth in 2015, 2016 and 2021 allowed for determination of the location of terminus flotation along line A-A′ to be calculated for these years (Fig. 4-13a; with ranges provided for 2015 and 2016 to account for the variability in ice thinning of 1 to 2 m a^{-1} (Young and others, 2020) compared to the 2021 ice thickness measurements). In 2015, both the high and low estimates for floatation were below 0, which indicates that the ice was floating for the lowermost ~350 m of the terminus as it entered Slims Lake. In contrast, after the drainage of Slims Lake in May 2016, no section of the terminus was floating in summer 2016, with 0.8 to 10.1 m of ice loss needed to induce floatation over the lowermost ~200 m at that time. In 2021 there was also no evidence of floatation, with at least 2.7 m of thinning required to induce floatation over the lowermost 27 m of the terminus, and more needed up-glacier of there.

Figure 4-13b indicates the region of the terminus that was likely floating, based on extrapolation of the 2015 floatation zone along line A-A′ and ice surface elevation contours, verified with the presence of water-filled crevasses and ponded water on the glacier surface in 5 m resolution RapidEye-3 imagery from September 8, 2015. This region accounts for the upper range in surface melt in Figure 4-13a and covers an area of 1.13 km^2, extending ~100 to 800 m inland from the terminus. In addition, the presence of large, tabular icebergs in Slims Lake are indicative of a floating terminus, as this is the condition typically required to produce these features.

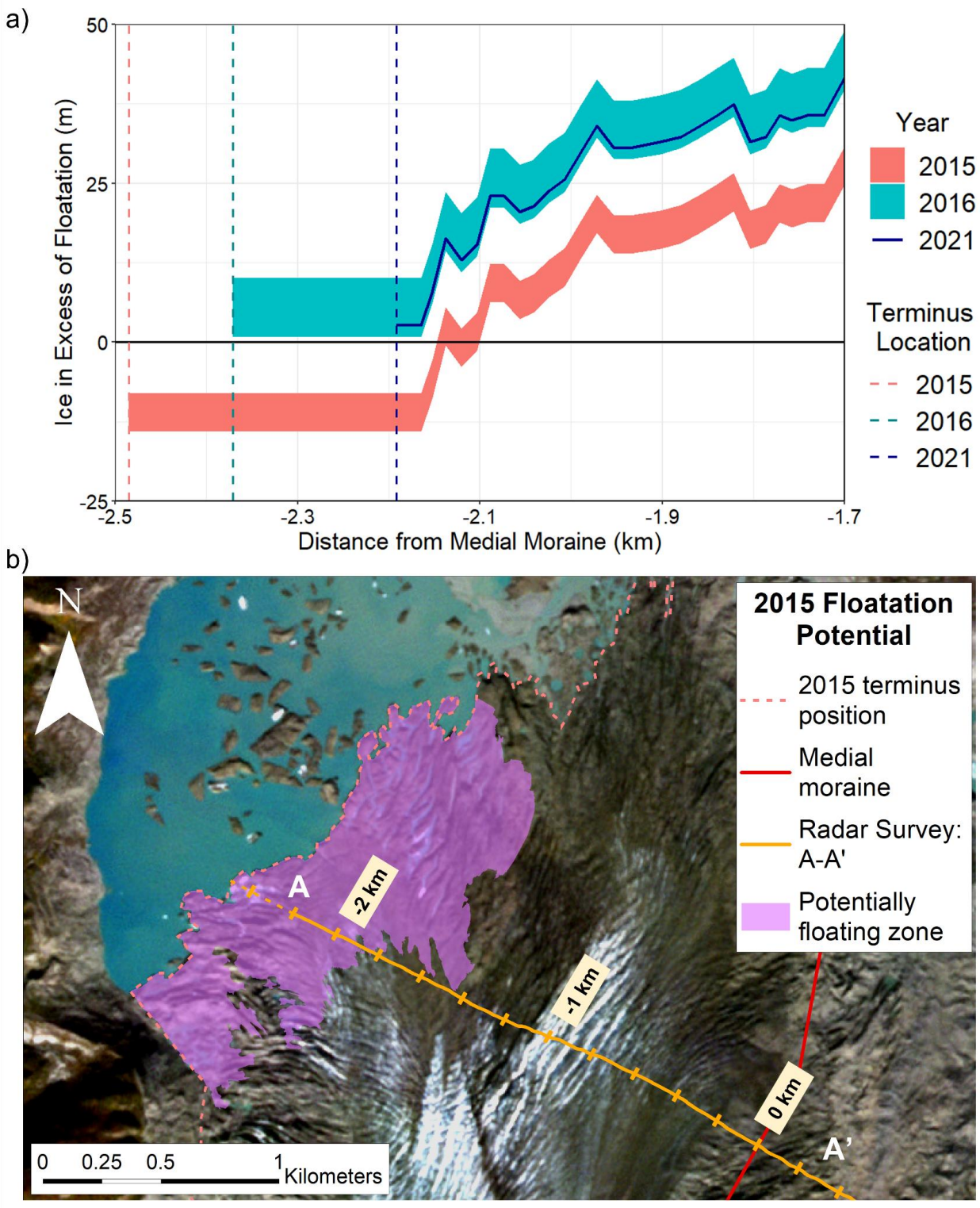

Figure 4-13: (a) Ice in excess of floatation at Kaskawulsh Glacier terminus in 2015, 2016 and 2021, along a section of radar line A-A' (see Fig. 4-4a for ice thicknesses). The vertical dashes represent the terminus extent for 2015 (coral), 2016 (green) and 2021 (dark blue). (b) Zone of likely floatation at the terminus of Kaskawulsh Glacier as it entered Slims Lake in 2015, based on ice surface elevation and presence of water-filled crevasses in RapidEye-3 imagery. Projection: UTM 7N; base image: RapidEye-3, September 8 2015

4.5 Discussion

4.5.1 Long-term changes in terminus position

The long-term photographic record highlighted in this study (Figs 4-2, 4-3) demonstrates that Kaskawulsh Glacier was still near its Little Ice Age maximum extent in 1899/1900. Previously, Borns and Goldthwait (1966) suggested that the glacier began advancing in the 1500s, reaching its maximum Little Ice Age (LIA) limit by ~1690. However, radiocarbon dating of tree fragments in the outermost terminal moraine by Reyes and others (2006) place the timing of maximum extent from 1717-1750. Their outline represents the maximum LIA extent of the glacier, with the north (Slims Lake) lobe dated to the mid-1750s, and the southern (Kaskawulsh Lake) lobe to 1717. The relative proximity of the 1899/1900 terminus position to the 1717/1750 moraines, along with a Geological Survey of Canada map of the glacier terminus from 1900 to 1904 (McConnell, 1905; see Fig. 4-2a in Flowers and others, 2014) indicate that there were only minor changes in the terminus position of Kaskawulsh Glacier from ~1750 until the start of the 20th century. The expansion of Kaskawulsh Glacier occurred concurrently with that of the coastal Gulf of Alaska glaciers, which reached their LIA maximum extent (or maintained their maximal positions) from 1790-1900 (Gaglioti and others, 2019).

Kaskawulsh Glacier has been retreating since the beginning of the 20th century, with rates increasing since the start of the 21st century (Fig. 4-5). The glacier has been experiencing long-term thinning in the terminus region compared to the LIA maximum extent, with estimated ice thickness loss from 1899 to 2021 ranging from 186 to 279 m, with an average of 227 m, based on a comparison of ice-free DEMs with 1899/1900 terminus extent along bedrock outcrops (i.e., ice marginal locations in Figs 4-2, 4-3). The total volume loss of the terminus from 2003-20 (extent of black polygon in Fig. 4-8) was 0.38 ± 0.005 km^3, at a mean thinning rate of 1.56 m a^{-1}, equivalent to 0.35 ± 0.005 Gt of ice. The formation of substantial proglacial lakes occurred at Kaskawulsh Glacier between 1900 and 1956, as they were not present in the 1899 or 1900 historical photos (Figs 4-2a, 4-3a). There was significant growth in Slims Lake after 1990, when it had drained completely, to a maximum of 3.6 ± 0.2 km^2 in 2015. Lake area grew steadily from 1995-2009, varied little between 2010-14, and then increased sharply in 2015 before draining in 2016 (Fig. 4-6). The size and location of Kaskawulsh and Slims lakes have evolved (Fig. 4-6a) simultaneously with terminus retreat (Fig. 4-5), with the lakes growing and changing location to occupy regions

previously covered by glacier ice. This glacier-lake evolution has also been observed across the Southern Alps in New Zealand, as demonstrated by Carrivick and others (2022).

4.5.2 Long-term changes in terminus velocity

The velocity patterns indicate that ice flow at the terminus is dominated by the north lobe (Figs 4-7, 4-11), which flows into Slims Lake, compared to the south lobe, which terminates in Kaskawulsh Lake. This velocity pattern has been evident since the mid-1990s, and along with ice thickness observations (Fig. 4-4a), indicates that significantly more ice is funnelled through the north lobe towards Slims Lake, whereas the south lobe has been relatively stagnant in comparison.

Borns and Goldthwait (1966) estimated glacier velocity near the terminus to be ~215 m a^{-1} for 1953-55, although the exact location is not known, precluding any detailed comparisons with our measurements. Waechter and others (2015) reported a peak winter velocity at cross-profile H-H′ of approximately 180 m a^{-1} in 1987-88, 60 m a^{-1} in 1997-98 and 80 m a^{-1} in 2011-12, which align with the winter RADARSAT-2 velocities reported here (Fig. 4-7). Average annual ITS_LIVE velocities decreased at H-H′ and I-I′ from 1995-99, from ~45 to ~20 m a^{-1} and ~30 to 15 m a^{-1}, respectively (Fig. 4-6b). From 2000-13, average velocities increased at cross-profile H-H′ from ~25 to ~75 m a^{-1} and at I-I′ from ~20 to ~70 m a^{-1} . The highest velocities observed at both H-H′ and I-I′ occurred in 2013, at ~135 m a^{-1}.

To understand the drivers of more recent changes of the velocity of the north lobe, analyses were undertaken of the relationship between the mean velocity at profiles G-G′, H-H′ and I-I′ and the changes in area of Slims Lake (Appendices 4-E and 4F). R2 values demonstrate that ~30% of the variance of the combined winter and annual average velocities at H-H′ and I-I′ is explained by Slims Lake area ($p < 0.05$), while the relationship at G-G′ is not significant. More variability is explained when average winter velocities are excluded (~50 and ~40%, for H-H′ and I-I′, respectively) (Appendix 4-F). This indicates that there is a relationship between changing ice velocities and Slims Lake extent close to the terminus, whereas up-glacier the influence of the lake size is minimal, and that this relationship is significant only when considering annual average velocities.

4.5.3 Rapid change in velocity after 2016 Slims Lake drainage and loss of floatation

Analysis of velocities over the 5-year periods before (2010-15), and after (2016-21), the Slims Lake drainage for each of the terminus lobes are shown in Appendix 4-G. Pre-drainage (2010-15) there was no significant change in velocity change for either lobe, nor within the combined terminus region. After the 2016 drainage, there was a statistically significant slowdown ($p \leq 0.05$) across the terminus at a mean rate of 3.5 m a^{-2}, with the slowdown dominated by the north lobe, decreasing at 4.0 m a^{-2} compared to the south lobe decreasing by 2.9 m a^{-2}.

Our analysis shows that, while Kaskawulsh Glacier winter velocities have been slowing prior to the May 2016 proglacial lake drainage, the velocity decreased markedly after 2016 to a low of <50 m a^{-1} in 2021 (Fig. 4-12b). The effect is most pronounced over the lower 5 km of the north lobe terminus, where velocities decreased from ~75 to <50 m a^{-1}, a 33% decrease. Annual average ITS_LIVE velocities (Fig. 4-11), while temporally limited up to 2018, indicate a similar drop in velocities from ~100 m a^{-1} in 2015, to ~60 m a^{-1} in 2018 within 5 km of the terminus, a 41% loss. From 5-10 km up-glacier, the signal is weaker, where velocities decreased from ~130 m a^{-1} in 2015 to 100 m a^{-1} in 2018, a 22% deceleration. This indicates that the effect of the proglacial lake might be localised, as beyond ~7 km up-glacier from the terminus the friction from the valley sides and the distance from the floating section can limit any additional dynamic thinning and acceleration.

The floatation data (Fig. 4-13) suggests that the last 325 to 375 m of the glacier terminus was floating in 2015, but that floatation has not occurred since then despite continued retreat, an increase in the lake size, and continued ice thinning. This suggests that the May 2016 drainage event and associated loss of floatation was a primary driver of the recent reductions in velocity across the glacier terminus, in combination with the ongoing reduction in ice thickness due to surface melt.

4.5.4 Lake theory: hydrology and flow dynamics

An additional possible driver slowing ice flow following lake drainage is adjustments to the basal hydrology. Channels form at the base of glaciers when there is a strong gradient in hydraulic potential which allows sufficiently fast water flow to melt the overlying ice (Röthlisberger, 1972; Shreve, 1972). This is influenced by the baseline or outlet potential; when a lake is present that is floating the terminus of a glacier, the outlet hydraulic potential is the same as the ice overburden

pressure. However, when that lake drains, the outlet pressure is atmospheric, immediately steepening the hydraulic gradient. The change in gradient would encourage faster water flow underneath the ice and therefore growth of larger and more efficient channels that can become lower pressure, and can draw more water from the distributed subglacial system, slowing down the ice further (Fountain and Walder, 1998).

If we take the ice thickness and surface elevation from near the centreline along radar line A-A′, and from near the terminus along radar line B-B′, we can calculate the hydraulic potential for both a full lake and drained lake scenario. We use the Shreve (1972) hydraulic potential equations with the assumption that water pressure underneath the ice is at overburden pressure:

$$\emptyset = \rho_w g z + \rho_i g H, \qquad (2)$$

where ρ_w is the density of water (1000 kg m^{-3}), ρ_i is the density of ice (917 kg m^{-3}), g is the acceleration due to gravity (9.81 m s^{-2}), z is the elevation of the bed (m), and H is the ice thickness (m). We calculate the average gradient of hydraulic potential using the following:

$$\nabla\emptyset = \frac{(\rho_w g z_1 + \rho_i g H_1) - (\rho_w g z_2 + Pw_2)}{D}, \qquad (3)$$

where z_1 and H_1 are the basal and ice thickness values (m) at the upper site, z_2 is the basal elevation (m) at the terminus, D is the distance between the upper site and terminus (m), and Pw_2 is the outlet water pressure either at overburden pressure (if the lake is full) or 0 if the lake is empty. This gives a value of 339.7 Pa m^{-1} when the lake is full and 440.6 Pa m^{-1} when the lake is empty, demonstrating a significant increase in hydraulic potential gradient that would directly impact flow rates of subglacial water. Even when water is at pressures lower than overburden, depending on the volumes entering the system, the change in hydraulic gradient will impact the rates that water flow to the outlet at atmospheric pressure.

Longitudinal stretching is another process which may have been influenced by the growth of Slims Lake (Fig. 4-6) as the glacier terminus thinned (Figs 4-8, 4-9) and the ice started to float (Fig. 4-13). When floatation occurs, there is a reduction in basal friction and increased velocities cause thinning to propagate up-glacier (Benn and Evans, 2010). This can also impact subglacial hydrology by reducing the overburden pressure and steepening the hydraulic gradient. This process was documented at Glaciar Upsala, in Southern Patagonia, where, once floatation and enhanced

basal sliding was induced, longitudinal stretching rates reached 0.22 a^{-1} (Naruse and Skvarca, 2000); as well as at Yakutat Glacier, Alaska, where 17% of total ice thinning was attributed to dynamic thinning from 2007-10 (Trüssel and others, 2013). A dGPS study in the Himalaya found that ice thickness loss was 3 times greater for a lake-terminating glacier compared to land-terminating, with numerical modelling indicating that this was driven by dynamically induced ice thinning along with a negative surface mass balance (Tsutaki and others, 2019). Similarly, Pronk and others (2021) found that ~50% of the lake-terminating glaciers in their study area experienced a velocity acceleration towards the glacier termini, which they attributed to dynamic thinning.

Thinner ice is more easily able to crevasse and to calve into a lake, thus increasing terminus retreat and allowing Slims Lake to grow (Warren and Kirkbride, 2003; Benn and others, 2007; Tsutaki and others, 2019). During the 2000-15 period of lake growth and velocity acceleration, crevassing at the terminus increased in both intensity and extent (Appendix 4-H). The frequent presence of large, tabular icebergs in Slims Lake suggests that calving is a more common process at the north lobe terminus, compared to the south lobe at Kaskawulsh Lake, where significantly fewer and much smaller icebergs are observed, and the ice is much thinner (Fig. 4-4a). This increase in longitudinal drag pulls ice at an accelerated rate from upstream until friction from the valley walls and the distance from the floating segment mitigate the additional dynamic thinning and acceleration (~5 km from glacier terminus), thus limiting the impact on up-glacier velocities.

The presence of a reverse bed slope (Fig. 4-4a), particularly over the northern portion of the terminus, indicates that as Kaskawulsh Glacier continues to retreat (up to 23 km as suggested by Young and others, 2020), deeper topography will be exposed. While a substantial portion of Slims Lake drained in 2016, it has started to grow again, and it will continue expanding as it infills exposed space vacated by retreat. Schoof (2007) has shown that steady grounding lines cannot be stable on reverse bed slopes because retreat into deeper water enhances ice flux, promoting additional terminus recession; however, Schoof's study does not account for lateral support, such as from valley walls, which may impact the degree of instability and be an influence for Kaskawulsh Glacier. As Slims Lake expands into the exposed trough, it will become easier for floatation to occur, which may cause velocities to increase, and for the grounding line to rapidly retreat (Sutherland and others, 2020). For example, rises in bedrock topography were found to strongly control glacier terminus fluctuations at Glaciar Upsala, Argentina (Naruse and Skvarca,

2000). Field and others (2021) also suggest that proglacial lake geometry and topographic setting (e.g., the ability for the surrounding basin to accommodate lake growth, as is possible under a reverse-slope regime) exert a key influence on glacier stability.

4.5.5 Comparisons with velocity changes at other proglacial lakes

The influence of proglacial lakes on glacier terminus velocities and glacier dynamics have previously been examined in locations such as Switzerland, New Zealand, Nepal and Iceland (Tsutaki and others, 2013; Haritashya and others, 2015; Baurley and others, 2020). For example, Robertson and others (2013) found that an increase in the size of a proglacial lake adjacent to Hooker Glacier, New Zealand, occurred simultaneously with an increase in terminus retreat, as ablation changed from melting to calving. Modelling of Yakutat Glacier found that while proglacial lake presence has a substantial immediate influence on glacier retreat rates via calving, this is subsequently compensated for through an increase in surface melt, leading to near-equal glacier volume loss over time (Trüssel and others, 2015). Haritashya and others (2015) reported that the lowermost ~3 km of Tasman Glacier, New Zealand, experienced a steady acceleration from near-stagnation to 40-50 m a-1 during the 2000's which coincided with the rapid growth of a proglacial lake, while a study of Rhonegletscher, Switzerland also demonstrated an increase in annual velocity by a factor of 2.7 at the glacier terminus during the formation of a proglacial lake over a 5-year period (Tsutaki and others, 2013). In the central and eastern Himalaya, Pronk and others (2021) found that velocities of land-terminating glaciers were on average less than half those of lake-terminating glaciers.

Numerical modelling has suggested that the presence of a proglacial lake caused the glacier to retreat more than 4 times further up-glacier, and ice acceleration 8 times higher, compared to the modelled glacier with the same climatic parameters terminating on land (Sutherland and others, 2020). In simulations of Pukaki Glacier in New Zealand, lake presence contributed up to 82% of the grounding line recession and 87% of ice velocity for the first 5000 years before influence declined, suggesting that the largest impact on glacier dynamics is during the transition between a land-terminating and lake-terminating environment (Sutherland and others, 2020). The relationship between proglacial lake size and glacier velocities is more moderate at Kaskawulsh Glacier compared to those predicted by numerical modelling, possibly due to complicating environmental/structural factors including the irregular bed shape and additional proglacial lake.

Regardless, this study provides a basis to investigate further the implications of increasing proglacial lake size on glacier dynamics.

4.6 Conclusions

This study has extended the photographic record of Kaskawulsh terminus changes to 120 years, almost doubling the length of the previous record of Foy and others (2011), demonstrating that terminus retreat since the end of the LIA continues, but has been increasing in recent years. The glacier has experienced fluctuations in annual and wintertime average velocities from 1995-2021, but two main trends are common between the velocity datasets. From 2000-15, annual average glacier velocities increased at a rate of ~5.5 m a^{-2}, while from 2010-15 average winter velocities increased by ~2 m a^{-2}. Associated with increasing velocities was the expansion of proglacial Slims Lake at the northern terminus, from ~0.2 km^2 in 1995 to ~3.6 km^2 in 2015. The spring 2016 drainage of Slims Lake instigated a major reduction in both winter and annual average terminus velocities through a loss of floatation along the northern terminus. Average winter velocities decreased at a rate of ~3.5 m a^{-2} from 2016-21 across the terminus zone, dominated by reductions in the northern lobe. From 2016-18, annual average velocities along the lowermost ~10 km of both the north and south glacier centrelines (Fig. 4-1) decreased by ~8 m a^{-1}. Approximately 45% of the change in annual average velocity is explained by the size of Slims Lake. Glacier velocities were mainly influenced within ~7 km of the glacier terminus, suggesting a localised control on glacier dynamics, although further studies are needed to understand if these controls will impact up-glacier velocities over time.

Although the 2016 drainage of Slims Lake ended terminus floatation and locally reduced glacier velocities, the probability of a new, even larger, lake forming is high as the glacier enters a reverse bed slope regime through continued terminus retreat (Young and others, 2020). As such, this scenario provides an opportunity to further study the projected retreat of Kaskawulsh Glacier and its application to glacier dynamics. Representing the mid-point on the climate sensitivity continuum between least sensitive (tidewater glaciers) to highest sensitivity (land-terminating glaciers) (Warren and Kirkbride, 2003), the impacts of various factors on lake-terminating glaciers are not yet fully understood and require further examination. Such linkages will likely be of increased importance in the coming decades as it has been hypothesised that there may be an

increase in proglacial lake formation with climate warming (Zhang and others, 2015; Cook and others, 2016; Furian and others, 2022).

4.7 Data availability

The photogrammetry dataset (DEM and Orthomosaic) generated for this study, together with our RADARSAT-2 wintertime glacier velocities, are available from the Polar Data Catalogue (https://polardata.ca/) under CCIN reference numbers 13285 and 13292, respectively. Original RADARSAT-2 data is available through MDA Geospatial Services (https://www.asc-csa.gc.ca/eng/satellites/radarsat2/order-contact.asp). Historical terrestrial photos are available from the Mountain Legacy Project website (https://mountainlegacy.ca). All satellite imagery (Landsat, Sentinel-2 and ASTER), air photos, and ITS_LIVE annual velocity mosaics are publicly available from data sources listed in the methods.

References

Bachelder J and 6 others (2020) Chemical and microphysical properties of wind-blown dust near an actively retreating glacier in Yukon, Canada. *Aerosol Science and Technology* **54**(1), 2-20. doi: 10.1080/02786826.2019.1676394

Barrand NE and Sharp MJ (2010) Sustained rapid shrinkage of Yukon glaciers since the 1957 - 1958 International Geophysical Year. *Geophysical Research Letters* **37**, 1-5. doi:10.1029/2009GL042030

Baurley NR, Robson BA and Hart JK (2020) Long-term impact of the proglacial lake Jökulsárlón on the flow velocity and stability of Breiðamerkurjökull glacier, Iceland. *Earth Surface Processes and Landforms* **45**, 2647-2663. doi: 10.1002/esp.4920

Benn DI, Warren CR and Mottram RH (2007) Calving processes and the dynamics of calving glaciers. *Earth-Science Reviews* **82**, 143-79. https://doi.org/10.1016/j.earscirev.2007.02.002

Benn DI and Evans DJA (2010) Glaciers and Glaciation, 2nd Edition. Hodder Education. United Kingdom. pp 789.

Bigelow DG, Flowers GE, Schoof CG, Mingo LDB, Young EM and Connal BG (2020) The role of englacial drainage of an ice-dammed lake, Kaskawulsh Glacier, Yukon, Canada. *Journal of Geophysical Research: Earth Surface* **125**, 1-21. https://doi.org/10.1029/2019JF005110

Borns HW and Goldthwait RP (1966) Late-Pleistocene fluctuations of Kaskawulsh Glacier, SW Yukon Territory, Canada. *American Journal of Science* **264**(8), 600-619. doi:10.1016/j.yqres.2006.06.005

Briggs R, Thibault C, Mingo L, and King T (2020) Usage of UAVs for Surveying and Monitoring Icebergs (Essay). *Journal of Ocean Technology* **15**(3), 46-57.

Brooks AH (1905) The Geography and Geology of Alaska. A Summary of Existing Knowledge. *United States Geological Survey Professional Paper No. 45*. Washington, Government Printing Office, 327.

Carrivick JL and 6 others (2022) Coincident evolution of glaciers and ice-marginal proglacial lakes across the Southern Alps, New Zealand: Past, present and future. *Global and Planetary Change*, **211**, 103792.

Ciracì E, Velicogna I and Swenson S (2020) Continuity of the mass loss of the world's glaciers and ice caps from the GRACE and GRACE Follow-On missions. *Geophysical Research Letters* **47**. doi: 10.1029/2019GL086926

Cook SJ, Kougkoulos I, Edwards LA, Dortch J and Hofmann D (2016) Glacier change and glacial lake outburst food risk in the Bolivian Andes. *Cryosphere* **10,** 2399-2413. https://doi.org/10.5194/tc-10-2399-2016

Denton GH and Stuiver M (1967) Late Pleistocene glacial stratigraphy and chronology, northeastern St. Elias Mountains. In: *Bushnell, V.C., and Ragle, R.H., eds. Icefield Ranges*

Research Project: Scientific results. New York: American Geographical Society; Montreal: Arctic Institute of North America. Vol. **1**:197-217.

Farinotti D and 6 others (2019) A consensus estimate for the ice thickness distribution of all glaciers on Earth. *Nature Geoscience*, **12**, 168-173. https://doi.org/10.1038/s41561-019-0300-3

Flowers GE, Copland L and Schoof CG (2014) Contemporary Glacier Processes and Global Change: Recent Observations from Kaskawulsh Glacier and the Donjek Range, St. Elias Mountains. *Arctic* **67**(1), 22-34. http://dx.doi.org/10.14430/arctic4356

Field HR, Armstrong WH and Huss M (2021) Gulf of Alaska ice-marginal lake area change over the Landsat record and potential physical controls. *The Cryosphere* **15**, 3255-3278. https://doi.org/10.5194/tc-15-3255-2021

Fountain AG and Walder JS (1998) Water flow through temperate glaciers. *Reviews of Geophysics **36**(3),* 299-328.

Foy N, Copland L, Zdanowicz C, Demuth M, and Hopkinson C (2011) Recent volume and area changes of Kaskawulsh Glacier, Yukon, Canada. *Journal of Glaciology* **57** (203), 515-525. https://doi.org/10.3189/002214311796905596

Furian W, Maussion F and Schneider C (2022) Projected 21st-Century Glacial Lake Evolution in High Mountain Asia. *Frontiers in Earth Science,* **10**:821798. doi: 10.3389/feart.2022.821798.

Gaglioti BV and 6 others (2019) Timing and potential causes of 19th-century advances in coastal Alaska based on tree-ring dating and historical accounts. *Frontiers in Earth Sciences* **7**(82). doi:10.3389/feart.2019.00082

Gardner AS, Fahnestock MA and Scambos TA (2022) ITS_LIVE Regional Glacier and Ice Sheet Surface Velocities. Data archived at National Snow and Ice Data Center; doi:10.5067/6II6VW8LLWJ7.

Girod L, Nuth C, Kääb A, McNabb R and Galland O (2017) MMASTER: Improved ASTER DEMs for Elevation Change Monitoring. *Remote Sensing* **9**(7), 704. https://doi.org/10.3390/rs9070704

Haritashya UK, Pleasants M and Copland L (2015) Assessment of the evolution in velocity of two debris-covered valley glaciers in Nepal and New Zealand. *Geografiska Annaler* **97**(3), 1-15. doi: 10.1111/geoa.12112

Haritashya UK and 9 others (2018) Evolution and controls of large glacial lakes in the Nepal Himalaya. *Remote Sensing* **10**(5): 798. doi: 10.3390/rs10050798

Hugonnet R and 10 others (2021) Accelerated global glacier mass loss in the early twenty-first century. *Nature* **592**, 726-731. https://doi.org/10.1038/s41586-021-03436-z

Kienholz C and 5 others (2015) Derivation and analysis of a complete modern-date glacier inventory for Alaska and northwest Canada. *Journal of Glaciology* **61**(227), 403-420. doi: 10.3189/2015JoG14J230

Kochtitzky W, Copland L, Painter M and Dow C (2020) Draining and filling of ice-dammed lakes at the terminus of surge-type Dan´ Zhùr (Donjek) Glacier, Yukon, Canada. *Canadian Journal of Earth Science* **57**, 1337-1348. dx.doi.org/10.1139/cjes-2019-0233

Krumwiede BS, Kamp U, Leonard GJ, Kargel JS, Dashtseren A and Walther M (2014) Recent Glacier Changes in the Mongolian Altai Mountains: Case Studies from Munkh Khairkhan and Tavan Bogd. In: Kargel J, Leonard G, Bishop M, Kääb A, Raup B (eds) Global Land Ice Measurements from Space. 481-508. Springer Praxis Books. Springer, Berlin, Heidelberg. https://doi.org/10.1007/978-3-540-79818-7_22

Lague D, Brodu N and Leroux J (2013) Accurate 3D comparison of complex topography with terrestrial laser scanner: Application to the Rangitikei canyon (N-Z). ISPRS *Journal of Photogrammetry and Remote Sensing* **82,** 10–26. https://doi.org/10.1016/j.isprsjprs.2013.04.009

Larsen CF, Burgess E, Arendt AA, O'neel S, Johnson AJ and Kienholz C (2015) Surface melt dominates Alaska glacier mass balance. *Geophysical Research Letters* ***42***(14), 5902-5908. https://doi.org/10.1002/2015GL064349

Lu J and Veci L (2016) Offset Tracking Tutorial: Sentinel-1 Toolbox. Array Systems Computing Inc.

Magnússon E and 6 others (2021) Development of a subglacial lake monitored with radio-echo sounding: case study from the eastern Skaftá cauldron in the Vatnajökull ice cap, Iceland. *The Cryosphere* **15**, 3731-3749. doi: 10.5194/tc-15-3731-2021.

McArthur JJ (1900) International Boundary Survey collection. Accession 1969-095 NPC, plates 62-66 (envelopes 6843-6847). Library and Archives Canada, Ottawa.

McConnell RG. (1905) Sketch map of Kluane Mining District, Yukon Territory. Ottawa: Geological Survey of Canada. http://dx.doi.org/10.4095/107320

Mingo L and Flowers GE (2010) An integrated lightweight ice-penetrating radar system. *Journal of Glaciology* ***56(198)***, 709-714. https://doi.org/10.3189/002214310793146179

Mountain Legacy Project (2017) Historical Photography. Retrieved from http://explore.mountainlegacy.ca.

Narod BB and Clarke GK (1994) Miniature high-power impulse transmitter for radio-echo sounding. *Journal of Glaciology* **40**(134), 190-194. https://doi.org/10.3189/S002214300000397X

Naruse R and Skvarca P (2000) Dynamic features of thinning and retreating Glaciar Upsala, Glacier in Southern Patagonia. *Arctic, Antarctic, and Alpine Research* **32**(4), 485-491. https://doi.org/10.2307/1552398

Nolan M, Larsen C and Sturm M (2015) Mapping snow depth from manned aircraft on landscape scales at centimeter resolution using structure-from-motion photogrammetry. *The Cryosphere* **9**(4), 1445-1463. https://doi.org/10.5194/tc-9-1445-2015

Pelto B, Maussion F, Menounos B, Radić V, and Zeuner M (2020) Bias-corrected estimates of glacier thickness in the Columbia River Basin Canada. *Journal of Glaciology* **66**, 1-13. doi: 10.1017/jog.2020.75

Pronk JB, Bolch T, King O, Wouters B and Benn DI (2021) Contrasting surface velocities between lake- and land-terminating glaciers in the Himalayan region. *The Cryosphere* **15**, 5577-5599. https://doi.org/10.5194/tc-15-5577-2021

Rabatel A, Sanchez O, Vincent C and Six D (2018) Estimation of Glacier Thickness From Surface Mass Balance and Ice Flow Velocities: A Case Study on Argentière Glacier, France. *Frontiers in Earth Science* **6**. doi: 10.3389/feart.2018.00112.

Reyes A, Luckman B, Smith D, Clague J and Van Dorp R (2006) Tree-Ring Dates for the Maximum Little Ice Age Advance of Kaskawulsh Glacier, St. Elias Mountains, Canada. *Arctic* **59**(1), 14-20.

RGI Consortium (2017) Randolph Glacier Inventory - A Dataset of Global Glacier Outlines: Version 6.0: Technical Report, Global Land Ice Measurements from Space, Colorado, USA. Digital Media. doi: https://doi.org/10.7265/N5-RGI-60

Robertson CM, Brook MS, Holt KA, Fuller, IC and Benn DI (2013) Calving retreat and proglacial lake growth at Hooker Glacier, Southern Alps, New Zealand. *New Zealand Geographer* **69**, 14-25. doi: 10.1111/nzg.12001

Röthlisberger H (1972) Water pressure in intra-and subglacial channels. *Journal of Glaciology, 11*, 177-203. https://doi.org/10.3189/S0022143000022188

Schellenberger T, Van Wychen W, Copland L, Kääb A and Gray L (2016) An Inter-Comparison of Techniques for Determining Velocities of Maritime Arctic Glaciers, Svalbard, Using Radarsat-2 Wide Fine Mode Data. *Remote Sensing* **8**(9), 785. https://doi.org/10.3390/rs8090785

Schoof C (2007) Ice sheet grounding line dynamics: Steady states, stability, and hysteresis, *Journal of Geophysical Research* **112**, F03S28, doi:10.1029/2006JF000664

Shean DE and 6 others (2016) An automated, open-source pipeline for mass production of digital elevation models (DEMs) from very high-resolution commercial stereo satellite imagery, *ISPRS Journal of Photogrammetry and Remote Sensing* **116**, 101-117. doi: 10.1016/j.isprsjprs.2016.03.012, 2016

Shean, DE (2021) pygeotools Documentation. Release 0.2.0.

https://pygeotools.readthedocs.io/en/latest/readme.html

Shreve R. (1972) Movement of Water in Glaciers. *Journal of Glaciology* **11**(62), 205-214. doi:10.3189/S002214300002219X

Shugar DH and 6 others (2017) River piracy and drainage basin reorganization led by climate-driven glacier retreat. *Nature Geoscience* **10**, 370-375. doi: 10.1038/ngeo2932

Shumskiy P (1960) Density of Glacier Ice. *Journal of Glaciology* **3**(27), 568-573. doi:10.3189/S0022143000023686

Solomon S and 7 others (2007) *Climate Change 2007: The Physical Science Basis. Contribution of Working Group I to the Fourth Assessment Report of the Intergovernmental Panel on Climate Change*. Cambridge University Press, Cambridge.

Sutherland JL and 5 others (2020) Proglacial lakes control glacier geometry and behavior during recession. *Geophysical Research Letters* **47.** https://doi.org/10.1029/2020GL088865

Trüssel BL, Motyka RJ, Truffer M and Larsen CF (2013) Rapid thinning of lake-calving Yakutat Glacier and the collapse of the Yakutat Icefield, southeast Alaska, USA. *Journal of Glaciology* **59**, 149-161. https://doi.org/10.3189/2013J0G12J081

Tsutaki S, Sugiyama S, Nishimura D, and Funk M (2013) Acceleration and floatation of a glacier terminus during formation of a proglacial lake in Rhonegletscher, Switzerland. *Journal of Glaciology* **59**(215), 559-571. https://doi.org/10.3189/2013JoG12J107

Tsutaki S, and 6 others (2019) Contrasting thinning patterns between lake- and land-terminating glaciers in the Bhutanese Himalaya. *The Cryosphere*, **13**, 2733-2750. https://doi.org/10.5194/tc-13-2733-2019

Van Wychen W, Copland L, Jiskoot H, Gray L, Sharp M and Burgess D (2018) Surface velocities of glaciers in western Canada from speckle-tracking of ALOS PALSAR and RADARSAT-2 data. *Canadian Journal of Remote Sensing* **44**(1), 57-66. doi: 10.1080/07038992.2018.1433529

Waechter A, Copland L and Herdes E (2015) Modern glacier velocities across the Icefield Ranges, St. Elias Mountains, and variability at selected glaciers from 1959 to 2012. *Journal of Glaciology* **61**(228), 624-634. doi: 10.3189/2015JoG14J147

Warren CR, and Kirkbride MP (2003) Calving speed and sensitivity of New Zealand lake-calving glaciers. *Annals of Glaciology*, **36**, 173-178. https://doi.org/10.3189/172756403781816446

Williamson SN and 9 others (2020) Evidence for elevation-dependent warming in the St. Elias Mountains, Yukon, Canada. *Journal of Climate*, **33,** 3253-3269. doi: 10.1175/JCLI-D-19-0405.1

Young EM, Flowers GE, Berthier E and Latto R (2020) An imbalancing act: the delayed dynamic response of the Kaskawulsh Glacier to sustained mass loss. *Journal of Glaciology* **67**(262), 313-330. https://doi.org/10.1017/jog.2020.107

Zemp M and 10 others (2019) Global glacier mass changes and their contributions to sea-level rise from 1961 to 2016. *Nature* **568**, 382-386. doi: 10.1038/s41586-019-1071-0

Zhang G, Yao T, Xie H, Wang W and Yang W (2015) An inventory of glacial lakes in the Third Pole region and their changes in response to global warming. *Global and Planetary Change* **131,** 148-157. doi: 10.1016/j.gloplacha.2015.05.013

Appendix 4-A: List of optical data used in this study. Dates are in YYYY-MM-DD for data from 1956 onwards.

Platform	Date	Resolution (m)	Purpose
Historical Photos	1899 & 1900	NA	Determination of terminus extent
Air Photo Mosaic (1:70,000)	1956-09-10	10	Determination of proglacial lake and terminus extent
Landsat-1	1972-09-02	60	Determination of proglacial lake and terminus extent
Landsat-1	1975-08-18	60	Determination of proglacial lake and terminus extent
Landsat-2	1980-06-25	60	Determination of proglacial lake and terminus extent
Landsat-5	1990-07-20	30	Determination of proglacial lake and terminus extent
Landsat-5	1995-06-09	30	Determination of proglacial lake and terminus extent
Landsat-5	1996-07-13	30	Determination of proglacial lake extent
Landsat-5	1997-06-30	30	Determination of proglacial lake extent
Landsat-5	1998-08-20	30	Determination of proglacial lake extent
Landsat-5	1999-08-23	30	Determination of proglacial lake extent
Landsat-7	2000-07-07	15	Determination of terminus extent
Landsat-7	2000-08-01	15	Determination of proglacial lake extent, crevasse analysis
Landsat-7	2001-07-19	15	Determination of proglacial lake and terminus extent
Landsat-7	2002-06-20	15	Determination of proglacial lake extent
Landsat-7	2002-07-06	15	Determination of terminus extent
Landsat-5	2003-08-25	30	Determination of proglacial lake and terminus extent
Landsat-5	2004-08-20	30	Determination of proglacial lake and terminus extent
Landsat-5	2005-07-11	30	Determination of proglacial lake and terminus extent
Landsat-7	2006-08-09	15	Determination of proglacial lake and terminus extent
Landsat-5	2007-06-01	30	Determination of proglacial lake and terminus extent
Landsat-7	2008-06-11	15	Determination of proglacial lake and terminus extent
Landsat-7	2009-06-11	15	Determination of proglacial lake extent
Landsat-7	2009-08-26	15	Determination of terminus extent
Landsat-7	2010-05-25	15	Seasonal comparison of proglacial lake extent
Landsat-7	2010-08-04	15	Determination of terminus extent
Landsat-7	2010-09-14	15	Determination of proglacial lake extent
Landsat-5	2011-06-23	30	Determination of terminus extent
Landsat-7	2011-07-22	15	Determination of proglacial lake
Landsat-7	2012-06-06	15	Determination of proglacial lake extent
Landsat-7	2012-08-18	15	Determination of terminus extent
Landsat-7	2013-05-25	15	Seasonal comparison of proglacial lake extent
Landsat-7	2013-09-13	15	Determination of proglacial lake and terminus extent
Landsat-8	2014-07-22	15	Determination of proglacial lake and terminus extent
Landsat-8	2015-07-25	15	Determination of proglacial lake extent
Landsat-8	2015-08-03	15	Determination of terminus extent
RapidEye-3	2015-09-08	5	Background imagery, determination of terminus extent
Landsat-7	2015-09-12	15	Crevasse analysis
Landsat-8	2016-07-04	15	Determination of proglacial lake extent
Sentinel-2	2016-09-25	10	Determination of terminus extent
Sentinel-2	2017-06-19	10	Seasonal comparison of proglacial lake extent
Sentinel-2	2017-08-08	10	Determination of proglacial lake and terminus extent
Sentinel-2	2018-07-04	10	Seasonal comparison of proglacial lake extent
Sentinel-2	2018-08-18	10	Determination of proglacial lake and terminus extent

Sentinel-2	2019-06-14	10	Seasonal comparison of proglacial lake extent
Sentinel-2	2019-08-03	10	Background imagery for maps
Sentinel-2	2019-09-05	10	Determination of proglacial lake and terminus extent
Sentinel-2	2020-09-06	10	Determination of proglacial lake and terminus extent
Sentinel-2	2021-05-19	10	Determination of proglacial lake extent
Sentinel-2	2021-06-01	10	Determination of proglacial lake extent
Sentinel-2	2021-07-31	10	Determination of proglacial lake extent
Sentinel-2	2021-09-19	10	Determination of proglacial lake extent

Appendix 4-B: List of DEMs used in this study.

Date (yyyy-mm-dd)	Platform	Resolution (m)	Uncertainty (m)		Purpose
			Vertical	Horizontal	
2003-05-06	ASTER	30	10	2	Determination of glacier ice elevation, ice elevation trend & ice volume loss
2006-07-12					
2016-06-10					
2018-05-08					
2020-07-16					
2012-10-29	SETSM WorldView	30	10	2	Determination of glacier ice elevation & ice elevation trend
2014-11-14					
2021-07-28; 2021-08-01	Fixed Wing Aircraft	0.5			Determination of glacier terminus floatation status, drained lake volumes & proglacial lake surface height

Appendix 4-C: Change in proglacial lake area at Kaskawulsh Glacier, 1956-2021.

Date (yyyy-mm-dd)	North: Slims Lake (km^2)	Uncertainty (km^2)	South: Kaskawulsh Lake (km^2)	Uncertainty (km^2)
1956-09-10	0.66	0.1	0.35	0.1
1972-09-02	0.21	0.1	1.44	0.4
1975-08-18	0.46	0.3	-	-
1980-06-25	0.04	0.1	1.36	0.5
1990-07-20	0.00	-	1.13	0.2
1995-06-09	0.19	0.1	-	-
1996-07-13	0.23	0.2	-	-
1997-06-30	0.65	0.3	-	-
1998-08-20	0.71	0.2	-	-
1999-08-23	0.56	0.2	-	-
2000-08-01	0.49	0.1	1.35	0.1
2001-07-19	0.65	0.1	-	-
2002-06-20-	0.85	0.1	-	-
2003-08-25	0.89	0.3	-	-
2004-08-20	0.89	0.3	-	-
2005-07-11	1.11	0.4	1.60	0.3
2006-08-09	1.51	0.2	-	-
2007-06-01	1.49	0.2	-	-
2008-06-11	1.34	0.1	-	-
2009-06-11	1.98	0.1	-	-
2010-09-14	1.81	0.1	1.96	0.2
2011-07-22	1.78	0.2	-	-
2012-06-06	1.72	0.1	-	-
2013-09-13	1.73	0.1	-	-
2014-07-22	1.73	0.2	-	-
2015-07-25	3.66	0.2	2.69	0.2
2016-07-04	1.13	0.1	3.15	0.1
2017-08-08	0.87	0.1	-	-
2018-08-18	0.89	0.1	2.50	0.1
2019-09-05	1.00	0.1	1.76	0.1
2020-09-06	1.22	0.1	1.26	0.1
2021-05-19	1.23	0.1	1.03	0.1
2021-06-01	1.23	0.1	1.14	0.1
2021-07-31	1.36	0.1	3.01	0.2
2021-09-12	1.2	0.1	0.99	0.1

Appendix 4-D: Summary of SAR imagery used to derive glacier surface velocities in this study. RCM = RADARSAT Constellation Mission; FBS = Fine-beam single; F = Fine; UF = Ultra-fine; M = Medium. Velocity error was calculated from the mean of apparent motion over stable ground adjacent to the glaciers.

Sensor	Beam Path/ Swath	Date 1	Date 2	Resolution (m)	Mode	Velocity error (m a^{-1})
ALOS PALSAR	245	2007-12-21	2008-02-05	10	FBS	8.5 - 15.0
ALOS PALSAR	243	2008-01-02	2008-02-17			
ALOS PALSAR	241	2008-01-14	2008-02-29			
ALOS PALSAR	242	2009-12-21	2010-02-05			
ALOS PALSAR	240	2010-01-02	2010-02-17			
ALOS PALSAR	244	2010-01-24	2010-03-11			
RADARSAT-2	F6	2011-01-03	2011-01-27	8	F	16.6
RADARSAT-2		2011-01-27	2011-02-20			
RADARSAT-2		2011-02-20	2011-03-16			
RADARSAT-2	F6F	2011-01-13	2011-02-06			
RADARSAT-2		2011-02-06	2011-03-02			
RADARSAT-2		2011-03-02	2011-03-26			
RADARSAT-2	F2N	2010-12-31	2011-01-24			
RADARSAT-2		2011-01-24	2011-02-17			
RADARSAT-2		2011-02-17	2011-03-13			
RADARSAT-2	U10W2	2012-02-18	2012-03-13	3	UF	12.7
RADARSAT-2		2012-03-13	2012-04-06			
RADARSAT-2	U9W2	2012-02-21	2012-03-16			
RADARSAT-2		2012-03-16	2012-04-09			
RADARSAT-2	U7W2	2014-02-03	2014-02-27	3	UF	7.2
RADARSAT-2		2014-02-27	2014-03-23			
RADARSAT-2	U17W2	2014-02-24	2014-03-20			
RADARSAT-2		2014-03-20	2014-04-13			
RADARSAT-2	U7W2	2015-01-29	2015-02-22	3	UF	8.4
RADARSAT-2		2015-02-22	2015-03-18			
RADARSAT-2	U17W2	2015-02-19	2015-03-15			
RADARSAT-2		2015-03-15	2015-04-08			
RADARSAT-2	U7W2	2016-01-24	2016-02-17	3	UF	6.7
RADARSAT-2		2016-02-17	2016-03-12			
RADARSAT-2	U17W2	2016-02-14	2016-03-09			
RADARSAT-2	U7W2	2017-01-18	2017-02-11	3	UF	5.6
RADARSAT-2		2017-02-11	2017-03-07			
RADARSAT-2	U17W2	2017-01-15	2017-02-08			
RADARSAT-2		2017-02-08	2017-03-04			
RADARSAT-2	U7W2	2018-01-13	2018-03-02	3	UF	2.5
RADARSAT-2	U6W2	2019-04-07	2019-05-01	3	UF	6.5
RADARSAT-2	U17W2	2019-04-11	2019-05-05			
RADARSAT-2	U17W2	2020-01-24	2020-02-17	3	UF	5.4
RADARSAT-2	U6W2	2020-01-27	2020-02-20			
RCM	15	2021-01-02	2021-01-14	16	M	14.7

Appendix 4-E: Changes in lake surface elevation, volume, and depth of proglacial lake

ASTER optical imagery was imported into ArcGIS (version 10.7), and visual inspection was undertaken to check for georeferencing, and any mismatches were realigned using the "shift" tool. The ortho-imagery was aligned using a bedrock outcrop on the north side of the glacier, the bedrock knob near the centre of the glacier terminus, and the mountains on the south side of the glacier. The lake outlines were then drawn using the "create features" tool in ArcGIS (version 10.7), and the area and perimeter were computed using the "compute geometries" tool. To ensure accuracy, a minimum of 75 points were used to delineate each outline.

Lake outlines from July 25, 2015 (before the drainage) and June 10, 2016 (after the drainage) were overlain, and the "erase" tool in ArcGIS (version 10.7) was used to isolate the area of newly exposed lakebed. The topography of the drained lakebed was extracted from the July 28/August 1, 2021 SfM DEM and converted into a Triangular Irregular Network, which was used as an input for the "polygon volume" tool in ArcGIS (version 10.7). This tool calculates the volume of a polygon beginning from a defined reference plane; this value was set at the lowest elevation of the 2016 drained lake surface (782.3 m asl), which was 14.6 m lower than the 2015 lake surface. This was then multiplied by the area of the 2016 lake and added to the 2015 drained lakebed volume to obtain the total lake volume change. The same process was used to calculate the change in lake volume between 2016 and 2021, which showed a 5.8 m decrease in water surface elevation.

Trend analysis

A custom R script was used to obtain velocity and elevation trends, by calculating descriptive statistics (e.g. mean, standard deviation, maximum/minimum values) on a pixel-by-pixel basis on stacked time-series of rasters. This script was run separately on multiple sequences of elevation rasters (using DEMs listed in Appendix 4-B) and velocity rasters (detailed below). A simple one-step linear regression was used to calculate each pixel's slope and significance. Some of the rasters required resampling to ensure that each had the same extent and resolution, which was undertaken using the bilinear interpolation method in ArcGIS (version 10.7) before undertaking the trend analysis. A comparison with the Shean (2021) makestack.py method showed nearly identical results, with differences primarily due to the raster resampling process.

To assess the impact of the proglacial lake drainage on surface velocity, the mathematical slope of each pixel value through time was calculated separately for velocity rasters from 2010-2015 and 2016-2021 (Appendix 4-G). To obtain average trends for the entire terminus region, and for the north lobe and the south lobe separately, the "zonal statistics" tool was used in ArcGIS (version 10.7) to calculate the mean of the mathematical slope over each specific area. Velocities within 500 m of the front of the glacier were excluded due to large inaccuracies in the velocity data in this region associated with rapid changes and calving at the terminus, and regions of heavily debris-covered dead ice.

Appendix 4-F: A comparison of ITS_LIVE, ALOS-PALSAR, RADARSAT-2 and RCM derived velocities (m a^{-1}) vs. Slims Lake area (km^2) at the three cross-profiles I-I', H-H' and G-G' (Fig. 4-1) from 1995-2021. Solid blue line shows the 1:1 relationship between the two variables, with a confidence interval of 95% (shaded zone). Table contains corresponding regression analysis (R^2 and p-values) for the linear model, divided based on seasonal time-period (winter vs. annual averages) and by cross-profile location (Fig. 4-1).

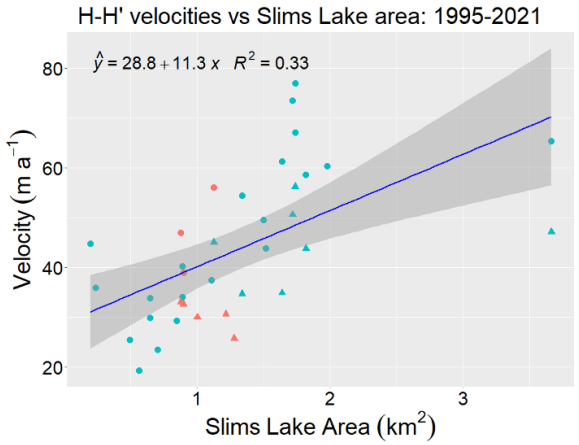

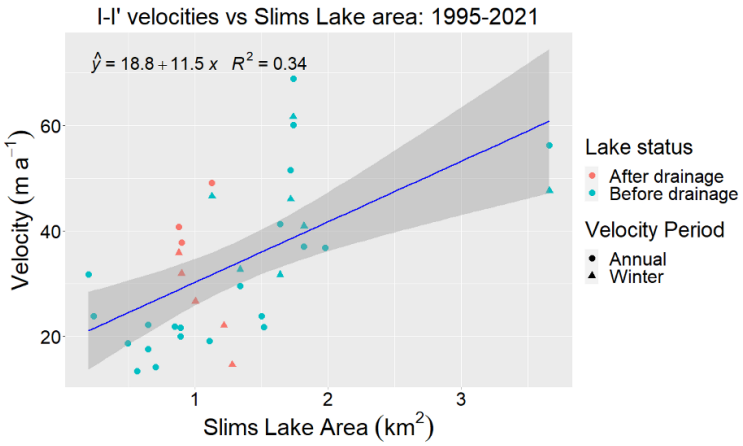

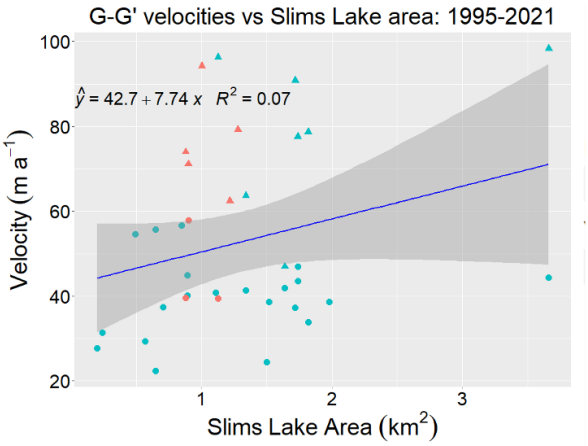

Cross-profile	Velocity time period	R^2	p-value
I-I'	Annual Average	0.40	0.0009
	Winter	0.19	0.1511
	Combined	0.34	0.0001
H-H'	Annual Average	0.52	0.00006
	Winter	0.27	0.0810
	Combined	0.33	0.0002
G-G'	Annual Average	0.006	0.7150
	Winter	0.10	0.3127
	Combined	0.07	0.1099

Appendix 4-G: Analysis of mean trends in velocity for 2010-2015 and 2016-2021 from RADARSAT-2 and RCM image pair velocity rasters for the terminus region, as defined by the 2020 terminus outline shown in Figure 4-5, with the centreline along the medial moraine serving as the division between the two lobes (Fig. 4-1). Note the north lobe feeds into Slims Lake, and south lobe feeds into Kaskawulsh Lake. The trends from 2010-2015 are not significant at the 95% confidence level, as p-values are greater than 0.05.

Time Period	**Velocity Trend (m a^{-2})**			**p-value**		
	North Lobe	**South Lobe**	**Terminus Average**	**North Lobe**	**South Lobe**	**Terminus Average**
2010-2015	3.6	2.9	2.0	0.14	0.09	0.39
2016-2021	-4.0	-2.9	-3.5	0.03	0.03	0.03

Appendix 4-H: A comparison of crevassing extent and intensity at Kaskawulsh Glacier terminus between (a) 2000 and (b) 2015. Landsat-7, band 8 imagery (15 m resolution). Projection: UTM Zone 7N. Dates are in YYYY-MM-DD.

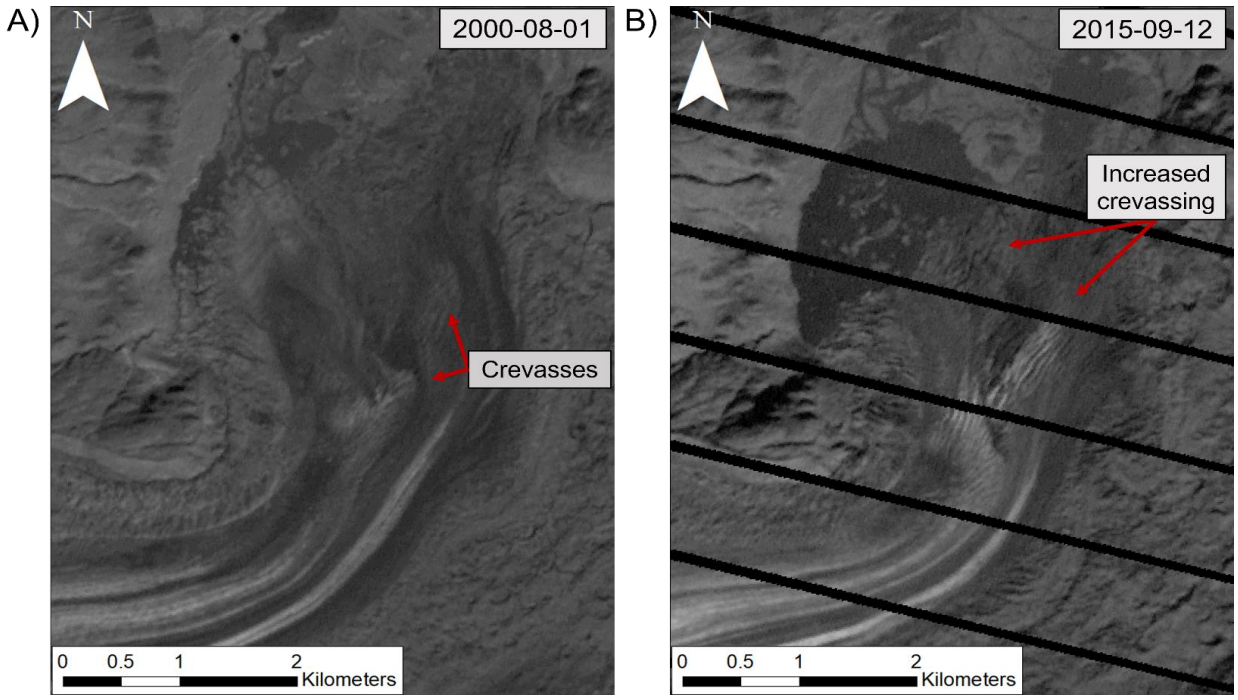

Chapter 5: Conclusions

This thesis presents an analysis of ice dynamics in the St. Elias Mountains on multiple temporal and spatial scales, including an updated regional assessment of surge-type glaciers and surging behaviour, a comprehensive analysis of the surging behaviour of Little Kluane Glacier, and an analysis of the impacts of a proglacial lake on glacier velocities at non-surging Kaskawulsh Glacier. This research demonstrates the value of combining field data alongside multiple remote sensing datasets and techniques to better understand ice dynamics of both surge-type and non-surging glaciers.

5.1 Summary

Analysis of annual average and winter velocities found that 231 (4.6%) of glaciers in the St. Elias Mountains are surge-type, with 66 (34%) of these glaciers observed to have surged since 1874 through either direct measurements or remote sensing observations. Surge-type glaciers comprise ~77% of the total glaciated area in the St. Elias Mountains, and are typically larger, longer, and flatter than non surge-type glaciers. From 1874 to 2023, there were 193 observed and dated glacier surges, and further analysis was possible for 55 events from 1985-2023. For glaciers with observed surges, these predominantly fall into two categories: Alaskan-style surges with short active and quiescent phases, and glacier pulses, which are episodic velocity accelerations limited in magnitude and which may represent an intermediate behaviour between normal flow and surging. Slow surges are also present at a couple of glaciers in this region, lasting up to 28 years or longer. In general, glacier surges initiate in the winter and terminate in the summer. There is a high variability in trunk-tributary interactions and terminus advance, although there are signs that surge magnitude is decreasing for multiple glaciers.

Observations of Little Kluane Glacier suggest that a partial surge of just the upper north arm likely occurred between 1963 and 1972, while a full surge occurred from 2013-18. The recent surge initiated from the upper north arm accumulation area in 2013, which developed into a full surge of the main trunk from 2017-18. Terminus positions show long-term retreat from 1949-2017, followed by rapid advance of >2 km from May to September 2018 with surface velocities reaching a peak of ~3600 m a^{-1} in summer 2018 over the lower ablation area. This was likely enhanced by the drainage of supraglacial lakes and streams to the glacier bed through crevassing as the surge progressed. This highlights the high variability of surging behaviour found in the St. Elias

Mountains, and suggests that it may be possible for glaciers to switch between partial and full surges. This may be due to the topographic conditions created by the partial surge, which enabled supraglacial water to pool and drain for several years during the build up to a full surge, potentially supplying water to the glacier bed, and enhancing basal sliding.

A hydrologic reorganization at the front of Kaskawulsh Glacier in 2016 provided the opportunity to examine the impact of a proglacial lake on local glacier velocities. First, a detailed history of the glacier from 1899-2020 was presented to demonstrate that long-term terminus retreat and thinning led to the partial drainage of proglacial Slims Lake as a topographic restriction at the glacier front was removed, allowing the lake to drain towards Alaska for the first time. Then, the impact of Slims Lake drainage was quantified, showing that terminus velocities increased at a rate of 3 m a^{-2} from 2000–12 during a period when the lake was growing in area. The rapid drainage of the lake in 2016 substantially altered the velocity profile, causing a reduction in mean annual velocities by 48% within 3 km of the terminus between 2015 and 2021, at an average rate of ∼12.5 m a^{-2}. A major reason for the rapid drop in glacier motion was a reduction in flotation of the lower part of the glacier terminus after lake drainage.

5.2 Contributions and limitations

Primary contributions of this thesis to the research community includes an updated dataset of wintertime glacier velocity fields across the St. Elias Mountains from 2014-21, and regional maps showing average quiescent velocities (1985-2018) and maximum surging velocities (1985-2023). Previous studies have mainly focused on one- and two-year snapshots (e.g., Waechter and others, 2015; Van Wychen and others, 2018, 2023), which do not provide adequate data for long-term characterizations of winter velocities. However, despite providing an additional 7 years of data, these velocity mosaics still contain gaps in coverage due to data availability, and therefore represent a limitation of this study.

An additional contribution consists of an updated surge-type glacier inventory for the St. Elias Mountains from 1874-2023, as well as the subsequent analysis of 55 observed surge events from 1985-2023. While previous work (Post, 1969; Clarke and others, 1986; Sevestre and Benn, 2015) had provided an inventory of surge-type glaciers in this region, and a broad analysis of their key characteristics (e.g., length, size and branchiness statistics), no analysis of the common behaviours of surge events had been provided. By analyzing 193 surge events, this study was able to determine

the general active and quiescent phase duration, and surge recurrence intervals. In addition, the analysis of 55 surge events from 1985-2023 provides a framework for categorizing glacier surges into four main types (Alaskan-style, pulsing, slow surge, partial surge) based on glacier velocity patterns, and changes in velocity magnitude between quiescent and active phases. These categorizations could be applied to other regions with clusters of surge-type glaciers to help improve global understanding of glacier surging. The detailed inventory also provides a significant contribution to studies of glacier surges by collecting and synthesizing existing literature into an easily searchable database, which future studies will be able to use to determine macro-level differences between surge-type and non-surging glaciers, including factors such as changes in mass balance, regional precipitation patterns, and terminus retreat rates.

While other studies of individual glacier surges in the study region had described Alaskan (e.g., Bevington and Copland, 2014; Kochtitzky and others, 2019; Nolan and others 2021) and slow surges (e.g., Frappé and Clarke 2007; De Paoli and Flowers, 2009), no study had previously analyzed a partial surge. The detailed study of Little Kluane Glacier not only presents the first reported partial surge in the region, but also suggests a mechanism that may cause partial surges to transition into full Alaskan-style surges, providing a novel contribution to our understanding of the interactions between surficial hydrology and surging. The conditions that led to this mechanism should be considered during future studies of other Alaskan-style surges. Prior studies have also considered the interactions between glacier tributaries and their trunks on a regional level (e.g., Sevestre and Benn, 2015), in other regions (e.g., Sund and others, 2009), and in the St. Elias Mountains (e.g., Altena and others, 2019), but few have demonstrated in detail that a small tributary can have such a major impact on a main glacier trunk. The findings at Little Kluane Glacier therefore contribute to new understanding of how trunk-tributary interactions can influence glacier surging propensity.

Finally, previous studies have focused on quantifying the influence of proglacial lake existence on velocities through modelling (e.g., Sutherland and others, 2020), or through temporally limited (e.g., 5 years) velocity observations (Tsutaki and others, 2013). However, no other study has quantified the impact of proglacial lake size and resulting ice floatation on glacier velocities with observations both before and after lake drainage. As proglacial lakes are predicted to increase in a warmer, wetter world, this study provides valuable context for glacier modelling and associated

changes in glacier mass balance and dynamics (Zhang and others, 2015; Cook and others, 2016; Furian and others, 2022). However, the lack of direct lake depth data presents a limitation for the Kaskawulsh work, and could be improved for future proglacial-lake studies.

5.3 Future work

This research has demonstrated the importance and limitations of long-term and multi-period observations in understanding glacier dynamics in the St. Elias Mountains, on both macro and local scales. To further improve our understanding of ice dynamics in this region there are a number of knowledge gaps that should be addressed.

At the local scale, individual glacier surge studies are still needed, as with the increasing temporal and spatial resolution of satellite and field data, it becomes possible to better infer the potential mechanisms that drive fast flow (e.g., such as at Little Kluane Glacier). For example, with the increasing availability of high resolution (3-5 m) Planet imagery (Planet, 2017), a future project could combine our record of glacier surges with optical images to scan Alaskan-style surge events to identify whether partial surges may have occurred elsewhere in the years leading up to a full surge. In addition, during the creation and analysis of the glacier surge inventory, it became clear that studies of individual glacier surges report many unique characteristics in different ways and on different temporal and spatial scales, often with the use of inconsistent terminology. For example, it is not always clear what the distinction is between the acceleration and active phases of a surge. Therefore, there is a need for the glaciology community to standardize some of the terminology, and to consistently report different stages of glacier surges (or if they are not experienced at all), such as the acceleration, active, and deceleration phases.

On a regional level, there is a need for increased winter velocity observations, as these measurements are essential for understanding the true initiation period of most surging glaciers, as well as the true magnitude of velocity increases between active and quiescent phases (Abe and Furuya, 2015; Van Wychen and others, 2023). SAR imagery is required to create winter velocity mosaics, as features on the glacier surface used for optical feature tracking (such with the ITS_LIVE dataset) are obscured by snow-cover, long shadows, and darkness during the winter months (Schellenberger and others, 2016; Van Wychen and others, 2018). SAR imagery can also be difficult to obtain due to security restrictions and tasking prioritization of other acquisition sites, which are often determined by federal government security priorities (e.g., the Government of

Canada) (Smyth and others, 2018). While a regional inventory of ice-marginal lake presence and change has recently been completed (Field and others, 2021), there still exists an opportunity to connect these changes with regional glacier velocities, to determine what the impact of changes in these lakes are on ice dynamics. There is also a need for an inventory of glacier termini positions over multiple (e.g., decadal) timescales, which would enable improved analysis of glacier mass balance patterns (Hugonnet and others, 2019), and which could be used alongside the surge inventory to better understand connections between mass balance and glacier surging. In terms of analysis, there is also a need for a comprehensive and focused examination of how glacier tributaries and main trunks interact in the context of surging in the St. Elias Mountains, as has been completed for other, smaller regions (Bhambri and others, 2022).

One major limitation to a variety of work is the current Randolph Glacier Inventory (RGI) GIS shapefile structure (Pfeffer and others, 2014). This database classifies all glacier tributaries and their main trunks under the same ID code, making it difficult to analyze and categorize their individual behaviour at a regional level. A modification to the RGI, such as a hierarchy of tributaries, could enable such an analysis. These shapefiles also require significant updating to account for glacier terminus retreat and separation of glaciers into multiple entities. Specifically, the RGI was designed to provide global glacier outlines as close as possible to the year 2000, representing a single snapshot in time that is inherently out-of-date considering the recent changes in glacier area (Pfeffer and others, 2014; Maussion and others, 2023). The RGI is a subset of the Global Land Ice Measurements from Space (GLIMS) database, which is multi-temporal, although this database lacks completeness and is not updated often (Raup and others, 2000). As such there is a need within the glaciology community for improved global glacier outline inventories that are updated more frequently.

Globally, there is a need to systematically analyze and categorize glacier surging behaviour based on velocity patterns in other regions where there are clusters of surge-type glaciers, such as the Karakoram, Svalbard, and the Canadian Arctic. Current studies have mainly considered changes in glacier surface elevation (Goerlich and others, 2020; Wu and others, 2020), terminus positions (Vale and others, 2021; Zhou and others, 2021), and crevassing or looped moraines (Sund and others, 2009; Herzfeld and others, 2021) when analyzing surge behaviour, with little research examining regional velocity changes in a systematic way. This has only recently become possible

due to the new ITS_LIVE dataset, which provides annual average glacier velocity mosaics from 1985-2018 globally (Gardner and others, 2019).

5.4 Larger context

Recent studies have emphasised the impact of anthropogenic climate change on the cryosphere, with increasing mean annual air temperatures amplified in glaciated regions at high latitudes and altitudes (Williamson and others, 2020; IPCC, 2021). This has led to widespread glacier retreat (WGMS, 2015; Gutiérrez and others, 2021) and mass loss (Hugonnet and others, 2021) across almost all glaciated regions. However, as glacier response time varies based on both glacier size and local characteristics, it is still poorly defined as to what committed ice mass losses will be as the climate continues to warm (Furbish and Andrews, 1984; Fox-Kemper and others, 2021; Young and others, 2021). In addition, increasing surface melt may increase basal lubrication and increase glacier velocities (Zwally and others, 2002), or may slow velocities by increasing the efficiency of subglacial drainage networks, decreasing the amount of water at the bed (Schoof, 2010; Burgess and others, 2013). Finally, the mechanisms underpinning fast glacier flow are thought to be similar for surging glaciers, which have a relatively limited ice mass to contribute to global sea level rise, and the ice sheets, which have the capability to release significantly more water to the oceans (Clarke, 1987). Taken together, these factors, known collectively as ice dynamics, represent major uncertainties in global sea level rise projections (IPCC, 2021). As such, there is high value in researching glacier velocity variability and ice dynamics, on both regional and individual glacier scales, and this importance is anticipated to increase as climate is expected to warm further.

References

Abe T and Furuya M (2015) Winter speed-up of quiescent surge-type glaciers. *The Cryosphere*, **9**, 1183-1190. doi:10.5194/tc-9-1183-2015.

Altena B, Scambos T, Fahnestock M and Kääb A (2019) Extracting recent short-term glacier velocity evolution over southern Alaska and the Yukon from a large collection of Landsat data. *The Cryosphere*, **13**(3), 795-814. doi: 10.5194/tc-13-795-2019.

Bhambri, R and 7 others (2022) Characteristics of surge-type tributary glaciers, Karakoram. *Geomorphology*, **403**, 108161. doi:10.1016/j.geomorph.2022.108161.

Bevington, A. and Copland, L. (2014): Characteristics of the last five surges of Lowell Glacier, Yukon, Canada, since 1948. Journal of Glaciology, 60(219), 113-123. doi: 10.3189/2014JoG13J134.

Burgess EW, Larsen CF and Forster RR (2013a) Summer melt regulates winter glacier flow speeds throughout Alaska. *Geophysical Research Letters*, **40**, doi:10.1002/2013GL058228.

Clarke CKC, Schmok JP, Ommanney SL and Collins SG (1986) Characteristics of surge-type glaciers. *Journal of Geophysical Research,* **91**(B7), 7165-7180. doi: 10.1029/JB091iB07p07165.

Clarke GKC (1987) Fast glacier flow: ice streams, surging, and tidewater glaciers. *Journal of Geophysical Research: Solid Earth*, **92**(B9), 8835-8841. doi: 10.1029/JB092iB09p08835.

Cook SJ, Kougkoulos I, Edwards LA, Dortch J and Hofmann D (2016) Glacier change and glacial lake outburst food risk in the Bolivian Andes. *Cryosphere*, **10**, 2399–2413. doi: 10.5194/tc-10-2399-2016.

De Paoli L and Flowers GE (2009) Dynamics of a small surge-type glacier using one-dimensional geophysical inversion. *Journal of Glaciology* **55**(194):1101-12. doi: 10.3189/002214309790794850

Field HR, Armstrong WH and Huss M (2021) Gulf of Alaska ice-marginal lake area change over the Landsat record and potential physical controls. *The Cryosphere*, **15**, 3255-3278. doi: 10.5194/tc-15-3255-2021.

Fox-Kemper B and 17 others (2021) Ocean, Cryosphere and Sea Level Change. In Climate Change 2021: The Physical Science Basis. Contribution of Working Group I to the Sixth Assessment Report of the Intergovernmental Panel on Climate Change [Masson-Delmotte, V., P. Zhai, A. Pirani, S.L. Connors, C. Péan, S. Berger, N. Caud, Y. Chen, L. Goldfarb, M.I. Gomis, M. Huang, K. Leitzell, E. Lonnoy, J.B.R. Matthews, T.K. Maycock, T. Waterfield, O. Yelekçi, R. Yu, and B. Zhou (eds.)]. Cambridge University Press, Cambridge, United Kingdom and New York, NY, USA, pp. 1211–1362, doi: 10.1017/9781009157896.011.

Furbish DJ and Andrews JT (1984) The use of hypsometry to indicate long-term stability and response of valley glaciers to changes in mass transfer. *Journal of Glaciology*, **30**(105), 199-211. doi: 10.3189/S0022143000005931.

Furian W, Maussion F and Schneider C (2022) Projected 21st-century glacial lake evolution in high mountain Asia. *Frontiers in Earth Science,* **10**, 821798. doi: 10.3389/feart.2022.821798.

Frappé TP and Clarke GKC (2007) Slow surge of Trapridge Glacier, Yukon Territory, Canada. *Journal of Geophysical Research Earth Surface* **112**(3), 1-17. doi: 10.1029/2006JF000607

Gardner AS, Fahnestock MA and Scambos TA (2019) [accessed Jan. 2022] ITS_LIVE Regional Glacier and Ice Sheet Surface Velocities. Data archived at National Snow and Ice Data Center; doi: 10.5067/6II6VW8LLWJ7.

Goerlich F, Bolch T and Paul F (2020) More dynamic than expected: an updated survey of surging glaciers in the Pamir. Earth System Science Data, 12, 3161–3176. doi: 10.5194/essd-12-3161-2020

Gutiérrez JM, and 15 others (2021) Atlas. In Climate Change 2021: The Physical Science Basis. Contribution of Working Group I to the Sixth Assessment Report of the Intergovernmental Panel on Climate Change [Masson-Delmotte V, Zhai P, Pirani A, Connors SL, Péan C, Berger S, Caud N, Chen Y, Goldfarb L, Gomis MI, Huang M, Leitzell K, Lonnoy E, Matthews JBR, Maycock TK, Waterfield T, Yelekçi O, Yu R and Zhou B (eds.)]. Cambridge University Press, Cambridge, United Kingdom and New York, NY, USA, pp. 1927–2058, doi:10.1017/9781009157896.021.

Herzfeld UC, Trantow T, Lawson M, Hans J and Medley G (2020) Surface heights and crevasse morphologies of surging and fast-moving glaciers from ICESat-2 laser altimeter data - Application of the density-dimension algorithm (DDA-ice) and evaluation using airborne altimeter and Planet SkySat data. *Science of Remote Sensing*, **3**, 100013. doi: 10.1016/j.srs.2020.100013

Hugonnet R and 10 others (2021) Accelerated global glacier mass loss in the early twenty-first century. *Nature*, **592**, 726-731. doi: 10.1038/s41586-021-03436-z.

IPCC (2021) Summary for Policymakers. In*: Climate Change 2021: The Physical Science Basis. Contribution of Working Group I to the Sixth Assessment Report of the Intergovernmental Panel on Climate Change* [Masson-Delmotte V, Zhai P, Pirani A, Connors SL, Péan C, Berger S, Caud N, Chen Y, Goldfarb L, Gomis MI, Huang M, Leitzell K, Lonnoy E, Matthews JBR, Maycock TK, Waterfield T, Yelekçi O, Yu R and Zhou B (eds.)]. In Press.

Kamb B (1987) Glacier surge mechanism based on linked cavity configuration of the basal water conduit system. *Journal of Geophysical Research: Solid Earth,* **92**(B9), 9083-9100. Doi: 10.1029/JB092iB09p09083.

Kochtitzky W and 6 others (2019) Terminus advance, kinematics, and mass redistribution during eight surges of Donjek Glacier, St. Elias Range, Canada, 1935 to 2016. *Journal of Glaciology* **65**(252), 565-579. doi: 10.1017/jog.2019.34.

Maussion F, and 11 others (2023) The Randolph Glacier Inventory version 7.0 User guide v1.0. doi:10.5281/zenodo.8362857. Online access: https://doi.org/10.5281/zenodo.8362857.

Nolan A, Kochtitzky W, Enderlin EM, McNabb R and Krutz KJ (2021) Kinematics of the exceptionally short surge cycles of Sít' Kusá (Turner Glacier), Alaska, from 1983 to 2013. *Journal of Glaciology* **67**(264), 744-758. doi: 10.1017/ jog.2021.29.

Pfeffer W, and 18 others (2014) The Randolph Glacier Inventory: A globally complete inventory of glaciers. *Journal of Glaciology*, **60**(221), 537-552. doi:10.3189/2014JoG13J176.

Planet Team (2017) Planet Application Program Interface: In Space for Life on Earth. San Francisco, CA. https://api.planet.com.

Post A (1969) Distribution of surging glaciers in western North America. *Journal of Glaciology* **8**(53): 229- 240. doi: 10.3189/S0022143000031221.

Raup BH, Kieffer HH, Hare TM and Kargel JS (2000) Generation of Data Acquisition Requests for the ASTER Satellite Instrument for Monitoring a Globally Distributed Target: Glaciers. *IEEE Transactions On Geoscience and Remote Sensing,* **38,**1105-1112.

Schellenberger T, Van Wychen W, Copland L, Kääb A and Gray L (2016) An Inter-Comparison of Techniques for Determining Velocities of Maritime Arctic Glaciers, Svalbard, Using Radarsat-2 Wide Fine Mode Data. *Remote Sensing*, **8**(9), 785. doi: 10.3390/rs8090785.

Schoof C (2010) Ice-sheet acceleration driven by melt supply variability. *Nature*, **468**, 803-806. doi: 10.1038/nature09618.

Sevestre H and Benn D (2015) Climatic and geometric controls on the global distribution of surge-type glaciers: implications for a unifying model of surging. *Journal of Glaciology*, **61**(288), 646-663. doi: 10.3189/2015JoG14J136.

Smyth J, Kroupnik G, Iris S and Wierus M (2018) RADARSAT Constellation Mission Data Policy. *IGARSS 2018 - 2018 IEEE International Geoscience and Remote Sensing Symposium*, Valencia, Spain, 6536-6539, doi: 10.1109/IGARSS.2018.8519481.

Sutherland JL and 5 others (2020) Proglacial lakes control glacier geometry and behavior during recession. *Geophysical Research Letters*, **47**, 1–11. doi: doi: 10.1029/2020GL088865

Sund M, Eiken T, Hagen JO and Kääb A (2009) Svalbard surge dynamics derived from geometric changes. *Annals of Glaciology* **50**(52), 50-60. doi: 10.3189/172756409789624265

Tsutaki S, Sugiyama S, Nishimura D and Funk M (2013) Acceleration and floatation of a glacier terminus during formation of a proglacial lake in Rhonegletscher, Switzerland. *Journal of Glaciology*, **59**(215), 559–571. doi: 10.3189/2013JoG12J107.

Vale AB, Arnold NS, Rees WG and Lea JM (2021) Remote Detection of Surge-Related Glacier Terminus Change across High Mountain Asia. Remote Sens. 2021, 13(7), 1309; doi: 10.3390/rs13071309.

Van Wychen W, Copland L, Jiskoot H, Gray L, Sharp M and Burgess D (2018) Surface velocities of glaciers in western Canada from speckle-tracking of ALOS PALSAR and RADARSAT-2 data. *Canadian Journal of Remote Sensing*, **44**(1), 57-66. doi: 10.1080/07038992.2018.1433529.

Van Wychen W, Bayer C, Copland L, Brummell E and Dow C (2023) Radarsat Constellation Mission derived winter glacier velocities for the St. Elias Icefield, Yukon/Alaska: 2022 and 2023. *Canadian Journal of Remote Sensing*, **49**(1), 1-10. doi: 10.1080/07038992.2023.2264395.

Waechter A, Copland L and Herdes E (2015) Modern glacier velocities across the Icefield Ranges, St. Elias Mountains, and variability at selected glaciers from 1959 to 2012. *Journal of Glaciology*, **61**(228), 624-634. doi: 10.3189/2015JoG14J147.

Williamson SN and 9 others (2020) Evidence for elevation-dependent warming in the St. Elias Mountains, Yukon, Canada. *Journal of Climate*, **33**, 3253–3269. doi: 10.1175/JCLI-D-19-0405.

Wu K, and 8 others (2015) Surging Dynamics of Glaciers in the Hunza Valley under an Equilibrium Mass State since 1990. *Remote Sensing*, **12**(18), 2922-2943. doi:10.3390/rs12182922.

Yde JC and Paasche Ø (2010) Reconstructing climate change: Not all glaciers suitable. *Eos, Transactions American Geophysical Union*, **91**(21):189–90. doi: 10.1029/2010EO210001

Young EM, Flowers GW, Berthier E and Latto R (2021) An imbalancing act: the delayed dynamic response of the Kaskawulsh Glacier to sustained mass loss. *Journal of Glaciology*, **67**(262), 313-330. doi: 10.1017/jog.2020.107

Zhang G, Yao T, Xie H, Wang W and Yang W (2015) An inventory of glacial lakes in the third pole region and their changes in response to global warming. *Global and Planetary Change*, **131**, 148–157. doi: 10.1016/j.gloplacha.2015.05.013

Zhou S, Yoa X, Zhang D, Zhang Y, Liu S and Min Y (2021) Remote Sensing Monitoring of Advancing and Surging Glaciers in the Tien Shan, 1990–2019. Remote Sensing, 13(10), 1973; doi: 10.3390/rs13101973.

Zwally HJ, Abdalati W, Herring T, Larson K, Saba J and Steffen K (2002) Surface melt induced acceleration of Greenland ice-sheet flow. *Science*, **297**, 218-222. doi: 10.1126/science.1072708.